

# 博士論文

Application of Computational Fluid Dynamic (CFD) in  
the modelling of internal and external building fire  
(建築火災(内装と外装)のモデリングにおける CFD の  
応用)

周 彪

## **Abstract:**

With rapid development of super-computer and fruitful theoretical modelling, the fire research performed with tests and theoretical analysis have been widely used. Some of results have made contributions to the current fire protection of building fire. However, as the new building materials and complex structures emerge nowadays, the fire protection of buildings performed with above new materials show a big challenge for the current research. At the same time, some severe fire accidents happened in the world which resulted in serious results. Therefore, research over building fire is necessary and urgent.

Regarding the internal building materials fire, the summarized knowledge from bench-scale fire test and intermediate scale could be useful for fire protection. However, the new fire features including high Heat Release Rate (HRR) and combustion gas toxicity have attracted more and more attentions. Regarding the new building material, the knowledge between building materials parameters and reaction-to-fire performance is still unclear. Regarding the external building materials fire, the available preliminary empirical equations have been used in the building fire protection. However, it does not work with respect to the case that the heavy melt-flow materials are performed in the external part. Furthermore, the effects of opening edge, core materials thickness and combustion heat intensity on the fire performance are unclear. The influence of external building materials parameters on the fire performance is unavailable.

Under this condition, this work attempts to use the Computational Dynamic Simulation (CFD) in the application of building fire. It hopes to solve several unsolved problems in building fire experimental tests, report the advantages and disadvantages of CFD in fire simulation, providing

an insight in the further study for CFD fire research and hoping to contribute for fire researchers who have no CFD background, to understand CFD well.

A series of experimental tests and simulation were carried out. The specimens were divided into two types, external building material and internal building materials. The tested internal building materials were composed of some polymers used widely and external building materials are consisted of ETICS fire and cedar façade. The tests for internal fire includes TG-DTA, Cone according to ISO 5660 standard method, and model-box test according to ISO TS 17431 standard method. The tests for external fire includes Intermediate Scale Calorimeter (ICAL) test according to ISO 14696 standard method, External Thermal Insulation Composite System (ETICS) façade fire, cedar timber façade fire according to JIS A 1310 standard method and Fire Propagation Apparatus (FPA) test according to ISO 12136 standard method. The numerical models were modeled by using popular fire CFD tools, such as FDS (version of 6.5), FireFOAM (version of 2.2.x) and ThermaKin (version of 2D).

Regarding the application of CFD in internal building materials fire, the pyrolysis model of polymer extruded polystyrene (XPS), polyurethane (Urethane), poly-isocyanurate (Nurate) and poly-isocyanurate containing fire-retardant (None-Nurate) were modeled using FDS and validated by Cone. Furthermore, the phenomena how coating layer influences Cone test was discussed by using FDS and verification tests. In addition, the capability of FDS to simulate model-box fire was evaluated using specimens Urethane and None-Nurate and validated by corresponding tests. It was found that the FDS could perform well for pyrolysis model. However, some limitation was also clear that lacking of flame heat flux model reduce about 15% heat flux in Cone. The simulation results are grid-dependent and the parameters-dependent. The heat of combustion and heat capacity imposes heavy effects on mass loss rate. When the simulation with

strong pyrolysis products and heavy smoke, the literature are unstable. During the simulation, the mixing-control model seems insufficient for fire which is characterized by complex flame spread and combustible gas diffusion. The discrepancy found at the beginning of test is attributed to the mixing-control model, which makes the predicted time to generate flashover much shorter than experimental time.

With respect to the application of CFD in external building materials fire, fire features of EPS ETICS was discussed by testing a series of EPS ETICS specimen, which vary heating intensity from 100 kW to 1100 kW, EPS thickness from 50 mm to 300 mm, polymer mortar type including SBR polymer mortar and acrylic resin mortar, reinforcement including one layer and two layer's glass fiber mesh, and opening edge treatment method differs from back-wrapping method to fire barrier method. When the EPS ETICS specimen was treated by back-wrapping opening edge treatment method, the peak temperature, EPS burn area, time (20 min) averaged temperature and heat flux density become low. The time (20 min) averaged temperature of each position from T1 to T5 versus EPS thickness is linear at heating intensity 300 kW or 600 kW. A comprehensive fire risk evaluation method of EPS ETICS based on EPS burn area and façade surface temperature profiles of JIS A 1310 tests is proposed. This method could easily classify the effect of mortar, reinforcement, EPS thickness and opening edge treatment method on EPS ETICS fire performance and also provide a method to predict the fire risk of EPS ETICS. It is concluded that in JIS A 1310 method, the fire risk of EPS ETICS could be classified by fire propagation index (FPI) and index method. The fire characteristics of window ejected fire were discussed by investigating the correlation between dimensionless temperature and vertical position  $z$  in an over-ventilated condition using a series of intermediate-scale tests with a 1.35 m (L)  $\times$  1.35 m (H)  $\times$  1.35 m (W) fire compartment (chamber 1) with window opening varied from 0.91 m (H)  $\times$  0.41



m (W) to 0.91 m (H) × 0.91 m (W) and HRR differed from 200 kW to 1000 kW. The Yokoi's correlation was modified on basis of the test results by considering the influence of fire plume re-attaching-to-wall behaviors, varied neutral plane positions and window opening aspect n. The heat characteristics of cedar façade exposed to controlled heat was discussed by using k-type thermocouples to record the temperature distribution over façade surface, calcium silicate board, and support frame. The HRR and THR were also recorded.

Error of the simulated MLR and HRR curves is approximately 13%-19 % compared with Cone Calorimeter test results. The discrepancies between the calculated and measured MLR and HRR curves can be explained by it that the flame heat flux is not accounted for in the FDS model. As discussed above, error of the calculated MLR and HRR curves could be well explained that the flame flux accounts for 15 % of external heat flux in FDS 6.5 and 18.0 % of external heat flux in ThermaKin2D. Therefore, a well modelling work of flame heat flux is needed in the next step research. The vertical direction flame spread is hard to be simulated by FDS. The large eddy simulation (LES) of buoyant window ejected fire plume which comes from the intermediate-scale compartment was modeled using FireFOAM. It was found that with optimal configuration the simulation results shows an agreement compared with tested data on the basis of discussion on flames shapes, temperature vertical distribution inside the chamber, temperature distribution versus vertical distance over external facade surface, heat flux density and temperature over non-combustible walls. The discrepancies are found in the bottom temperature of fire compartment. Temperature profiles vs. vertical distance inside chamber of simulation was believed to be lower than experimental values in the region which is near the bottom of the chamber. FDS is more sensitive to grid mesh size change. The FireFOAM simulation takes high computer cost. After the modelling the cedar pyrolysis model and validation by FPA test, the cedar façade fire was

modeled by optimal gird size and input parameters. The good agreements indicates with the optimal input, an intermediate-scale cedar façade fire could be well reproduced using FireFOAM model. The importance of parameters over time-to-pHRR, pHRR and THR of cedar façade fire are compared.

Regarding the fire stop configuration in a three layer's cedar façade of building, it is found that both the position and width of fire stop would show heavily effects on the cedar façade fire spread. It is found that the distance should be designed to avoid the 0.8 m and 1.2 m because when the fire stop performed with these two distance, the fast spread flame and highest THR are found. It is hard to make a choice between fire prevention and architectural aesthetics, which is believed to be necessary to be taken into account. The discussion is based on the comparison of the difference of fire prevention capacity. Before the determination of optimal fire stop configuration, it is better to conduct the numerical prediction firstly.

### **Key words:**

CFD; Internal building fire; External building fire; FDS (6.5); FireFOAM (2.2.x); ThermaKin (2D); Experimental tests;

# Contents

1. Introduction .....	9
1.1 Problems in building fire research .....	9
1.2 CFD introduction .....	11
1.3 Necessity of CFD .....	14
1.3.1 Low cost, short time and high accuracy .....	15
1.3.2 Impossible to calculate Navier-Stokes equation (N-S) without computer .....	16
1.3.3 Rapid computer development .....	16
1.3.4 Prediction before experiment .....	16
1.3.5 Complex architecture and building materials .....	17
1.4 Research objectives and scope .....	18
1.5 Significance and innovation .....	19
1.6 PhD structure .....	20
1.7 Summary .....	24
2. Comparison of three CFD fire tools .....	26
2.1 Introduction .....	26
2.2 The introduction of three popular CFD fire tools .....	26
2.2.1 FDS .....	26
2.2.2 ThermaKin2D .....	34
2.2.3 FireFOAM2.2.x .....	37
2.3 Comparison of main available fire CFD tools .....	41
2.3.1 FDS .....	41
2.3.2 ThermaKin2D .....	44

2.3.3 FireFOAM .....	45
2.4 Summary .....	48
3. Utilization of CFD model to simulate internal building fire.....	50
3.1 Introduction .....	50
3.2 Experimental materials and planning .....	50
3.2.1 Materials.....	50
3.2.2 Experimental planning.....	51
3.3 Experimental results and discussion.....	54
3.3.1 Thermogravimetry (TG) results and discussion .....	54
3.3.2 Cone Calorimeter results and discussion .....	60
3.3.3 The model-box fire test results and discussion .....	68
3.4 Simulation configuration and results discussion .....	74
3.4.1 Results of Cone modelling.....	74
3.4.2 Melt effect on XPS Cone tests.....	81
3.4.3 The coating effects on the MLR curves .....	82
3.4.4 Modelling of model-box test .....	86
3.5 Summary .....	92
4. Utilization of CFD model to simulate external building fire .....	94
4.1 Introduction .....	94
4.2 Experimental materials and planning .....	95
4.2.1 Experimental materials .....	95
4.2.2 Experimental planning.....	96
4.3 Tests results and discussion .....	104

4.3.1 Cone tests results and discussion .....	104
4.3.2 ICAL results and discussion .....	109
4.3.3 EPS ETICS façade fire test results and discussion .....	111
4.3.4 Experimental study of EPS ETICS Masonry façade reaction-to-fire performance: A fire risk evaluation method .....	132
4.3.5 Experimental study on temperature profile of an intermediate-scale window ejected fire plume under an over-ventilated condition .....	148
4.3.6 Timber FPA test results and discussion.....	171
4.3.7 Timber façade fire results and discussion .....	174
4.4 Simulation results and discussion .....	177
4.4.1 Modelling of EPS ETICS fire .....	177
4.4.2 Large eddy simulation of buoyant window ejected fire plume from intermediate-scale compartment fires using FireFOAM .....	188
4.4.3 Numerical study of cedar façade fire .....	202
4.5 Summary .....	219
5. Conclusions .....	224
6. References .....	230
Acknowledgement .....	239

# 1. Introduction

In this chapter, the introduction of research background, CFD tools and thesis structure are presented. With an aim to show why CFD is necessary, the problems in building fire research is firstly summarized. Then the necessity of CFD is outlined by several reasons: 1. Low cost, short time and high accuracy. 2. Impossible to calculate Navier-Stokes equation (N-S) without computer. 3. Rapid computer development 4. Useful prediction before experimental test. 5. Complex architecture and building materials shows a new and big challenge for building safety. Following this is the CFD introduction which is performed by introducing the concepts, background of CFD, and the traditional CFD calculation flows with four steps. Furthermore, the overview of CFD fire tools is presented briefly. Finally, research scope, significance and innovation and structure of PhD thesis are shown.

## 1.1 Problems in building fire research

- The tests are expensive.

Although the reaction-to-fire performance of materials can be evaluated by bench scale tests, the large-scale test is usually believed to well reproduce the real fire. Regarding the large-scale test, it takes a long time to prepare and a big fund to set up the test configuration. The test place is also very limited since it is very dangerous. Utilization of CFD could be a potential method for fire research since it is much cheaper than traditional large-scale fire tests.

- The repeatability of large-scale tests is fair.

During the large-scale tests, some parameters are difficult to control under the certain condition. For example, wind speed and direction showed a heavy effect on fire test. Control of wind seems impossible. The system error in the measurement enlarges in the high temperature region. In the case of intermediate-

scale fire test, the repeatability is fair. The conclusions made based on a series of tests could be useful for fire protection engineer.

- Very hard to get some field information.

With respect to fire research, the heat transfer is one of important factors to accelerate fire spread. To well understand the temperature field or heat flux field would be useful for explanation of fire observation. However, the temperature information got from thermocouple is found to be different from gas temperature. The temperature value of thermocouple depend on the material parameters of alloy, convective heat, radiation heat received from the bead surface. The similar situation also happens in the measurement of heat flux using heat flux meters. Take another case for example, the neutral plane is an important factor for calculation of window spilled fire plume. In the intermediate-scale tests, the neutral plane position seems difficult to get because of high temperature (over 1500 k), which is defined as the location of zero pressure difference varying vertical height of opening. In the model-box test, the influence of building parameters on the reaction-to-fire performance is hard to be got by traditional tests.

- Very hard to understand fire mechanism of complex fire.

For example, the façade is defined to be the connection between inside part and outside part of a building. Although it is believable that façade fire take place low frequently, the resultant results including fire spread and combustion toxicity gas do harm to people's safety. Recently, combustible façade presents an increased fire hazard. The typical façade fire including CCTV fire in 2009 and Shanghai fire in 2010 has caused large property loss. External thermal insulation composite systems (ETICS) are quite common in constructions. However, the combustible insulation core induces serious fire disasters. Expanded polystyrene (EPS) is one of common thermal insulation thermoplastic materials used in ETICS. EPS ETICS consist of adhesive, EPS insulation material, cement, reinforcing mesh and finishing coat. In our lab, a series of EPS ETICS which vary opening edge treatment, heat intensity, finishing coat and thickness of core materials, had been

conducted. The detailed fire mechanism of such complex configuration seems still unclear, although some empirical results had been concluded and used to improve fire resistance of ETICS <sup>[1, 2]</sup>. For example, although the knowledge of temperature profile of window ejected fire plume has been subjected to many researches, the parameters of test influence on the temperature distribution is still insufficient. In another case, the reaction-to-fire performance of new organic building materials could be got using Cone or TG. However, the fire mechanism of model-box and effects of building materials parameters on the fire performance are still needed to be further studied. The effects of timber façade parameters on the reaction-to-fire performance is still unclear.

## **1.2 CFD introduction**

The full name of CFD is Computational Fluid Dynamics, a third method for scientific research, which is widely used in the field of fluid industry. It is taking its place next to experimental development and mathematical theory as a way to new discoveries in science and engineering <sup>[3]</sup>. The CFD has been used successfully in the field of many industry fields over the past decade. For example, CFD has been to be an important tool for medical research in the field of biomedical industry. In the field of heating and air conditioning, the CFD shows a merit in the building simulation. Regarding the fire research, fire simulation has been a necessary part. With the amazing development of super computer technology, CFD is intended to be one of important methods for fire research in future.

When mentioned the dynamic of fluid, the solution of Navier-Stokes equation is indispensable. It is known to all that fire dynamics embraces numerous complex configuration and chemical interactions which are consisted of combustion, thermodynamics, fluid dynamics, multi-phase effects and radiation <sup>[4]</sup>. Navier-Stokes equations have a wide application in the field of flow research. For example, the flow phenomena



in a strong wind, water flow in a tube, the blood flow in the lungs and so on. Traditionally, the fluid flow is divided into several types according to the definition of fluid. The vector form of Navier-Stokes equations for compressible fluid could be the following:

$$\rho \left( \frac{\partial u}{\partial t} + u \cdot \nabla u \right) = -\nabla p + \nabla \cdot \left( \mu (\nabla u + (\nabla u)^T) - \frac{2}{3} \mu (\nabla \cdot u) I \right) + F$$

Inertial force    press force            viscosity force            body force

Where  $\rho$  is the density;  $u$  is the flow velocity;  $\nabla$  is the divergence;  $p$  is pressure;  $t$  is the time;  $\mu$  is viscosity;  $F$  is the body force;  $I$  is the identity matrix. Actually, it is a momentum conservation equation for fluid. In the controlled conservation equations, the resolution of partial differential equation is necessary. The traditional CFD flows are described in the Fig.1. It consists of modeling of the geometric domain, discretization of the modeled domain, algebraic equations and numerical iteration solutions.

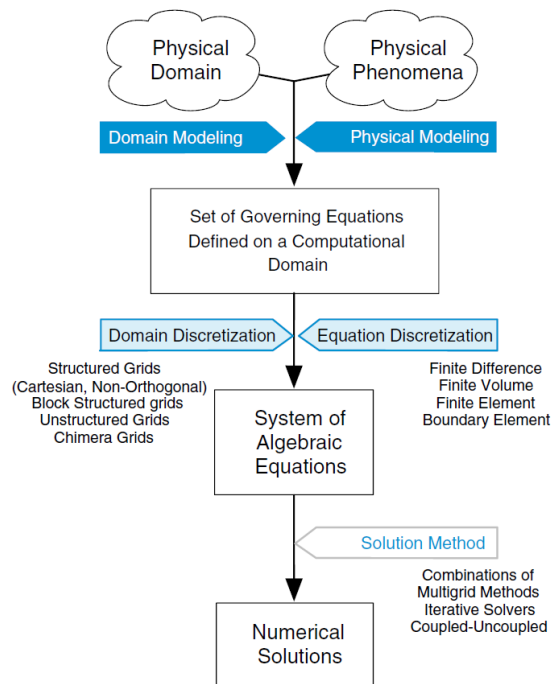


Fig.1 Traditional CFD flows

- In the first step, a physical phenomenon which could mathematically formulated and validated would be modelled by two levels, one features the physical geometry of the domain and the other one represents the physical problems of user interest. During this process, usually some factors that has no relationship with user interest or has no influence over user interest could be simplified even in some time. For example, when the parameter variety in Z axis is non-relevant to results, a three-dimensional domain could be changed into a two-dimensional model. Sometimes, a symmetry model could be considered to reduce computational domain. In some cases, some physical boundary condition may be reduced or coarsened, or replaced with appropriate mathematical representations.
- In the second step, the geometric discretization of the physical domain would be conducted by subdividing the configured domain into discrete non-overlapping cells or elements. It sets up the domain with aim to form a grid or mesh system. Currently, a great many of techniques to form a mesh is available.
- In the third step, equation discretization would be carried out by a procedure which change the governing partial differential equations into a set of algebraic equations in the form of  $[x] = b$  , which relates to a global matrix and vectors.
- In the final step, final solution of the above equation could be got using an iterative solver.

Regarding fire modeling using the CFD tools, it is proposed in 1970s with the development of computer code UNDSAFE-I <sup>[5]</sup>, then the JASMINE and FLOW-3D <sup>[6]</sup> were developed latterly. In the early attempts to model fire, it has shown that fire could be adequately represented by a volumetric heat source. In some case, the combustion source was removed. This simple attempts only solve transport equation governing mass, momentum, and energy with the addition of a simple turbulence model. The numerical simulation with addition of the volumetric heat source method was reported to be able to predict and analyze the smoke

movement in different conditions <sup>[7]</sup>. Then a large-eddy simulation (LES) code which called Fire dynamics simulators (FDS) was developed by National Institute of Standards and Technology (NIST) for solving low-speed flows with attempts to reproduce smoke and heat transport. It is suitable for solving thermally driven flow numerically by computing Navier–Stokes equations. FDS are now a popular CFD tool even after it has been used for about 25 years in fire related research, suitable for simulation of flow distribution and concentration of fire pollutants <sup>[8]</sup>. This tool has been subjected to numerous validation studies <sup>[8]</sup>. Regarding the modeling of solid pyrolysis, a code ThermaKin was developed by Federal Aviation Administration <sup>[9]</sup> in 2008. ThermaKin has been successful in numerous validation studies on the combustion simulation in a cone calorimetric scenario <sup>[10]</sup>. With the rapid development of fluid dynamics knowledge and high speed super computer, the CFD ability has been widely boarded. With respect to another fire simulation tool called FireFOAM, it was developed by Yi et al. in 2011 from FM Global and applied it successfully to simulate purely buoyant fire plumes <sup>[11]</sup>. It was concluded that the FireFOAM model could reproduce small-scale fire plumes. The details of these popular CFD tools would be summarized in the chapter 2.

### **1.3 Necessity of CFD**

In the past research, most of fire knowledge are got by using experimental techniques and theoretical approaches. The experimental study usually provide a direct observation for fire flame by camera or thermal camera, heat by thermocouples, heat flux by heat flux meters, pressure variety during fire by pressure sensor, air movement by velocity meters and so on. There are two types of error always exists in experimental methods. One is system error, usually it could be avoided by the duplicate tests. The other one is measurement error. In some case, it is very difficult to reduce it. The usual method to reduce or minimize this error is to conduct the calibration test before real measurement. Comparably, the theoretical models

could provide a better understanding of fire using mathematical models of physical model and the defined boundary conditions. The limitations from the above mentioned two traditional fire research methods impels fire researchers continuously to find new methods for fire research. Among available methods, CFD is believed to be a potential method for fire research. The importance of CFD tool in fire is described in the subsequent sections:

### 1.3.1 Low cost, short time and high accuracy.

Comparison of different scales of fire test methods is shown in table 1. With respect to the micro-scale and bench-scale test, the advantage of CFD methods is not so obvious. However, compared with intermediate and large-scale test, CFD features many advantages consisting of low cost, good repeatability and high accuracy. The high expensive experimental fee has limited the test for large-scale fire. Furthermore, the continuous maintenance of this fire equipment also needs a big fund. In fire test, the field information is important, such as, temperature field, heat flux fields, and radiation heat fields and so on. Utilization of traditional measurements to get the above fields seems difficult. However, CFD could easy calculate the fields with optimal parameters input.

Table 1 Comparison of different fire test methods

Fire tests	Test expense	Repeatability	Time	Examples
Micro-scale	Fair	Good	Short	MCC,TG
Bench-scale	Expensive	Good	Short	Cone
Intermediate-scale	Expensive	Fair	Long	ICAL
Large-scale	Very expensive	Fair	Long	JIS A 1310
CFD technology	Cheap	Excellent	Shortest	Most (in future, all )

### **1.3.2 Impossible to calculate Navier-Stokes equation (N-S) without computer.**

In the study of fluid dynamic, N-S equation is the core equation, which governs the conservation of parameter variety. The N-S equation includes a time-dependent continuity equation which controls conservation of mass, three time-dependent equations for conservation of momentum and a time-dependent equation for conservation of energy. It indicates that four independent and six dependent variables exist in the above equations. Four independents are t time, x, y, and z spatial coordinates. Six dependent variables are the pressure, density, temperature and velocity vector in three direction. The dependent variables varying four independent variables. Furthermore, handwriting work seems insufficient for solving differential or partial differential equation because of the large calculation.

### **1.3.3 Rapid computer development**

A supercomputer is defined as it that a computer which is equipped with a high level of performance. The significant progress of supercomputer has been made at the beginning of 21<sup>st</sup> century. It showed in size and calculation speed. Currently, a series of equipment are being conducted in China, United States, European Union, Taiwan and Japan to set up an even faster, more powerful and more technologically superior extra-scale supercomputers <sup>[12]</sup>. The calculation speed in the unit of floating-point operations per second (FLOPS) is approaching the value of a hundred quadrillions. With the merit of super computer, the attempts to solve very complicated physical problems with CFD are being conducted in study of fluid dynamics issues.

### **1.3.4 Prediction before experiment**

Since the fire test costs largely in fire research, the optimal configuration or design of experiment is

necessary. Utilization of CFD tools to predict reaction-to-fire performance of complex physical configuration before test is an effective method. It could save time and money for researcher. Furthermore, it provide a well understanding of fire mechanism during the CFD modelling process.

CFD also is necessary for development of new materials. The material with treatment of fire retardant would be safe to use in buildings. Without CFD, all the optimization of materials parameters would be conducted by a series of tests. It is not just time-consuming and also money-consuming. In some case, even the good material is found finally based on a great many tests and several years. The well understanding of fire mechanism, the effects of parameters on reaction-to-fire performance is not got. When the CFD technology is employed to well understand the influence of materials parameters on the material performance, the development of material would be accelerated by shortening research time and saving budget fund.

CFD is very useful for building design. It is known to all that the building safety level is the first thing for occupant. Not only the structure and design should meet the safety requirement of building, but also the building should meet the requirement of fire protection or fire evacuation.

### **1.3.5 Complex architecture and building materials**

Currently, with the development of art and building technology, a great many of complex architecture has been designed for different functions. The complexity consists of complex structure and organic materials, which has attracted more and more attention from fire research aspect. The traditional methods for fire risk evaluation seems difficult to provide accuracy information because of new challenges from structure and organic materials. Fox example, the smoke movement or exhaust for the lower building with less than six floors could be easily calculated by empirical equation. Large population and improved building technology

impel high-rise buildings to serve for occupant. In Japan, the high-rise building is defined in the scale of building height. When the building height is between 30 m and 60 m, it could be called high-rise buildings according the Building Standards Act (term 20th) and Fire Protection Act (term 8-2).

Furthermore, the complexity is also shown in the variety of building materials. With an aim to improve thermal performance of building, a variety of organic polymers has been produced and successfully used in building <sup>[13]</sup>. For example, External thermal insulation composite systems (ETICS) are quite common in new constructions and refurbishment buildings with design-oriented goals of sustainability and energy efficiency. Thermoplastic expanded polystyrene (EPS) has been widely used as insulation core. The polymer cement mortar is also widely used in the building external surface. Once these organic materials are exposed to fire, the heavily and toxic smoke would spread rapid and heat release rate is much larger than inorganic material. All the above mentioned factors increase the difficulty to use traditional and empirical equation to evaluate fire risk levels. With help of CFD, the situation was changed. Even the optimal evacuation method could be got through CFD calculation.

#### **1.4 Research objectives and scope**

This study hopes to mitigate or reduce fire accidents of building, which is carried out by using CFD technology to investigate the fire mechanism of internal and external building fire, to well understand the building material parameter's effects on the fire performance, to discuss the behavior of intermediate-scale window ejected fire plume, to reproduce the cedar façade fire. The building fire is divided into two types, one is internal building fire and the other one is external building fire. The specimens used for internal building materials include polymers, such as Urethane and Nurate. The samples used for external building materials are consisted of EPS ETICS and cedar.

## 1.5 Significance and innovation

In Japan, the CFD research of building fire was seldom reported. Most of fire research has been subjected to the traditional method including theoretical derivation and experimental tests. In the past decades, the knowledge got from traditional methods has been validated and used in fire protection. They had made a great contribution to fire research, which is worth celebrating. A great many original theory was proposed and validated by the real tests. In addition, the approximation method summarized according to the experimental tests played an important role in the fire protection. It is not an exaggeration to say that the fire researcher is hardworking and smart, especially in the details of fire test and theory.

With the rapid development of computer in 2000, the fire research in the USA or Europe has been accelerated. The optimization work was effectively conducted by using CFD, although the CFD technology in that times was not adequate for complex conditions. In Japan, some fire researchers had noticed the importance of CFD and conducted part of calculation research at the beginning of 2000. However, the CFD improvement in Japan was slowly. The reasons could be summarized in the followings: 1. Most of fire researcher have little background of computer. The FDS is written by Fortran 90 and FireFOAM is using C++. Without the computer ability, it seems hard to conduct real CFD research. 2. Most of fire researcher have little background of fluid dynamics. The well understanding of fluid knowledge is necessary for fire simulation. When the new model is developed, the well knowledge of combustion model, radiation model, turbulence model and N-S models are important. 3. The CFD research was got little attention. Although the simulation results varying input models and parameters, its results are believed to provide an insight in the understanding of fire mechanism. 4. Lack of international recognition. It is known to all that when the model proposed by us are verified by many other labs, the codes are good. The good communication with CFD development group should be not ignored.



Under this atmosphere, Prof.Noguchi from the University of Tokyo kindly conduct my CFD research with an aim to well understand application of CFD in external and internal building fire. In this study, with an aim to try simulating building fire using CFD tools, both the experiments and simulation are conducted. The discussion is separated into two types, interior building fire and external building fire. The interior building fire tests are consisted of Cone and model-box test. The external building fire tests include the JIS A 1310 calibration test varying heating intensity and opening aspect, Intermediate Scale Calorimeter (ICAL) test, External Thermal Insulation Composite System (ETICS) façade fire, cedar timber façade fire and Fire Propagation Apparatus (FPA) test. The new founding summarized from experimental tests are disclosed. Therefore, this study would report both experimental study and CFD study. The CFD tools include FDS (version 6.5), ThermaKin (version 2D) and FireFOAM (2.2.x). The experimental results would be used to well understand CFD model. This study hopes to provide a deep understanding of fire CFD tool application. The PhD thesis structure is described in the subtext.

## **1.6 PhD structure**

The research flow of this study is shown in the following Fig.2.

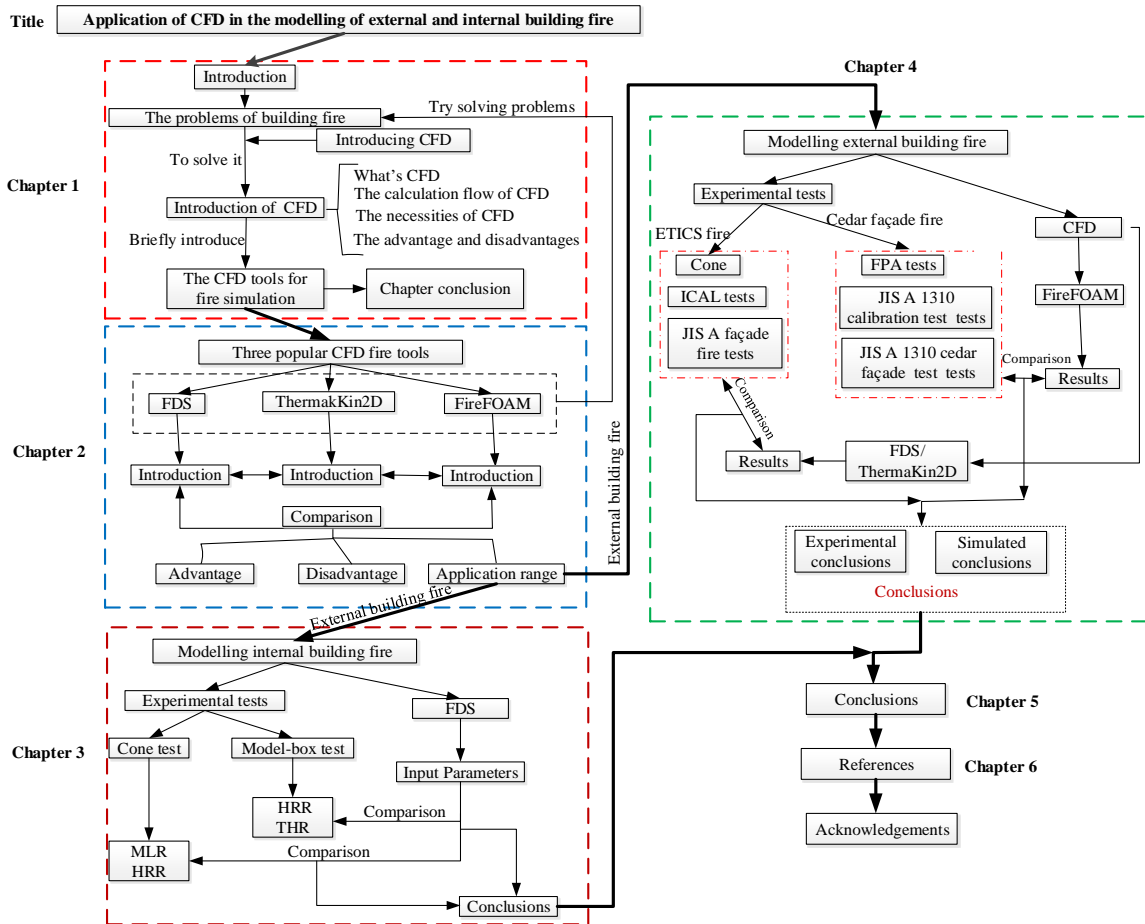


Fig.2 The research flow of the present study

Chapter 1 provides the necessary background for introducing the CFD. Importance of CFD in building fire and problems in building fire research are included for well understanding that why the CFD tools in building fire is necessary. The significance and innovation of this study is described to well understand the research background and object. In addition, the PhD structure is summarized to briefly make an outline of this study.

Chapter 2 overviews the available popular CFD fire tools. The governing conservation equation for fluid flow are illustrated, which features the derivations of the conservation of mass, continuity, energy equation and transportation equations. This is followed by the comparison of three CFD tools. The conclusion which

is good or not is not included in this study. The researchers would get to know the basic knowledge of three CFD tools after reading the content of this chapter, which helps to understand the following parts.

Chapter 3 presents the utilization of CFD models to interior building fire (see Fig.3). Several building materials were tested firstly by Cone and TG. The tested materials include expanded polystyrene (EPS) foam, extruded polystyrene (XPS) foam, urethane and non-combustible urethane. The pyrolysis model was set up using optimal grid and parameters. The intermediate-scale of burn box fire are reproduced using FDS. The parameters effects on the reaction-to-fire performance is discussed, which provide an insight in the development of new fire retardant materials.

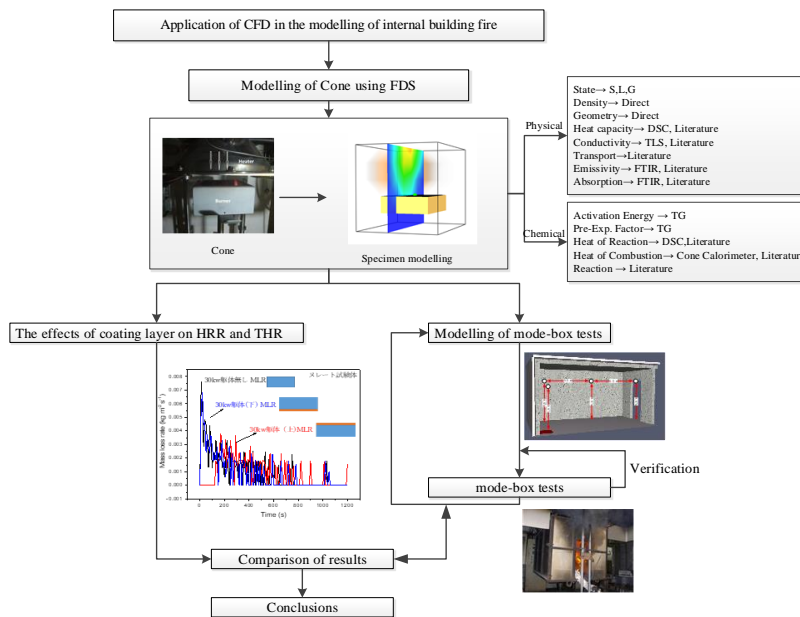


Fig.3 Research flow of the chapter 3

Chapter 4 is devoted to the utilization of CFD models to external building fire (see Fig.4). The materials selected as research objects are ETICS and Cedar timber. The ETICS pyrolysis model was modelled using FDS and ThermaKin2D. The flame flux influence on the ETICS specimen pyrolysis is proposed using FDS results and verified by ThermaKin2D results. Furthermore, the effects of EPS melt-flow on the ETICS

façade fire tests are discussed by comparing ETICS model of FDS and experimental results. Because in the current version of FDS, melt-flow is still hard to be simulated. Regarding the experimental ETICS façade fire tests, the effects of EPS thickness, heating intensity, opening edge treatment method and finishing coating are described on the basis of tested results. A comprehensive ETICS façade fire risk evaluation method was proposed by using fire propagation index (FPI) theory, which innovatively proposes an effective ETICS façade fire risk prediction. This is followed by discussing temperature profile of ejected fire plumes from an intermediate-scale compartment under an over-ventilated condition varying heating intensity from 300 kW to 900 kW. The Yokoi's correlation  $\Theta$  vs.  $\frac{z}{r_0}$  was modified based on the test results by taking into account the influence of fire plume re-attaching-to-wall behaviors, varied neutral plane positions and window opening aspect n. The new length scale  $r'_0$  was defined as  $r'_0 = \sqrt{\frac{W(1-x)H}{\pi}}$  (x is ratio of neutral plane position  $z_0$  and window opening height H) without assumption that neutral plane is a constant 0.5 H. The new correlation  $\Theta'$  vs.  $\frac{z}{r'_0}$  was divided into two type of plots consisting of the non-flame fire plume ejected from window and fire plume with flames spilled out of window. Although the accurate method to predict the position of neutral plan is unavailable, one alternative,  $x = \frac{z_0}{H} = \frac{1}{1 + (\frac{T_g}{T_a})^{1/3} (1 + \frac{\dot{m}T}{\dot{m}_a})^{2/3}}$  (x is ratio of neutral plane position  $z_0$  and window opening height H) was used in the proposed new correlation. This is followed by a large eddy simulation (LES) study of ejected fire plumes from an intermediate-scale compartment under an over-ventilated condition performed with heat release rates (HRR) 300 kW, 600 kW and 900 kW. After this, a large eddy simulation (LES) and experimental study of cedar façade performance with heating intensity 900 kW is discussed after the pyrolysis model of cedar modelled and optimized according to the results of Fire Propagation Apparatus (FPA) test.

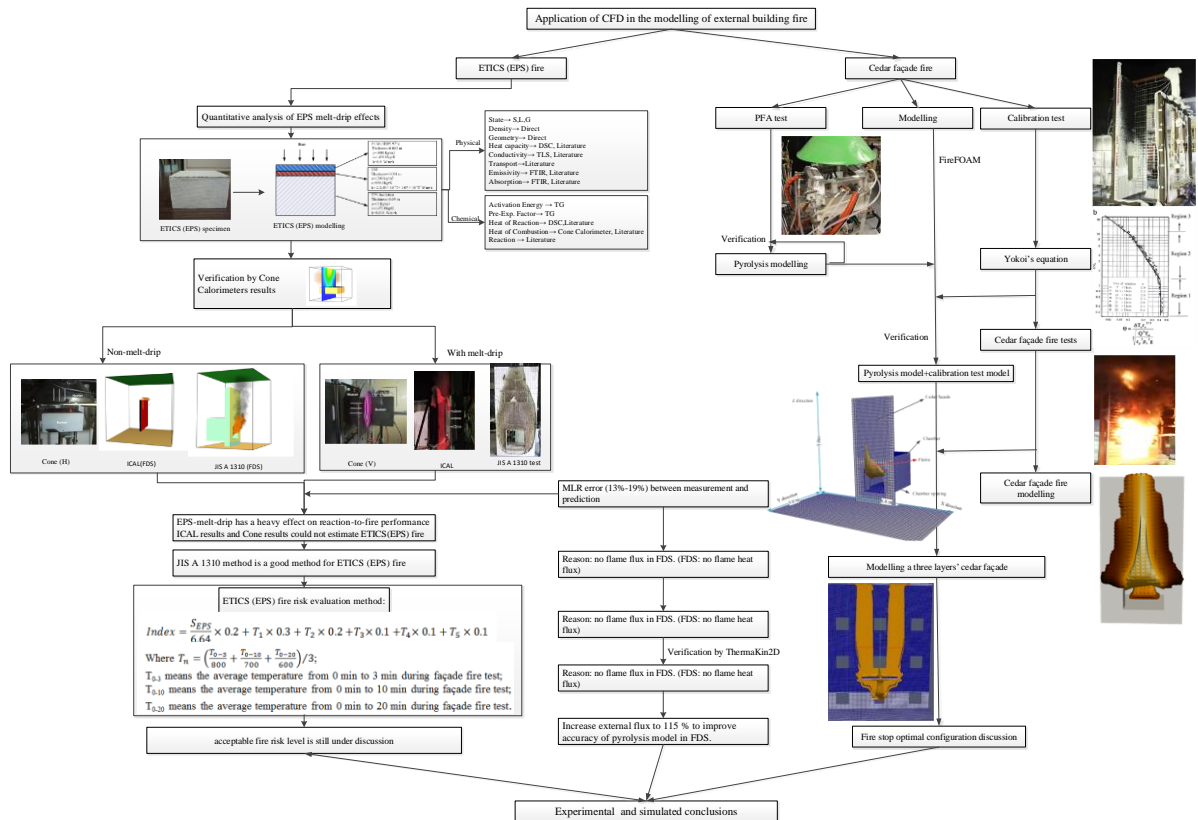


Fig.4 Research flow of the chapter 4

Chapter 5 outlines the conclusions from experimental tests and simulated results. The research direction for further step is presented.

Chapter 6 presents the references which are cited in the previous section.

Finally, the acknowledgement is listed. During the three and half year's study in The University of Tokyo, I got many help from others.

## 1.7 Summary

In this chapter, firstly CFD introduction is performed by introducing the concepts and background of CFD. The traditional CFD calculation flows are described and divided into four steps. In addition, the

overview of CFD fire tools is presented briefly. Importance of CFD is outlined by several reasons: 1. Low cost, short time and high accuracy. 2. Impossible to calculate Navier-Stokes equation (N-S) without computer. 3. Rapid computer development 4. Useful prediction before experimental test. 5. Complex architecture and building materials shows a new and big challenge for building safety. Furthermore, the problems in building fire research is described to briefly answer why the CFD in fire is necessary. Following this, significance and innovation and structure of PhD thesis are summarized. In the next chapter, the three popular CFD tools would be introduced in details.

## 2. Comparison of three CFD fire tools

### 2.1 Introduction

In this chapter, the comparison of three popular CFD fire tools, FDS (version 6.5), FireFOAM (version 2.2.x) and ThermaKin (version 2D) is conducted by introducing the basic application range, comparing the advantages and disadvantages and disclosing the representative features of each tool. The typical characters are firstly discussed. This is followed by the analysis of advantages and disadvantages of each tool. Finally, a comparison table is obviously summarized. This chapter hope to provide an obvious and deep understanding of each fire tool, which is useful for understanding of subtext.

### 2.2 The introduction of three popular CFD fire tools

#### 2.2.1 FDS

Once the CFD fire tools is involved, it is necessary to mention the popular fire simulation tool FDS, which is using Fortran90 code. FDS has been validated by industry level and academic levels <sup>[14]</sup>. The LES code developed by National Institute of Standards and Technology (NIST), is a practical tool for simulating fire-induced environment <sup>[15]</sup>. This tool has been subjected to numerous validations and calibration studies. The governing equations are followings <sup>[16]</sup>:

Conservation equation for mass

$$\frac{\partial \rho}{\partial t} + \nabla(\rho u) = \dot{m}_b'''$$

Conservation equation for individual gaseous species

$$\frac{\partial}{\partial t}(\rho Y_\alpha) + \nabla \cdot (\rho Y_\alpha u) = \nabla \cdot (\rho D_\alpha \nabla Y_\alpha) + \dot{m}_\alpha''' + \dot{m}_{b,\alpha}'''$$

Conservation equation for momentum

$$\rho \left( \frac{\partial u}{\partial t} + (u \cdot \nabla)u \right) + \nabla p = \rho g + f_b + \nabla \cdot \tau_{ij}$$

Transport equation for sensible enthalpy

$$\frac{\partial}{\partial t}(\rho h_s) + \nabla \cdot (\rho h_s u) = \frac{D\bar{p}}{Dt} + \dot{q}''' - \nabla \cdot \dot{q}''$$

where  $\rho$  stands for density;  $u$  stands for three components of velocity,  $u=[u,v,w]^T$ ;  $T$  stands for temperature;  $D_\alpha$  represents diffusion coefficient;  $Y_\alpha$  features mass fraction of  $\alpha$ th species;  $\dot{m}_{b,\alpha}'''$  represents production of species  $a$  by evaporating particles;  $\sum \dot{m}_{b,\alpha}''' = \dot{m}_b'''$ ;  $p$  represents pressure;  $g$  is acceleration of gravity;  $f_b$  is external force vector;  $\tau_{ij}$  is stress tensor;  $h_s$  is sensible enthalpy;  $\dot{q}'''$  is heat release rate per unit volume from a chemical reaction;  $\dot{q}''$  is conductive and radiation heat fluxes;  $t$  is time.

The main features of FDS model in default operation are introduced in the subtext:

#### A) Low Mach.

If Mach number (local magnitude of fluid velocity versus the speed of sound)  $< 0.3 M$  and the flow is quasi-steady and isothermal, compressibility effects will be small and simplified incompressible flow equations can be used [17]. The incompressible and compressible fluid difference could be easily distinguished by the mass conservation form during calculation. The the mass conservation or continuity equation in the flux form could be described in the following:

$$\frac{\partial \rho}{\partial t} + \nabla(\rho u) = 0$$



Regarding some kinds of fluid, the pressure and temperature has no significant changes. This fluid is approximated as the incompressible fluid, which indicates that  $D\rho/Dt = 0$ . The mass conservation equation for incompressible flow is equivalent to  $\nabla(\rho u) = 0$ . In that case, the mass conservation equation would not calculate the density during the whole simulation. This is not equivalent to it that  $\rho$  is the same in anywhere. It features the pressure and temperature changes effects on the density could be reasonably ignored. By this, the calculation speed would be increased sharply to avoid enormously complex computational task. Comparably, the density of each elements in the domain would be computed for each time step during compressible fluid. Furthermore, the important body force, buoyancy force, are calculated using different equations in compressible and incompressible fluid. In the incompressible fluid, Boussinesq approximation is widely used to predict the buoyancy force  $\rho g$ . The Boussinesq approximation equation is the following <sup>[3]</sup>:

$$\rho = \rho_{\infty}[1 - \beta(T - T_{\infty})]$$

Where,  $\rho_{\infty}$  describes the density of atmosphere fluid,  $T_{\infty}$  features the temperature of atmosphere fluid,  $\beta$  is the coefficient of volume expansion. In the compressible fluid, the buoyancy force could be directly computed by  $\rho g$  because the density of each element of each time step is calculated.

## **B) Large-eddy simulation (LES)**

Solving the N-S equation is necessary for CFD simulation. The resolution of N-S equation varies the types of fluid. It is known to all that laminar flows are stable and turbulent flows are chaotic, diffusive causing rapid mixing, time-dependent, and involve three dimensional vorticity fluctuations with a broad range of time and length scales <sup>[18]</sup>. During turbulence modelling, an energy cascade concept was developed by Kolmogorov <sup>[19]</sup> and widely accepted. It indicates that turbulence consists of eddies of difference sizes. The smallest turbulent eddies are separated using the Kolmogorov micro length ( $\eta$ ) and time scale ( $t_{\eta}$ ) :

$$\eta = \left(\frac{\nu^3}{\varepsilon}\right)^{1/4} ; \tau_\eta = \left(\frac{\nu}{\varepsilon}\right)^{1/2}$$

Where, the  $\nu$  stands for the molecular kinematic viscosity and  $\varepsilon$  features the average turbulence kinetic energy of dissipation. The direct numerical solution (DNS) could calculate N-S equation accuracy without any assumption. However, the huge grid would result in an enormous computational cost, which has been limited by the current super computer technology capacity. Under this condition, with an aim to get the reasonable accuracy of fluid and smaller computational cost, a method named LES was proposed that the calculation consisted of large scale and small scale turbulent structure. The large one is directly simulated and small scale one is modeled using sub-grid scale model. The interior to classify large one or small one is the spatial statistical filter <sup>[20]</sup>:

$$\langle v(x, t) \rangle = \iiint F(x - \lambda: \Delta) v(x, t) d^3 \lambda$$

By this filter equation, values of  $v$  in the scales larger than  $\Delta$  would be kept for resolved.  $F$  stands for the filter function,  $\langle \rangle$  features a filtered variable.  $\Delta$  is a filter width. Here, another important turbulence model is introduced. The Reynolds Averaged Navier-Stokes (RANS) equations <sup>[21]</sup>, which consisted of a time-mean value component and a fluctuating one, are used widely in industry fields. When conducting the fire simulation, it is necessary to choose appropriate turbulence model based on the physical model and parameters. The difference of each turbulence has been discussed in a great many research work, here, the details is not listed. Fig.5 features the turbulence modeling, which is from reference.

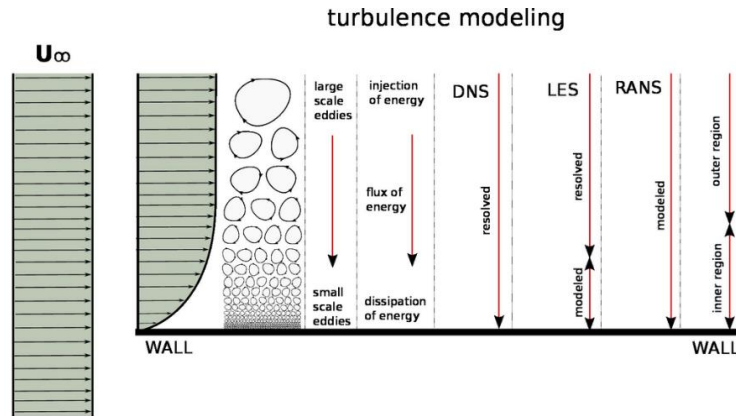


Fig.5 The description of LES, DNS and RANS [3].

### C) Explicit

The concept explicit and second-order is involved when the partial equation was discretized into a set of algebraic equation. In the explicit numerical method, the variables are computed directly on the basis of the already known values. In the next, an example is used to show the difference between explicit and implicit method. Take the heat transfer equation for example:

$$\frac{\partial T}{\partial t} = \kappa \frac{\partial^2 T}{\partial x^2}$$

Explicit method:  $\frac{T_i^{n+1} - T_i^n}{\Delta t} = \kappa \frac{T_{i+1}^n - 2T_i^n - T_{i-1}^n}{\Delta x^2} \rightarrow T_i^{n+1} = T_i^n + \Delta t \kappa \frac{T_{i+1}^n - 2T_i^n - T_{i-1}^n}{\Delta x^2}$ . It indicates that the

major advantage of explicit finite difference methods is that they are simple and computational speeds fast.

The drawback is the stable solution are got only when the  $0 < \frac{\Delta t \kappa}{\Delta x^2} < 0.5$ .

Implicit method:  $\frac{T_i^{n+1} - T_i^n}{\Delta t} = \kappa \frac{T_{i+1}^{n+1} - 2T_i^{n+1} - T_{i-1}^{n+1}}{\Delta x^2} \rightarrow T_i^{n+1} = T_i^n + \Delta t \kappa \frac{T_{i+1}^{n+1} - 2T_i^{n+1} - T_{i-1}^{n+1}}{\Delta x^2}$ . The partial

derivatives  $\frac{\partial^2 T}{\partial x^2}$  are predicted at the new timestep.

### D) Structured, uniform grid

Regarding the finite volume method, mesh generation is very important in the simulation. The topological information would be set up after the mesh generation, which includes elements or cells arrangement and relations between each other. It is known to all that in practice, the physical configuration of the problem needs to be solved is usually complex. In general, the physical domain could be discretized into structured and unstructured grid system. With respect to a structured mesh, three dimensional elements are marked with local index i, j, k. Although the structured mesh has showed advantages in the coding and calculation speed, the fair geometric flexibility limits its application in industry. The fair mesh flexibility was improved a little by using multiple blocks to form the physical configuration. Although the structured and uniform grid has been the staple of numerical simulation, the unstructured grid mesh become more and more popular <sup>[22]</sup>. The mesh flexibility was increased sharply using the unstructured grid mesh. Fig.6 represents the description of structured grid and unstructured grid. Using the divergence theorem, which is relatively straightforward, it could be transformed from  $\overline{\nabla\phi}_c = \frac{1}{V_c} \int_{V_c} \nabla\phi dV$  to  $\overline{\nabla\phi}_c = \frac{1}{V_c} \int_{\partial V_c} \phi d\mathbf{S}$ . In it,  $d\mathbf{S}$  stands for the outward pointing surface vector. With respect to discrete faces, it could be further transformed as:  $\overline{\nabla\phi}_c V_c = \int_{face} \phi d\mathbf{S}$ . Finally,  $\int_{face} \phi d\mathbf{S}$  could be approximated in the form of  $\overline{\nabla\phi}_c = \frac{1}{V_c} \sum_{f=nb(c)} \overline{\phi}_f S_f$ . Therefore, if the  $V_c$  is very small (fine mesh), the results would be approaching the real value. However, when the  $V_c$  is set to a large value (coarse mesh), the error between approximated value and real value would be increased reasonably. This could describe the influence of grid size on the calculation results.

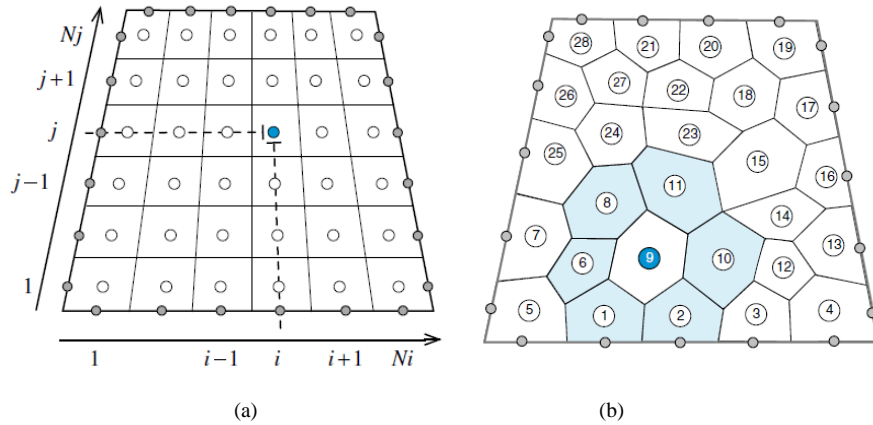


Fig.6 The description of structured grid and unstructured grid [3] (a) structured mesh (b) un-structured mesh

### E) Simple immersed boundary method for treatment of flow obstructions <sup>[23]</sup>

The complex physical configuration of fluid necessities the good resolution of unstructured meshes. In addition, physical complexity is combined with some special conditions. Under this condition, the computational cost would be increased sharply. The method to cope with the flow complexity but meanwhile keep the accuracy and high efficiency of simulation performed on the grids is needed. By using this method, the desired value of velocity is imposed directly on the boundary without any influence of dynamical process. That is to say, the boundary condition has no relationship with the frequencies of flow. Furthermore, it was found that the stability of the time integration is not effected. In the FDS, this method has been incorporated.

### F) Deardorff eddy viscosity subgrid closure

In the description of LES in FDS, turbulence model means the modeling for the closure for SGS flux terms. With an aim to solve equations, turbulent viscosity or turbulent diffusivity is modelled in FDS. Regarding the diffusivity coefficient, it could be got using a constant Schmidt number and Prandtl number. Therefore, the turbulent viscosity is still need to be modelled. The Deardorff eddy viscosity  $\mu_t$  has been validated and used widely in the comparison of full-scale experiments <sup>[24]</sup>.

### G) Constant turbulent Schmidt and Prandtl numbers

The Schmidt number <sup>[25]</sup> is defined as:  $S_c = \frac{\nu}{D}$ . Where  $\nu = \mu/\rho$  is the momentum diffusivity,  $D$  is the mass diffusivity. The  $S_c$  is employed to physically represent the ratio of thickness of the hydrodynamic and mass transfer boundary.

The Prandtl number <sup>[25]</sup> is defined as:  $P_r = \frac{\mu C_p}{k} = \frac{\nu/\rho}{k/\rho C_p} = \frac{\nu}{\alpha}$ .  $\alpha = k/\rho C_p$  is the thermal diffusivity,  $\nu = \mu/\rho$  is the momentum diffusivity. The  $P_r$  is used for physically featuring the ratio of hydrodynamic boundary layer to thermal boundary layer.

### H) Eddy dissipation concept for single-step reaction between fuel and oxidizer

Eddy Dissipation Concept (EDC) means that the combustion is modelled with a simple “mixed is burnt” approximation <sup>[26]</sup>. In some cases, it is called mixing-controlled fast chemistry. The EDC model is used in current version of FDS, which could be described in the following:

$$\dot{m}_F^m = -\rho \frac{\min(Z_F, Z_A/s)}{\tau_{mix}}$$

Where  $\dot{m}_F^m$  is the chemical mass production rate of species fuel per unit volume.  $Z_F$  and  $Z_A$  are the lumped mass fractions of Fuel and Air, respectively, and  $s$  is the mass stoichiometric coefficient for Air. The quantity  $\tau_{mix}$  is a time scale for mixing in the form of:  $\tau_{mix} = \max(\tau_{chem}, \min(\tau_d, \tau_u, \tau_g, \tau_{flame}))$ .  $\tau_{chem}$  is the chemical time scale.  $\tau_d$  is the mixing time to vary as the square of the filter width.  $\tau_{flame}$  shows the flame height presenting a limit to the reaction time scale. The acceleration time scale  $\tau_g$  represents the time required to travel a distance  $\Delta$  starting from rest.  $\tau_u$  features the advective time scale constant. Where  $\tau_d = \frac{\Delta^2}{D_f}$ ;  $\tau_u = \frac{C_u \Delta}{\sqrt{(2/3)k_{sgs}}}$ ;  $\tau_g = \sqrt{2\Delta/g}$ . Here,  $D_f$  is the diffusivity of the fuel species,  $k_{sgs}$  is the unclosed sub-grid kinetic energy per unit mass,  $C_u = 0.4$ ,  $g = 9.8 \text{ m/s}^2$ .

## D) Gray gas radiation with finite volume solution to the radiation transport equation

The thermal radiation model is one of the important model in CFD. The radiation transport equation (RTE) for a non-scattering gray gas:  $s \cdot \nabla I(x,s) = \kappa(x)[I_b(x) - I(x,s)]$ . In the CFD simulation, it is hard to solve the the spectral dependence of  $I$ ,  $I_b$ , and  $\kappa$ . A method to divide radiation spectrum into a relatively small number of bands is adopted in the current version of FDS. The details of radiation model could be found in the literature [1].

### 2.2.2 ThermaKin2D

Pyrolysis model is important in the CFD study. Up to 30 components could be specified in the ThermaKin2D, which is suitable for modelling the multi-layers or multi-reactions pyrolysis model. Furthermore, the heat flux received from flame has been modelled in the current version of code. ThermaKin2D could be used to perform multi-layer pyrolysis simulation of materials including composites. It is written by the C++. The one-dimensional version of ThermaKin could be used to reproduce Cone tests. The details would be introduced in the subtext. First the basic knowledge of ThermaKin2D is shown in the followings [27]:

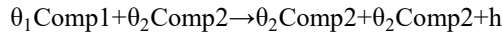
#### A) Components and reactions

In the ThermaKin2D, each component is represented by density, heat capacity, thermal conductivity, gas transfer coefficient, emissivity, and absorption coefficient. The density, heat capacity, thermal conductivity, gas transfer coefficient are temperature-dependent parameters, which is modelled by the following equation:

$$\text{property} = p_0 + p_1 T + p_2 T^n$$

Where  $p_0, p_1, p_2$  and  $n$  are constant parameters, which is material dependent. With this method to define the temperature-dependent parameters, the continuity of simulation could be increased.

### B) Reaction



Where  $\theta$  represents stoichiometric coefficients and  $h$  features the heat of reaction. The reaction rate in a unit volume of materials could be described in the following:  $r = A \exp\left(-\frac{E}{RT}\right) \xi_{\text{comp1}} \xi_{\text{comp2}}$ . Here,  $A$  stands for Arrhenius pre-exponential factor and  $E$  features activation energy.  $R$  features the molar gas constant. The  $\xi$  represents the concentration of a given component expressed in the units of mass per unit volume.

### C) Heat and mass transfer

The Fourier's law is used in model to describe the conduction of heat in the form of:  $q_x = k \frac{\partial T}{\partial x}$ .  $q_x$  features the heat flux in the fixed direction.  $k$  represents the thermal conductivity of materials. The Beer-Lambert law is used to describe the thermal radiation. It is in the form of  $\frac{\partial I_{\text{ex}}}{\partial x} = -I_{\text{ex}} \sum_{i=1}^N \alpha_i \xi_i$ .  $I_{\text{ex}}$  stands for the flux of radiation in  $x$  direction.  $\alpha_i$  represents the absorption coefficient of  $i$ -th component.

The mass transfer is approximated to be expressed as:  $J_g^x = -\rho_g \lambda \frac{\partial \left(\frac{\xi_g}{\rho_g}\right)}{\partial x}$ . Where,  $J_g^x$  features the mass flux of gas  $g$  in the direction of  $x$ .  $\lambda$  represents the gas transfer coefficient of materials.  $\rho_g$  stands for the density of gas  $g$ .

### D) Mass and energy conservation equations

The overall behavior of a pyrolyzing object is described by mass and energy conservation equations [28]. In ThermaKin2D, these equations are formulated in terms of rectangular finite elements. Each element is characterized by component masses and temperature. An application of the law of conservation of mass to



the g-th component in element R yields is shown in the following:

$$\frac{\Delta m_g^R}{\Delta t} = V^R \sum_{j=1}^{N_r} \theta_r^g r_j^R + \lambda^{LR} \rho_g^{LR} S \frac{\left( \frac{m_g^L / \rho_g^L}{V^L} - \frac{m_g^R / \rho_g^R}{V^R} \right)}{\Delta x}$$

Where  $m_g^R$  is the change in the component mass during the time  $\Delta t$  in kg. The terms on the right hand side of the equation are contributions from reaction and mass transfer from element L.  $\theta_r^g$  is the stoichiometric coefficient in front of component g in the j-th reaction. This coefficient is set to be negative when the component is a reactant and positive when it is a product. LR superscript refers to averages of the parameters obtained for each of the two elements.  $\Delta x$  is the distance between the centers of the elements in m. m is mass in kg/m<sup>3</sup>. V is volume in m<sup>3</sup>. t is time in s.  $\theta$  is stoichiometric coefficient.  $\lambda$  is gas transfer coefficient in m<sup>2</sup>/s. r is rate of reaction in kg/(m<sup>3</sup>·s).  $\rho$  is density in kg/m<sup>3</sup>. S is surface area in m<sup>2</sup>.

An application of the law of conservation of energy to element R yields <sup>[29]</sup>:

$$c^R \frac{\Delta T^R}{\Delta t} = V^R \sum_{j=1}^{N_r} h_r^g r_j^R + k^{LR} S \frac{(T^L - T^R)}{\Delta x} + \frac{1}{2} \sum_{g=1}^{N_g} c_g^{LR} (T^L - T^R) j_g^{LR}$$

Where,  $\Delta T^R$  is the temperature change in the element in K. Nr is the number of reactions. The terms on the right hand side of the equation account for heat generation by reactions and conduction and convection of heat from element L.  $j_g^{LR}$  is the rate of flow of gas g from L to R in kg/(m<sup>2</sup>·s). j is the rate of mass transfer. h is the heat of reaction in J/kg. k is thermal conductivity W/(m·k). T is temperature in K. c is heat capacity in J/(kg·K).

Regarding the boundary condition for each equation, please see more details in the reference [17].

## E) Solution method

To discretise the conservation equations into a series of algebraic equations, the material would be changed into rectangular volumes of identical dimensions. Regarding the 1D case, the thickness  $\Delta x$  is limited to  $5 \times 10^4$ . With respect to 2D case, the  $\Delta x$  and  $\Delta y$  are limited to  $1.5 \times 10^3$ , respectively. The total mesh should be less than  $2.2 \times 10^6$ . The time integration during the simulation time  $\Delta t$  is based on the Crank-Nicolson scheme. ThermaKin2D is coded by ANSI/ISO C++ and its standard library.

### 2.2.3 FireFOAM2.2.x

The FireFOAM, developed by Yi et al. from FM Global and oriented to be used in simulation of large-scale industrial fires, is a popular CFD tool in fire research field. FireFOAM is an object-oriented, C++-based, second-order accurate, finite volume solver with implicit time integration<sup>[11, 30]</sup>. It uses a massively parallel computing capability using Message Passing Interface (MPI) protocols, employs a Favre-filtered compressible flow formulation and provides a choice between several modeling options for the treatment of turbulence, combustion and thermal radiation<sup>[31]</sup>. Main models are briefly introduced in the followings:

#### A) Transport Equations

FireFOAM numerically solves the mass, momentum, species and sensible enthalpy equations, which are shown in the followings<sup>[32]</sup>:

$$\frac{\partial \bar{\rho}}{\partial t} + \frac{\partial \bar{\rho} \tilde{u}_j}{\partial x_j} = 0$$

$$\frac{\partial \bar{\rho} \tilde{u}_i}{\partial t} + \frac{\partial \bar{\rho} \tilde{u}_i \tilde{u}_j}{\partial x_j} = \frac{\partial}{\partial x_j} \left( \bar{\rho} (v + v_{sgs}) \left( \frac{\partial \tilde{u}_i}{\partial x_j} + \frac{\partial \tilde{u}_j}{\partial x_i} - \frac{2}{3} \frac{\partial \tilde{u}_k}{\partial x_k} \delta_{ij} \right) \right) - \frac{\partial \bar{p}}{\partial x_i} + \bar{\rho} g_i$$

$$\frac{\partial \bar{\rho} \tilde{Y}_k}{\partial t} + \frac{\partial \bar{\rho} \tilde{u}_j \tilde{Y}_k}{\partial x_j} = \frac{\partial}{\partial x_j} \left( \bar{\rho} \left( D_k + \frac{v_{sgs}}{Pr_i} \right) \frac{\partial \tilde{Y}_k}{\partial x_j} \right) + \bar{\omega}_k$$

$$\frac{\partial \bar{\rho} \tilde{h}_s}{\partial t} + \frac{\partial \bar{\rho} \tilde{u}_j \tilde{h}_s}{\partial x_j} = \frac{D\bar{p}}{Dt} + \frac{\partial}{\partial x_j} \left( \bar{\rho} \left( \alpha + \frac{v_{sgs}}{Pr_i} \right) \frac{\partial \tilde{h}_s}{\partial x_j} \right) - \frac{\partial \bar{q}_j''}{\partial x_j} + \dot{q}_F'''$$

Where the  $\sim$  is the Favre filter operator,  $\rho$  is the density,  $u$  is the velocity,  $v$  is the molecular viscosity,  $v_{sgs}$  is the subgrid viscosity,  $p$  is the pressure from the stat equation  $\bar{p} = \bar{\rho} R_g \tilde{T}$ ,  $g$  is the gravity,  $Y_k$  is the species mass fraction,  $D_k$  is the molecular diffusivity,  $\dot{\omega}_k'''$  is the mass reaction rate for species  $k$ ,  $h_s$  is the sensible enthalpy,  $\alpha$  is the thermal diffusivity,  $\dot{q}_j''$  is the heat flux, and  $\dot{q}_F'''$  is the energy release rate per unit volume. The above equations are coupled by PISO and SIMPLE solutions.

## B) Turbulence model

There are many turbulence models in the fireFOAM. Here, four representative compressible turbulence models were selected: homogeneousDynOneEqEddy, lowReOneEqEddy, Smagorinsky, OneEqEddy, Smagorinsky. The k-equation model solves a differential equation for sub-grid turbulent kinetic energy  $k_{sgs}$ , expressed as [33-35]:

$$\frac{\partial(\bar{\rho} k_{sgs})}{\partial t} + \frac{\partial(\bar{\rho} \tilde{u}_j k_{sgs})}{\partial x_j} - \frac{\partial}{\partial x_j} \left( \bar{\rho} (v + v_{sgs}) \frac{\partial k_{sgs}}{\partial x_j} \right) = \bar{\rho} \left( \frac{2}{3} \left( k_{sgs} + v_{sgs} \frac{\partial \tilde{u}_k}{\partial x_k} \right) \frac{\partial \tilde{u}_i}{\partial x_i} - 2 v_{sgs} \widetilde{S_{ij} S_{ij}} \right) - \epsilon_{sgs}$$

Where the strain rate is  $\widetilde{S_{ij}} = \frac{\partial \tilde{u}_i}{2 \partial x_j} + \frac{\partial \tilde{u}_j}{2 \partial x_i}$ , the rate of dissipation of sub-grid turbulent kinetic energy is

$\epsilon_{sgs} = \frac{C_\epsilon k_{sgs}^{3/2}}{\Delta}$ , and the sub-grid turbulent eddy viscosity is obtained by  $v_{sgs} = C_k k_{sgs}^{1/2} \Delta$ . Where the modeling

coefficient  $C_k = 0.5$ , and the filter size is  $\Delta = \sqrt[3]{\Delta x \Delta y \Delta z}$ . The turbulent mixing time scale is:  $\tau_{turb} = \frac{k_{sgs}}{\epsilon_{sgs}}$

## C) Combustion model

In FireFOAM, combustion is modelled with the classical concept of a global combustion equation combined with the Eddy Dissipation Combustion Model (EDM) [26]. In modified EDM model, the reaction

rate is :  $\tau_{\text{turb}} = \frac{\Delta^2}{\alpha}$ ,

$$\overline{\dot{q}}_F = \frac{\bar{\rho}}{\min\left(\frac{\tau_{\text{turb}}}{C_{EDM}}, \frac{\Delta^2}{C_{\text{diff}}\alpha}\right)} \frac{\bar{\rho}}{\tau_{\text{turb}}} \min\left(\tilde{Y}_F, \frac{\tilde{Y}_{O_2}}{r_s}\right)$$

Where the modeling coefficient is  $C_{EDM} = 10$ ,  $\tilde{Y}_F$  and  $\tilde{Y}_{O_2}$  are the fuel and oxygen mass fraction respectively. In the EDM model, the reaction time scale is assumed to be infinitely fast and reaction rate is therefore governed by the sub-grid turbulent mixing, where the coefficient  $C_{\text{diff}}$  is set equal to 0.4.

#### D) Radiation model

A classical approach Finite Volume Discrete Ordinates Method (FvDOM) is used for thermal radiation.

#### E) The model of radioactive heat flux received from the flame

In the FireFOAM, the radioactive heat flux received from the flames is calculated by the following:

$$\dot{q}_{\text{rad}}'' = (1-\beta) \times \varepsilon_{\text{flame}} \sigma (T_{\text{rad}}^4 - T_w^4)$$

Where  $(1-\beta)$  is the effect of radiation blockage the effect of radiation blockage (due to fuel vapors, combustion products and soot particles) near the cold wall [36, 37].

#### F) Thermocouple model

With an aim to get accuracy temperature profiles, a thermocouple model of FireFOAM was used for temperature measurement. The thermocouple model could be described in the following [38]:

$$\rho_{tc} c_{tc} \left(\frac{V_{tc}}{A_{tc}}\right) \frac{dT_{tc}}{dt} = \varepsilon_{tc} (G - \sigma T_{tc}^4) + h_{tc} (T_g - T_{tc}) \rho_{tc}$$

$\rho_{tc}$  is the mass density of thermocouple,  $c_{tc}$  is heat capacity of thermocouple,  $V_{tc}$  is the volume of thermocouple  $A_{tc}$  is surface area of thermocouple,  $\varepsilon_{tc}$  stands for surface emissivity of the thermocouple bead,  $G$  is the irradiation received by the thermocouple,  $h_{tc}$  is the convective heat transfer coefficient.  $T_g$  represents the local gas temperature,  $T_{tc}$  features the thermocouple bead temperature,  $\sigma$  is the Stefan–Boltzmann constant.

### G) Heat flux meter model

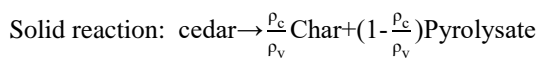
A heat flux meter model was incorporated into the FireFOAM. Considering the heat flux measured by flux meter consisting of emitted and absorbed radiation at a solid surface, the heat flux meters was modeled according to the following equation:

$$\dot{q}_{meter}'' = \varepsilon_{meter} (\dot{q}_{in}'' - \sigma T_{meter}^4) + h_{meter} (T_g - T_{meter})$$

Where,  $\dot{q}_{meter}''$  is the net heat flux received,  $\varepsilon_{meter}$  is surface emissivity of the flux meter with a value of 0.85.  $h_{meter}$  is defined as the same method with  $h_{tc}$ .  $T_{meter}$  is the temperature of flux meter, which is the same with thermocouple temperature.

### H) The 1D Arrhenius model

The 1D Arrhenius model  $\dot{m}''' = -\rho A \exp(-\frac{E_A}{RT_s})$  is used. Where  $\dot{m}'''$  features the mass loss rate.  $A$  represents pre-experiment index.  $E_A$  stands for activation energy.  $R$  is constant.  $T$  stands for temperature. The detailed introduction of pyrolysis model is disclosed in the followings [39].



Energy conservation:  $\frac{\partial}{\partial t} (\rho c_p T) = \frac{\partial}{\partial x} (k \frac{\partial T}{\partial x}) + \dot{\omega}_v''' \Delta H_{p,v}$

Mass conservation:  $\frac{\partial}{\partial t}(\rho Y_v) = \dot{\omega}_v$

Volumetric mass consumption rate:  $\dot{\omega}_v = \left[ \frac{\rho Y_v}{(\rho Y_v)_0} \right]^n (\rho Y_v)_0 A \exp\left(-\frac{E_a}{RT}\right)$

Mass loss rate:  $MLR = \left(1 - \frac{\rho_c}{\rho_v}\right) \int_0^L \dot{\omega}_v dx$

Where  $\rho_v$  and  $\rho_c$  are densities (kg/m<sup>3</sup>) of cedar material and char, respectively. Density ( $\rho$ ) and thermal conductivity (kW/m/K) are bulk values averaged by the volume fractions of virgin and char, while specific heat ( $c_p$ ) is averaged based on mass fractions.  $Y_v$  is the mass fraction of virgin material; in each control volume the char mass fraction is given by  $1 - Y_v$ .  $\Delta H_{p,v}$  is the heat of pyrolysis (J/kg),  $n$  is the reaction order,  $A$  is the pre-exponential factor (s<sup>-1</sup>),  $R$  is the universal gas constant (8.314 J/mol/K),  $E_a$  is the activation energy (J/mol), and  $T$  is the temperature (K). The subscript 0 designates initial conditions before heating and pyrolysis.  $L$  is the thickness of the solid (m) and  $t$  and  $x$  are temporal and spatial variables.

## 2.3 Comparison of main available fire CFD tools

### 2.3.1 FDS

Above contents could provide basic knowledge of each CFD tool, which is useful for the CFD beginner to understand the parameters needed during the simulation. In turn, when the results of simulation becomes far away from the experimental results, the parameters which need optimization could be located rapidly. According to personal understanding of FDS, the advantages and disadvantages are summarized in the followings:

## **Advantages:**

### **A) Calculation speed fast**

In the FDS calculation, the conservation equations of density, momentum and energy are solved using finite difference method (FDM). Furthermore, the code is written by Fortran 90, which is very convenient for industry scale simulations. In the past, we have did a large scale building (50 m high) fire simulation. The results of simulation are used to provide the knowledge of fire protection or smoke exhausting after fire.

### **B) A good 3D virtualization**

The good virtualization including the smoke and flame help fire researcher or users to well understand the fire spread mechanism. When I first use FDS in 2008 year, the virtualization was shocked me deeply. Especially, the user could experience the scene by using a function inside the smokeview. The scene is well build with a similar smoke movement compared with a real fire. The smokeview is specially developed for the FDS data post processing. It has made an important contribution for fire drill, which is intended to be a new tool for fire drill.

### **C) Low computer cost**

The accuracy results and low cost seems hard to hold at the same time. However, some models in FDS are simplified to accelerate computational speed, when the little effects of these models showed in results compared with huge computational cost. Furthermore, the parallel calculation is also used in FDS.

### **D) Many models from its library**

The FDS has lasted at about 25 years since it was firstly proposed in 1993. Many famous CFD experts

have made contribution for FDS. The relevant reports are available.

#### **E) Many available reference materials**

In the architecture field, it is a little new for us to fluently use CFD tools. However, the reference materials could be found freely in the website of FDS, which is <https://pages.nist.gov/fds-smv/>. It consists of FDS User's Guide, FDS Technical Reference Guide, FDS Verification Guide, FDS Validation Guide, FDS Configuration Management Plan, SMV User's Guide, SMV Technical Reference Guide and SMV Verification Guide until 2018-3-16. The new one are still being renewed. Furthermore, a discussion forum could be found in the above website. When the problems including technical or usage problems are found, the answer could be get by posting it or directly discussing it with different FDS users.

#### **Disadvantages:**

##### **A) Many simplification in model**

Regarding the attempts to evaluate or develop FDS code, it is better to know the model used in it firstly. However, the user from the architecture field easily could be satisfied by the performance of FDS.

##### **B) Structured mesh**

During the building fire simulation, the structured mesh could give reasonable results. As the rapid development in architecture technology and building materials, the complexity of computational domain is challenging the structured mesh. Currently, the accuracy of computational domain with less complexity could be improved by multi-blocks. For example, the hot smoke movement along with an arc tunnel perhaps reproduced by FDS using multi-blocks technology. When the discussion focused on the effects of hot smoke on the walls of arc tunnel, the structured mesh is limited. This issue may be solved in future since it has limited the application of FDS in the complex computational domain.



### **C) Code is hard to read**

The utilization of FORTRAN not only accelerate the calculation speed, but also increase the difficulty to know the code well. Many abbreviations are involved in the code of FDS. When the code development is conducted, it is better firstly to discuss the existing code configuration with FDS experts to avoid the mistakes.

### **D) Fortran 90**

Currently, the new program language is emerging. Among these language, the C++ has showed the flexibility compared with old Fortran 90. Furthermore, the user-oriented language advantage of C++ has attracted more and more attentions.

## **2.3.2 ThermaKin2D**

ThermaKin2D is professional in pyrolysis model. According to the personal understanding the thermaKin2D, the advantages and demerits are summarized to briefly provide an information for beginner or fire researcher not from CFD fields.

### **Advantages:**

#### **A) Professional in pyrolysis modeling**

Just as discussed in the above parts, up to 30 components or reaction could be defined in it. The temperature-dependent parameters are characterized by multi-curves, not a constant value during the whole simulation. Regarding the basic parameters which varies largely with temperature, the attempts to model pyrolysis using thermaKin seems reasonable. It also provide a potential method for multi-layers pyrolysis model to identify the contribution of the individual layers .

### **B) The definition of heat flux from flames during pyrolysis**

The flame heat flux is not accounted for in the FDS model during pyrolysis, which could be lower the mass loss rate during the Cone test. Comparably in ThermaKin2D, a simple CI model is used which could feature the effects of flame effects on the surface of materials. In the next part, the detailed discussion would be conducted by comparing the FDS and ThermaKin.

#### **Disadvantages:**

##### **A) 1D or 2D simulation**

Currently, the new 2D dimensional ThermaKin has been available. Although it is very professional in multi-layers and multi-reaction, the 3D dimensional ThermaKin is expectant.

### **2.3.3 FireFOAM**

FireFOAM is professional in fire simulation. According to the personal understanding the FireFOAM2.2.x, the merits and demerits are summarized to briefly provide a reference for beginners or fire researcher without CFD background.

#### **Advantages:**

##### **A) Computer language C++ (object oriented )**

FireFOAM is C ++-based code. Comparably, C++ is relative easy to read and change code. The details of C++ could easily find in the references.

##### **B) A great many of support from OpenFOAM**

OpenFOAM has an extensive range of features to solve complex fluid flows involving chemical

reactaons, turbulence and heat transfer, to acoustics, solid mechanics and electromagnetics <sup>[32]</sup>. FireFOAM is a solver of OpenFOAM which used specially in fire simulation. The FireFOAM could use the library of OpenFOAM.

### **C) Flexible mesh**

Both structured and unstructured meshes could be used for FireFOAM. This feature broadens the application for complex fluid configuration.

### **D) 3D Virtualization**

The post processing software is paraview. It is very flexible and powerful.

### **Disadvantages:**

#### **A) Computational cost**

The computational cost used in FireFOAM is a little high. In some cases, the results of simulation with a fine mesh is huge. Near all my simulation are conducted in a super computer called Reedbush from The University of Tokyo. The large data is challenging for the data storage and transfer from super computer to personal PC. However, the computational cost is related with accuracy of results. Coarse mesh could be performed in a traditional PC.

#### **B) Few references**

The few references could be found in the available website. Nearly most of published works are from FM Global. Under this situation, it seems hard to master it by personal study. The brief summary of above discussion is described in the Fig.7.

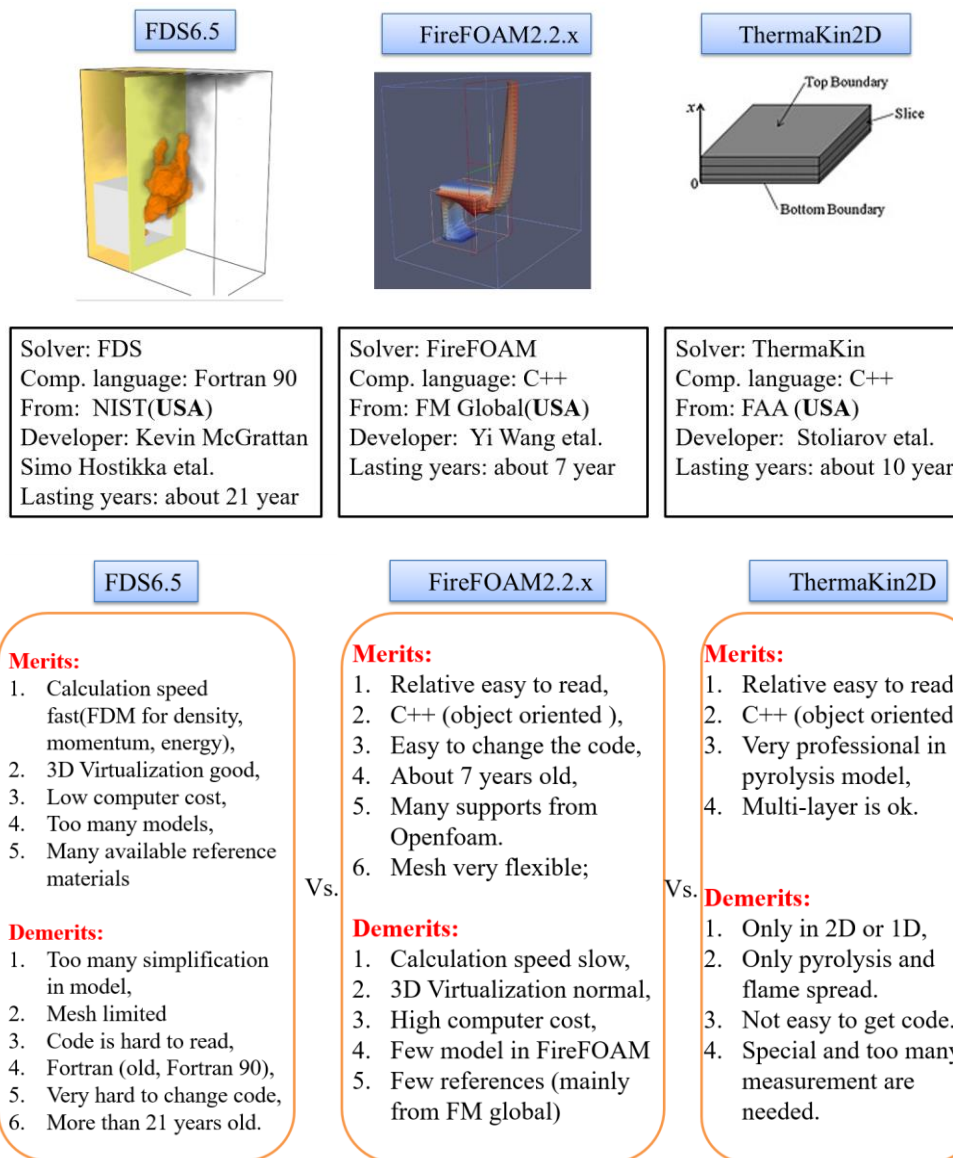


Fig.7 The brief introduction of three fire tools

The application field of three CFD tools are summarized in the following table 2. It is found that the fire tools are case or condition-dependent. ThermaKin is professional in the pyrolysis model compared with others. FireFOAM shows a merit on the flame spread and combustion. In general, FDS is a comprehensive tool for fire simulation, which has been validated and reported in plenty of references. When the fire produced heavily smoke, the FDS is preferred. The smoke model in FireFOAM is being developed.

Table 2 Comparison of basic performance and application range of three tools

Items		FDS (6.5)	FireFOAM (2.2.x)	ThermaKin (2D)
Basic performance	Calculation speed	+	+	+
	Easy to change code	+	+	+
	Virtualization technology	+	+	—
	Computer cost	+	+	+
	Available library support	+	+	+
	Available reference	+	+	+
	Flexible mesh	+	+	+
	Code lasted time	+	+	+
Application range	Fire plumes	+	+	—
	Pool fires	+	+	—
	Air movement during fire	+	+	—
	Flame fspread	+	+	—
	Compartment fires	+	+	—
	Sprinklers	+	+	—
	Tunnel fires	+	+	—
	Combustion model	+	+	+
	Smoke concentration	+	+	—
	Velocity	+	+	—
	Burning rate	+	+	+

Note: + features a good index. — represents that the index is not available.

## 2.4 Summary

In this chapter, the three open CFD tools are introduced. Firstly, the basic knowledge of each tool is presented to provide the necessary knowledge for CFD beginner or fire researcher without CFD background.

Then the difference among these CFD tools is reviewed and summarized to well understand these models according to the available papers. This is followed by chapter 3 that utilization of FDS in the internal building fire.

Regarding the internal building fire simulation, the FDS and ThermaKin were used because both of FDS and ThermaKin are professional in the modeling of multi-layer and multi-reaction. More specific, the ThermaKin was used to verify the flame heat flux effects on the solid pyrolysis process. The capacity to model the pyrolysis of polymer and model-box fire is detailed in the chapter 3.

In the external building fire simulation, such as façade fire, the FireFOAM was chosen on the basis of facts that FireFOAM could reproduce fire plume and could provide the good virtualization of fire flame which is important in the evaluation of fire spread. The capacity to model the flame spread and simple one-reaction pyrolysis is described in the chapter 4.

# 3. Utilization of CFD model to simulate internal building fire

## 3.1 Introduction

In this chapter, the utilization of CFD model in the interior building fire is conducted. The experimental materials are shown firstly. Then the experimental tests including Cone test performed with four materials according to ISO 5660-1 standard method and model-box test performed with two materials according to ISO TS 17431 standard method are disclosed. The Cone test for each specimen is under three different radiation levels. The coating layer effects on the Cone test of Nurate is discussed. With an aim to get optimal input parameters and configuration, the pyrolysis parameters are performed by a Bruker TG-DTA2000SA at five different and constant heating rates. The attempts to try modelling corresponding building fire is carried out using FDS because FDS is a comprehensive tool for both pyrolysis and compartment fire. This is followed by comparison of simulated and tested results. The influence of pyrolysis parameters on the Cone test is discussed on the basis of simulation results.

## 3.2 Experimental materials and planning

### 3.2.1 Materials

In the chapter, four types of interior building materials are used. The name is XPS, Polyurethane (Urethane), Polyisocyanurate (Nurate), HFO-cyanurate (Non-Nurate). The details of materials are listed in the table 12. All the specimens are provided by Nippon Aqua Co., Ltd.

### 3.2.2 Experimental planning

#### A) Thermogravimetry (TG) method

With aim to get the pyrolysis model parameters for simulation, the TG tests were conducted. The pre-exponential factor  $A$  and activation energy  $E$  are obtained from TG method. The thermal analysis experiments were performed with a Bruker TG-DTA2000SA, just as shown in Fig.8. The runs were carried out in dynamic conditions at five different and constant heating rates: 10, 15, 20, 25 and 30 K/min. Each sample was placed in a crucible with a lid and pinhole. The sample weights ranged from 3 to 5 mg. The thermo-gravimetric weight loss curve (TG, mg) and the weight loss derivative curve (DTG,  $\text{mg min}^{-1}$ ) were recorded as a function of time and temperature. The thermal analysis experiments were performed with a Bruker TG-DTA2000SA. The runs were carried out in dynamic conditions at five different and constant heating rates: 10, 15, 20, 25 and 30 K/min.



Fig. 8 The description of TG facility



## B) Cone Calorimeter according to ISO 5660-1 standard method

The experimental MLR and HRR were obtained using Cone. The heat released was measured using a Cone Calorimeter from Toyoseiki Ltd., just as shown in Fig.9. The set-up, calibration, and measurements were in accordance with the ISO 5660-1 standard method [40]. Samples were mounted horizontally by using a specimen holder with edge frame. The bottom of the holder was lined with ceramic fiber blanket. The bottom and sides of each sample were wrapped with a 0.02 mm thick aluminium foil. The heat release calculations were based on the measurement of oxygen, carbon monoxide, and carbon dioxide concentrations in dried exhaust gas. Duplicate tests were conducted at heat fluxes of 30 kW/m<sup>2</sup> and 50 kW/m<sup>2</sup>. Samples were prepared by cutting a panel (50 mm thick) into 100 mm × 100 mm square pieces.



Fig.9 The description of Cone used in this section

### C) The model-box fire test according to ISO TS 17431 standard method <sup>[41]</sup>

With aim to evaluate internal building materials reaction-to-fire performance, the model-box tests were carried out according to TS 17431 method. ISO/TS 17431 is a method for simulating an intermediate-scale fire, in which fire takes place in the corner of a fixed small room. The small room is equipped with a small door. During the test, the flame shape, heat release rate and total heat release rate curves varying test time could be got. This method is a preliminary test method for evaluation of fire toxic, fire spread, heat release rate. The model layout is described in the reference <sup>[42]</sup>. In this study, the model-box fire test according to ISO TS 17431 standard method was conducted by using the urethane and None-Nurate foam. During the test, the heat release calculations could be got by measuring oxygen, carbon monoxide, and carbon dioxide concentrations in exhaust gas. The four thermocouples are employed to record the temperature profiles during the whole test. The test was conducted in the General Building Research Corporation of Japan (GBRC) which located in the Osaka of Japan. The Fig.10 gives the description of this standard method.

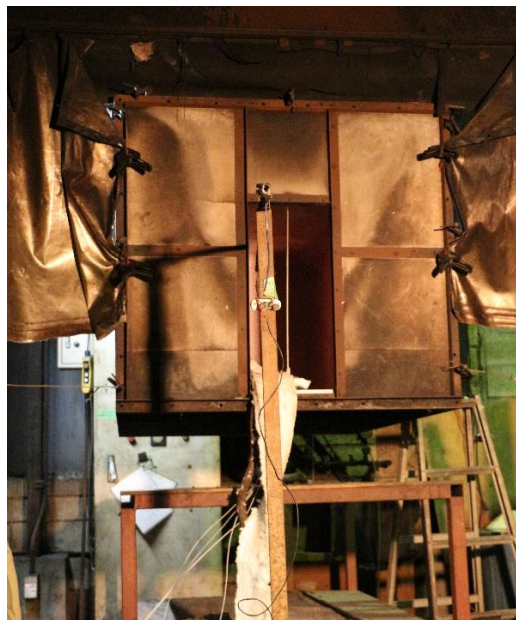


Fig.10 The description of ISO TS 17431 standard method

### 3.3 Experimental results and discussion

#### 3.3.1 Thermogravimetry (TG) results and discussion

The simulation of the DTG curves is based upon the kinetic law commonly used for a single weight loss [43]:

$$\frac{d\alpha}{dt} = A e^{-\frac{E}{RT}} (1 - \alpha)^n$$

If  $\beta$  is the constant heating rate:  $dT = d\beta \cdot dt$  and it follows that:

$$\frac{d\alpha}{dT} = \frac{A}{\beta} e^{-\frac{E}{RT}} (1 - \alpha)^n$$

Which integration becomes:

$$\int_0^\alpha \frac{d\alpha}{(1 - \alpha)^n} = \int_{T_0}^T \frac{A}{\beta} e^{-\frac{E}{RT}} dT = \frac{AE}{\beta R} \left\{ -\frac{e^x}{x} + \int_{-\infty}^x \frac{e^x}{x} dx \right\} = \frac{AE}{\beta R} p(x)$$

Where  $x = -E/(RT)$ . It is assumed that  $T_0$  is low enough for the lower limit to be negligible. In this study, the pyrolysis model is simplified in the first order reaction. When  $n=1$ , the following simplification is obtained:

$$\ln(1 - \alpha) = -\frac{AE}{\beta R} p(x)$$

To calculate the  $p(x)$ , the authors have chosen Lyon's approximation [44].

$$p(x) = \frac{e^x}{x(x - 2)}$$

Table 3, table 4, table 5 and table 6 feature the TG results of XPS, Urethane, Nurate and None-Nurate, respectively. Fig.11, Fig.12, Fig.13 and Fig.14 show the representative TG results description of XPS, Urethane, Nurate and None-Nurate, respectively.

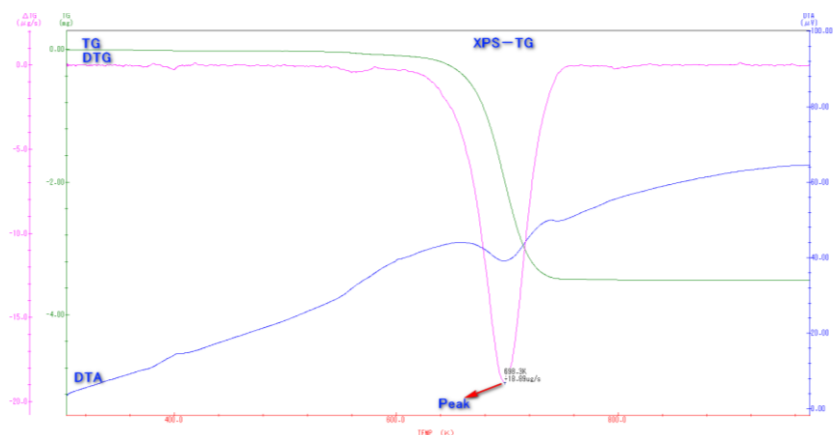


Fig.11 The representative description of TG, DTG and DTA curve of XPS Note: TG: real-time weight in mg, DTA: dT/dm change VS. temperature ( temp./mg),  $\Delta TG=DTG$ : Derivative thermo-gravimetric (-dm/dt).

Table 3 Results of XPS-TG varying heating rate

Heating rate /K/min	Original weight /mg	Tpeak(DTG) /k	Peak of DTG /μg/s	After test /mg	Char ratio /%
10	3.2	692.1	12.56	0	0
15	3.4	698.3	18.89	0	0
20	3.5	703.5	24.91	0	0
25	3.3	705.9	29.19	0	0
30	4.4	709.8	51.74	0	0

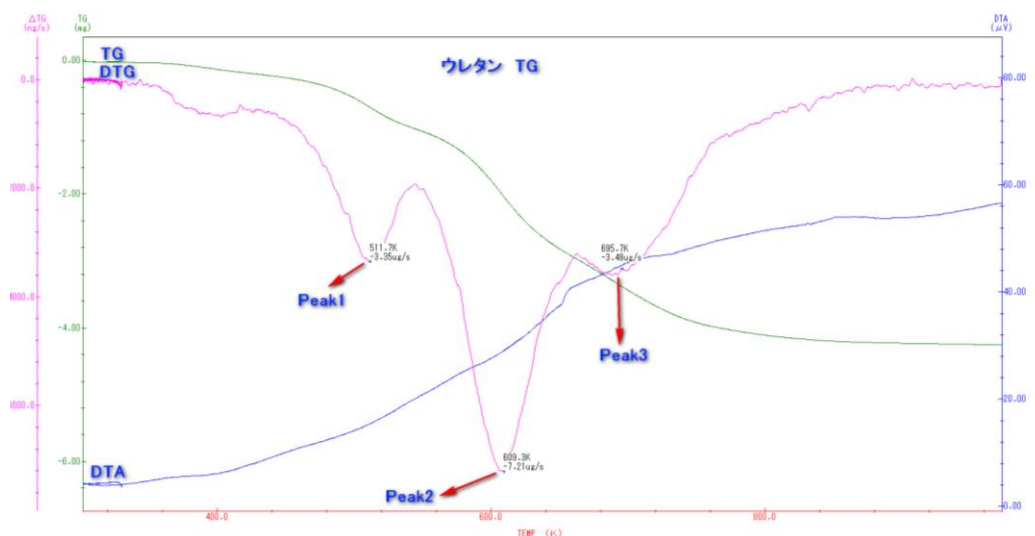


Fig.12 The representative description of TG, DTG and DTA curve of urethane

Table 4 Results of urethane-TG varying heating rate

Heating rate /K/min	Original weight /mg	Tpeak1(DTG) /k	Peak1 of DTG /μg/s	Tpeak2(DTG) /k	Peak2 of DTG /μg/s	Tpeak3(DTG) /k	Peak3 of DTG /μg/s	After test /mg	Char ratio /%
10	1.5	518.2	0.81	585.6	1.45	725.3	0.59	0.08	5.3
15	5.2	511.7	3.35	609.3	7.21	692.1	3.6	0.96	18.5
20	3.6	525.1	3.36	606.3	5.94	0	0	0.72	20.0
25	2.9	528.1	2.9	597.8	5.41	0	0	0.95	32.8
30	2.0	529.5	2.09	610.8	5.26	735.1	2.31	0.27	13.5

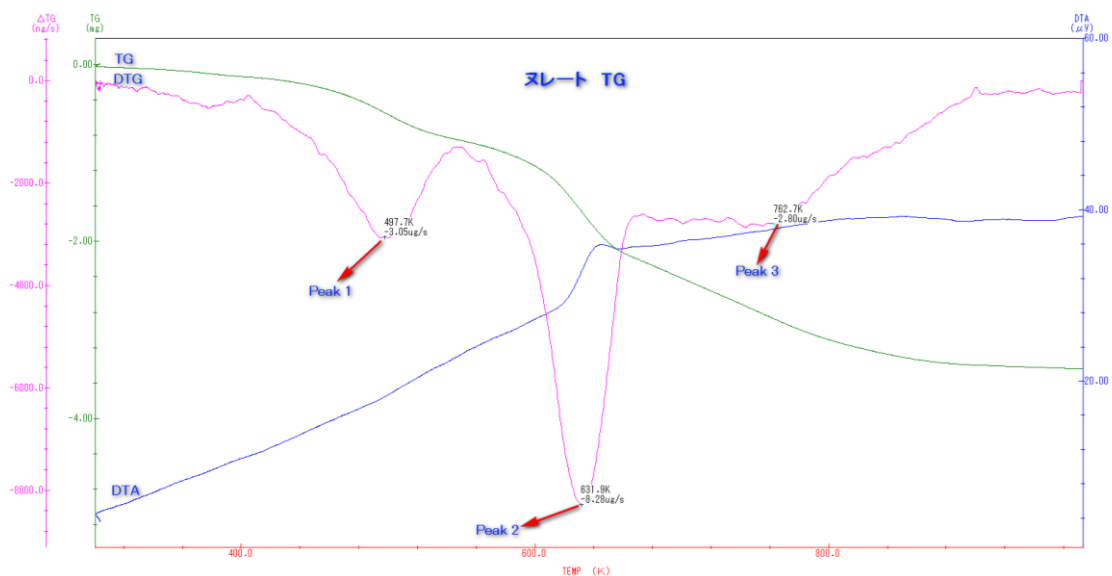


Fig.13 The representative description of TG, DTG and DTA curve of nurate

Table 5 Results of Nurate-TG varying heating rate

Heating rate /K/min	Original weight /mg	Tpeak1(DTG) /k	Peak1 of DTG /μg/s	Tpeak2(DTG) /k	Peak2 of DTG /μg/s	Tpeak3(DTG) /k	Peak3 of DTG /μg/s	After test /mg	Char ratio /%
10	3.4	480.4	1.34	609.0	3.5	719.1	1.10	0.64	18.82
15	3.3	488.4	2.03	618.1	4.94	735.5	1.64	0.71	21.52
20	4.4	497.7	3.05	631.9	8.28	760.0	2.78	0.97	22.05
25	4.8	511.5	4.04	635.2	10.98	756.3	4.02	0.94	19.58
30	3.9	495.1	3.9	632.4	10.06	768.0	3.62	0.98	25.13

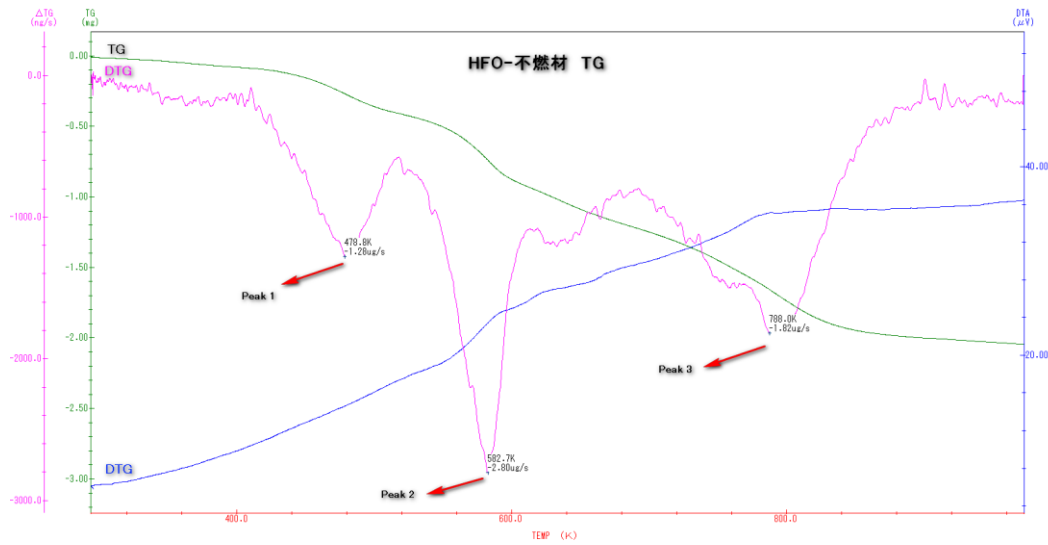


Fig.14 The representative description of TG, DTG and DTA curve of None-Nurate

Table 6 Results of None-Nurate

Heating rate /K/min	Original weight /mg	Tpeak1(DTG) /k	Peak1 of DTG /μg/s	Tpeak2(DTG) /k	Peak2 of DTG /μg/s	Tpeak3(DTG) /k	Peak3 of DTG /μg/s	After test /mg	Char ratio /%
10	3.7	482.9	1.10	578.4	2.07	787.9	0.95	1.92	51.89
15	3.2	478.8	1.28	582.7	2.80	795.1	1.81	1.17	36.56
20	4.0	489.1	1.91	590.4	4.33	801.4	3.2	1.45	36.25
25	4.9	505.8	2.84	595.0	7.3	814.1	4.56	1.87	38.16
30	3.6	492.5	2.34	592.9	5.48	808.3	3.86	1.56	43.33

With an aim to describe the calculation method for the E and A, the None-Nurate is used. The activation energy E and pre-exponential factor A of None-Nurate materials pyrolysis is disclosed in the followings.

Table 7 gives the heating rate and fractional mass loss temperatures for pyrolysis of material. Here T (0.05) stands for the temperature of 5 % of material volatilization. By analogy, T (0.99) represents for the temperature of 99 % or all of material volatilization. Plot of natural logarithm of heating rate vs. the

reciprocal temperature for volatile fractions  $\alpha=0.05, 0.1, 0.2, 0.5, 0.7, 0.9$  and  $0.99$  for None-Nurate is described in Fig. 15. Activation energy vs. fractional weight loss for None-Nurate is shown in Fig.16. Plot of  $\ln[\beta/T]$  vs.  $\ln[2+E_a/RT]+E_a/RT$  TG for thermal degradation of None-Nurate at complete conversion is got in Fig.17 . From it, E and A are  $78.27 \text{ kJ/mol}$  and  $1.03 \times 10^{10}$ , respectively.

Table 7 Heating rate and fractional mass loss temperatures for pyrolysis of None-Nurate material

Heating rate $\beta$ /K/min	T(0.05) K	T(0.1) K	T(0.2) K	T(0.5) K	T(0.7) K	T(0.9) K	T(0.99) K
10	434.7	460.4	494.5	589.3	678.8	805.1	958.8
15	423.8	464.1	518.3	634.6	746.8	818.3	941.3
20	413.2	465.2	522.6	648.5	758.0	826.2	941.6
25	425.0	479.7	533.9	648.4	760.2	834.5	941.7
30	421.6	471.4	526.8	652.5	764.5	834.9	930.6

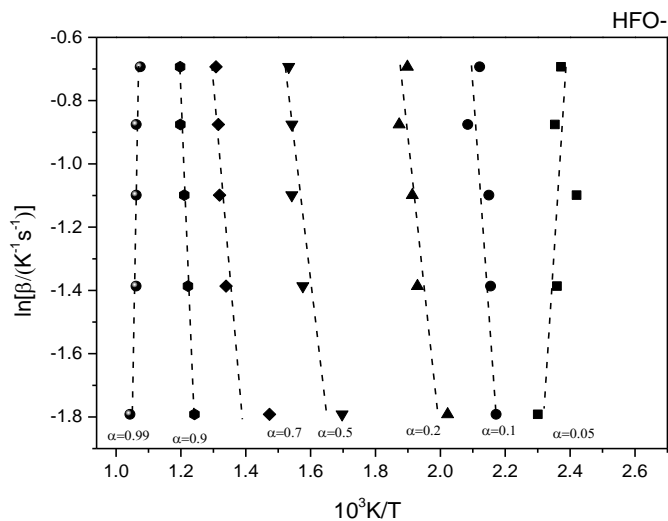


Fig. 15 Plot of natural logarithm of heating rate vs. the reciprocal temperature for volatile fractions  $\alpha=0.05, 0.1, 0.2, 0.5, 0.7, 0.9$  and  $0.99$  for None-Nurate material.



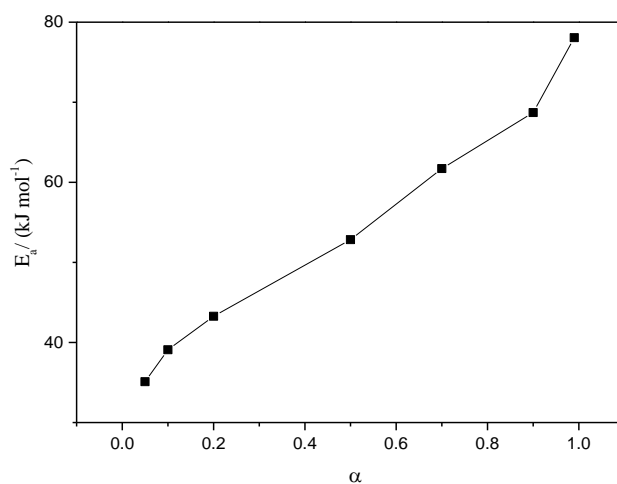


Fig.16 Activation energy vs. fractional weight loss for None-Nurate material

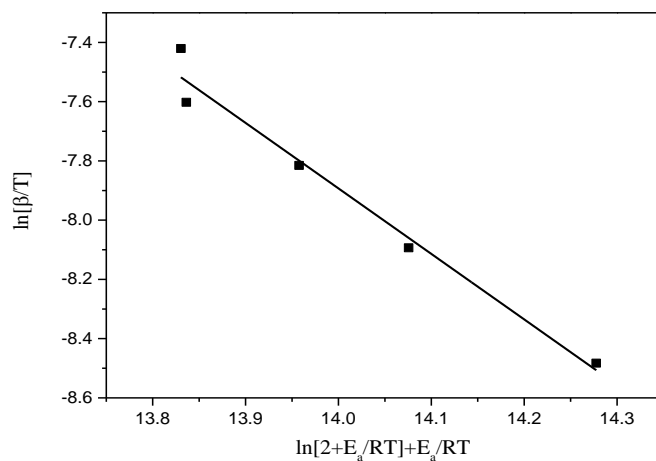


Fig.17 Plot of  $\ln[\beta/T]$  vs.  $\ln[2+E_a/RT]+E_a/RT$  for thermal degradation of None-Nurate material at complete conversion

### 3.3.2 Cone Calorimeter results and discussion

The heat released was measured using a Dual Cone Calorimeter from Fire Testing Technology Ltd.. The set-up, calibration, and measurements were in accordance with the ISO 5660-1 standard method <sup>[40]</sup>. Samples were mounted horizontally by using a specimen holder with edge frame. The bottom of the holder was lined with ceramic fiber blanket. The bottom and sides of each sample were wrapped with a 0.02 mm

thick aluminium foil. The heat release calculations were based on the measurement of oxygen, carbon monoxide, and carbon dioxide concentrations in dried exhaust gas. Duplicate tests were conducted at heat fluxes of 30 kW/m<sup>2</sup> and 50 kW/m<sup>2</sup>. Samples were prepared by cutting a panel (50 mm thick) into 100 mm × 100 mm square pieces. Fig. 18 shows pictures of the specimen test configuration. During Nurate tests, the effects of coating layer on the reaction-to-fire performance is discussed. The coating materials used here is a 5 mm thickness of calcium silicate board. The tested mass loss rate (MLR) and heat release rate (HRR) of XPS, Urethane, Nurate, None-Nurate are presented in Fig.19, Fig.20, Fig.21 and Fig.22, respectively. The detailed results which include pHRR, HRR(mean 60 s), HRR(mean 180 s), HRR(mean 300 s), t<sub>extinguishing</sub>, HOC(mean heat of combustion) and MLR(mean mass loss rate) are disclosed in table 8, table 9 and table 10, respectively. Table 11 features the comparison of coating and uncoating reaction-to-fire performance.

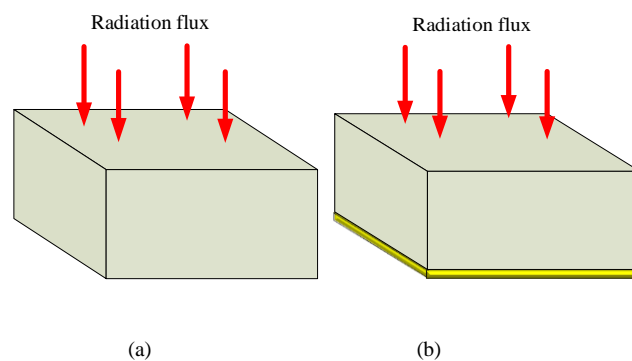


Fig.18 The description of test configuration (a) no coating layer (躯体なし) (b) with coating layer (躯体有)

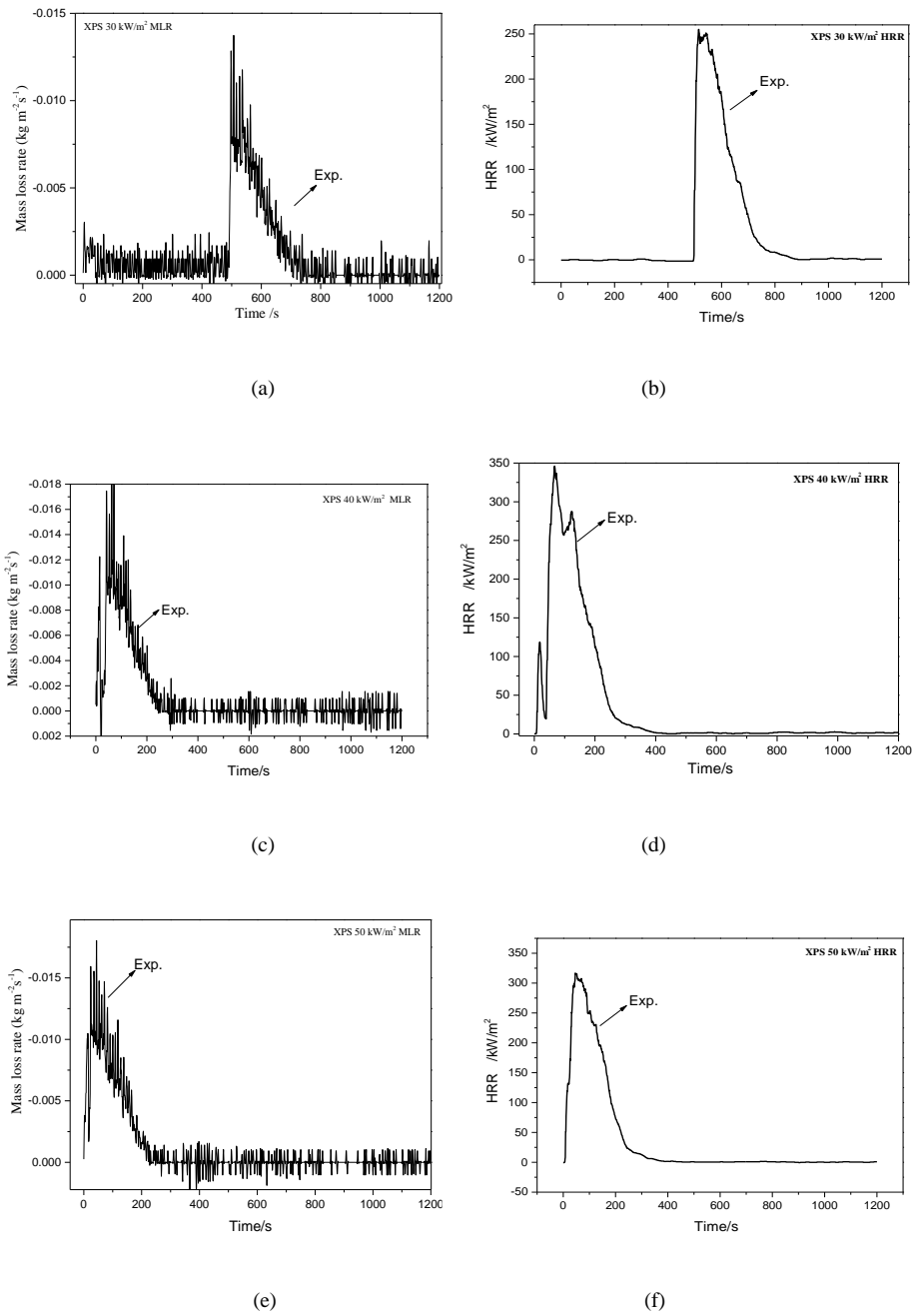
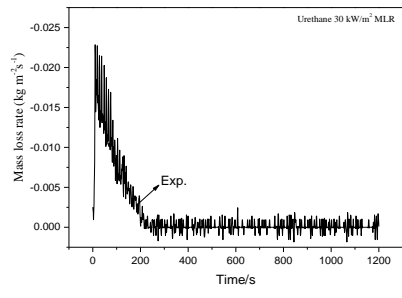
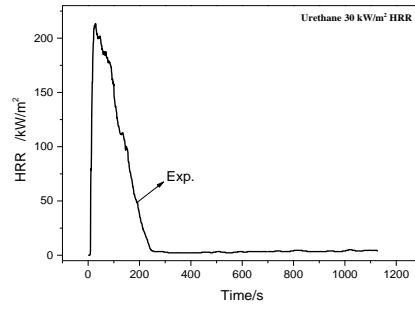


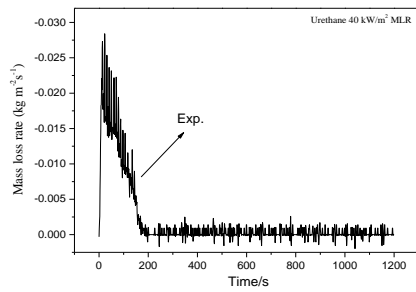
Fig.19 XPS mass loss rate and Heat release rate histories varying with different radiation (a) MLR of radiation 30 kW/m<sup>2</sup> (b) HRR of radiation 30 kW/m<sup>2</sup> (c) MLR of radiation 40 kW/m<sup>2</sup> (d) HRR of radiation 40 kW/m<sup>2</sup> (e) MLR of radiation 50 kW/m<sup>2</sup> (f) HRR of radiation 50 kW/m<sup>2</sup>



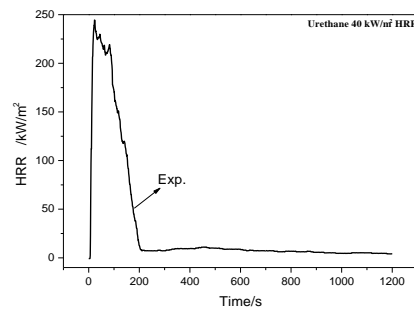
(a)



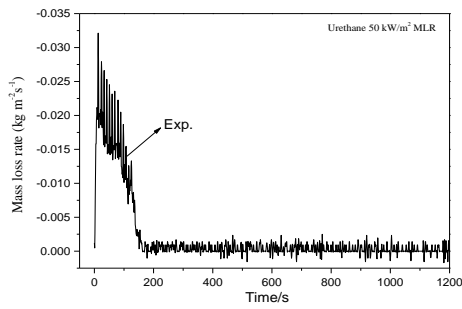
(b)



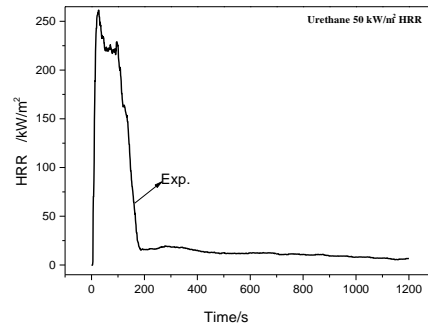
(c)



(d)



(e)

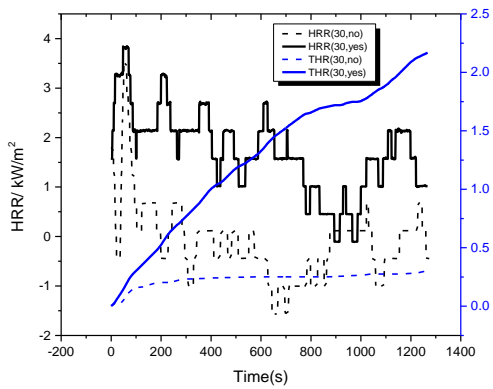


(f)

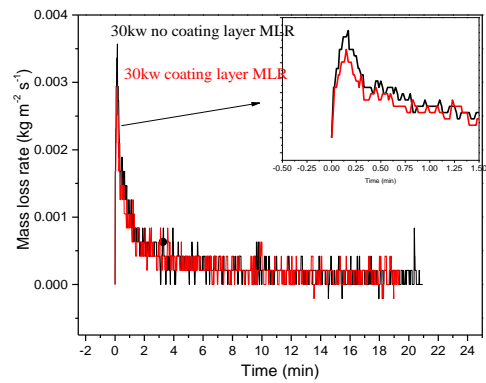
Fig.20 Urethane mass loss rate and Heat release rate histories varying with different radiation (a) MLR of radiation 30 kW/m<sup>2</sup> (b)

HRR of radiation 30 kW/m<sup>2</sup> (c) MLR of radiation 40 kW/m<sup>2</sup> (d) HRR of radiation 40 kW/m<sup>2</sup> (e) MLR of radiation 50 kW/m<sup>2</sup> (f)

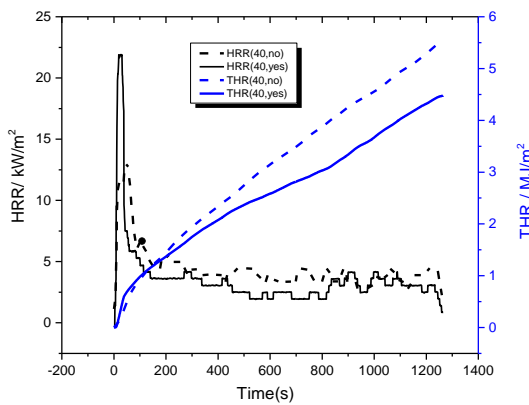
HRR of radiation 50 kW/m<sup>2</sup>



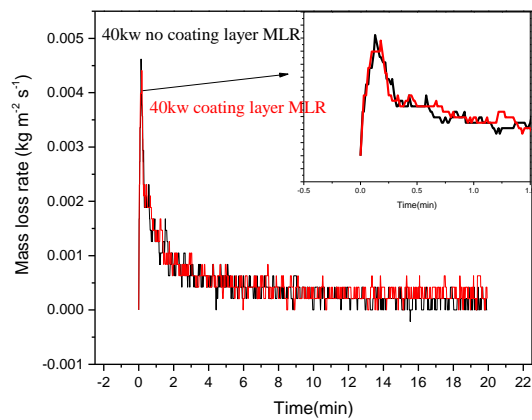
(a)



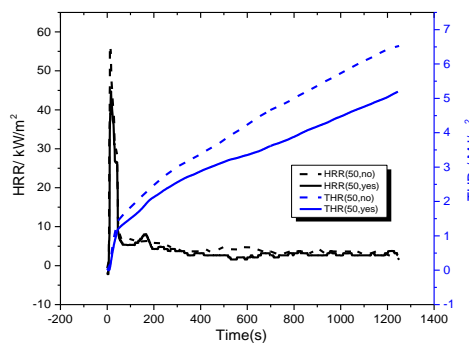
(b)



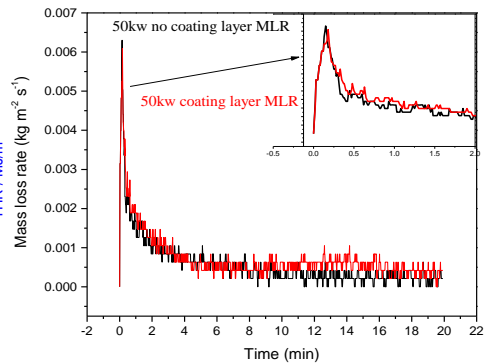
(c)



(d)



(e)



(f)

Fig.21 Nurate mass loss rate and Heat release rate histories varying with different radiation (a) MLR of radiation 30 kW/m<sup>2</sup> (b) HRR of radiation 30 kW/m<sup>2</sup> (c) MLR of radiation 40 kW/m<sup>2</sup> (d) HRR of radiation 40 kW/m<sup>2</sup> (e) MLR of radiation 50 kW/m<sup>2</sup> (f)

HRR of radiation 50 kW/m<sup>2</sup>

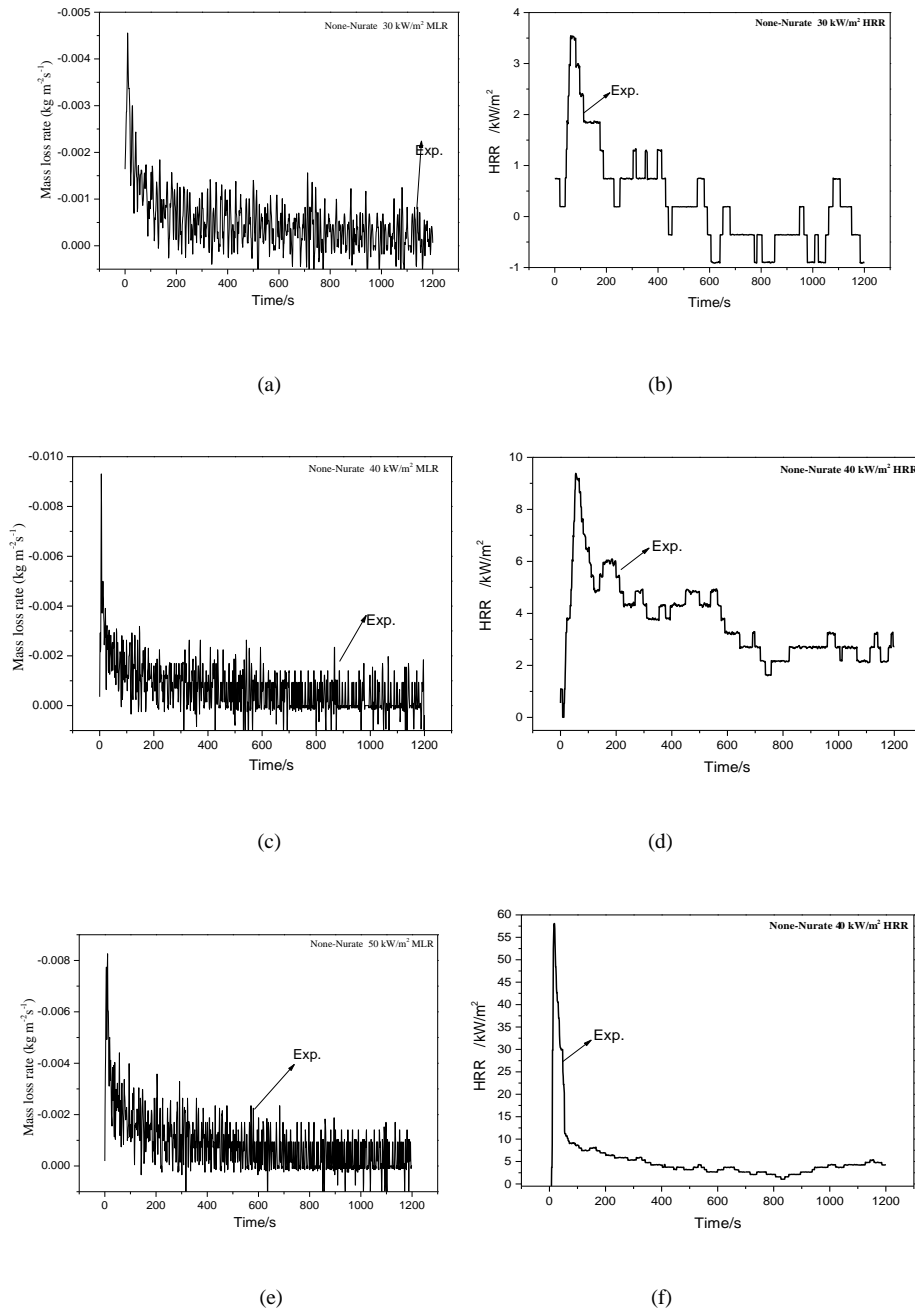


Fig.22 None-Nurate mass loss rate and Heat release rate histories varying with different radiation (a) MLR of radiation 30  $\text{kW/m}^2$  (b) HRR of radiation 30  $\text{kW/m}^2$  (c) MLR of radiation 40  $\text{kW/m}^2$  (d) HRR of radiation 40  $\text{kW/m}^2$  (e) MLR of radiation 50  $\text{kW/m}^2$  (f) HRR of radiation 50  $\text{kW/m}^2$

Table 8 Summary of cone test results at radiation level of 30 kW/m<sup>2</sup>

Parameter	Unit	XPS	Urethane	Nurate	None-Nurate
THR	MJ/m <sup>2</sup>	35.17	29.72	10.1	0.62
pHRR	kW/m <sup>2</sup>	255.01	213.4	35.03	3.55
HRR(mean 60 s)	kW/m <sup>2</sup>	214.08	173.88	20.96	0.94
HRR(mean 180 s)	kW/m <sup>2</sup>	172.36	138.63	17.06	1.86
HRR(mean 300 s)	kW/m <sup>2</sup>	114.76	88.96	16.38	1.39
t <sub>ig</sub>	s	494.4	5.2	9.1	NT
t extinguishing	s	754	225	488	NT
HOC(mean heat of combustion)	MJ/kg	25.13	15.45	12.4	1.01
MLR(mean mass loss rate)	g/s·m <sup>2</sup>	5.58	9.308	0.703	0.552

Table 9 Summary of cone test results at radiation level of 40 kW/m<sup>2</sup>

Parameter	Unit	XPS	Urethane	Nurate	None-Nurate
THR	MJ/m <sup>2</sup>	45.2	36.06	15.32	4.44
pHRR	kW/m <sup>2</sup>	345.95	244.48	66.61	9.38
HRR(mean 60 s)	kW/m <sup>2</sup>	128.65	199.05	41.49	4.24
HRR(mean 180 s)	kW/m <sup>2</sup>	204.57	158.36	34.68	5.57
HRR(mean 300 s)	kW/m <sup>2</sup>	145.03	99.05	29.21	5.3
t <sub>ig</sub>	s	5.3	3.2	3.2	NT
t extinguishing	s	347	188	458	NT
HOC(mean heat of combustion)	MJ/kg	30.22	15.4	14.56	5.24
MLR(mean mass loss rate)	g/s·m <sup>2</sup>	8.362	6.399	1.079	0.805

Table 10 Summary of cone test results at radiation level of 50 kW/m<sup>2</sup>

Parameter	Unit	XPS	Urethane	Nurate	None-Nurate
THR	MJ/m <sup>2</sup>	44.36	42.24	15.82	6.56
pHRR	kW/m <sup>2</sup>	316.75	261.56	74.62	58.09
HRR(mean 60 s)	kW/m <sup>2</sup>	211.41	207.59	49.36	29.04
HRR(mean 180 s)	kW/m <sup>2</sup>	215.85	168.76	38.64	15.14
HRR(mean 300 s)	kW/m <sup>2</sup>	144.82	108.14	34.17	11.5
t <sub>ig</sub>	s	3.1	2.3	2.7	2.8
t extinguishing	s	304	165	382	61
HOC(mean heat of combustion)	MJ/kg	29.86	16.56	14.29	6.11
MLR(mean mass loss rate)	g/s·m <sup>2</sup>	8.524	5.718	1.106	0.985

Table 11 Summary of cone test results at radiation level (Nurate)

Parameter	Unit	Coating-30 kW		Coating-40 kW		Coating-50 kW	
		No	Yes	No	Yes	No	Yes
THR	MJ/m <sup>2</sup>	0.28	2.09	5.28	4.32	6.42	5.04
pHRR	kW/m <sup>2</sup>	3.53	3.84	12.96	21.91	56.63	44.74
HRR(mean 60 s)	kW/m <sup>2</sup>	1.53	3.09	10.76	12.8	26.39	21.82
HRR(mean 180 s)	kW/m <sup>2</sup>	1.05	2.62	7.56	7.27	13.19	11.39
HRR(mean 300 s)	kW/m <sup>2</sup>	0.74	2.55	6.5	5.86	10.05	8.57
t <sub>ig</sub>	s	6.3	NT	3.4	4.0	3.4	3.2
t extinguishing	s	19	NT	17	21	46	262
HOC(mean heat of combustion)	MJ/kg	0.63	4.9	8.76	6.19	8.44	5.13
MLR(mean mass loss rate)	g/s·m <sup>2</sup>	0.391	0.367	0.554	0.556	0.67	0.815

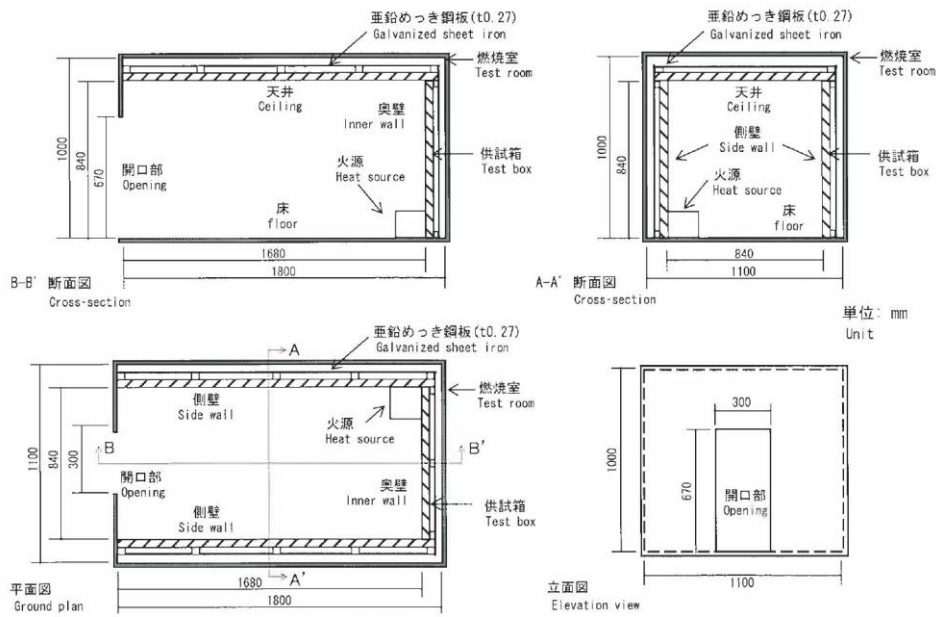


### 3.3.3 The model-box fire test results and discussion

In the model-box tests, temperature profiles of four locations inside the box were measured using k-type thermocouple. Regarding the model-box test performed with None-Nurate specimen under 40 kW heating intensity, a sharp peak with a value of 383 kW showed in the history of HRR curve after the test at  $t=52$  s. Then the combustion reach a steady state. The HRR about 244 kW lasts from 96 s to 600 s. The decrease in HRR was inferred to be attributed to the formation of charring layer over the surface of material. The HRR sharp increase also results in a temperature peak. It was found that the difference of temperature inside the model-box is not so large. When the time reaches 600 s, the difference of four temperature is much smaller. This is relative to the combustion states including the under-ventilation and over-ventilation condition. When the combustion inside the model-box is controlled by inflow air, the temperature inside the compartment box was reported to be the same. Fig.23 features the description of model-box fire test and description of specimen configuration and thermocouple location. Fig.24 represents the description of HRR and THR histories varying test time. Fig.25 discloses the description of temperature histories varying test time. Fig.26 describes the model-box test scene using None-Nurate at  $t=0$  s,  $t=30$  s,  $t=60$  s,  $t=120$  s,  $t=600$  s and after test, respectively.

Regarding the model-box test using urethane specimen, the flashover showed at 37 s, which is consist with the sharp HRR increase at 37 s. Before flashover, the heavily smoke was found and no flames were observed. The serious combustion was found during the 2 min test. The HRR increase from 0 to 816 kW within 49 s. After flashover, the flame spills out. There is no flame inside the model-box. However, a long flame was observed in the location over model-box. The temperature of location, which is near window opening, is much higher than the value of location near burner. This is caused by the under-ventilation combustion. Fig.23 shows the description of model-box fire test and features description of specimen configuration and

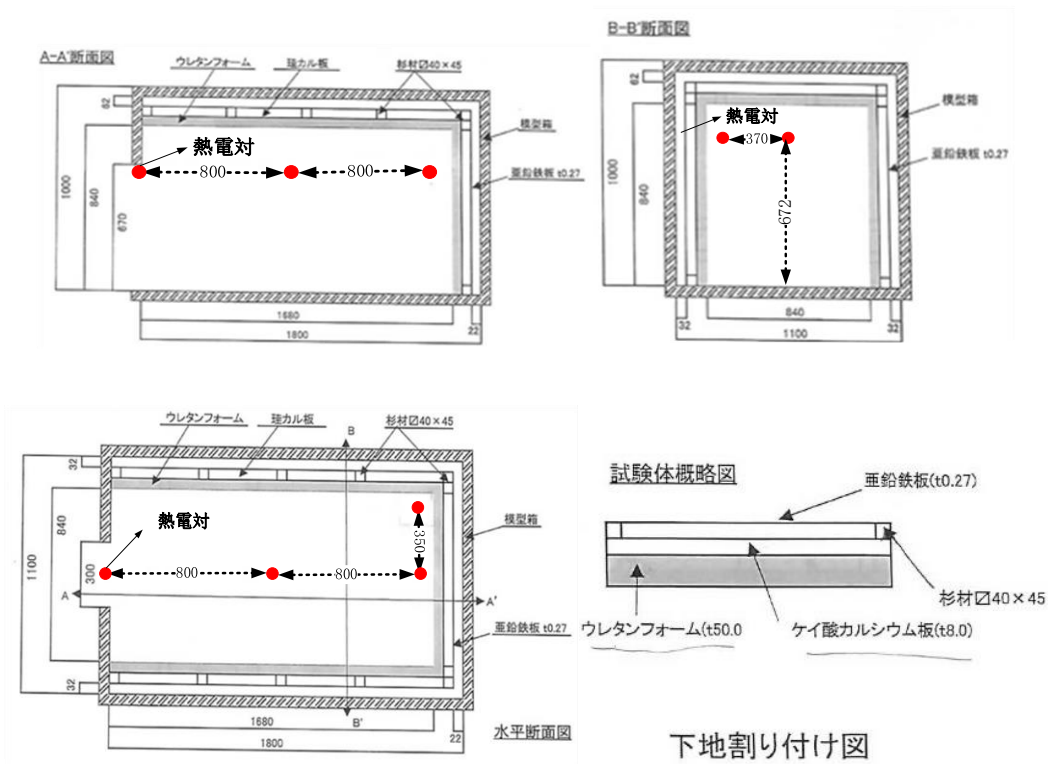
thermocouple location. Fig.24 discloses the description of HRR and THR histories varying test time. Fig.25 represents the description of temperature histories varying test time. Fig.27 describes the model-box test scene using None-Nurate at  $t=0$  s,  $t=30$  s,  $t=60$  s,  $t=120$  s,  $t=600$  s and after test, respectively.



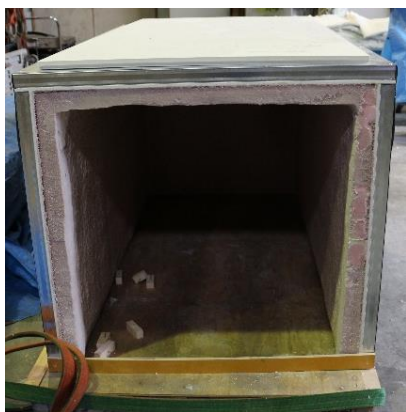
(a)



(b)



(c)



(d)



(e)

Fig.23 The description of model-box fire test (a) description of cross section, ground plan and elevation view (b) the model-box used for test (c) the thermocouple configuration (d) the None-Nurate specimen (e) the urethane specimen

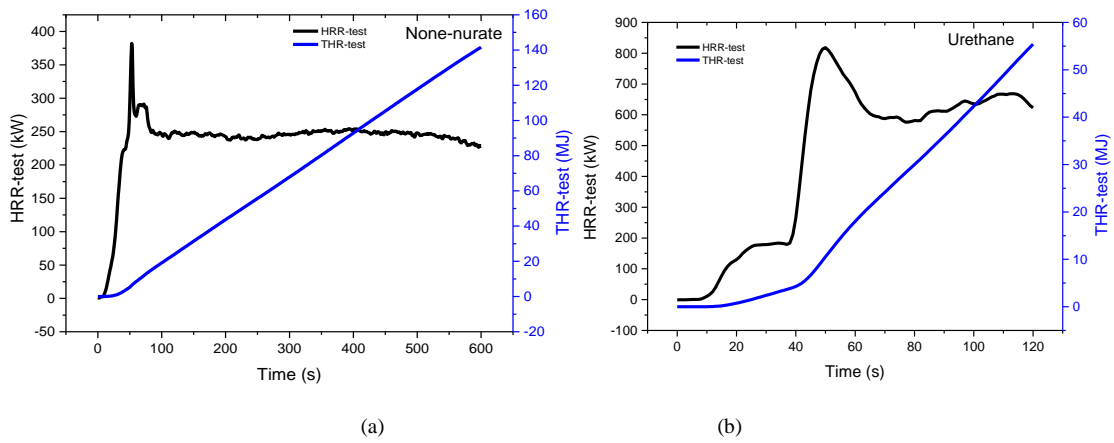


Fig.24 The description of HRR and THR histories varying test time

(a) None-nurate specimen (b) Urethane specimen

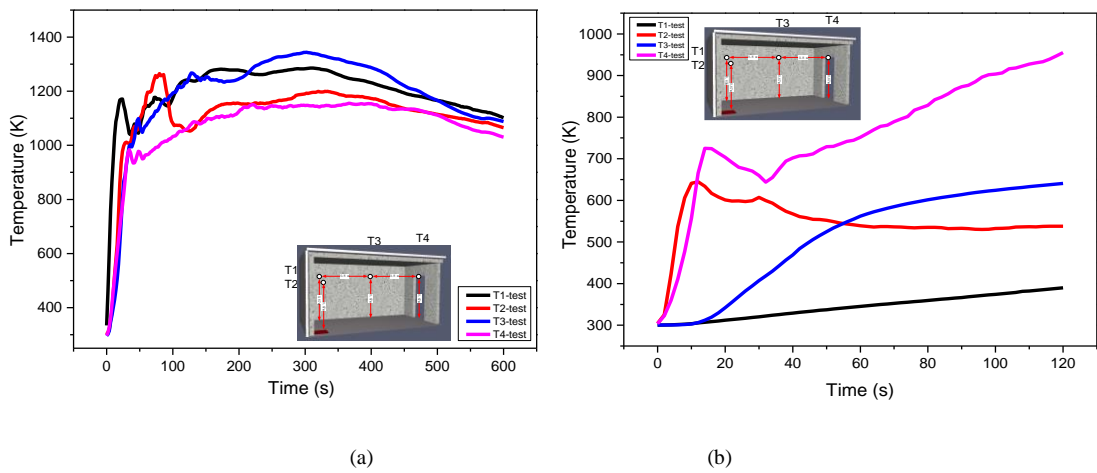


Fig.25 The description of temperature histories varying test time

(a) None-nurate specimen (b) Urethane specimen



(a)



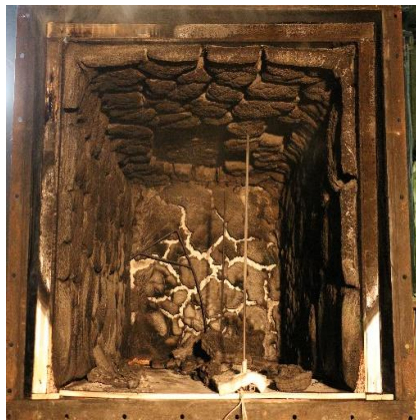
(b)



(c)



(d)



(e)



(f)

Fig.26 The description of model-box test scene using None-Nurate (a)  $t=0$  s (b)  $t=30$  s (c)  $t=60$  s (d)  $t=120$  s (e)  $t=600$  s (f) the description of internal specimen after model-box test





(a)



(b)



(c)



(d)



(e)



(f)

Fig.27 The description of model-box test scene using Urethane (a)  $t=0$  s (b)  $t=30$  s (c)  $t=60$  s (d)  $t=120$  s (e)  $t=600$  s (f) the description of internal specimen after model-box test

## **3.4 Simulation configuration and results discussion**

### **3.4.1 Results of Cone modelling**

#### **A) Simulation tool**

All the simulation of this study is conducted in the presence of supercomputer called Reedbush, which is located in The University of Tokyo. The FDS6.5 has been available in the Reedbush system. The method to load and use FDS 6.5 could be easy found in the website of Reedbush. The Reedbush system is separated into two types, Reedbush-U and Reebush-H. The difference between the two systems is with or without the accelerator. The Reedbush-U with CPU only is consisted of nodes and subsystems. The each node in Reedbush-U includes the CPU that Intel Xeon E5-2695v4 (Broadwell-EP 2.1 GHz 18 core) x2 socket, 1209.6 GF and Mem 256 GB (DDR4-2400, 153.6 GB/sec). Comparably, the Reedbush-H is similar with the Reedbush-U. However, the accelerators and improved subsystems are in Reedbush-H. The accelerator is NVIDIA Tesla P100×2. The storage is the shared storage Luster Filesystem, which is 5.04 PB with a speed of 145.2GB per second. The maximum node for us is 16 nodes. The token for us is 17,200 per year. The token calculation method is node-dependent.

#### **B) Material parameters**

The input parameters are shown in Tab.12. The source indicates how to get the parameters.

Table 12 Parameters of building materials

Component:	XPS	Urethane	Nurate	None-Nurate	Source
State:	S	S	S	S	Company
Density: kg/m <sup>3</sup>	21.6	41.8	36.8	49.2	Company
Heat capacity: J·kg <sup>-1</sup> ·K <sup>-1</sup>	5350 <sup>[45]</sup>	2076 <sup>[46]</sup>	1470 <sup>[47]</sup>	1470	Reference
Conductivity: W·m <sup>-1</sup> ·k <sup>-1</sup>	0.03656	0.02013	0.02103	0.02128	Company
Heat of combustion: kJ/g	35.8	8.15	8.34	8.34	Cone
Pre-Exp. Factor:s-1	4.34e11	6.41e10	1.46e87	1.03e10	TG
Activation Energy: kJ/kmol	61.09	71.62	75.26	78.02	TG
Heat of reaction: kJ/g	1.76 <sup>[13]</sup>	1.40 <sup>[13]</sup>	1.20 <sup>[13]</sup>	1.20	Reference
Transport: m <sup>2</sup> /s	1e-5	1e-5	1e-5	1e-5	Estimated
Emissivity	0.7	0.7	0.7	0.7	Estimated
Absorption Coef. m <sup>-1</sup>	700	1000	1000	1000	Estimated

### C) Sensitivity of mesh grid and parameters

Before the simulation, the sensitivity of mesh size was conducted firstly with 50 kW/m<sup>2</sup> radiation. The computational domain is in the size of  $L \times W \times H = 100 \text{ mm} \times 100 \text{ mm} \times 50 \text{ mm}$ . The simulated MLR varying mesh size is shown in the Fig.28 (a). MLR and HRR comparison of different mesh size and experiment (the dot is experiment, lines are simulation curves) are described in it. From both of Fig.28 (a), it is found that simulation results depend heavily on mesh size. As mesh size increases from 0.020 m to 0.066 m, the peaks of MLR and HRR decrease largely correspondingly. However, the pyrolysis stop time increases as mesh size enlarges.

Usually the calculation time step plays an important role in calculation process, in this study, a series of



calculation time step varying from 0.01 s to 0.10 s was used to evaluate the effects on simulation results.

The simulation result varying with calculation time step is shown in Fig.28 (b). From it, it is found that calculation time step has no serious effect on simulation results.

In addition, the sensitivity of each parameters is discussed by varying each parameter, which is shown in Fig.28 (c). It is found that when the value of conductivity, emissivity, density increase, the pMLR increase accordingly. However, the pMLR was reduced as the heat capacity increases. The activation energy shows an effect on the pMLR.

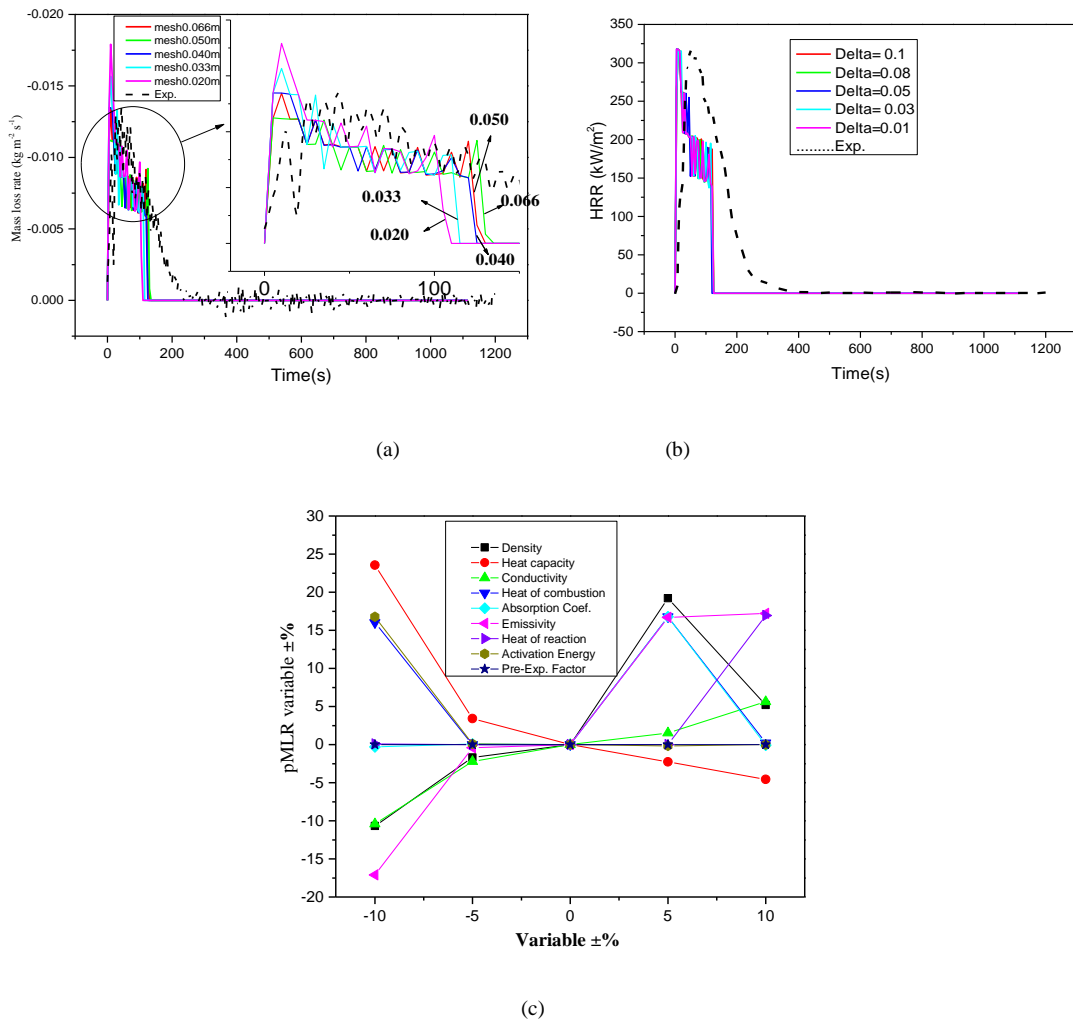


Fig.28 The sensitivity results varying parameters (a)MLR varying mesh size (b)MLR varying calculation time step Delta (c) MLR varying each parameter

#### D) Comparison of simulation and experimental results

With the accurate input and optimal grid mesh size, the comparison of simulation and experiment of XPS, urethane, nurate, None-Nurate are described in the Fig.29, Fig.30, Fig.31 and Fig.32, respectively. In general, it shows a good agreement between tested data and simulated results except the XPS under 30 kW/m<sup>2</sup>, MLR and HRR histories represent similar behaviour qualitatively with experimental results. Discrepancies may be substantial for a low radiation flux but the general trends are reproduced well. For example, the time of simulated MLR and HRR is delayed by approximately 280 s on average at the beginning of test. In the Cone test, the HRR is calculated in the form of  $\dot{q} = (1.31 \times 10^3) \times 1.10 \times C \times \frac{(0.2095 - X_{O_2})}{(1.105 - 1.5 X_{O_2})}$ . Where the  $\dot{q}$  features the heat release rate in the unit of kW.  $C$  is the orifice plate coefficient in kg<sup>1/2</sup>m<sup>1/2</sup>K<sup>1/2</sup>,  $X_{O_2}$  represents the oxygen concentration in outgas. Comparably, the HRR was predicted by the equation  $HRR = \Delta H(\text{heat of combustion}) \times \dot{m}(\text{mass loss rate})$  in simulation. Regarding the polymer, the heat of combustion varies combustion conditions during the whole test. In the simulation, utilization of constant heat of combustion results in a discrepancy with respect to the HRR, which is reasonable.

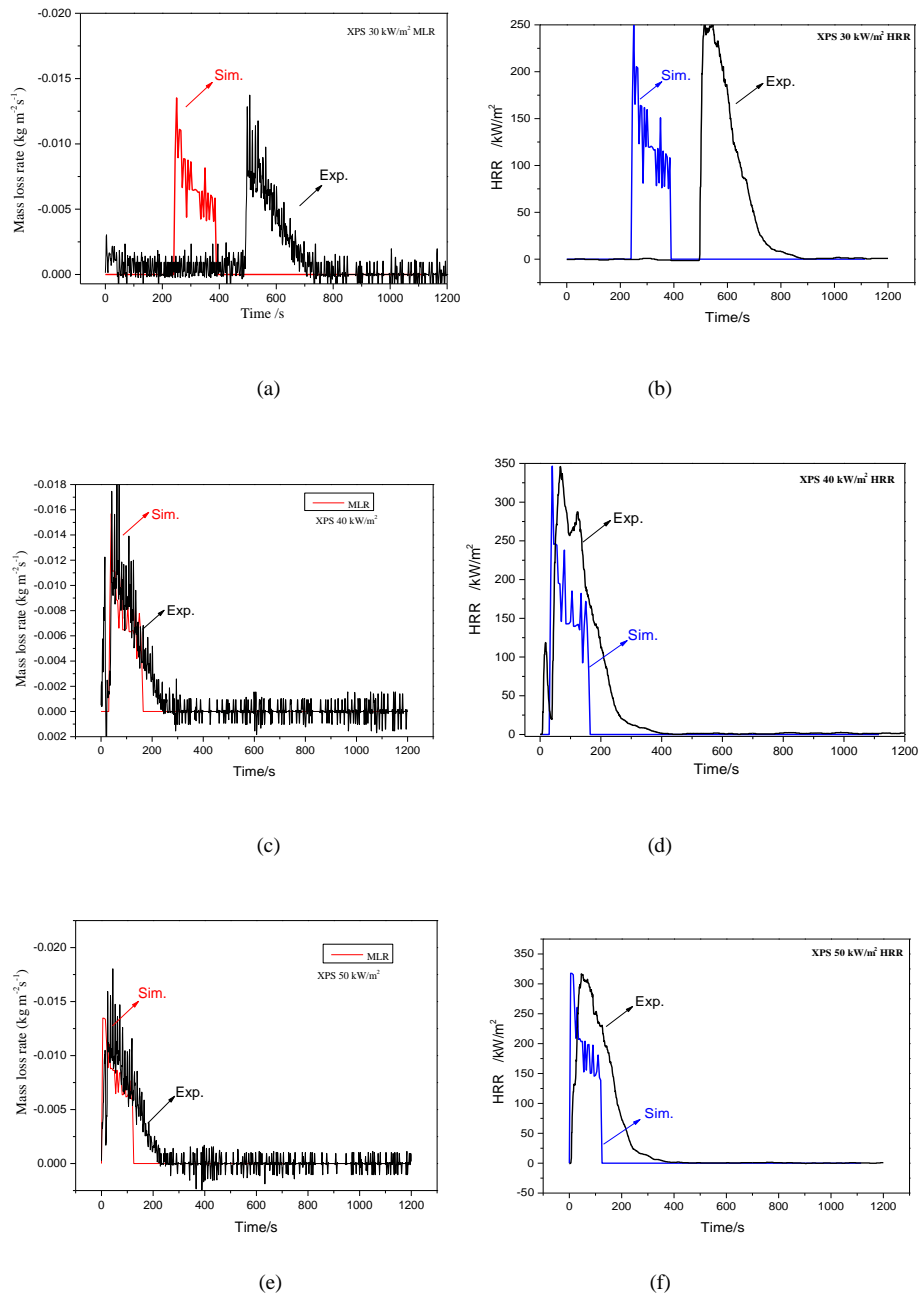
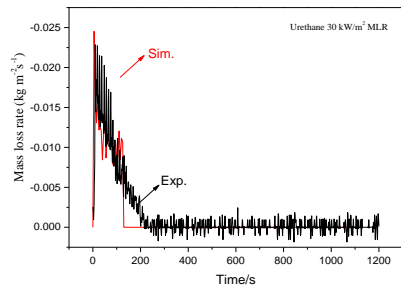
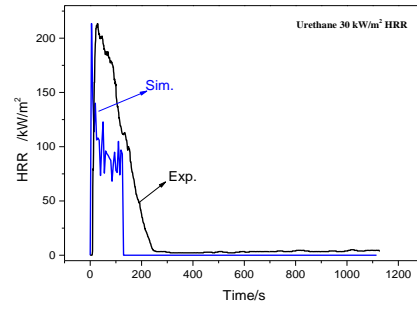


Fig.29 Comparison of simulated and experimental results using XPS

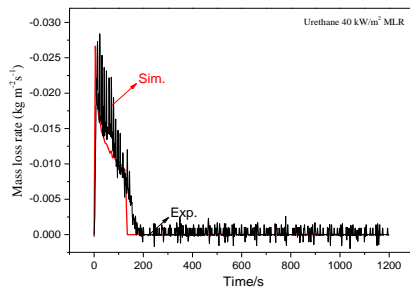
(a) MLR of radiation 30 kW/m<sup>2</sup> (b) HRR of radiation 30 kW/m<sup>2</sup> (c) MLR of radiation 40 kW/m<sup>2</sup> (d) HRR of radiation 40 kW/m<sup>2</sup> (e) MLR of radiation 50 kW/m<sup>2</sup> (f) HRR of radiation 50 kW/m<sup>2</sup>



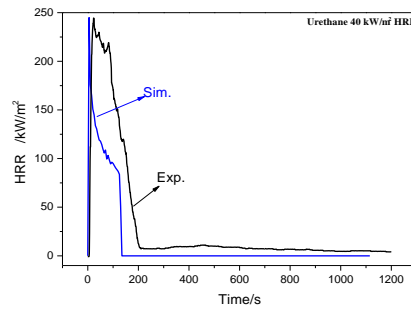
(a)



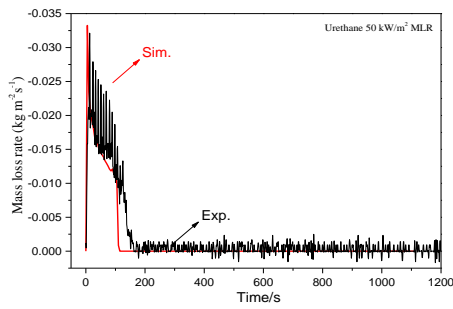
(b)



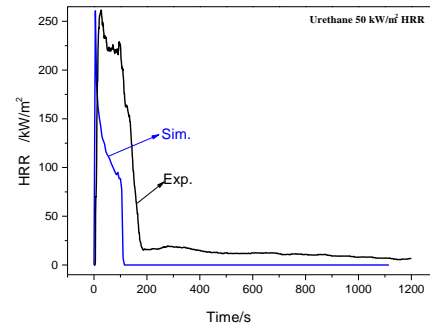
(c)



(d)



(e)



(f)

Fig.30 Comparison of simulated and experimental results using Urethane

(a) MLR of radiation 30 kW/m<sup>2</sup> (b) HRR of radiation 30 kW/m<sup>2</sup> (c) MLR of radiation 40 kW/m<sup>2</sup> (d) HRR of radiation 40 kW/m<sup>2</sup> (e) MLR of radiation 50 kW/m<sup>2</sup> (f) HRR of radiation 50 kW/m<sup>2</sup>

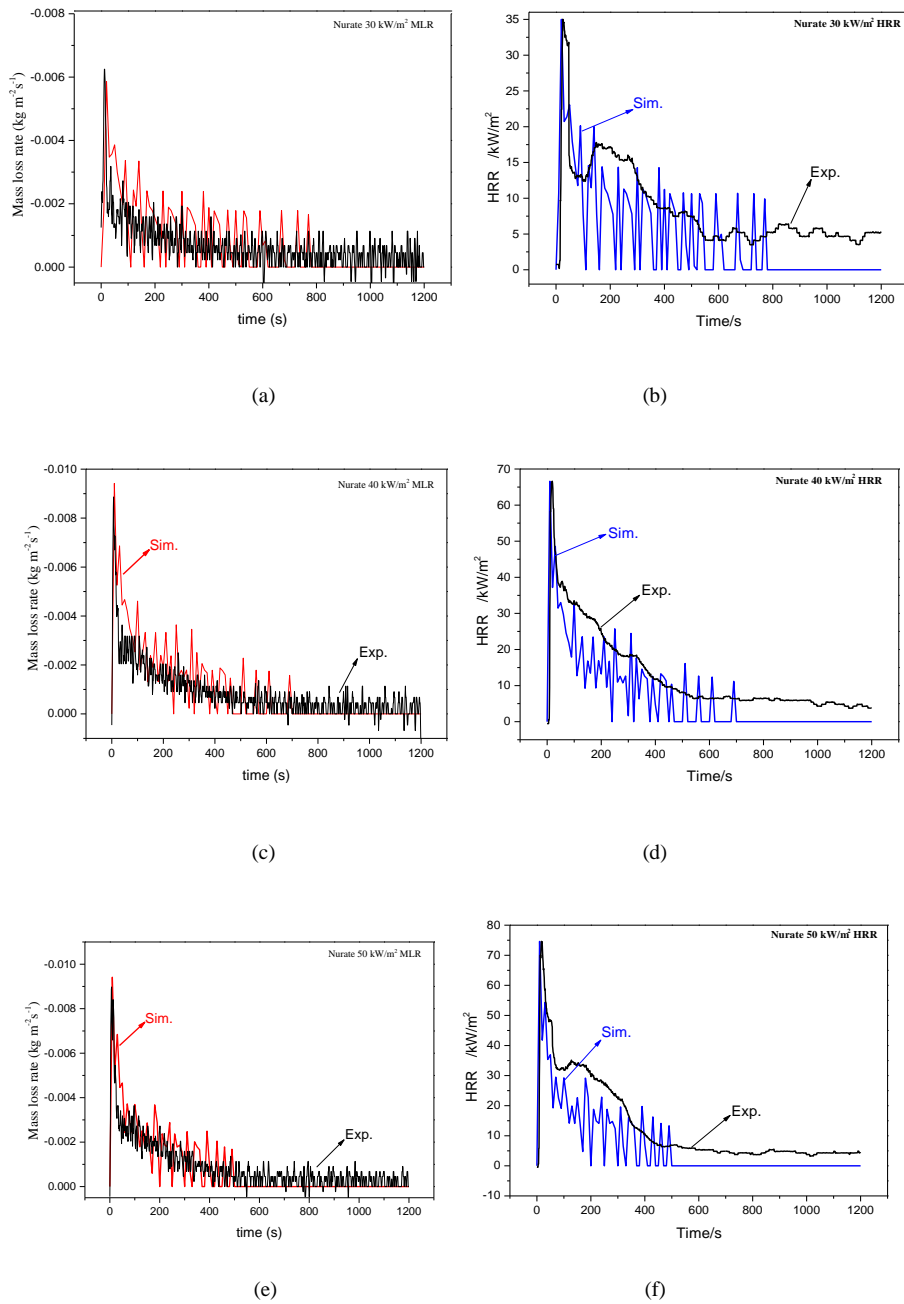


Fig.31 Comparison of simulated and experimental results using Nurate

(a) MLR of radiation 30 kW/m<sup>2</sup> (b) HRR of radiation 30 kW/m<sup>2</sup> (c) MLR of radiation 40 kW/m<sup>2</sup> (d) HRR of radiation 40 kW/m<sup>2</sup> (e) MLR of radiation 50 kW/m<sup>2</sup> (f) HRR of radiation 50 kW/m<sup>2</sup>

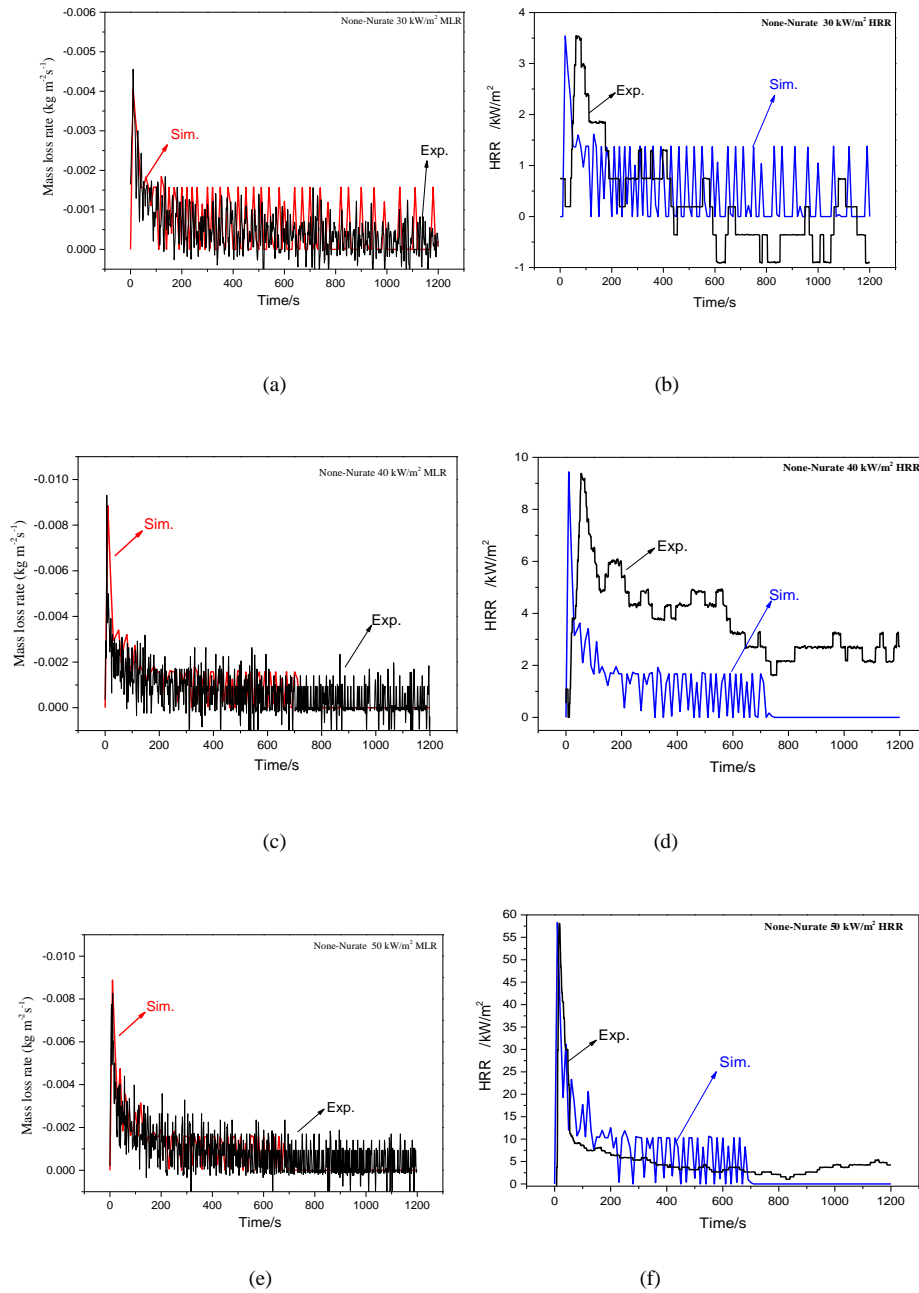


Fig.32 Comparison of simulated and experimental results Non-Nurate

- (a) MLR of radiation 30 kW/m<sup>2</sup> (b) HRR of radiation 30 kW/m<sup>2</sup> (c) MLR of radiation 40 kW/m<sup>2</sup> (d) HRR of radiation 40 kW/m<sup>2</sup>  
 (e) MLR of radiation 50 kW/m<sup>2</sup> (f) HRR of radiation 50 kW/m<sup>2</sup>

### 3.4.2 Melt effect on XPS Cone tests

During XPS (30 kW/m<sup>2</sup>) Cone test, it is found that when the XPS was exposed to radiation 30 kW/m<sup>2</sup>,

it would melt quickly to form molten liquid. The distance between heating source and specimen surface increases from 2 cm to 7 cm during Cone test. Under this condition, the received radiation was reduced by about 40 %. When the external heat flux of XPS in simulation changes from 30 kW/m<sup>2</sup> to 21 kW/m<sup>2</sup>, the predicted MLR and HRR agree well with Cone test. This is ascribed to the distance enlargement between heating source and specimen surface, which results in a relative low heat flux irradiated on the surface of molten liquid. The results are shown in Fig.33.

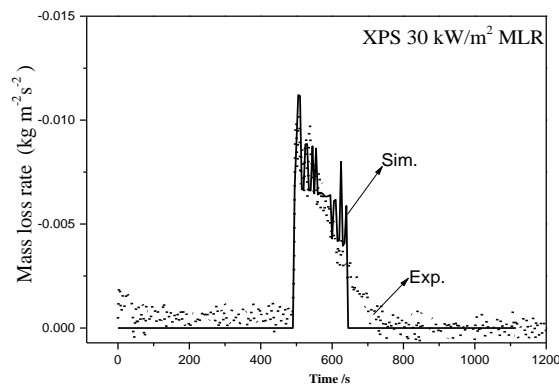


Fig.33 MLR comparison of simulation and experiment using XPS

As for FDS, melt model is still in development and unavailable. In addition, the temperature-dependent parameters are hard to be accurately defined by FDS code. Although currently the RAMP function is available in FDS, the continuity of simulation history still needs to be improved. MLR and HRR of insulation materials (without considering melt process) could be predicted by using FDS code with accurate input parameters obtained from measurement.

### 3.4.3 The coating effects on the MLR curves

The heat transfer over the solid is important in the fire spread model. The heat transfer calculation method in the FDS is firstly introduced in the subtext. The 1D heat transfer is in the following <sup>[14]</sup>:

$$\rho_s c_s \frac{\partial T_s}{\partial t} = \frac{\partial}{\partial x} \left( k_s \frac{\partial T_s}{\partial x} \right) + \dot{q}_s'''$$

$T_{s,i}$  stands for the temperature at the center of solid cell, which is iterated using a Crank-Nicolson scheme.

And therefore the boundary condition becomes:

$$-k_{s,1} \frac{T_{s,1}^{n+1} - T_{s,0}^{n+1}}{\delta r_{1/2}} + \left( \frac{h}{2} + 4\varepsilon\sigma \left( T_{s,1/2}^n \right)^3 \right) \frac{T_{s,1}^{n+1} - T_{s,0}^{n+1}}{2} = h \left( T_g - \frac{1}{2} T_{s,1/2}^n \right) + \dot{q}_{r,in}'' + 3\varepsilon\sigma \left( T_{s,1/2}^n \right)^4$$

The temperature at node 0 could be described in the following:

$$T_{s,0}^{n+1} = \frac{\frac{k_{s,1}}{\delta r_{1/2}} - \left( \frac{h}{2} + 4\varepsilon\sigma \left( T_{s,1/2}^n \right)^3 \right)}{\frac{k_{s,1}}{\delta r_{1/2}} + \left( \frac{h}{2} + 4\varepsilon\sigma \left( T_{s,1/2}^n \right)^3 \right)} T_{s,1}^{n+1} + \frac{h \left( T_g - \frac{1}{2} T_{s,1/2}^n \right) + \dot{q}_{r,in}'' + 3\varepsilon\sigma \left( T_{s,1/2}^n \right)^4}{\frac{k_{s,1}}{\delta r_{1/2}} + \left( \frac{h}{2} + 4\varepsilon\sigma \left( T_{s,1/2}^n \right)^3 \right)}$$

RFACF2 QDXKF

If during the simulation, a non-insulated backing is installed in Cartesian geometry, the temperature ranked node N+1 could be calculated in the above method. However, when the insulated backing is installed in the simulation,  $\varepsilon, \dot{q}_{r,in}'', h$  are set to 0.

$$T_{s,0}^{n+1} = T_{s,1}^{n+1}$$

Here,  $k_s$  stands for Conductivity;  $\rho_s$  is Density;  $c_s$  is Heat capacity;  $\dot{q}_s'''$  is heat consisting of chemical reactions and radiative absorption;  $\dot{q}_{s,c}'''$  is heat production rate given by the pyrolysis models;  $\dot{q}_{s,r}'''$  is radiative absorption heat;  $T_s$  is solid phase temperature;  $N_m$  is the number of material components forming the solid;  $X_\alpha$  features volume fraction of component  $\alpha$ ,  $X_\alpha = \frac{\rho_{s,\alpha}}{\rho_\alpha} / \sum_{\alpha'=1}^{N_m} \frac{\rho_{s,\alpha'}}{\rho_{\alpha'}}$ ;  $\rho_{s,\alpha}$  represents the component densities;  $Y_\alpha$  stands for the mass fraction of component  $\alpha$ ;  $h$  features heat transfer coefficient;  $\dot{q}_c''$  shows convective flux;  $\dot{q}_r''$  indicates radiative flux.

With an aim to investigate the effects of coating material on the heat transfer, a 5 mm thick of calcium silicate board is installed in simulation at the positions both above and bottom of Nurate. The MLR of three



configurations are disclosed in Fig.34. It is included that in simulation under 30 kW/m<sup>2</sup>, the coating layer on the surface and bottom could result in a 50 % and 10.5 % reduction of pMLR, respectively. Under the high radiation 40 kW/m<sup>2</sup> and 50 kW/m<sup>2</sup>, it shows similarly that the coating layer on the surface and bottom could reduce 54.1 % and 2.1 % of pMLR, respectively. Comparably, the coating layer on the bottom was observed to reduce a 17.6 %, 4.5 % and 3.3 % under the 30 kW/m<sup>2</sup>, 40 kW/m<sup>2</sup> and 50 kW/m<sup>2</sup>, respectively, which is disclosed in Fig.35. Usually, it is not hard to understand one case that the coating layer on the surface could reduce the mass loss rate. This could be explained that the less heat was transferred into the Nurate layer by using a coating layer on the nurate surface.

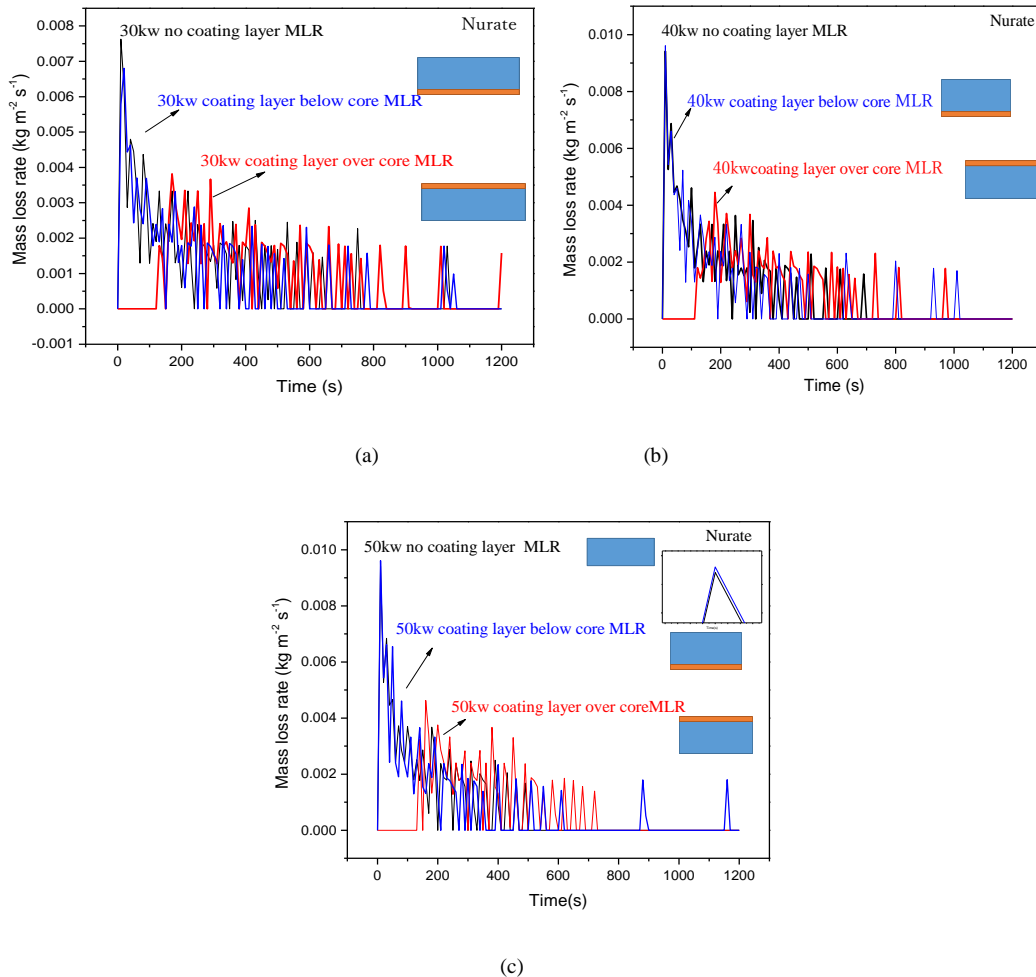


Fig.34 Effects of coating layer on the MLR of Nurate by simulation (a) MLR with 30 kW/m<sup>2</sup> (b) MLR with 40 kW/m<sup>2</sup> (c) MLR with 50 kW/m<sup>2</sup>

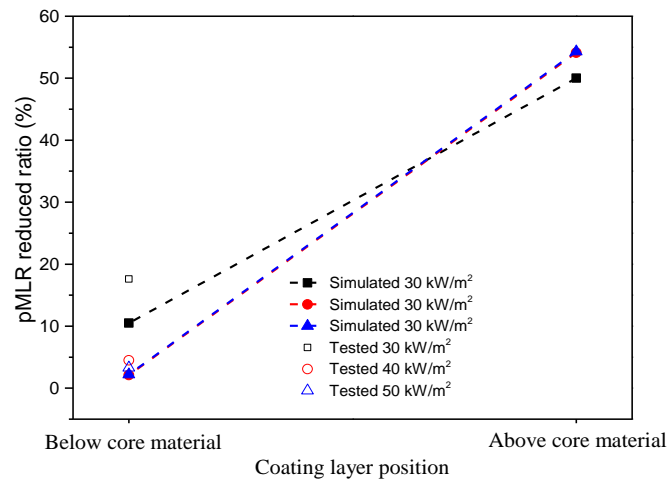


Fig.35 The pMLR reduced ratio versus coating layer position

With respect to coating layer installation in the bottom of Nurate, the reduction of pMLR is caused by the heat accumulation because of the insulation back. This is insistent with simulation. However, the pMLR reduced ratio of simulation is much higher than experimental values, which is also presented in the table 13. Furthermore, the pHRR and SPR were found to be increased as the pMLR decreases. The smoke production rate is relevant with status of combustion. The coating layer installation in the bottom of Nurate results in a slow combustion. The FDS could predict the reaction-to-fire performance.

Table 13 the reduction caused by coating layer from the tested results of Cone

Items	pMLR %	pHRR %	SPR %	SC %	SEA %
30kw coating layer below	↓17.6	↑9.6	↑6.1	↑4.5	↓77.2
40kw coating layer below	↓4.5	↑70.0	↑21.5	↓17.7	↓13.3
50kw coating layer below	↓3.3	↑26.5	↑4.7	↑2.6	↓99.0

Note: SPR= Smoke production rate; SC=Smoke concentration; SEA= the smoke extinction area.

### 3.4.4 Modelling of model-box test

In this part, the model-box is modelled with the pyrolysis model of Urethane and None-Nurate, which are verified in the previous simulation. The grid sensitivity is conducted firstly with it ranging from 2.5 cm to 10 cm. Although the simulation performed 1.25 cm was conducted, the error of instability happens many times. Therefore, it is meaningless for this study. The comparison of simulated and experimental HRR and THR curves varying test time is shown in Fig.36. Fig.37 represents the simulated thermocouple temperature information. Fig.38 and Fig.39 feature the simulated flame profiles at  $t=0$  s,  $t=30$  s,  $t=60$  s,  $t=120$  s,  $t=180$  s and 600 s, respectively. The discussion are followings:

#### ■ None-Nurate model-box simulation results

Regarding the None-Nurate simulation results, the HRR increases sharply to 400 kW because the None-Nurate was ignited rapid, which could be easily found in the description of test scene. Then the formation of coating layer over polymer resulted in the low combustion. The HRR decreases as the test time increases from 100 s to 600 s. Compared with experimental HRR, the simulated HRR was found to be low. This could be explained by it that in the simulation, the None-Nurate was cracked into many small parts, which could provide more volatile to support continuous combustion. However, the 1D pyrolysis model used in the current version of FDS seems insufficient for this phenomena. In the simulation, the formation of coating layer reduces the HRR. This is hard to be simulated using current version of FDS. Considering the above reasons, it is reasonable that the simulated HRR is lower than tested one.

In the comparison of experimental temperature and simulation performed 5 cm, it is obvious that the simulated T1 is similar with the experimental T1. The T1 features the temperature profile of location above the burner. It means the flame temperature could be reproduced by the current version of FDS. The

simulated T2 is believed to be similar with experimental T2. However, the large discrepancy is found in the T3 and T4 comparison of simulation and experiments. The temperature increase of T3 and T4 is attributed to the flame spread and pyrolysis gas diffusion. Using the current version of FDS to predict this process seems difficult.

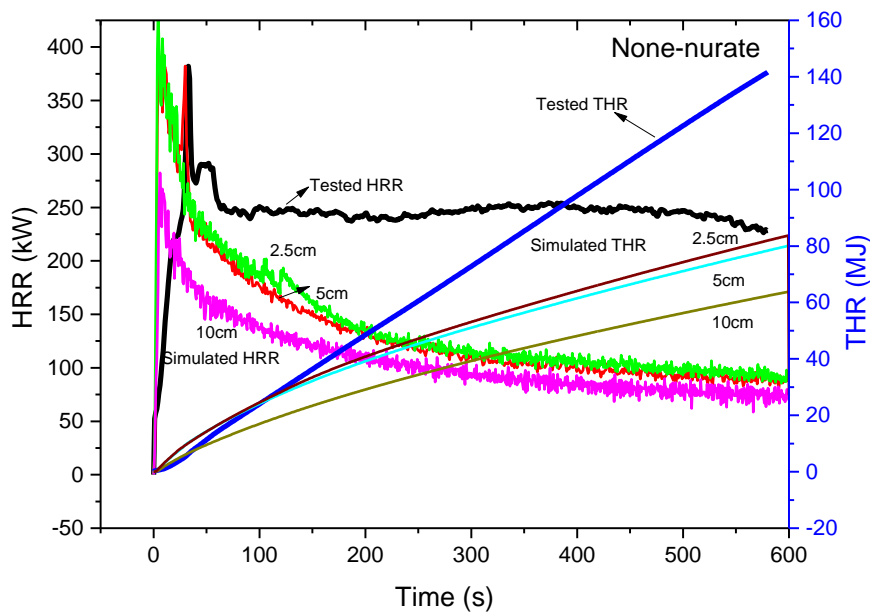
Regarding the mode-box test using None-Nurate performed 10 cm, the simulated T1, T2 and T3 are found to be much lower than experimental values. Comparably, the simulated T4 shows a similar trend with experimental one. The comparison of simulation and experiment indicates that simulated results are grid-dependent. In addition, when the pyrolysis gas diffuses heavily and is accompanied with heavily smoke, it seems very hard to be reproduced using current version of FDS. The mixing-control model for combustion is not suitable for complex flame spread and combustible gas diffusion.

#### ■ Urethane model-box simulation results

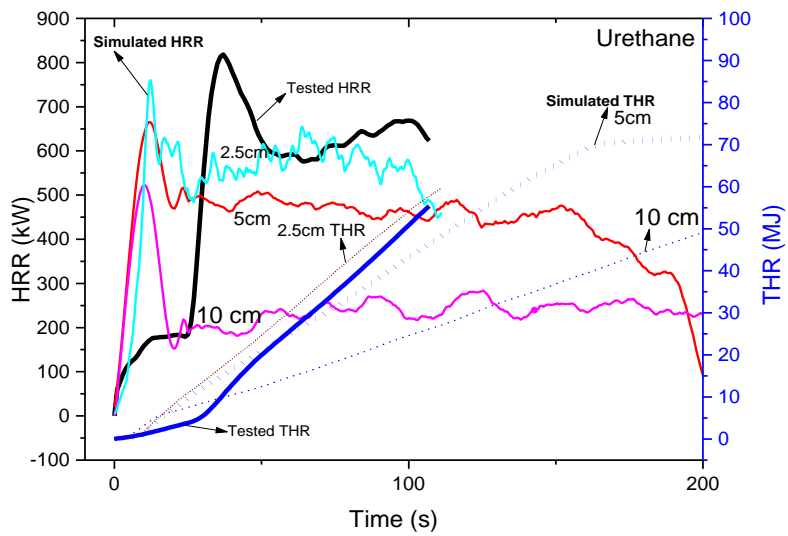
Regarding the simulation performed urethane, the 2.5 cm grid could give a better results compared with experimental tests. Although the first peak delays about 26 s compared with experimental test. During the urethane model-box test, the heavy smoke was observed at the beginning of test. In addition, the pyrolysis products, mainly combustible gas, were generated in a short time. The insufficient air inside the compartment results in the low HRR. However, HRR increased sharply because of flashover. When the combustible gas, which is mixed with sufficient fresh air, was heated at the place near opening, the serious fire happened at 48 s. In the simulation, the mixing time is very short compared with experimental mixing time. The FDS mainly use the single-step and mixing-controlled combustion model. This method features that a fuel component reacts with oxygen to the combustion products during one small scale of mixing controlled step. During the mixing controlled calculation, only the lumped species are computed. This means that the major reactants and products of combustion would be not solved because they are already

pre-tabulated in the code. Therefore, the simulated HRR of urethane shows no corresponding description about the delay in HRR. In general, the similar trend is disclosed between simulation and experiment. The discrepancy found at the beginning of test is attributed to the mixing controlled model used in default FDS model.

With respect to the temperature histories of urethane model-box test, the big discrepancy is found in the both simulations performed 5 cm and 10 cm. The temperature histories much more steady compared with experiments. The serve change in temperature was inferred to be the results of complex combustion status including pyrolysis products generation, under-ventilation fire and over-ventilation fire. This is hard to reproduce by using current version of FDS. This is also verified by the analysis of none-urethane model-box test. The current version of FDS is not suitable for complex flame spread and pyrolysis gas diffusion. The predicted time to generate flashover is much shorter than experimental time.

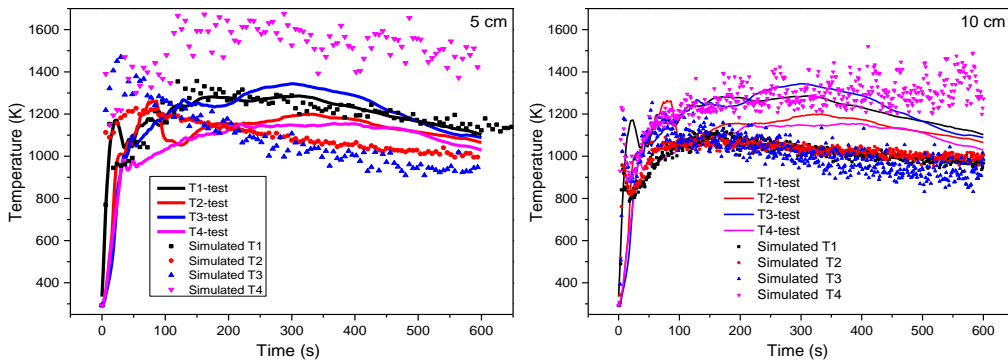


(a)



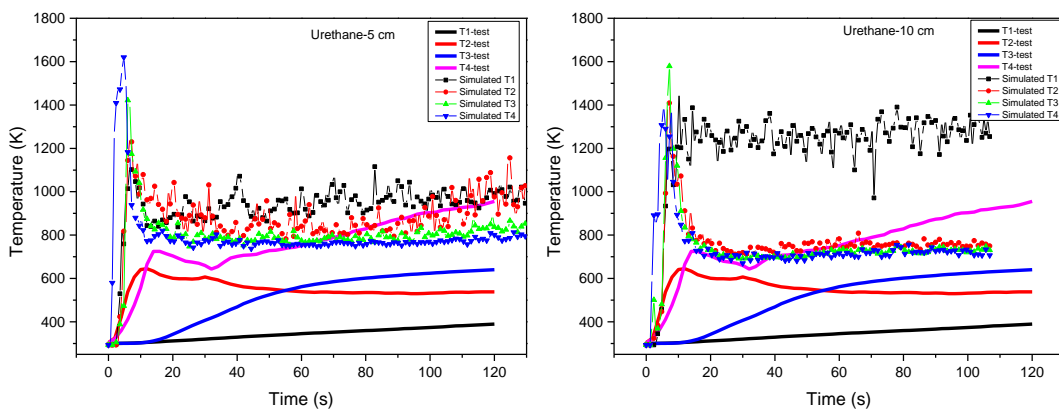
(b)

Fig.36 The comparison of HRR and THR histories varying test time (a) the results of None-Nurate (b) the results of urethane



(a)

(b)



(c)

(d)

Fig.37 The comparison of temperature histories varying test time (a) the results of None-Nurate using 5 cm gird (b) the results of None-Nurate using 10 cm gird (c) the results of urethane using 5 cm gird (d) the results of urethane using 10 cm gird

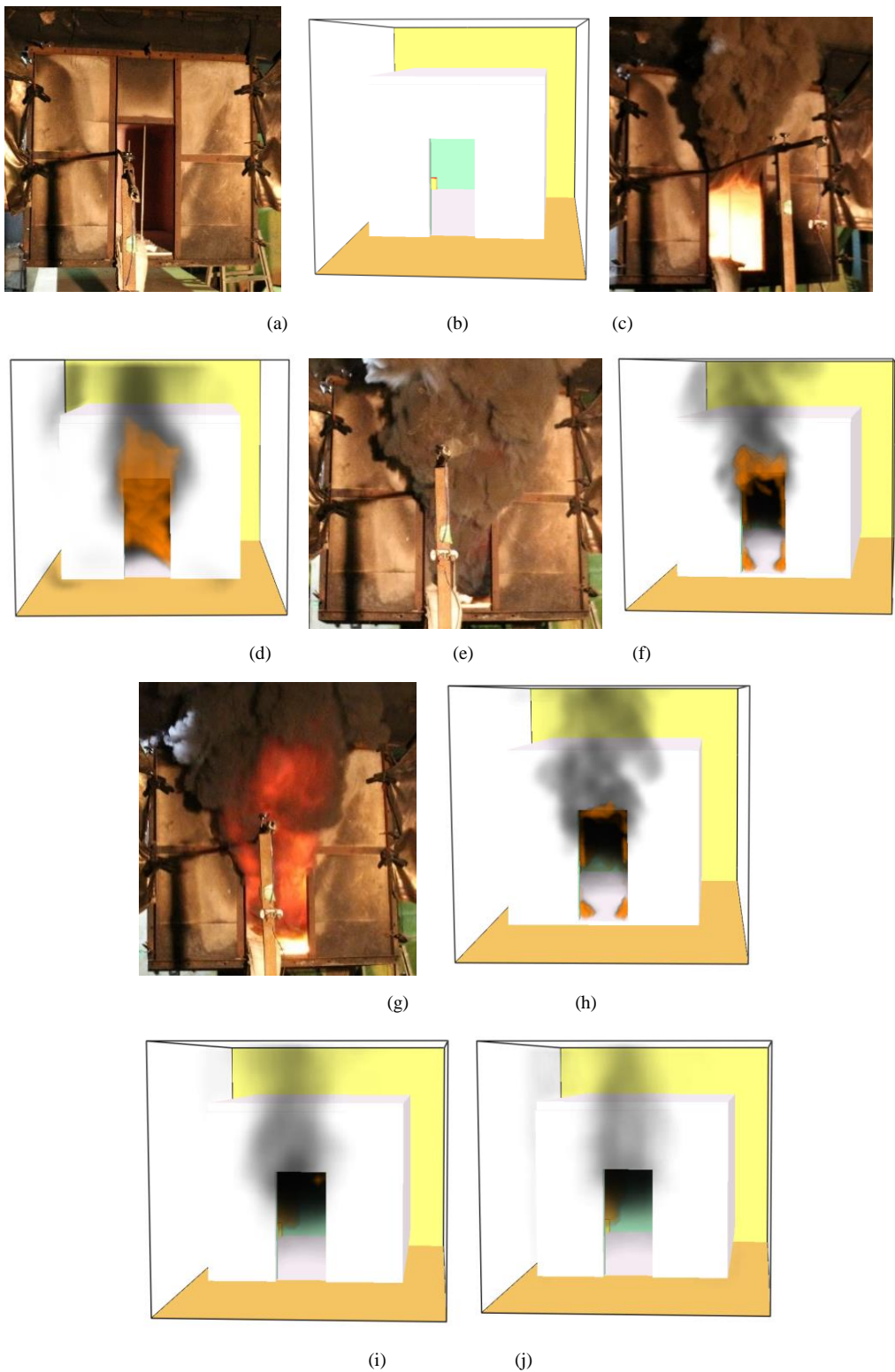


Fig.38 The comparison description of model-box test scene using None-Nurate

(a) experiment at t=0 s (b) simulation at t=0 s (c) experiment at t=30 s (d) simulation at t=30 s (e) experiment at t=60 s (f) simulation at t=60 s (g) experiment at t=120 s (h) simulation at t=120 s (i) simulation at t=180 s (j) simulation at t=600 s

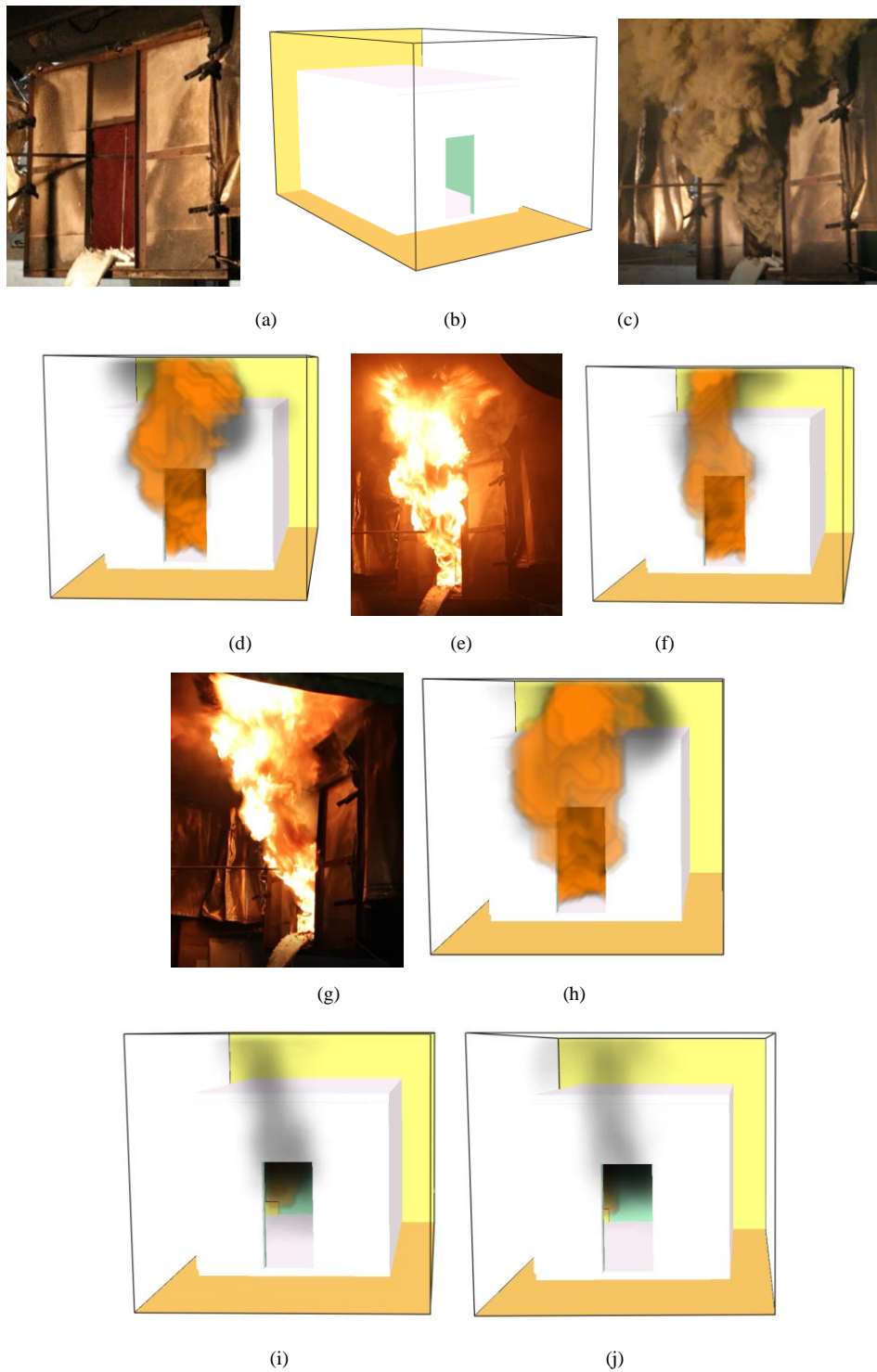


Fig.39 The comparison description of model-box test scene using None-Nurate

(a) experiment at  $t=0$  s (b) simulation at  $t=0$  s (c) experiment at  $t=30$  s (d) simulation at  $t=30$  s (e) experiment at  $t=60$  s (f) simulation at  $t=60$  s (g) experiment at  $t=120$  s (h) simulation at  $t=120$  s (i) simulation at  $t=180$  s (j) simulation at  $t=600$  s.



### 3.5 Summary

In this study, interior building materials fire were modelled by using FDS. The validation tests include Cone test and model-box test. With the accurate input parameters and without considering melt model, the MLR and HRR curves derived from FDS simulation agree with experiment data (Cone). It is found that the simulated results is mesh size-dependent. The calculation time step shows little effect on the simulation results. As mesh size increases from 0.020 m to 0.066 m, the peaks of MLR and HRR decrease largely correspondingly. However, the pyrolysis stop time increases as mesh size enlarges. Regarding the pyrolysis model, the sensitivity of each parameters is discussed by varying each parameter. It is concluded that the value of conductivity, emissivity, and density versus pMLR is linear, respectively. However, the pMLR reduced as the heat capacity increased. The activation energy shows a heavy effect on the pMLR.

The effects of coating layer on the Nurate is simulated by installing a 5 mm thick of calcium silicate board in simulation at the positions both above and bottom of Nurate. It is included that coating layer on the surface and bottom could result in a 50 % and 10.5 % reduction of pMLR under 30 kW/m<sup>2</sup>, respectively. Under the high radiation 40 kW/m<sup>2</sup> and 50 kW/m<sup>2</sup>, it shows similarly that the coating layer on the surface and bottom could reduce 54.1% and 2.1 % of pMLR, respectively. Comparably, the coating layer on the bottom was observed to reduce a 17.6 %, 4.5 % and 3.3 % under the 30 kW/m<sup>2</sup>, 40 kW/m<sup>2</sup> and 50 kW/m<sup>2</sup>, respectively. The coating layer installation on the above of Nurate could be explained that the less heat was transferred into the Nurate layer. With respect to coating layer installation in the bottom of Nurate, the reduction of pMLR is inferred to be caused by the heat accumulation because of the insulation back. This is insistent with 1D heat transfer theory in simulation. Comparison experimental and simulated Cone test of installation coating layer in the bottom of Nurate shows that the pMLR reduced ratio of simulation is much higher than experimental values. However, the similar trends are well reproduced by using FDS.

Regarding the model-box simulation, it is found that the simulated HRR is grid-dependent. The big discrepancy of temperature histories of urethane model-box test is found in the both simulations performed 5 cm and 10 cm. The simulated temperature histories is steadier than experimental values. B) Regarding the mode-box test using None-Nurate performed 10 cm, the comparison of simulation and experiment indicates that simulated results are grid-dependent.

In the future, the followings should be studied in the further study.

- A) In the current version of FDS, the dynamic mesh is not available. This limitation restricts the application of FDS in the materials which had serious melt-flow.
- B) Furthermore, the continuity of simulation history needs to be improved.
- C) When the complex combustion status combined with the yield of pyrolysis products of under-ventilation fire and over-ventilation fire, it is hard to reproduce by using current version of FDS. The current version of FDS is not suitable for complex flame spread and pyrolysis gas diffusion. The predicted time to generate flashover is much shorter than experimental time.
- D) The mixing-control model for combustion is not suitable for complex flame spread and combustible gas diffusion.

# 4. Utilization of CFD model to simulate external building fire

## 4.1 Introduction

This chapter attempts to model the external building fire. The representative external building materials are External Thermal Insulation Composite Systems (ETICS) specimens and cedar specimens. With an aim to verify the simulation results and report the new finding from experimental tests, a series of tests were carried out.

The following tests were performed.

- A) Regarding the EPS ETICS fire, the experimental Cone tests of ETICS specimens in the both horizontal and vertical direction were conducted.
- B) In addition, the intermediate-scale calorimeter (ICAL) of an ETICS specimen according to ISO 14696 standard method was carried out.
- C) The opening edge treatment and EPS thickness effects on the façade fire reaction-to-fire performance was reported. A potential method to evaluate fire risk of ETICS was proposed and discussed. The calibration tests according to the JIS A 1310 façade fire standard method varying heating intensity, chamber size and opening aspect n were performed.
- D) With respect to the window ejected fire plume of the calibration test, a thermocouple mesh and a series of heat flux meters were used to record the temperature information of fire plume and heat flux density varying vertical distance, respectively. The new correlation between dimensionless temperature  $\theta$  versus vertical distance were discussed by taking into account the

influence of fire plume re-attaching-to-wall behaviours, varied neutral plane positions and window opening aspect n.

- E) In addition, the pyrolysis model of cedar was conducted at two radiation levels performed with Fire Propagation Apparatus (FPA). The cedar façade fire using standard method was tested for simulation verification.

This is followed by the simulation configuration and discussion.

- A) With respect to simulation, the Cone of ETICS was modelled and discussed.
- B) The none-melt flow EPS ETICS was simulated using FDS to show the influence of melt-flow on the heat release rate (HRR) and total heat release rate (THR).
- C) The flame heat flux imposed on the solid surface was also compared using ThermaKin.
- D) Furthermore, the large eddy simulation of buoyant window spill plume from intermediate-scale compartment fires was performed using FireFOAM and compared with experimental results.
- E) The large eddy simulation of cedar façade fire was conducted using FireFOAM and compared with experimental results.

## **4.2 Experimental materials and planning**

### **4.2.1 Experimental materials**

In the part, the tested external building materials include the External Thermal Insulation Composite Systems (ETICS) specimen, cedar façade and JIS A 1310 calibration test without combustible materials. The EPS ETICS varies EPS thickness, opening edge treatment, enforcement mesh and coating layers. The cedar specimen of size in  $L \times W \times H = 100 \text{ mm} \times 100 \text{ mm} \times 19 \text{ mm}$ . During the JIS A 1310 calibration test,

the test varies heating intensity, opening size and chamber size.

## 4.2.2 Experimental planning

### A) Cone fire tests introduction

With aim to evaluate the reaction-to-fire performance and get input parameters for simulation. The Cone tests were carried out in both horizontal and vertical direction. The heat released was measured using a Dual Cone Calorimeter from Fire Testing Technology Ltd., just as shown in Fig.40. The set-up, calibration, and measurements were in accordance with the ISO 5660-1 standard method [40]. During the Cone tests, the specimen were installed in both horizontal and vertical direction by using a specimen holder with edge frame. The specimen was made by the Nohara Co. Ltd., Japan and according to the standard JIS A 1310 method. The bottom of the holder was lined with ceramic fiber blanket. Both the bottom and sides part of tested specimen were wrapped with a 0.02 mm thick aluminium foil. The heat release calculations were got on the basis of measurement results of oxygen, carbon monoxide, and carbon dioxide concentrations in exhaust gas.

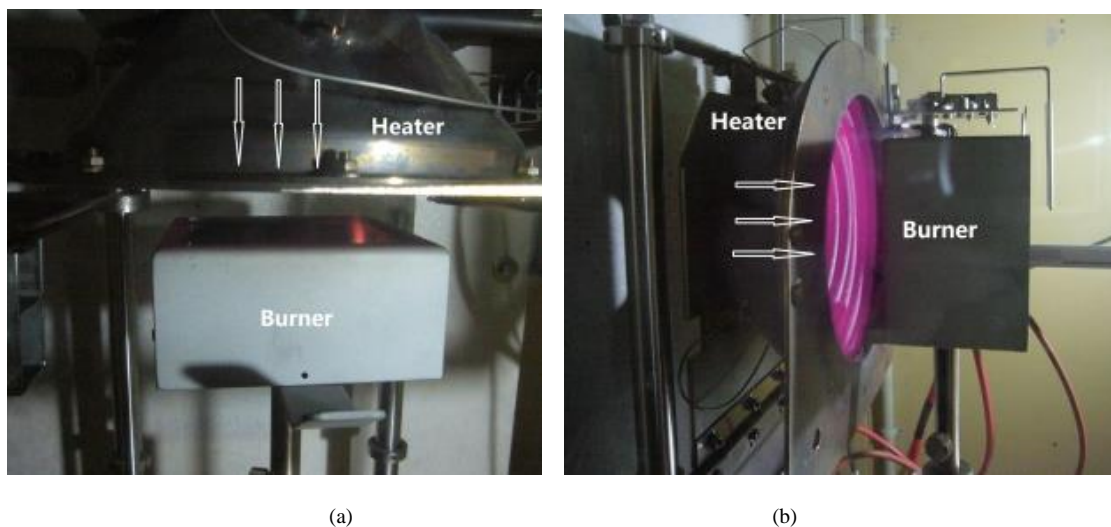


Fig.40 The description of Cone from FTT in (a) horizontal direction (b) vertical direction

## B) Intermediate-scale calorimeter (ICAL) according to ISO 14696 standard method introduction

To evaluate well the EPS ETICS specimen in a 1 m × 1 m size, ICAL was used. ICAL test is an ISO standard method which could be used to evaluate reaction-to-fire performance of materials, products and assemblies <sup>[48]</sup>. By this method, the ignitability, heat release rates, mass loss rates and visible smoke development of materials, products and assemblies under well-ventilated conditions could be got. In the current study, the ICAL is used to measure the heat release rate from a 1 m<sup>2</sup> specimen in a vertical orientation. It consisted of radiant panel assembly in a vertical orientation, radiant panel constant irradiance controller, water-cooled heat shield, specimen holder, weighing platform, exhaust collection system, gas flow meter, and data acquisition system. The specimens were exposed to a uniform and constant heat flux from a gas fired radiant panel up to 50 kW/m<sup>2</sup>. Electrically heated wires were used for piloted ignition. The heat release rate was ascertained by measurement of the oxygen consumption as determined by the oxygen concentration and flow in the exhaust product stream. In this study, the irradiation was set at 30 kW/m<sup>2</sup>.

Fig.41 shows the layout of ICAL tests.



Fig.41 The description of ICAL tests

### C) JIS A 1310 facade fire test method <sup>[49]</sup> introduction

With an aim to know fire mechanism of EPS ETICS façade fire, investigate into the factors which effect on fire performance and propose a fire risk prediction method for EPS ETICS specimen, a series of EPS ETICS specimens were carried out according to JIS A 1310 façade fire test. Furthermore, the fire behavior of cedar façade was evaluated using this standard method. Façade fire test method consists of propane gas combustion chamber (size in  $L \times W \times H = 1350 \text{ mm} \times 1350 \text{ mm} \times 1350 \text{ mm}$ ), fire spreading opening (size in  $L \times W = 910 \text{ mm} \times 910 \text{ mm}$ ), gas burner (size in  $L \times W = 600 \text{ mm} \times 600 \text{ mm}$ ), specimen substrate and specimen support frame. Chamber was used to produce different heating intensity fire, which is conducted by controlling high purity propane combustion. The specimen substrate was made by laying two pieces of calcium silicate board of 12 mm thickness and the joint of the first layer is not overlapped with joint of second layer. Specimen support frame made of stainless steel was employed to support specimen substrate and the specimen tested. The interior surface of chamber was coated by a thickness of 25 mm ceramic fiber blanket. The temperature and heat flux density information varied with test time are recorded by utilization of a series of k-type thermocouples and SBG01 heat flux meters on finishing coat surface of façade test specimen in the height of 0 mm (T0 for temperature), 500 mm (T1 for temperature, HF1 for heat flux density), 900 mm (T2, HF2), 1500 mm (T3, HF3), 2000 mm (T4, HF4) and 2500 mm (T5, HF5) away from the top of the opening, respectively. Heat release rate (HRR) and total heat release rate (THR) were also calculated by the common methodology Oxygen Consumption Calorimetry (OC). During OC measurement, a Gas-Analysis equipment was used to record oxygen concentration ranged from 0.009% to 20.9 % in every two seconds. Before façade fire test, the 4 Liter alcohol combustion was used to calibrate the whole equipment condition. Then chamber heating intensity in kW was determined by controlling the mass flow of high purity propane. After façade fire test, the outlook of specimen and EPS burn area S were observed and calculated. Before each façade fire test, the calibration test was carried out by laying a thickness of 25

mm ceramic fiber façade. In this part, the cedar façade fire test is conducted using this standard method. In JIS A 1310 façade fire test, the test specimen was vertically installed, just as shown in Fig.42. Fig.42 (a) is a simple model of JIS A 1310 façade fire test method. Fig.42 (b) and Fig. 42 (c) show the EPS ETICS and cedar faced fire test, respectively. The Fig.42 (d) indicates the thermocouple configuration during the façade fire test.

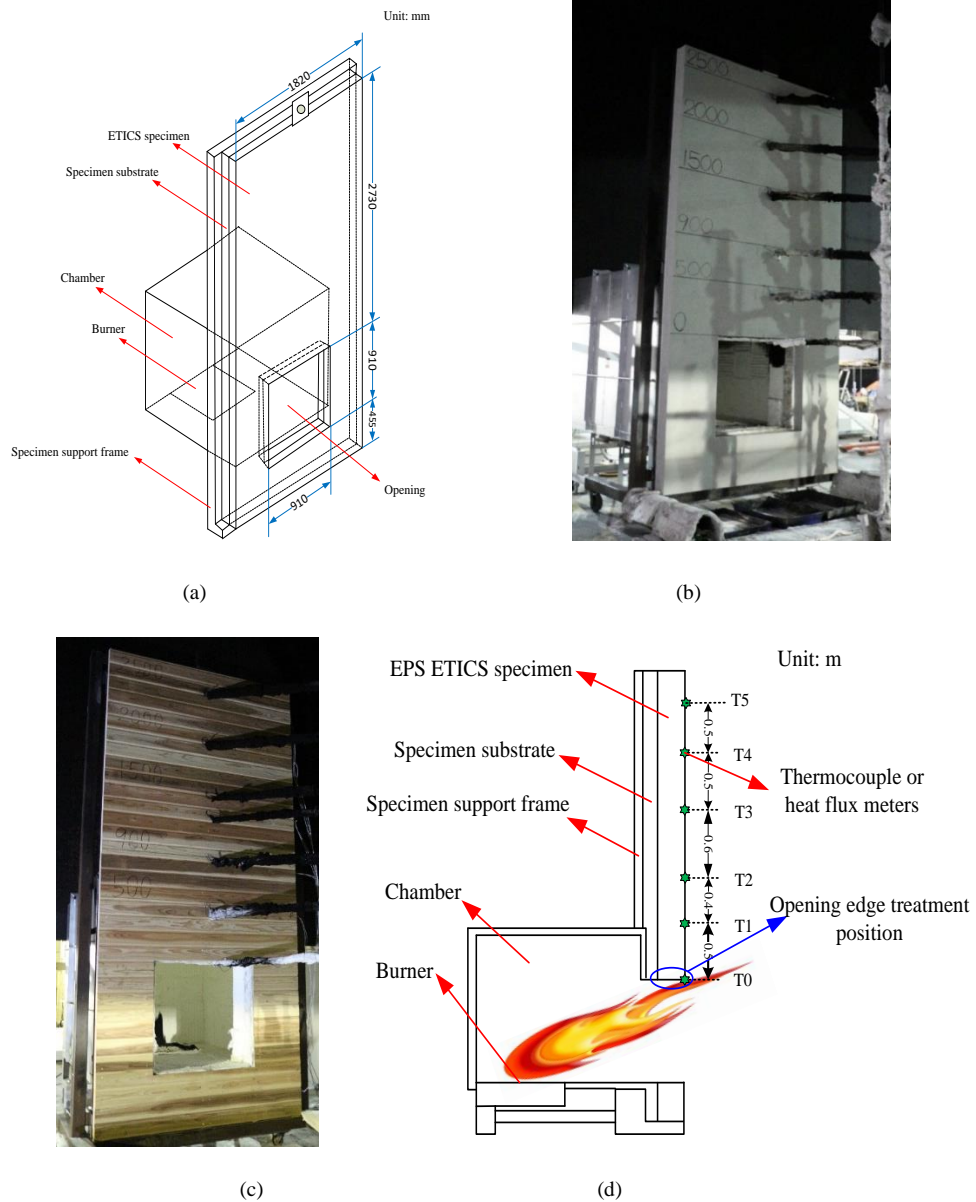


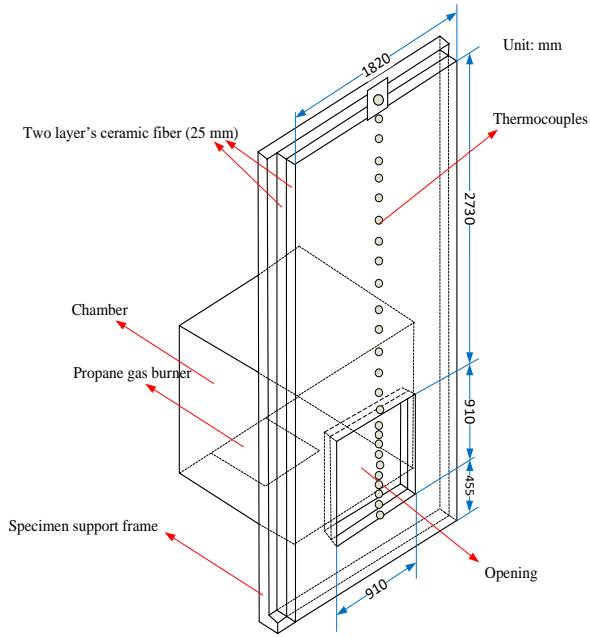
Fig.42 Description of experiment layout (a) a simple model of experiment (b) the experimental EPS ETICS layout (c) the experimental cedar façade fire test layout (d) description of thermocouples and heat flux meters installation



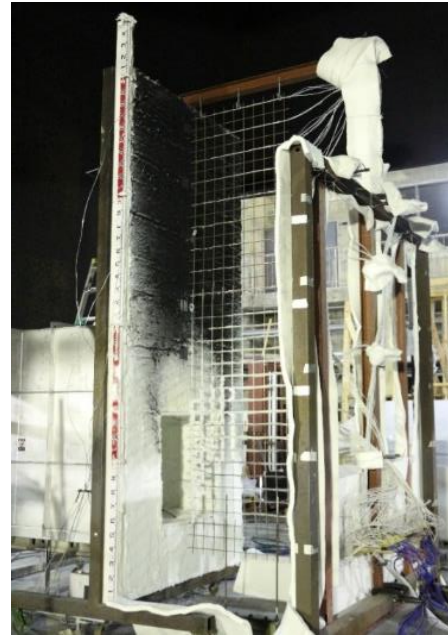
#### **D) JIS A 1310 calibration test description introduction**

The behavior of window ejected fire plume was investigated by using JIS A 1310 method which varying with the heating intensity, opening size, and chamber size. The experiment method is according to the calibration test of JIS A 1310 façade fire test, just as shown in Fig.43. Façade fire test facility consisted of propane gas combustion chamber (size in  $L \times W \times H = 1350 \text{ mm} \times 1350 \text{ mm} \times 1350 \text{ mm}$ ), fire spreading opening (size in  $L \times W = 910 \text{ mm} \times 910 \text{ mm}$ ), gas burner (size in  $L \times W = 600 \text{ mm} \times 600 \text{ mm}$ ), specimen substrate and specimen support frame. The opening size and opening aspect varied  $W \times H = 510 \text{ mm} \times 910 \text{ mm}$  ( $n=1.12$ ),  $W \times H = 710 \text{ mm} \times 910 \text{ mm}$  ( $n=1.56$ ),  $W \times H = 910 \text{ mm} \times 910 \text{ mm}$  ( $n=2$ ),  $W \times H = 910 \text{ mm} \times 610 \text{ mm}$  ( $n=2.98$ ) and  $W \times H = 910 \text{ mm} \times 410 \text{ mm}$  ( $n=4.44$ ), respectively. The Chamber was with a  $10.1069 \text{ m}^2$  of inner surface area and it was used to produce different heating intensity fire, which was conducted by the controlled high purity propane combustion. The gas burner was filled with the ceramic fiber ball to produce propane gas with a uniform speed. The specimen substrate was made by laying two pieces of 12 mm thickness calcium silicate board and the joint of the first layer was not overlapped with joint of second layer. Specimen support frame made of stainless steel was employed to support specimen substrate and the specimen tested. The interior surface of chamber was coated by a thickness of 25 mm ceramic fiber blanket. The test was carried out by laying a thickness of 25 mm ceramic fiber on the specimen support frame. A k-type thermocouples tree was used to record the temperature information varying test time. The thermocouples were fixed at the position from the bottom of opening to the upper of façade wall. HRR and THR were calculated by the common methodology Oxygen Consumption Calorimetry (OC). During OC measurement, the gas-analysis equipment was used to record oxygen concentration ranged from 0.009% to 20.9 % in every two seconds. Before fire test, the 4 Liter alcohol combustion was used to calibrate the whole equipment condition. Then chamber heating intensity in kW was determined by controlling the mass flow of high purity propane. The side view of fire plume behavior was measured by

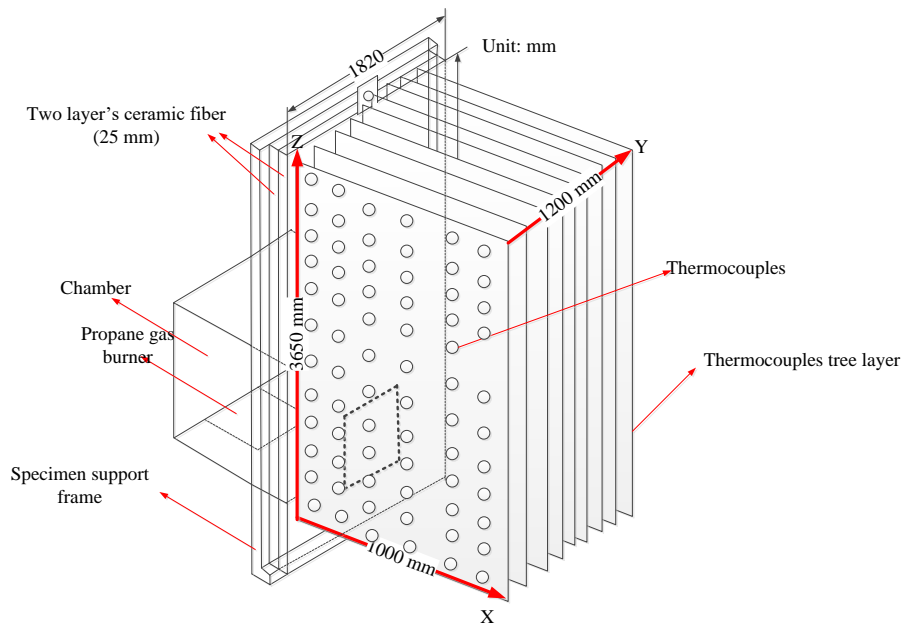
employing a thermal camera named FLIR SC620, which was bought from FLIR Systems, Inc.. All the experiments were finished in the Building Research of Institute of Japan located in Tsukuba. The results are shown in the subtext.



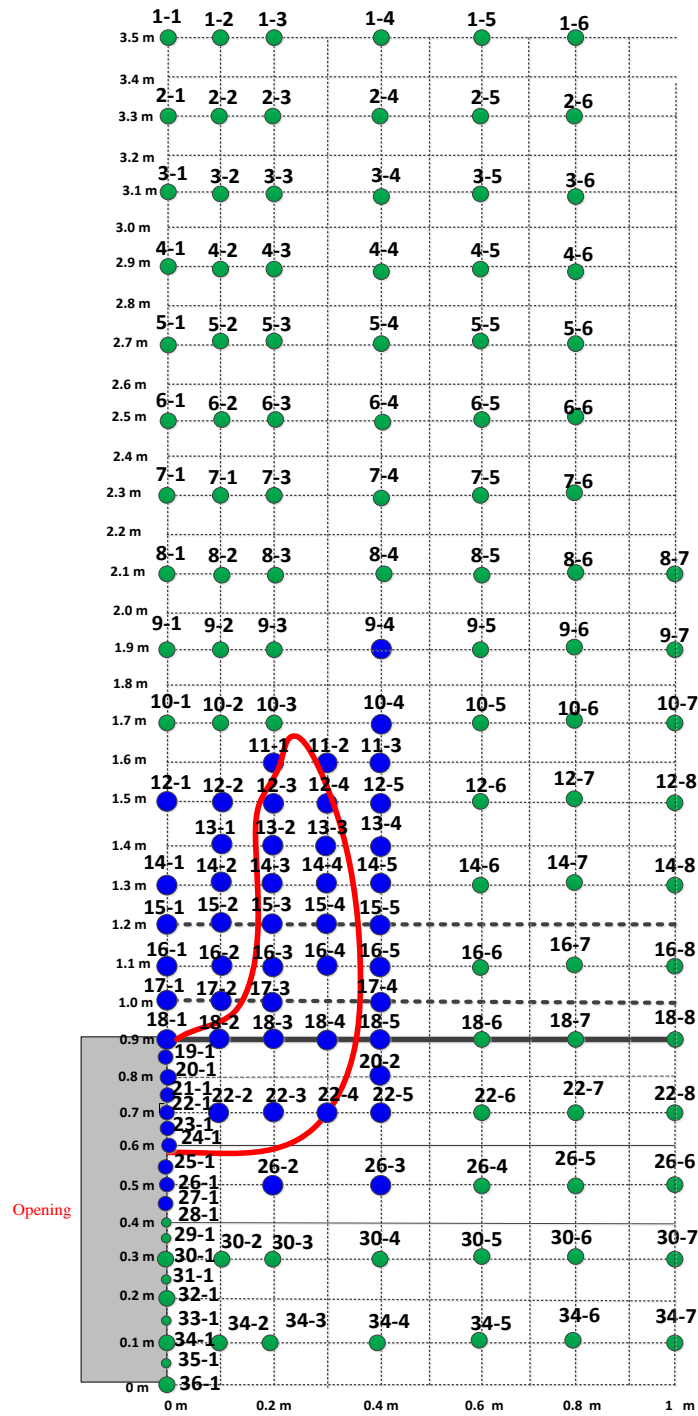
(a)



(b)



(c)



(d)

Fig.43 Experiment layout introduction

(a) A simple model of experiment (b) the experimental layout in our lab (c) The thermocouples mesh position during the test (d) the configuration of thermocouples on the mesh. The green ones is the usual thermocouple. The blue ones are the fire-retardant thermocouple, which is coated with a 2 mm thick of ceramic fiber tube.

#### **E) Timber FPA test introduction**

The pyrolysis model of cedar is necessary for simulation. The corresponding parameters could be got using FPA tests. The FPA phased from Fire Testing Technology was employed to measure the mass loss rate (MLR) and chemical HRR. The tests were conducted in the Tianjin Fire Research Institute of MPS according to the standard test method ASTM E2058-13a <sup>[50]</sup> and ISO 12136 <sup>[51]</sup>. The detailed introduction of FPA has been disclosed in the literature <sup>[52]</sup>. During the FPA experiments, a humidity control and delivery system <sup>[53]</sup> was used to set the relative humidity (RH) of the gas supply to the FPA. With an aim to ensure flow uniformity, the gas supplies was fed by using mass flow controllers to go through a bed of glass beads. The test conditions were followings: ambient temperature 20 °C, ambient pressure 102.924 kPa and relative humidity 23%. Square cedar samples of size in  $L \times W \times H = 100 \text{ mm} \times 100 \text{ mm} \times 19 \text{ mm}$  were placed in an insulated sample holder and mounted horizontally on a load cell , which was used to dynamically record sample mass information. Considering that the heat flux of position located at the vertical 0.5 m away from the upper of opening is near  $50 \text{ kW/m}^2$ , in this study, FPA experiments were performed by exposing cedar samples to both low and high heat flux levels, 15 and  $45 \text{ kW/m}^2$ , respectively. For each heat flux level, duplicate experiments were conducted. The results consisted of mass loss, MLR and chemical HRR. The MLR histories were obtained by using Savitsky-Golay filters, which keeps the temporal size of the filter between one and two times the full-width-half-magnitude size of the narrowest transient peak of interest <sup>[54]</sup>. The Fig.44 shows the layout of FPA experimental configuration.

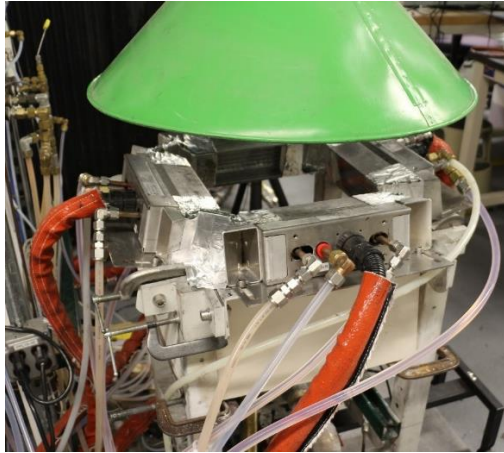


Fig.44 The description of FPA facility

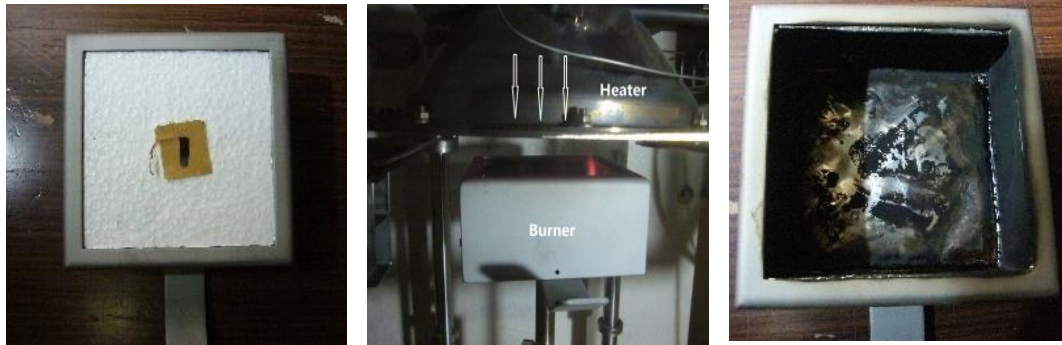
## 4.3 Tests results and discussion

### 4.3.1 Cone tests results and discussion

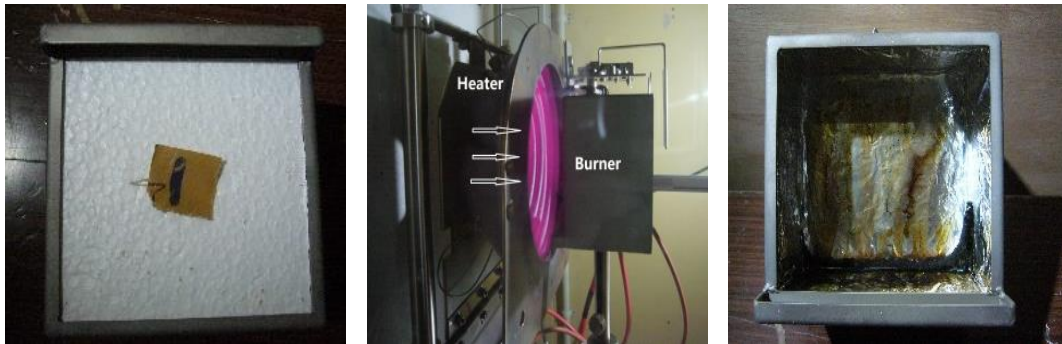
#### A) EPS- Cone (H) and Cone (V) test

As for non-melt flow materials, usually, a general relation that  $HRR(V) = 0.7 HRR(H)$  is adequately approximated [55]. It clearly verifies that the thin, boundary-layer type flames occurring in the vertical orientation provide a lower heat flux than the pool-like flames in the horizontal orientation. However, when EPS exposed to irradiation  $30 \text{ kW/m}^2$ ,  $pHRR(V)$  is only 1.4 % of  $pHRR(H)$  and  $THR(V)$  is only 2.4 % of  $THR(H)$ . Fig.45 shows EPS Cone (H) test scene and EPS Cone (V) test. It is believed that EPS melt-drip effect causes  $pHRR$  and  $THR$  to decrease by 98.6 % and 97.6 % in Cone test. The EPS burner installation are shown in Fig.45 (a) and Fig.45 (d). And the irradiation direction is disclosed in Fig.45 (b) and Fig.45 (e). After Cone (H) test, no residual EPS molten was found in Cone (H) test (just as shown in Fig.45 (c)). However, EPS molten in the bottom of burner was observed after Cone (V) test, just as shown in Fig.45 (f). The observation is consistent with previous report when PS foam (thickness=10 mm) exposed to irradiances  $30 \text{ kW/m}^2$  and  $50 \text{ kW/m}^2$ , the  $pHRR(V)$  is 68 % and 73 % of  $pHRR(H)$ . When PS foam

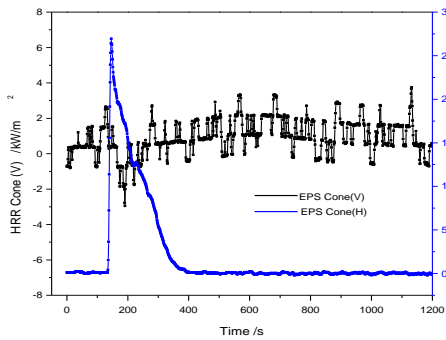
(thickness=20 mm) exposed to irradiances 30 kW/m<sup>2</sup> and 50 kW/m<sup>2</sup>, the pHRR (V) is 76 % and 56 % of pHRR (H). EPS melt-drip showed a clear decrease effect on the HRR measurement of EPS Cone test.



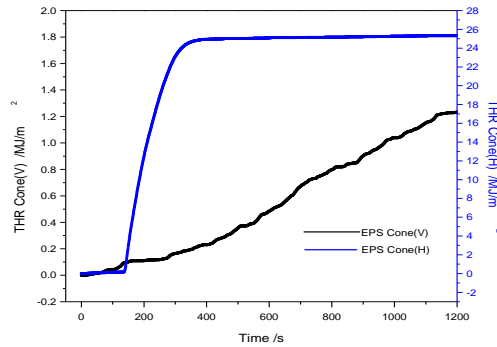
(a) (b) (c)



(d) (e) (f)



(g)



(h)

Fig.45 Description of EPS Cone test.

(a) An EPS sample installing in the burner (b) EPS sample exposed to 30 kW/m<sup>2</sup> when t=168 s (c) Burner after Cone (H) test (d) An EPS sample installing in the burner (e) EPS sample exposed to 30 kW/m<sup>2</sup> when t=45 s (f) Burner after Cone (V) test (g) HRR history varying test time (h) THR history varying test time

## B) EPS ETICS - Cone (H) and Cone (V) test

The Fig.46 features the EPS ETICS configuration. Fig.46 (a) represents the model parameters and Fig.46 (b) shows the section figure of EPS ETICS specimen. The HRR and THR comparison of Cone (V) and Cone (H) with EPS ETICS specimen are described in Fig.47. It is found that when EPS ETICS subjected to irradiation  $30 \text{ kW/m}^2$ , pHRR (V) is 79.2 % of pHRR (H) and THR (V) is 16.7 % of THR (H). This is inferred to be ascribed to EPS melt-drip effect. EPS ETICS Cone (H) and Cone (V) test scenes were described in Fig.47 (a) and Fig.47 (d), respectively. And the irradiation direction is disclosed in Fig.47 (b) and Fig.47 (d). Little EPS molten was found after Cone (H) test (just as shown in Fig.47 (c)). Comparably, EPS molten was observed in the bottom of burner after Cone (V) test, just as shown in Fig.47 (f). From the comparison of Cone (V) and Cone (H) tests with EPS specimen and EPS ETICS specimen, it is clear EPS melt-drip has a decrease effect on pHRR and THR in bench-scale Cone (V) test. In industry, the thickness of EPS used in ETICS varies from 50 mm to 200 mm. Compared with Cone (V) test, ICAL test specimen has a large size in vertical direction, which is more similar with industrial installation method. In the next part, ICAL test was carried out to measure HRR and THR of EPS specimen and EPS ETICS specimen. Tests were conducted at heat fluxes of  $30 \text{ kW/m}^2$  and  $50 \text{ kW/m}^2$ . Samples were prepared by cutting an EPS ETICS panel (53 mm thick) into  $100 \text{ mm} \times 100 \text{ mm}$  square pieces. The MLR and HRR varying test time are shown in Fig.48. Table 14 shows the summary of test under  $30 \text{ kW/m}^2$  irradiation level.

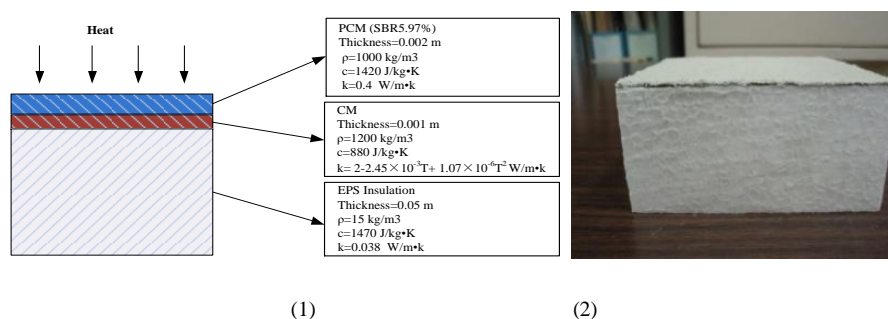


Fig.46 The description of ETICS parameters (a) the model parameters (b) the section figure of EPS ETICS



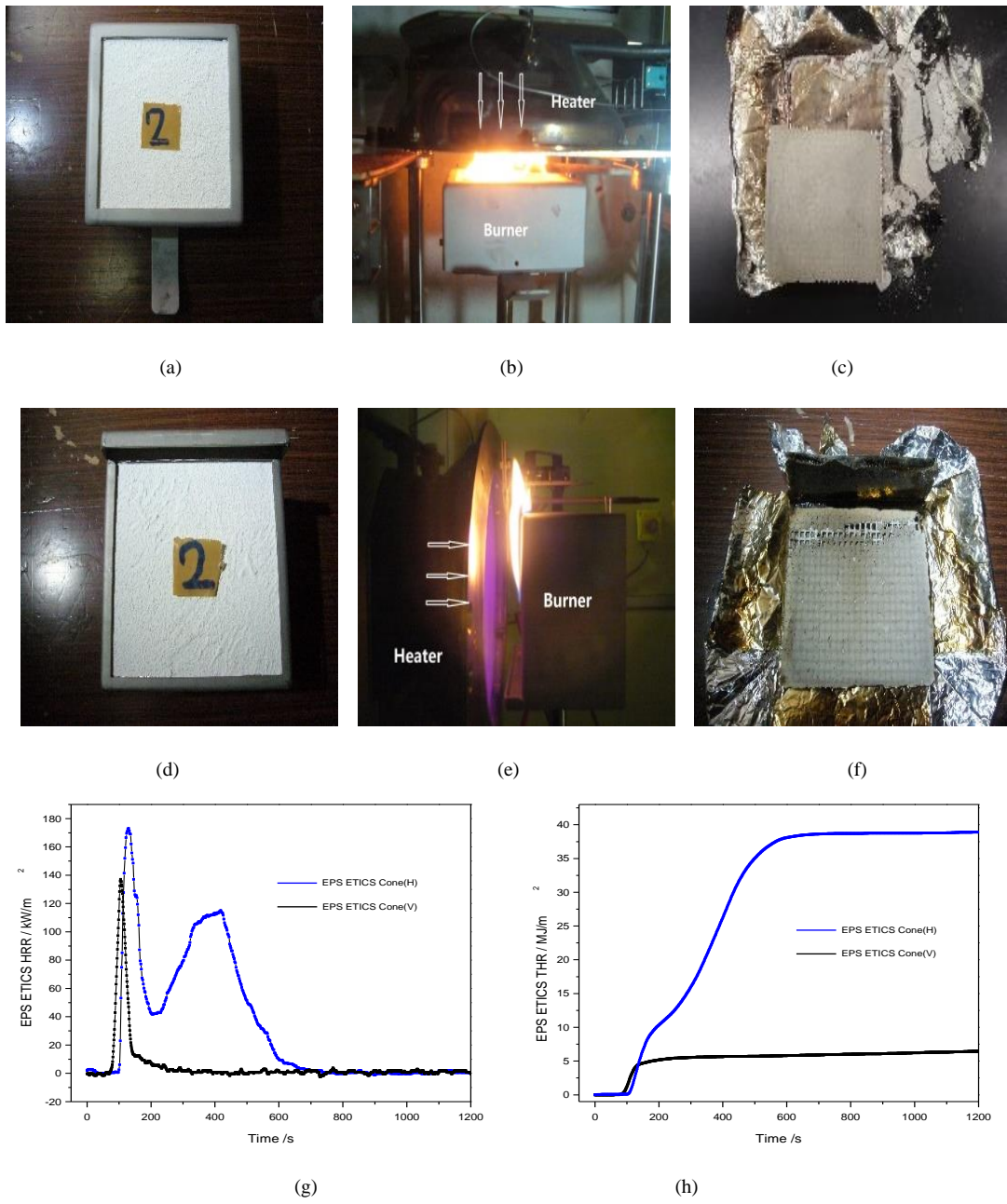


Fig.47 EPS ETICS Cone test scene.

(a) An EPS ETICS sample installing in the burner (b) EPS ETICS sample exposed to  $30 \text{ kW/m}^2$  when  $t=154 \text{ s}$  (c) Burner after Cone (H) test (d) An EPS ETICS sample installing in the burner (e) EPSETICS sample exposed to  $30 \text{ kW/m}^2$  when  $t=82 \text{ s}$  (f) Burner after Cone (V) test. (g) HRR comparison of EPS ETICS in both vertical and horizontal direction (h) THR comparison of EPS ETICS in both vertical and horizontal direction



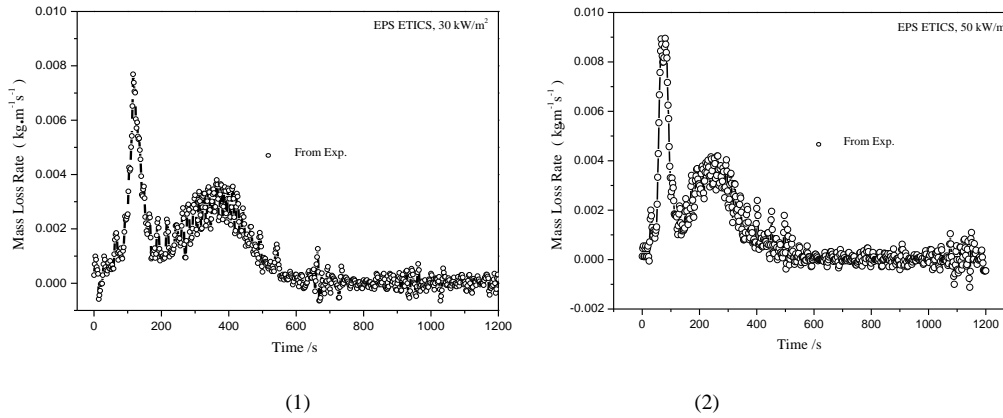


Fig.48 Results of HRR and THR (1) MLR 30 kW/m<sup>2</sup> (2) MLR 50 kW/m<sup>2</sup>

Table 14 Summary of test under 30 kW/m<sup>2</sup> irradiation level

Items	Units	Cone test (30 kW/m <sup>2</sup> )			
		EPS	EPS	EPS ETICS	EPS ETICS
Direction		V	H	V	H
THR	MJ/m <sup>2</sup>	1.2	25.3	6.5	38.9
pHRR	kW/m <sup>2</sup>	3.7	269.4	137.1	173.0
HRR(mean 60 s)	kW/m <sup>2</sup>	0.2	1.4	9.6	122.8
HRR(mean 180 s)	kW/m <sup>2</sup>	0.5	50.2	29.0	78.7
HRR(mean 300 s)	kW/m <sup>2</sup>	0.3	77.0	18.5	86.1
t <sub>ig</sub>	s	No	135.0	53.0	96.9
t extinguishing	s	No	392.0	102.0	486.2
HOC	MJ/kg	3.0	32.2	18.6	29.0
MLR	g/s·m <sup>2</sup>	2.8×10 <sup>-3</sup>	5.0	2.5×10 <sup>-3</sup>	2.8
SEA	m <sup>2</sup> /kg	886.4	1125.7	63.7	412.5
pHRR	V/H	0.014		0.792	
THR	V/H	0.047		0.167	

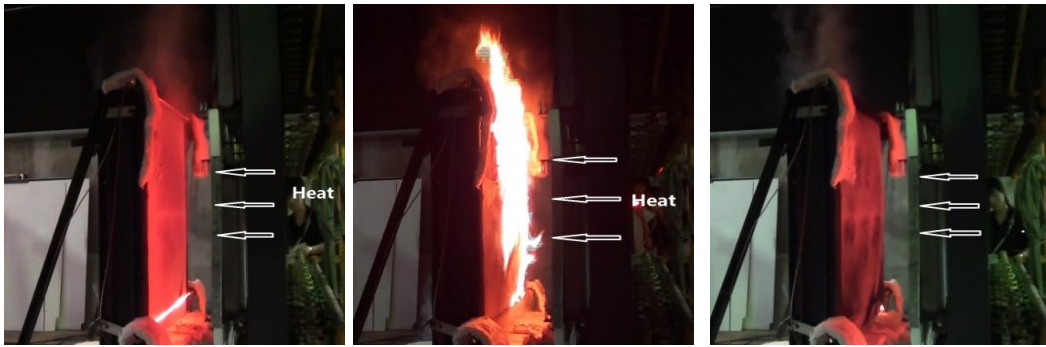
Note: MLR= mean mass loss rate; SEA=specific extinction area; HOC=mean heat of combustion; ×=no data

The results are summarized in the table 14. The ratios of vertical value and horizontal value in pHRR and THR are shown in it. It is found that the measurement direction influences heavily on the results of

Cone. The pHRR of EPS in vertical direction is only 0.014 of values in horizontal direction. The pHRR of EPS ETICS in vertical direction is only 0.792 of values in horizontal direction. The THR of EPS in vertical direction is only 0.047 of values in horizontal direction. The THR of EPS in vertical direction is only 0.167 of values in horizontal direction. In the cite construction, the EPS ETICS usually are performed in the vertical direction. The reaction-to-fire performance of EPS ETICS in vertical direction is hard to be evaluated on the basis of results in horizontal direction. The new method for evaluation of EPS ETICS reaction-to-fire performance should be improved or modified in the future.

#### **4.3.2 ICAL results and discussion**

The Fig.49 features the ICAL test scene. Fig.49 (f) represents the THR and HRR history of ICAL EPS ETICS test at 30 kW/m<sup>2</sup> irradiation. The pHRR of EPS ETICS using Cone in vertical direction is only 0.726 of value using ICAL test in vertical direction. The THR of EPS ETICS using Cone in vertical direction is 2.200 times of value using ICAL test in vertical direction. It is obvious that the discrepancy in results of Cone (V) and ICAL (V) impulses a new evaluation method for EPS ETICS reaction-to-fire performance. The correlation between Cone (V), ICAL (V) and façade fire test needs further study. By it, the reasonable reaction-to-fire performance of EPS ETICS could be got by Cone or ICAL, without large scale of façade fire test. Table 15 discloses the summary of tests including Cone and ICAL under 30 kW/m<sup>2</sup> irradiation level.



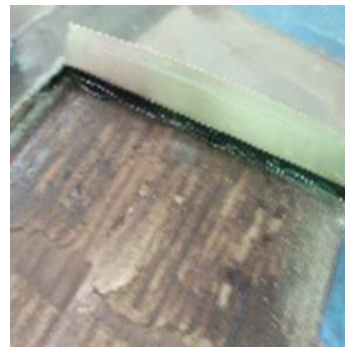
(a)

(b)

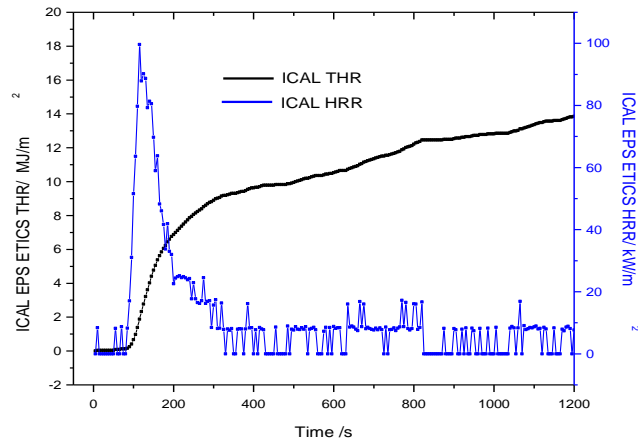
(c)



(d)



(e)



(f)

Fig.49 EPS ETICS ICAL test scene under  $30 \text{ kW/m}^2$  irradiation.

(a)  $t=105 \text{ s}$  (b)  $t=180 \text{ s}$  (c)  $t=286 \text{ s}$  (d) The EPS molten flowed out from the bottom of specimen (e) The surface of coating was removed after ICAL test (f) THR and HRR history of ICAL EPS ETICS test at  $30 \text{ kW/m}^2$  irradiation.

Table 15 Summary of test including Cone and ICAL under 30 kW/m<sup>2</sup> irradiation level

Items	Units	Cone test	ICAL test
Direction		V	V
THR	MJ/m <sup>2</sup>	6.5	14.3
pHRR	kW/m <sup>2</sup>	137.1	99.6
HRR(mean 60 s)	kW/m <sup>2</sup>	9.6	1.4
HRR(mean 180 s)	kW/m <sup>2</sup>	29.0	19.3
HRR(mean 300 s)	kW/m <sup>2</sup>	18.5	29.7
t <sub>ig</sub>	s	53.0	41.0
t extinguishing	s	102.0	286.0
HOC	MJ/kg	18.6	×
MLR	g/s·m <sup>2</sup>	2.5×10 <sup>-3</sup>	×
SEA	m <sup>2</sup> /kg	63.7	×
pHRR	ICAL/Cone		0.726
THR	ICAL/Cone		2.200

Note: MLR= mean mass loss rate; SEA=specific extinction area; HOC=mean heat of combustion; ×=no data.

#### 4.3.3 EPS ETICS façade fire test results and discussion

The façade is defined as the connection between the inside and outside of building. Although façade fire is low frequently events, the resulting consequences in terms of extent of fire spread and property loss can be potentially very high <sup>[56]</sup>. Recently, combustible façade presents an increased fire hazard. External Thermal Insulation Composite Systems (ETICS) are widely used as façade in buildings since the decades due to its thermal advantages, low cost and ease of application <sup>[57]</sup>. Expanded polystyrene (EPS) is one of common thermal insulation thermoplastic materials used in ETICS. It seems necessary to find an optimal

method to inhibit or alleviate upward flame spread. The EPS ETICS specimen reaction-to-fire performance needs to be well understood and quantified. .

EPS ETICS consist of adhesive, EPS insulation material, cement, reinforcing mesh and finishing coat. However, most current research has concentrated on the characteristics of single component reaction-to-fire performance, such as EPS reaction-to-fire performance <sup>[58-60]</sup>, adhesive reaction-to-fire performance <sup>[61]</sup>, polymer-modified concrete <sup>[62, 63]</sup> and finishing coat reaction-to-fire performance <sup>[64, 65]</sup>. Furthermore, it has been widely acknowledged that performance of facade cladding systems in case of a fire cannot be fully assessed by laboratory tests <sup>[66]</sup>. Fire behaviour of EPS with sandwich panel structure <sup>[67, 68]</sup> is characterized by using large-scale room fire tests according to the ISO 9705 or ISO 13784-1 protocols. In our previous large-scale fire investigation, evaluation method of fire propagation over external combustible exterior wall systems was set up <sup>[69]</sup> and tested <sup>[1, 70, 71]</sup>. As for opening edge treatment method, it is believed to be critical to alleviate or inhibit a vertical flame spreading. Currently, although it is clear that EPS ETICS reaction-to-fire performance will show a complex reaction-to-fire performance in a fire because of EPS tendency to melt and drip, little knowledge of relationship between EPS ETICS reaction-to-fire performance and opening edge treatment, heating intensity and EPS burn area is available.

This part presents findings and the testing results of EPS ETICS reaction-to-fire performance regarding the effective opening edge treatment method, details works involving relationship between opening edge treatment methods and EPS ETICS façade reaction-to-fire performance, explores different EPS ETICS thickness effects on EPS ETICS façade reaction-to-fire performance, discusses the heating intensity effects on the EPS burn area.

**A) JIS A 1310 facade fire test method <sup>[49]</sup>**

Test condition of each EPS ETICS specimen is described in Table 16. Details of EPS burn area S, EPS

burn areas above opening  $S_a$  and below opening  $S_b$  are given in table 17. Time (20 min) averaged temperature of each thermocouple position T1 to T5 is disclosed in table 18.

Table 16 The description of EPS ETICS specimen for each façade fire test

Test NO.	EPS thickness/mm	Edge treatment methods	Fire barrier	Heating intensity /kW
NO.1	50 mm	Back-wrapping	No	300
NO.2	50 mm	Stick	No	300
NO.3	50 mm	EPS exposed without treatment	No	300
NO.4	50 mm	Stick+ Rock wool (0.06 m )	Yes	300
NO.5	50 mm	Stick+ Rock wool (0 m )	Yes	300
NO.6	100 mm	Back-wrapping	No	600
NO.7	100 mm	Stick	No	600
NO.8	200 mm	Back-wrapping	No	600
NO.9	200 mm	Stick	No	600
NO.10	200 mm	Back-wrapping	No	300
NO.11	300 mm	Back-wrapping	No	300
NO.12	50 mm	Back-wrapping	No	600
NO.13	100 mm	Back-wrapping	No	300
NO.14	100 mm	Back-wrapping	No	900
NO.15	200 mm	Back-wrapping	No	900
NO.16	100 mm	Back-wrapping	No	1100
NO.17	200 mm	Back-wrapping	No	1100

Table 17 Details of EPS burn area S, EPS burn area above opening  $S_a$  and below opening  $S_b$ .

Test NO.	Above opening $S_a$ (m <sup>2</sup> )	Below opening $S_b$ (m <sup>2</sup> )	EPS burn area S (m <sup>2</sup> )	$S_a / S_b$ ratio
NO.1	1.88	0.45	2.33	4.18
NO.2	2.09	0.42	2.51	4.98
NO.3	2.27	0.60	2.87	3.78
NO.4	2.71	0.56	3.27	4.84
NO.5	2.04	0.58	2.62	3.52
NO.6	3.73	1.18	4.91	3.16
NO.7	4.65	1.67	6.32	2.78
NO.8	4.38	1.41	5.79	3.11
NO.9	4.97	1.59	6.56	3.13
NO.10	3.57	1.13	4.70	3.16
NO.11	4.38	1.42	5.80	3.08
NO.12	2.98	0.98	3.96	3.04
NO.13	2.63	0.85	3.48	3.09
NO.14	4.80	1.60	6.4	3.00
NO.15	4.97	1.67	6.64	2.98
NO.16	4.97	1.67	6.64	2.98
NO.17	4.97	1.67	6.64	2.98

Table 18 Time (20 min) averaged temperature of each position from T1 to T5.

Test NO.	T1	T2	T3	T4	T5
NO.1	420.6	313.5	223.0	179.6	151.1
NO.2	452.9	336.3	237.1	192.4	160.4
NO.3	380.3	302.7	223.5	182.4	153.4
NO.4	421.3	319.5	231.8	185.3	157.3
NO.5	437.6	329.0	237.8	188.3	156.1
NO.6	566.5	472.1	345.1	280.7	230.2
NO.7	580.1	465.2	347.8	281.0	225.7
NO.8	609.7	524.8	371.3	301.7	278.3
NO.9	590.5	520.1	405.0	371.5	311.1
NO.10	508.5	396.9	277.1	219.1	176.5
NO.11	593.3	459.6	326.4	253.6	202.4
NO.12	552.3	475.6	350.6	284.4	229.3
NO.13	465.5	355.0	258.8	205.1	169.5
NO.14	518.9	488.8	375.5	299.6	264.6
NO.15	877.9	571.6	470.8	435.2	341.8
NO.16	714.5	703.8	587.2	460.8	375.6
NO.17	826.2	731.2	728.9	589.8	453.9

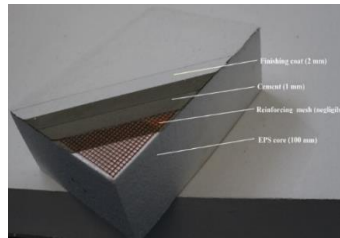
### B) Preparation of EPS ETICS specimen

The horizontal section of EPS ETICS specimen was shown in Fig.50 (a). It consists of four layers from top to down, finishing coat made of polymer cement mortar, cement, reinforcing mesh made of fire glass fiber and EPS. Usually, the thickness of polymer cement mortar and cement are 2 mm and 1 mm, respectively. In present research, EPS thickness varies from 50 mm to 300 mm.

Presently, the preparation of EPS ETICS specimen is described in the followings. Firstly, specimen



support frame made of stainless steel was prepared in size of  $W \times L = 1820 \text{ mm} \times 4100 \text{ mm}$ ). There was an opening (size in  $L \times W = 910 \text{ mm} \times 910 \text{ mm}$ ) in the middle of support frame, just as shown in Fig.50 (b). Two pieces of calcium silicate board with a thickness of 12 mm was laid and fixed on the specimen support frame (See Fig.50(c)). Then EPS panel was laid and fixed on it, which is shown in Fig.50 (d). After EPS coating with fire glass fiber reinforcing mesh, the cement is used to fix the reinforcing mesh, just as shown in Fig.50 (e). Finally, the finishing coat made of polymer cement mortar is laid on the surface of cement, which is described in Fig.50 (f).



(a)



(b)



(c)



(d)



(e)



(f)

Fig.50 The description of EPS ETICS specimen preparation

(a) The horizontal section EPS ETICS specimen (b) specimen support frame (c) specimen substrate (d) EPS panel laying on specimen substrate (e) cement laying on reinforcing mesh (f) finishing coat laid on the cement

### C) EPS ETICS opening edge treatment methods

In our experiments, five types of opening edge treatment were tested, which include back-wrapping, stick, EPS exposed without treatment, Stick+ rock wool (0.06 m) and Stick+ rock wool (0 m). The details of each opening edge treatment are described in Fig.51. The EPS used here is melted at about 85-110 °C and ignited at about 290 °C.

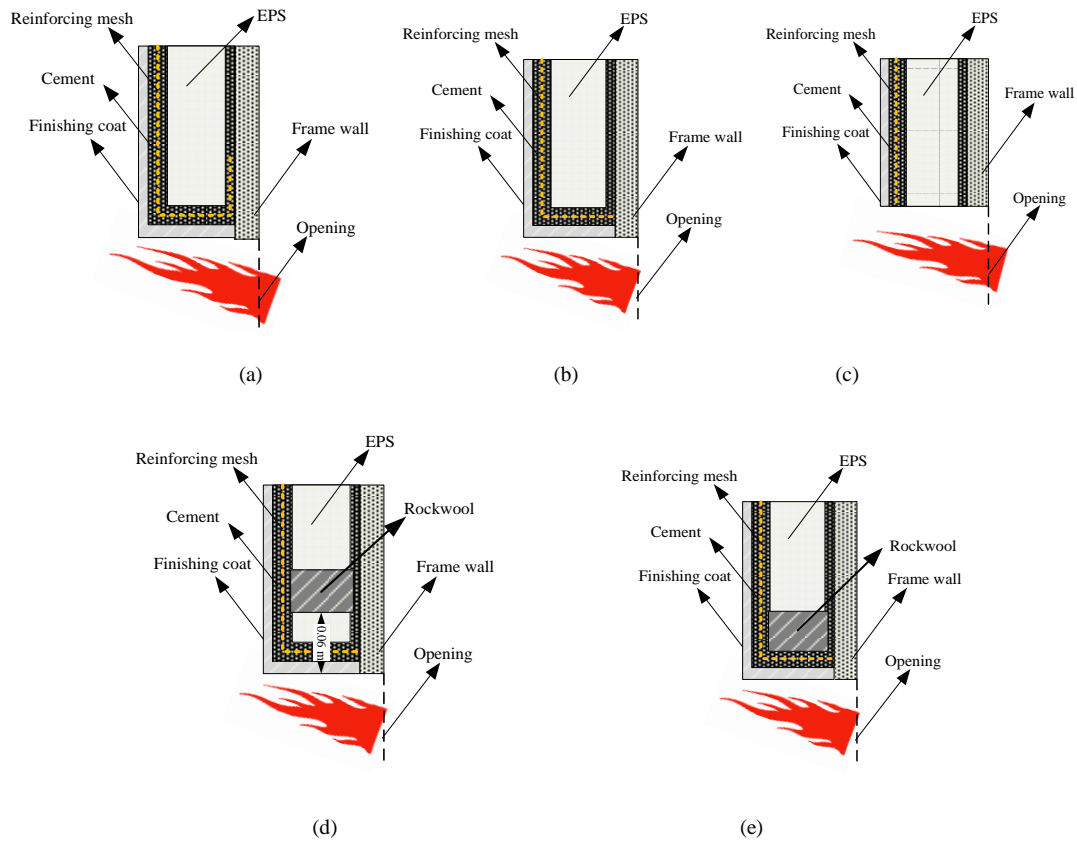


Fig.51 The description of opening edge treatment methods of test from NO.1 to NO.5

(a) Back-wrapping section figure (b) Stick section figure (c) EPS exposed without treatment section figure (d) Stick+ rock wool (0.06 m) section figure (e) Stick+ rock wool (0 m) section figure

The traditional edge treatment method of EPS ETICS is stick, which is disclosed in Fig.51 (b). It is widely acknowledged that when EPS is exposed to a flame, molten EPS drops down and causes downward fire spreading. Considering that molten EPS is easy to cause downward fire spread, the reinforcing mesh made of fire glass fiber is wrapped back to reduce molten EPS dropped down. This idea is realized by back-

wrapping method. The difference between back-wrapping and stick lies in whether reinforcing mesh back wrapped, just as shown in Fig.51 (a) and Fig.51 (b). As for EPS ETICS building, the EPS exposed without treatment is prohibited. Here, EPS exposed without treatment (Fig.51 (c)) is acted as a control group test to compare with different opening edge treatment methods.

Fire barrier is one of effective methods to inhibit vertical flame spread, which has been widely used in EPS ETICS building. Presently, fire barrier made of rock wool is installed in the two methods. The difference between two methods lies in the vertical distance away from the top of opening. Installation of fire barrier made of rock wool on traditional edge treatment method was thought to be a good method for flame spread inhibition. In the present work, stick+ rock wool (0.06 m) means that the opening of specimen is treated by stick method and installing a fire barrier made of rock wool (size in  $H \times L \times W = 150 \text{ mm} \times 1820 \text{ mm} \times 50 \text{ mm}$ ) at 0.06 m away from the top of the opening, just as shown in Fig.51 (d). Stick+ rock wool (0 m) means that the opening of specimen is treated by stick method and directly installing a fire barrier made of rock wool (size in  $H \times L \times W = 150 \text{ mm} \times 1820 \text{ mm} \times 50 \text{ mm}$ ) at the top of opening (see Fig.51 (e)). All the specimens are tested based on the JIS A 1310 standard façade fire method.

#### **D) Effects of opening edge treatment method on EPS ETICS reaction-to-fire performance (Test NO.1 to NO.5 )**

When the window spreading fire happens, the window opening edge treatment plays an important role in alleviating upward flame spread. With an aim to compare five opening edge treatment effects on façade fire performance, five façade fire tests are conducted employing EPS (50 mm) ETICS specimen with heating intensity 300 kW. Before each test, the calibration test without combustible façade was carried out firstly to calibrate the equipment condition. Then the façade fire test NO.1 to NO.5 are conducted subsequently.

#### **■ EPS burn area**

After each façade fire test, the EPS burn area ( $S$ ,  $m^2$ ) including above opening part ( $S_a$ ,  $m^2$ ) and below opening part ( $S_b$ ,  $m^2$ ) was calculated by laying a  $0.1\text{ m} \times 0.1\text{ m}$  mesh over tested specimen. The details of EPS burn  $S$  is disclosed. EPS ETICS specimen opening edge treated by back-wrapping has the smallest EPS burn area  $S$  among test NO.1 to NO.5. The  $S_a$  of test NO.2 is larger than it of NO.1 while  $S_b$  of test NO.1 is larger than it of NO.2. This is inferred to correlate with the reinforcing back-wrapping effect. When the opening edge is treated by back-wrapping method, the molten EPS is difficult to drop out but easy to drop down inside of ETICS. It makes a contribution for a larger  $S_b$ . Moreover, even after 20 min façade fire test, it was observed that the most parts of opening edge were kept and the residual cement attached to reinforcing mesh firmly. It is described in Fig.52 (a). With the help of back-wrapped reinforcing mesh, the cement attached to reinforcing mesh can be in part to prevent heat from entering into inside of EPS ETICS specimen. In addition, molten EPS flows down to the upper of opening during test, then it absorbs heat from the flame to decompose. Under this condition, partial heat was introduced into the inside of EPS ETICS specimen. On the basis of above analysis, back-wrapping method with a smaller  $S_a$  than test NO.2 is reasonable.



(a)



(b)



(c)



(d)



(e)

Fig.52 The description of opening edge after façade fire test from NO.1 to NO.5

(a) Back-wrapping (b) Stick (c) EPS exposed without treatment (d) Stick+ rock wool (0.06 m) (e) Stick+ rock wool (0.0 m)

As for traditional stick method (NO.2), during façade fire test the reinforcing mesh easily departed from specimen substrate to form a narrow space. Subsequently, molten EPS drops out from it to cause downward fire spread. Fig.52 (b) gives the description of opening edge after 20 min façade fire test. It can be seen that even after 20 min façade fire test a small flame still exists from the narrow space. Compared with EPS

exposed without treatment method acting as a control group (NO.3), both stick and back-wrapping method could be used to prevent EPS from burning largely. When the EPS ETICS specimen performance untreated opening edge was heated by 300 kW, the EPS above opening promptly melt and started to drop down. It was found that EPS below the opening was ignited soon by dropped EPS. Furthermore, molten EPS is observed easily to cause finishing coat below opening to be ignited, which was found during test NO.3. The description of opening edge after 20 min façade fire test is shown in Fig.52 (c) .Therefore, an optimal opening edge treatment is necessary for EPS ETICS façade. Considering fire barrier is commonly used in the inhibition of vertical façade fire, EPS ETICS specimen with fire barrier made of rock wool installed on two positions are tested and discussed in the followings.

Presently, the fire barrier made of rock wool is installed with the traditional opening edge treatment stick method. The upper of opening is a key part for fire prevention. When fire barrier made of rock wool is installed directly on the top of opening (Test NO.5),  $S_a$  of NO.5 is smaller than the one of NO.2 and  $S_b$  of NO.5 is much larger than the one of NO.2. This is inferred to be ascribed to effect of fire barrier. On the one hand, fire barrier prevents molten EPS from heating by the flame. This agrees with it that even after 20 min façade fire test, the upper of opening looks good, which is given in Fig.52 (e). On the other hand, a part of heat comes from fire plume is reflected downwards because of fire barrier to result in a large  $S_b$  area. Furthermore, fire barrier is believed to make a contribution for a long flame reattached to façade surface. This is verified by that even the EPS located at 2.4 m away from the top of opening is burnt out, which is found in test NO.5. The stick method without fire barrier is believed to be superior to stick method performed with installation of fire barrier directly on upper of opening.

The EPS burn area  $S$  of NO.4 is the largest one among these five methods. This is believed to correlate with enlarging flame effect caused by fire barrier. It was observed that even EPS located at 2.5 m away from the top of opening is burnt out during test NO.4. Furthermore, it was found that during façade fire test,

the reinforcing mesh departed from specimen substrate panel forming a space (see Fig.52 (d)). The heat could easily enter into EPS ETICS inside through the space. On the basis of the EPS burn area  $S$ , it is clear that fire barrier made of rock wool is not a good method for opening edge treatment.

### ■ Peak temperature of each position from T1 to T5

When vertically installed EPS is exposed to a strong heat flux, it will exhibit a complex combustion. As an important index, peak temperature during façade fire is used to evaluate EPS ETICS reaction-to-fire performance. Peak temperature of test NO.1 to NO.9 during 20 min test time is shown in Fig.53. It can be found that peak temperature of NO.3 for each position is the lowest one among five edge treatment methods. It is ascribed to substantial unburnt molten EPS drop. In the present work, the emphasis of peak temperature is focused on T1, T2 and T3. The peak temperature of T1 position from test NO.1 to NO.5 is 458.4 °C, 537.0 °C, 433.0 °C, 581.1 °C and 557.7 °C, respectively. The peak temperature of T2 position from test NO.1 to NO.5 is 346.6 °C, 382.0 °C, 328.0 °C, 424.7 °C and 397.7 °C, respectively. The peak temperature of T3 position from test NO.1 to NO.5 is 249.1 °C, 261.0 °C, 248.0 °C, 285.8 °C and 265.8 °C, respectively. Comparison of test NO.2, NO.4 and NO.5 shows that installation of fire barrier causes peak temperature of T1 to increase by 44.1 °C and 20.7 °C. Comparison of test NO.1 and NO.2 indicates that back-wrapping method could reduce peak temperature of T1, T2 and T3 by 78.6 °C, 35.4 °C and 11.9 °C, respectively.

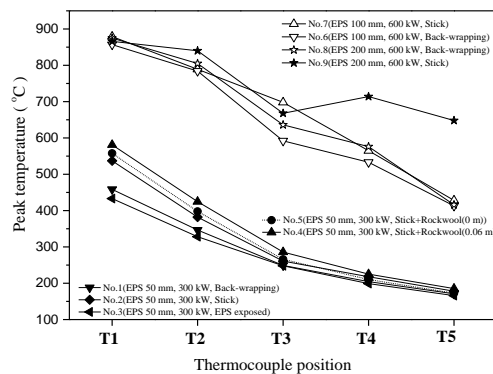


Fig.53 Peak temperature of each thermocouple during façade fire test NO.1 to NO.9

#### ■ Time (20 min) averaged temperature of each position from T1 to T5

In addition to peak temperature, time averaged temperature during façade fire test is also acted as another important index for evaluation of façade combustion profiles. The time (20 min) averaged temperature of T1 position from test NO.1 to NO.5 is 420.6 °C, 452.9 °C, 380.3 °C, 421.3 °C and 437.6 °C, respectively. The time (20 min) averaged temperature of T2 position from test NO.1 to NO.5 is 313.5 °C, 336.3 °C, 302.7 °C, 319.5 °C and 329.0 °C, respectively. The time (20 min) averaged temperature of T3 position from test NO.1 to NO.5 is 223.0 °C, 237.1 °C, 223.5 °C, 231.8 °C and 237.8 °C, respectively. Comparison of test NO.1 and NO.2 indicates that back-wrapping method could reduce time (20 min) averaged temperature of T1, T2 and T3 by 32.3 °C, 22.8 °C and 14.1 °C, respectively. Furthermore, comparison of test NO.2, NO.4 and NO.5 shows that installation of fire barrier causes time (20 min) averaged temperature of T1 to decrease by 31.6 °C and 15.3 °C.

#### ■ Heat flux density profiles of test NO.1 to NO.5

During façade fire tests, the heat flux density of position HF1 to HF5 was also recorded, which is shown in Fig.54. Comparison of heat flux curves varied with test time indicates that little change is found in the position of HF3, HF4 and HF5 of each EPS ETICS specimen. The peak heat flux density of HF1 position from test NO.1 to NO.5 is 16.71 kW/m<sup>2</sup>, 20.27 kW/m<sup>2</sup>, 25.39 kW/m<sup>2</sup>, 20.78 kW/m<sup>2</sup> and 36.10 kW/m<sup>2</sup>, respectively. The peak heat flux density of HF2 position from test NO.1 to NO.5 is 11.81 kW/m<sup>2</sup>, 10.86 kW/m<sup>2</sup>, 9.68 kW/m<sup>2</sup>, 7.25 kW/m<sup>2</sup> and 11.57 kW/m<sup>2</sup>, respectively. The time averaged heat flux density of HF1 position from test NO.1 to NO.5 is 10.77 kW/m<sup>2</sup>, 12.51 kW/m<sup>2</sup>, 15.66 kW/m<sup>2</sup>, 10.11 kW/m<sup>2</sup> and 17.22 kW/m<sup>2</sup>, respectively. The time averaged heat flux density of HF2 position from test NO.1 to NO.5 is 9.00 kW/m<sup>2</sup>, 6.53 kW/m<sup>2</sup>, 7.95 kW/m<sup>2</sup>, 5.41 kW/m<sup>2</sup> and 9.34 kW/m<sup>2</sup>, respectively. Comparison of test NO.1 and NO.2 indicates that back-wrapping method could reduce peak heat flux of HF1 by 3.56 kW/m<sup>2</sup> and decrease



time averaged heat flux of HF1 by  $1.74 \text{ kW/m}^2$ . The time averaged heat flux density of HF2 of test NO.2 is found to be lower than it of test NO.1.

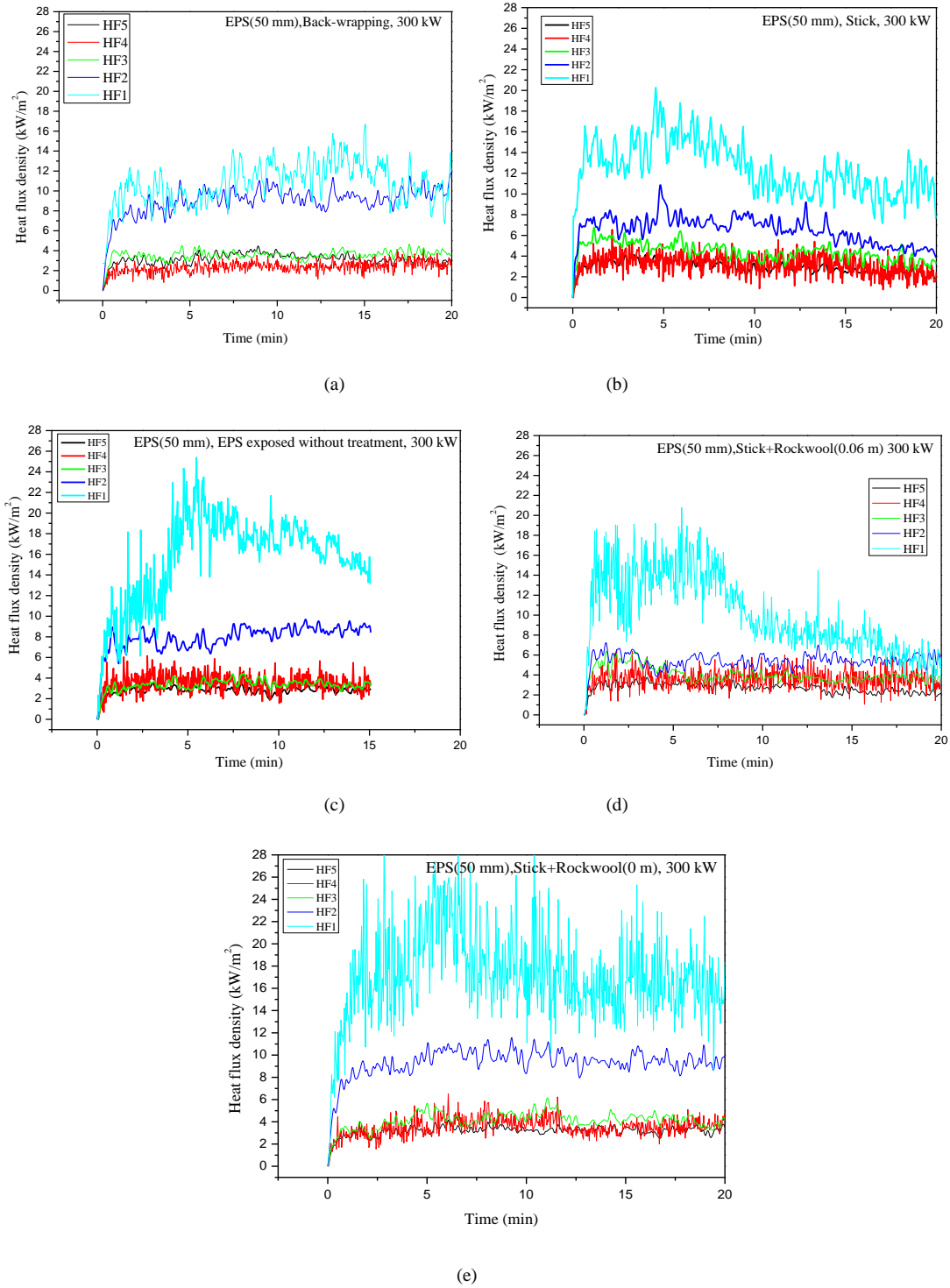









Fig.54 Heat flux density histories of NO.1 to NO.5 (a) test NO.1 (b) test NO.2 (c) test NO.3 (d) test NO.4 (e) test NO.5

## ■ Experiment description of NO.1 to NO.5

During each façade fire test, flame profiles are recorded by camera, which are summarized in table 19. The weak combustion was observed during test NO.1 performed back-wrapping method. It is verified by a lower peak temperature and a lower time (20 min) averaged temperature during test NO.1. The weak combustion started from  $t=120$  s and lasted for nearly all the test time, which is shown in table 19 test NO.1. Regarding test NO.2 with stick method, the serious combustion appeared at  $t=177$  s and lasted for nearly 655 s. When test time approaching 1185 s, the combustion became weak, which is described in table 19 test NO.2. Just as discussed above, the serious combustion is ascribed to molten EPS dropping out from a space created by reinforcing mesh departed from specimen substrate panel. EPS was ignited at 104 s in control group test NO.3. The substantial molten EPS accompanying with combustion and pyrolysis dropped down at 162 s, which is described in table 19 test NO.3. It indicates the optimal opening edge treatment method is necessary.

When EPS ETICS specimen performed traditional stick method with installation of fire barrier at 0.06 m away from the top of opening (test NO.4) was tested, finishing coat was ignited at 120 s. A serious combustion was observed at 180 s and it became weak at 960 s, which is disclosed in table 19 NO.4. When EPS ETICS specimen performed traditional stick method with fire barrier directly installed on the top of opening (test NO.5) was tested, a serious combustion appeared at about 480 s then become weak at 960 s. It was observed that the flame was enlarged at 660 s compared with the edge treatment performed without fire barrier (test NO.2), which is shown in table 19 NO.5. From description of test scenes, it is clear that back-wrapping is a good method for EPS ETICS opening treatment.

Table 19 Experimental description of test from NO.1 to NO.5

Test No.	Façade fire test scene description			
Back-wrapping method Test No.1				
	t=0 s	t=120 s	t=390 s	t=1032 s
Stick method Test No.2				
	t=0 s	t=177 s	t=832 s	t=1185 s
EPS exposed without treatment Test No.3				
	t=0 s	t=104 s	t=162 s	t=850 s
Stick+ rock wool (0.06 m) Test No.4				
	t=0 s	t=120 s	t=180 s	T=960 s
Stick+ rock wool (0 m) Test No.5				
	t=0 s	t=480 s	t=660 s	T=960 s

**E) Comparison of back-wrapping and traditional stick method with a thick EPS at heating intensity 600 kW (from test NO.6 to NO.9)**

Considering the complexity of EPS ETICS façade fire, back-wrapping and stick method are compared based on 50 mm EPS ETICS heated by 300 kW seems insufficient. Presently, EPS ETICS with a thick EPS (100 mm or 200 mm) and 600 kW heating intensity are used to further evaluate back-wrapping method. Test NO.6 and NO.8 are carried out by testing an EPS ETICS (100 mm EPS for NO.6, 200 mm for NO.8) specimen with opening edge treated by back-wrapping method. Test NO.7 and NO.9 are conducted by testing an EPS ETICS (100 mm EPS for NO.7, 200 mm for NO.9) specimen with opening edge treated by stick method. After façade fire test, EPS burn area  $S$  of test NO.6, NO.7, test NO.8 and NO.9 was calculated as 4.91 m<sup>2</sup>, 6.32 m<sup>2</sup>, 5.79 m<sup>2</sup> and 6.56 m<sup>2</sup>, respectively. It is found that back-wrapping method could reduce EPS (100 mm) burn area  $S$  by 1.41 m<sup>2</sup> and decrease EPS (200 mm) burn area  $S$  by 0.77 m<sup>2</sup>. It is observed that back-wrapping method makes a contribution for reducing peak temperature of T1 position by 22 °C (EPS=100 mm) and by 9 °C (EPS=200 mm). As for time (20 min) averaged temperature, back-wrapping method could reduce it of T1 position by 13.6 °C (EPS=100 mm) and by 19.2 °C (EPS=200 mm). Comparison of test NO.8 and NO.9 shows time (20 min) averaged temperature of T3, T4, and T5 of back-wrapping method are 33.7 °C, 69.8 °C and 32.8 °C lower than it from stick method, respectively. It indicates that back-wrapping method could make a contribution for vertical flame inhibition by reducing temperature of T3, T4, and T5. Furthermore, comparison of temperature histories of test NO.6 and NO.7 indicates that back-wrapping method shortens time of the serious combustion, just as shown in Fig.55 (a) and Fig.55 (b). In Fig.55 (c) and Fig.55 (d), two peaks are observed in curves. The former peak temperature derives from finishing coat combustion. The latter peak temperature is inferred to be ascribed to EPS combustion. It clarifies that back-wrapping method can effectively reduce temperature derived from EPS combustion and

weaken the EPS ETICS combustion.

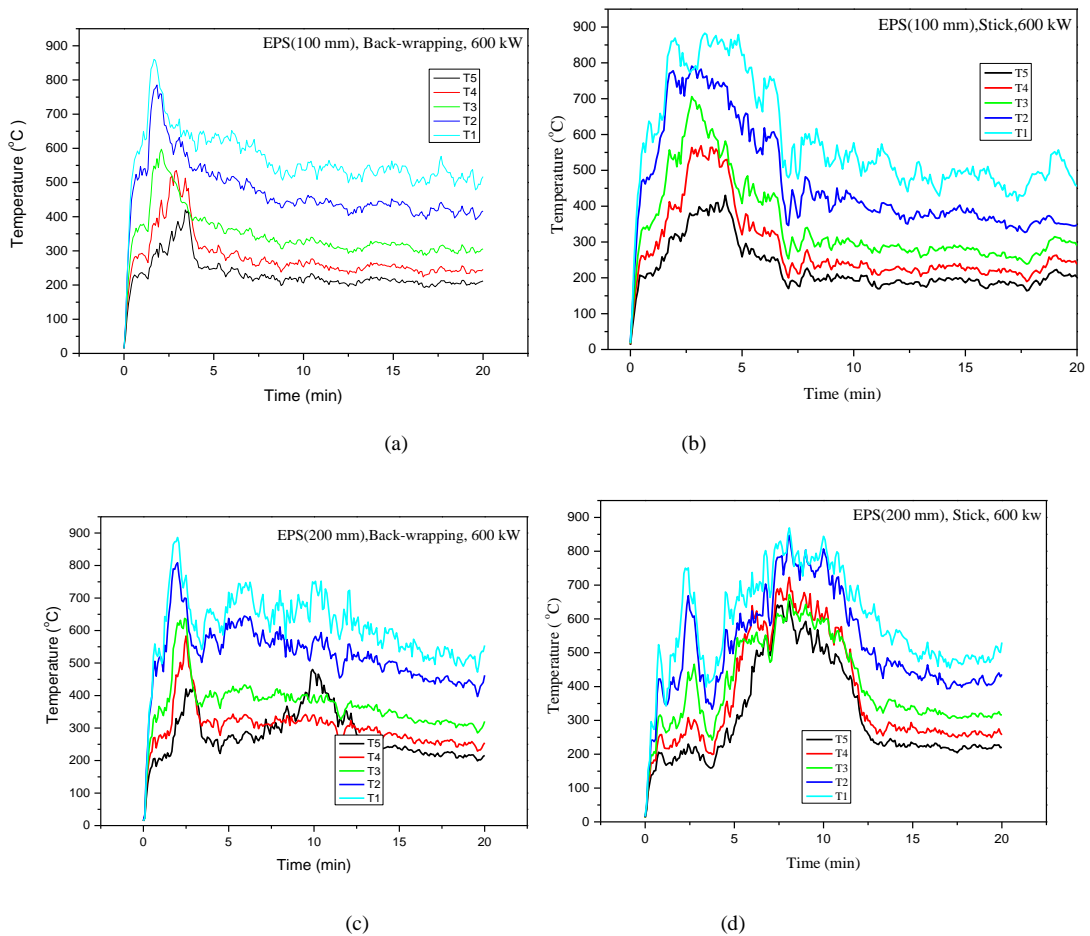


Fig.55 Temperature histories varied with test time during façade fire test NO.6 to NO.9

(a) test NO.6 (b) test NO.7 (c) test NO.8 (d) test NO.9

**F) Effects of EPS thickness on EPS ETICS façade reaction-to-fire performance (tests from NO.10 to NO.17)**

In industry, the thickness of EPS used in ETICS building varies from 50 mm to 300 mm. Once EPS ETICS fire caused by window ejection fire happens, it is difficult to determine the EPS burn area inside the cement layer because outlook of façade looks good after window fire. It has brought a trouble for building rehabilitation. Until now, little knowledge of relationship between EPS thickness and façade fire

performance is available. Presently, a series of EPS ETICS specimens with opening edge treated by back-wrapping method are investigated with respect to EPS thickness effects on façade reaction-to-fire performance. The tests are carried out by varying EPS thickness from 50 mm to 300 mm and chamber heating intensity from 300 kW to 1100 kW. In the followings, effects of EPS thickness on the EPS burn area and time (20 min) averaged temperature are discussed, respectively.

#### ■ Effects of EPS thickness on EPS burn area

EPS burn area  $S$  varied heating intensity and EPS thickness is described in Fig.56. The total EPS area used in present test is  $6.64 \text{ m}^2$ . Regarding the same thickness of EPS, the EPS burn area  $S$  increases as heating intensity rises. Especially, EPS burn area  $S$  of EPS ETICS with a thickness of 100 mm or 200 mm versus heating intensity are linear when the heating intensity rises between 300 kW and 900 kW. With respect to the same heating intensity, EPS burn area  $S$  increases as EPS thickness rises. In particular with heating intensity 300 kW or 600 kW, EPS burn area  $S$  versus thickness is found to be linear when the EPS thickness differs between 50 mm and 300 mm. It is noted that, when heating intensity approaching 900 kW or above, nearly all the EPS was burnt out.

Furthermore, it is observed that the average  $S_a/S_b$  of test NO.6, NO.8, NO.10, NO.11, NO.12, NO.13, NO.14, NO.15, NO.16 and NO.17 is 3.058. The above mentioned tests differ from EPS thickness (from 50 mm to 300 mm) and heating intensity (from 300 kW to 1100 kW). Usually, the outlook of EPS ETICS is kept good after façade fire. It is difficult to determine EPS area needed to be repaired. However, the EPS burn area above opening  $S_a$  is easy to be estimated. By this ratio and  $S_a$ , the EPS burn area below opening  $S_b$  could be easily estimated. Under this condition, this ratio is believed to be useful for EPS ETICS building repair after window fire.

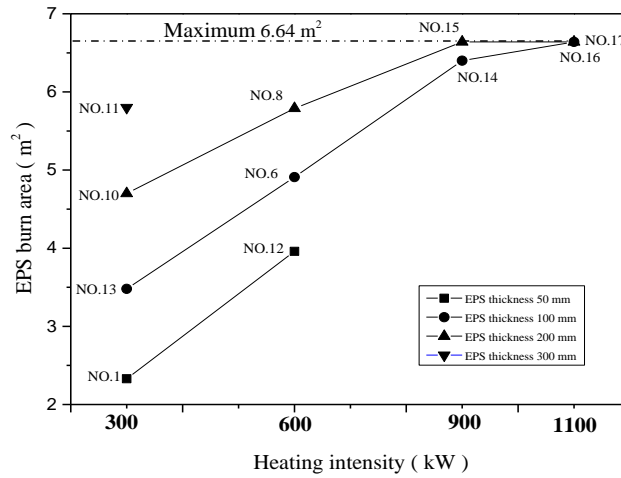


Fig.56 EPS burn area varied with change of heating intensity and EPS thickness.

■ **Effects of EPS thickness on the time (20 min) averaged temperature**

Time (20 min) averaged temperature of T1 to T5 using 300 kW heating intensity from test NO.1, NO.13, NO.10 and NO.11 is given in the Fig.57. Time (20 min) averaged temperature of T1 to T5 using 600 kW heating intensity of test NO.12, NO.6 and NO.8 is summarized in Fig.58. It can be found that time (20 min) averaged temperature of each position from T1 to T5 increases as EPS thickness rises. Generally, the time (20 min) averaged temperature of each position from T1 to T5 versus EPS thickness is linear regarding the same heating intensity 300 kW or 600 kW.

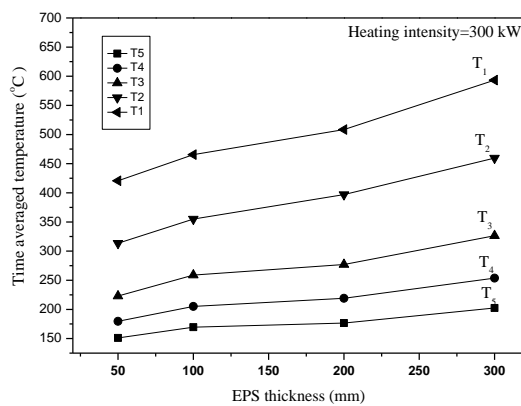


Fig.57 Time (20 min) averaged temperature of T1 to T5 of test NO.1, NO.13, NO.10 and NO.11

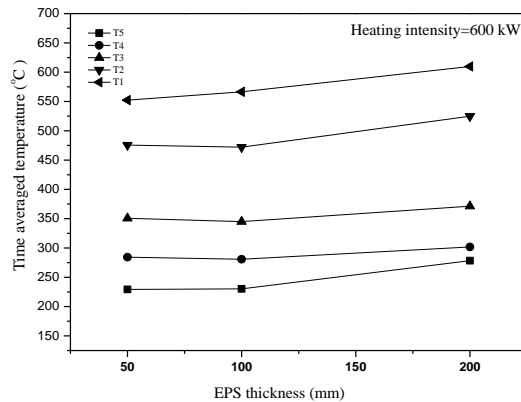


Fig.58 Time (20 min) averaged temperature of T1 to T5 of test NO.12, NO.6 and NO.8.

### G) Summary

In this study, a series of EPS ETICS specimens varied with opening edge treatment and EPS thickness are tested according to JIS A 1310 façade fire test method by using different heating intensity from 300 kW to 1100 kW. Before each façade fire test, calibration test was carried out firstly. EPS burn area, temperature varied with test time and heat flux density as a function of time during façade tests are recorded and discussed. On the basis of a small EPS burn area, a low peak temperature, a low time (20 min) averaged temperature and heat flux density of HF1, back-wrapping method is believed to be a good opening edge treatment used in EPS ETICS building. Effects of EPS thickness on EPS ETICS façade reaction-to-fire performance is reported. It is also observed that average  $S_a/S_b$  of EPS ETICS specimen with back-wrapping opening edge treatment approaches 3.058. This ratio is believed to be useful for EPS ETICS building rehabilitation after window spreading fire. The time (20 min) averaged temperature of T1 to T5 versus EPS thickness is nearly linear regarding the same heating intensity 300 kW or 600 kW when the EPS thickness differs between 50 mm and 300 mm.



#### **4.3.4 Experimental study of EPS ETICS Masonry façade reaction-to-fire**

##### **performance: A fire risk evaluation method**

External Thermal Insulation Composite Systems (ETICS) are used in buildings since the decades due to its thermal advantages, low cost and ease of application. The principal design of an ETICS includes wall construction, insulation material, cement bound mortar with reinforcement, rendering, and fixation by dowels and mortar. The Television Cultural Center (TVCC) ETICS fire (core material: Extruded Polystyrene (XPS) foam) burned at night on February 9, 2009. Residential Building ETICS Fire (core material: polyurethane (PU) foam) happened on November 15, 2010, killed 58 residences and injured 71. The attention on ETICS fire was increased sharply after the serious exterior cladding (core material: polyethylene foam) fire happened in London on June 14, 2017. EPS is believed to be one of the common thermal insulation thermoplastic polymers acted as outside of façade. When EPS foam exposed to heat, melt-drip results in a serious fire in both upward and downward direction. Furthermore, the fire extinguisher from outside is very hard to put out core material fire. Therefore, a suitable evaluation method for EPS ETICS reaction-to-fire performance is necessary and urgent.

The main emphasis of available EPS ETICS researches are focused on probabilities of fire spread assessment <sup>[72]</sup>, fire safety of EPS ETICS during transport, construction and end use conditions <sup>[73]</sup>, fire rescue analysis of EPS ETICS <sup>[74]</sup>, fire barrier influence on EPS ETICS reaction-to-fire performance <sup>[75]</sup> and heat flux density effects on the EPS ETICS fire performance <sup>[76]</sup>. Although these studies could be useful for EPS ETICS fire performance investigation, little knowledge of influence mortar, reinforcement, EPS thickness and opening edge treatment method on the EPS ETICS reaction-to-fire performance is available. Furthermore, it is widely acknowledged that EPS ETICS consist of adhesive, EPS insulation material, cement, reinforcing mesh and finishing coat. However, some investigations are only concentrated on the

characteristics of single component fire performance, such as EPS, adhesive, polymer-modified concrete and finishing coat reaction-to-fire performance. It seems impossible to use the fire performance of a single component to evaluate EPS ETICS fire performance, which are very complicated. In our past researches, it was found that the large scale façade tests according to the ISO 13785-1 was difficult to evaluate the downward fire spread. Furthermore, in the ISO test method, the burner installed directly on the bottom of test specimens was found to be filled with resident unburnt polymer because of heavy melt-flow procedure [70]. Considering the defects of ISO 13785-1 and no clear standards in Japan, the JIS A 1310: 2015 façade fire test method has been set up and issued. Although it is clear that EPS ETICS would exhibit a complex fire performance in a fire, little knowledge of a quantitative fire risk evaluation method of EPS ETICS is available.

In this part, a series of EPS ETICS specimens varied with opening edge treatment and EPS thickness are tested according to JIS A 1310 façade fire test method by using different heating intensity from 300 kW to 1100 kW. Before each façade fire test, calibration test was firstly carried out. A quantitative evaluation method for EPS ETICS fire risk based on JIS A 1310 test results is proposed and compared with Fire propagation index (FPI) method.

#### **A) EPS ETICS façade fire test**

In JIS A 1310 façade fire test, the test specimen was vertically installed, just as shown in Fig.59 (a) and Fig.59 (b). The installations of thermocouple positions are given in Fig.59(c). Heat release rate (HRR) and total heat release rate (THR) was calculated by the common methodology Oxygen Consumption Calorimetry (OC). During OC measurement, the gas-analysis equipment was used to record oxygen concentration ranged from 0.009% to 20.9 % in every two seconds. After 20 min façade specimen test, time averaged temperature of each thermocouple position  $T_{0-3}$  (0-3 min),  $T_{0-10}$  (0-10 min) and  $T_{0-20}$  (0-20 min)

were calculated respectively. The outlook of an EPS ETICS specimen after JIS A 1310 test is shown in Fig.59 (d). EPS burn area S was obtained by a statistic method that laying a 100 mm×100 mm mesh over façade surface, just as shown in Fig.59 (e).

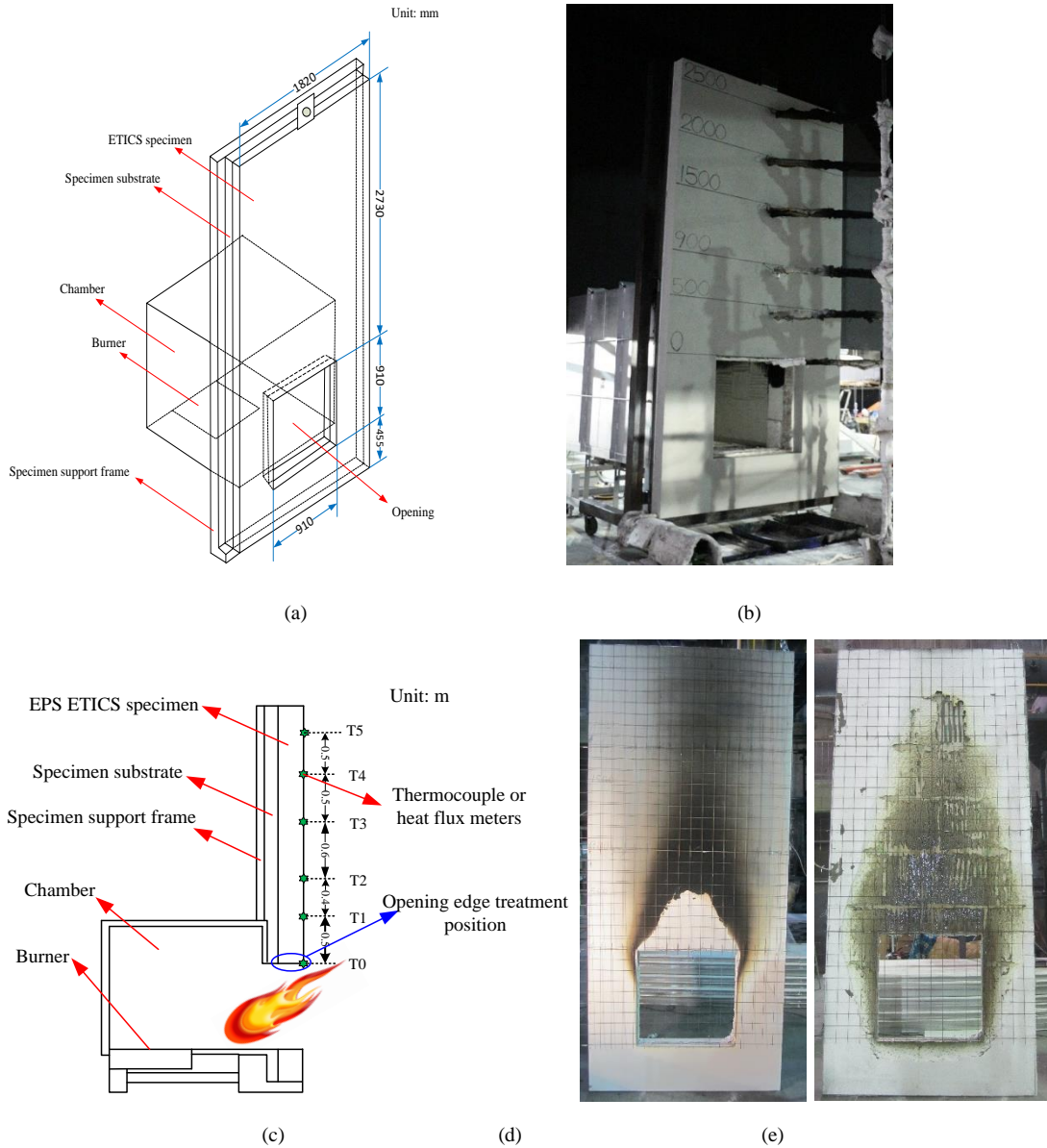


Fig.59 Experiment layout (a) a simple model of experiment (b) the experimental layout (c) thermocouples installation position description (d) the outlook of an EPS ETICS specimen after JIS A 1310 test (e) EPS burn area after removing residual mortar

## B) Chamber burner combustion coefficient of calibration test

Just as previous report shows that performance of facade cladding systems in case of a fire cannot be fully assessed by laboratory tests <sup>[66]</sup>. In Japan, JIS A 1310: 2015 facade fire test method was set up and issued. In this study, the calibration test was carried out firstly with a 25 mm thick ceramic fibers installing on a 50 mm calcium silicate panel. The 20 min calibration test was carried out by employing different heating intensity from 350 kW to 1100 kW. The THR and HRR are calculated by oxygen-consuming method during 20 min facade fire test. Chamber burner combustion coefficient of calibration test was described in Table 20. In it, theoretical THR was calculated by gas volume (L/min)/60(s)/22.4×2217.8 kJ/mol. The averaged complete combustion coefficient from 350 kW to 1100 kW is 86.3%. Although incombustible propane gas may have an effect on facade fire performance, in this study its influence is ignored because all the specimens are under the same test condition.

Table 20 Chamber burner combustion coefficient of calibration test

Heating intensity /kW	THR /MJ	pHRR /kW	Theoretical THR /MJ	Complete combustion coefficient / %
350	378.0	372.8	397.6	95.1
600	670.1	662.3	775.8	86.4
650	754.4	703.9	855.4	88.2
850	959.6	956.0	1174.4	81.7
900	1056.4	1021.4	1333.8	79.2
950	1111.4	1057.3	1254.0	88.6
1100	1334.8	1242.7	1572.9	84.9

### C) Repeatability of calibration test with heating intensity 600 kW

Repeatability of measurements is defined as the variation in repeat measurements performed on the same subject and tested conditions <sup>[77]</sup>. It means that variability in large-scale measurements performed on the

same subject and tested conditions in a repeatability study could be the errors because of the measurement process itself. In fire research, the repeatability and reproducibility of fire tests are important [78]. For example, it has reported that regarding the peak heat release rate, a cone calorimeter round robin resulted in 17 % and 23 % of repeatability and reproducibility, respectively [79]. With an aim to clarify the repeatability of the calibration test, the calibration tests are carried out in four different time with the same test condition within two years. The repeatability test NO.1, NO.2, NO.3 and NO.4 were conducted in the January of first year, August of first year, January of second year, August of second year, respectively. Detailed experimental condition is shown in the table 21, which includes atmosphere pressure, ambient temperature, humidity, and vapor partial pressure. The **INDEX** value in table 21 was calculated by the method. The standard deviation error of repeatability test could be calculated by the following equation:

$$\sigma_{repeatability} = \sqrt{\frac{\sum_{i=1}^n (x_i - \bar{x})^2}{n - 1}}$$

Where  $\sigma_{repeatability}$  is the standard deviation error of repeatability test;  $x_i$  is value of each sample;  $\bar{x}$  is the average value of all the samples; n is number of sample. By calculation,  $\sigma$  is 0.017. Furthermore, it was also found that high humidity has a decrease effect on the **INDEX** value, just as comparison of NO.2 and NO.3 with NO.1 and NO.4. When the humidity is high, **INDEX** value of NO.2 (humidity 71%) and NO.3 (humidity 60%) are 3.9 % and 4.4 % lower than average value.

Table 21 Repeatability test results of heating intensity 600 kW

Test	<b>INDEX</b> value	Atmosphere pressure /hpa	Ambient temperature /°C	Humidity /%	vapor partial pressure / hpa
NO.1	0.346	1021.8	10.1	57	7.0
NO.2	0.324	1011.6	28.2	71	28.0
NO.3	0.322	1017.2	6.9	60	6.0
NO.4	0.357	1012.5	22.9	49	7.3

#### D) Fire risk evaluation of EPS ETICS based on JIS A 1310 façade fire test

It is known that HRR is hard to evaluate the fire risk of EPS ETICS varying EPS thickness. Considering that the downward and upward fire spreading was observed during JIS A 1310 façade fire test, the fire risk evaluation based on EPS burn area and façade surface temperature profiles is proposed by the following:

$$\text{INDEX} = \frac{S_{\text{EPS}}}{6.64} \times 0.2 + T_1 \times 0.3 + T_2 \times 0.2 + T_3 \times 0.1 + T_4 \times 0.1 + T_5 \times 0.1$$

Where  $T_n = \left( \frac{T_{0-3}}{800} + \frac{T_{0-10}}{700} + \frac{T_{0-20}}{600} \right) / 3$ ;  $T_{0-3}$  means the average temperature from 0 min to 3 min during 20 min façade fire test;  $T_{0-10}$  means the average temperature from 0 min to 10 min during 20 min façade fire test;  $T_{0-20}$  means the average temperature from 0 min to 20 min during 20 min façade fire test.

#### E) Effects of opening edge treatment on INDEX

A series of EPS ETICS specimens were tested with JIS A 1310 façade fire test method. The tests differed from heating intensity, mortar component, EPS thickness, cement thickness, reinforcement and opening edge treatment method. The **INDEX** values based on test results are shown in table 22. The **INDEX** value varying a series of different specimens and heating intensities is described in Fig.60. Before testing specimen, calibration tests varying with heating intensity from 100 kW to 1100 kW were carried out firstly, just as described from NO.1 to NO.10 of table 22. Opening edge treatment method effects on the **INDEX** values was discussed by conducting test from NO.11 to NO.19. Test NO.23, NO.16, NO.24, NO.26, NO.11, NO.22, NO.20, NO.18, NO.25 and NO.27 are used to disclose influence of heating intensity on the **INDEX** values. Test NO.32, NO.33, NO.34, NO.36, NO.35, NO.11, NO.20, NO.21, NO.23, NO.22, NO.16, NO.18, NO.24, NO.25, NO.26 and NO.27 are employed to clarify the EPS thickness effects on the **INDEX** values. Test NO.16, NO.28, NO.18, NO.29, NO.26, NO.34, NO.27 and NO.36 are used to describe the influence of mortar types on the **INDEX** values. The reinforcement method is shown by compared NO.30 with NO.22.

The FPI is in the unit of  $(m/s^{1/2})/(kW/m)^{2/3}$ .

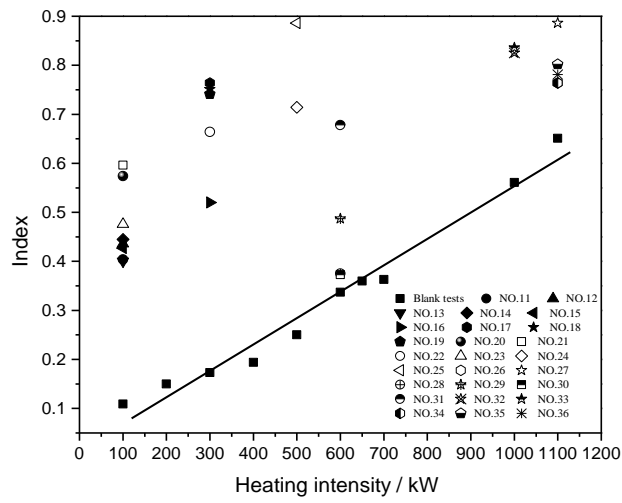


Fig.60 INDEX value varying a series of different specimens and heating intensities

Table 22 Test results varying a series of specimens

NO.	Heating intensity /kW	EPS density / kg/m <sup>3</sup>	EPS thickness /mm	Mortar component (2mm)	Cement thickness /mm	reinforce ment	Opening edge treatment method	FPI	INDEX value	Pass /Fail
1	100								0.109	
2	200								0.15	
3	300								0.173	
4	400			Calibration test without combustible façade					0.194	
5	500								0.250	
6	600								0.337	
7	650								0.36	
8	700								0.363	
9	1000								0.561	
10	1100								0.651	
11	300	15	50	SBR	1	One layer	Back-wrapping method	13.5	0.404	
12	300	15	50	SBR	1	One layer	Stick method	13.5	0.436	

13	300	15	50	SBR	1	One layer	EPS exposed without treatment method	13.5	0.400	
14	300	15	50	SBR	1	One layer	Stick+ rock wool (0.06 m) method	13.5	0.445	
15	300	15	50	SBR	1	One layer	Stick+ rock wool (0 m) method	13.5	0.427	
16	600	15	100	SBR	1	One layer	Back-wrapping method	17.3	0.667	
17	600	15	100	SBR	1	One layer	Stick method	17.3	0.764	
18	600	15	200	SBR	1	One layer	Back-wrapping method	20.9	0.741	
19	600	15	200	SBR	1	One layer	Stick method	20.9	0.751	
20	300	15	200	SBR	1	One layer	Back-wrapping method	20.9	0.574	
21	300	15	300	SBR	1	One layer	Back-wrapping method	17.4	0.596	
22	600	15	50	SBR	1	One layer	Back-wrapping method	13.5	0.664	
23	300	15	100	SBR	1	One layer	Back-wrapping method	17.3	0.476	
24	900	15	100	SBR	1	One layer	Back-wrapping method	17.3	0.714	Pass
25	900	15	200	SBR	1	One layer	Back-wrapping method	20.9	0.886	Fail
26	1100	15	100	SBR	1	One layer	Back-wrapping method	17.3	0.774	
27	1100	15	200	SBR	1	One layer	Back-wrapping method	20.9	0.886	
28	600	15	100	Acrylic resin	1	One layer	Back-wrapping method	18.5	0.375	
29	600	15	200	Acrylic resin	1	One layer	Stick+ rock wool (0 m) method	22.4	0.487	
30	600	15	50	SBR,(4mm )	2	Two layer	Back-wrapping method	11.5	0.373	



31	600	18	200	Acrylic resin	1	One layer	Back-wrapping method	21.4	0.678	
32	1000	18	100	Acrylic resin	1	One layer	Back-wrapping method	20.0	0.825	Pass
33	1000	18	200	Acrylic resin	1	One layer	Back-wrapping method	21.4	0.836	Fail
34	1100	15	100	Acrylic resin	1	One layer	Back-wrapping method	18.5	0.764	
35	1100	15	150	Acrylic resin	1	One layer	Back-wrapping method	20.9	0.802	
36	1100	15	200	Acrylic resin	1	One layer	Back-wrapping method	22.4	0.781	

Comparison of different opening edge treatment methods is shown in Fig.61. It is well known that opening edge treatment method plays an important role in the prevention of façade fire caused by window fire. There are four types of opening edge treatment methods used widely in EPS ETICS façade. The test NO.13 was used as a control group. With respect to EPS thickness=50 mm and heating intensity=300 kW, the lowest **INDEX** value 0.400 is from test NO.13. During test NO.13, it was observed that EPS was ignited at 104 s and the substantial EPS molten accompanying with combustion and pyrolysis dropped down at 162 s. The serious combustion is ascribed to EPS molten dropping out from a space created by reinforcing mesh departed from specimen substrate panel. It could make a contribution for a low **INDEX** value. The traditional edge treatment method of EPS ETICS is stick (Test NO.12). Considering that EPS molten is easy to cause downward fire spread, the reinforcing mesh made of fire glass fiber is wrapped back to reduce EPS molten dropped down. This idea is realized by the back-wrapping method. It is found that back-wrapping method (Test NO.11) could reduce 7.9 % of **INDEX** value than it from stick method (Test NO.12). Regarding test NO.12 performed stick method, the serious combustion appeared at t=177 s and lasts for nearly 655 s. When test time approaching 1185 s, the combustion become weak. Furthermore, a weak combustion was observed during test NO.11 performed back-wrapping method. It is verified by low peak

temperature and time (20 min) averaged temperature during façade fire test. The weak combustion started from  $t=120$  s and lasted for nearly all the test time. Compared with **INDEX** value of test NO.11, installing of fire barrier is believed to increase 10.1% and 5.6 % of **INDEX** value, which are shown in test NO.14 and test NO.15. During test NO.14, a serious combustion started from 180 s and became weak at 960 s. In test NO.15, the serious combustion formed at about 480 s then became weak at 960 s. Regarding EPS ETICS performed with 100 mm EPS, the **INDEX** of test NO.17 (stick method) is 14.5 % higher than **INDEX** of test NO.16 (back-wrapping method). With respect to EPS ETICS performed with 200 mm EPS, the **INDEX** of test NO.19 (stick method) is 1.3 % higher than **INDEX** of test NO.18 (back-wrapping method). Based on the above discussion, EPS ETICS specimen test performed back-wrapping method has the low **INDEX** value.

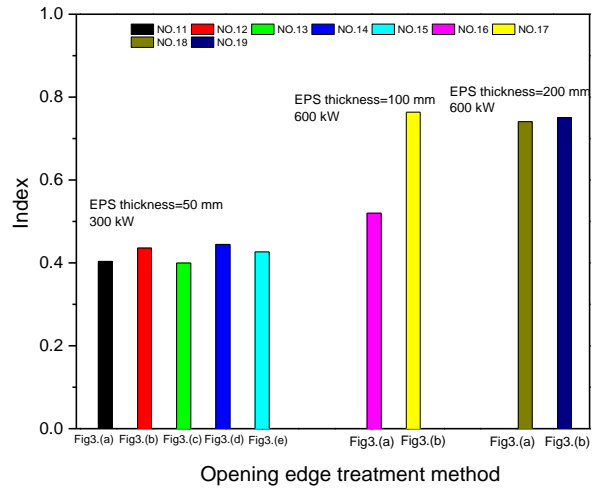


Fig.61 INDEX value varying different opening edge treatment methods

**F) Effects of heating intensity, EPS thickness, mortar and reinforcement on INDEX calculation**

The influence of heating intensity on **INDEX** value is described in Fig.62. The heating intensity varies 300 kW to 1100 kW and EPS thickness differs from 50 mm to 200 mm. As for ETICS performed with the same EPS thickness, the **INDEX** value increases as the heating intensity changes from 300 kW to 1100 kW.

The relationship between EPS thickness, heating intensity and **INDEX** values is disclosed in Fig.63. It is found that the **INDEX** value versus EPS thickness used in EPS ETICS is linear with the same heating intensity. Currently, two types of mortars are widely used in the EPS ETICS of Japan. The **INDEX** values varying with two different mortars with the same specimen are shown in Fig.64. Compared with EPS ETICS performed SBR polymer mortar, performance of Acrylic resin mortar could easily reduce the **INDEX** value. With respect to heating intensity 600 kW, the **INDEX** of EPS ETICS performed acrylic resin mortar is 43.8 % (EPS thickness=100 mm) and 34.3 % (EPS thickness=200 mm) lower than **INDEX** values of EPS ETICS performed with SBR mortar. As for high heating intensity 1100 kW, the **INDEX** of EPS ETICS performed acrylic resin mortar is 1.3 % (EPS thickness=100 mm) and 11.9 % (EPS thickness=200 mm) lower than **INDEX** values of EPS ETICS performed with SBR mortar. The reinforcement method including one layer glass fiber mesh and two layer glass fiber mesh is discussed in Fig.65. It clearly indicates that two layer's fiber mesh reinforcement method is superior to one layer's mesh since the lower **INDEX** value from the EPS ETICS performed two layer's glass fiber mesh. In summary, the **INDEX** evaluation method could be used to clarify different heating intensity, EPS thickness, polymer mortar type, and reinforcement method.

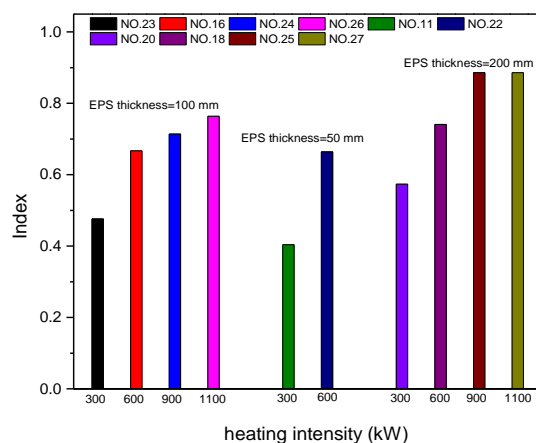


Fig.62 **INDEX** value varying different heating intensity with the same specimen

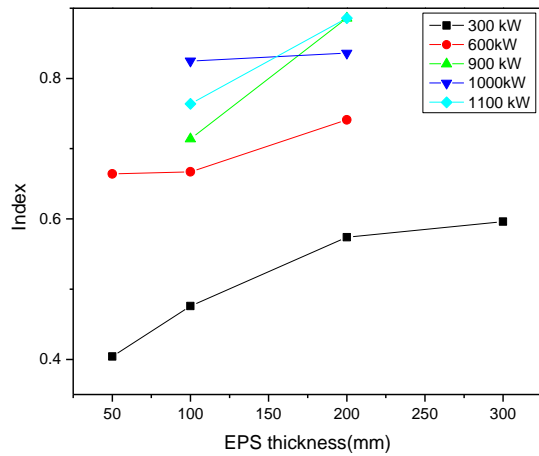


Fig.63 INDEX value varying different EPS thickness and heating intensities

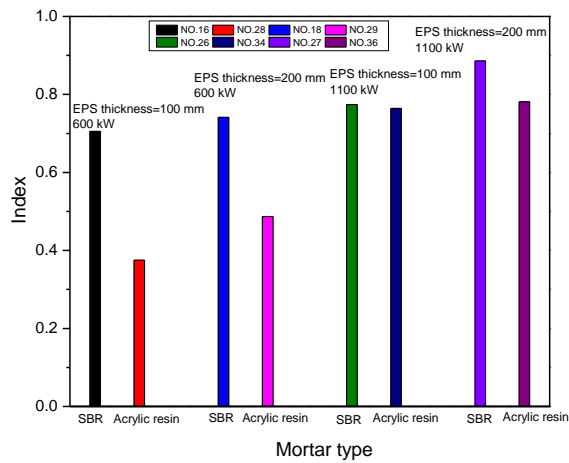


Fig.64 INDEX value varying mortar types with the same specimen

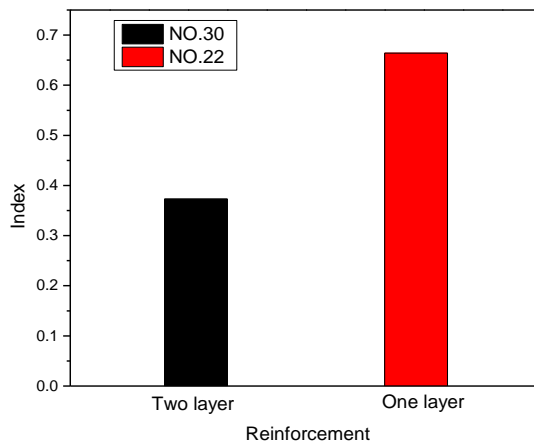


Fig.65 INDEX value varying different reinforcement methods

**G) Fire risk evaluation of EPS ETICS based on JIS A 1310 façade fire test**

Fire propagation index (**FPI**) is an important index which is used for the evaluation of fire spread. Both small-scale and large-scale fire spread test results of various materials calculated using **FPI** indicates that **FPI** could be suitable for both propagating and non-propagating<sup>[80]</sup>. In the propagating fire, no fire spread was observed beyond the ignition zone. Comparably, the fire spread rapidly beyond ignition location. The flame propagation rate in the small-scale and large-scale apparatus showed good correlation and satisfied the engineering relationships derived from the fundamental flame propagation theories. The following relationship was found for the flame propagation rate<sup>[81]</sup>.

$$u^{1/2} = \frac{\delta^{1/2} q_{fs}''}{\Delta T_{ig} \left( \frac{\pi}{4} k \rho c_p \right)^{1/2}}$$

Where  $\Delta T_{ig}$ ,  $k$ ,  $\rho$  and  $c_p$  are the ignition temperature of the polymeric material above ambient in K, thermal conductivity in kW/m/K, specific heat in kJ/kg/K, density in kg/m<sup>3</sup> of the solid, respectively.  $u$  is the upward fire propagation rate in mm/s.  $\delta$  is the characteristic forward heat transfer distance which is a constant in m.

The heat flux of flame transferred ahead of the pyrolysis front can be expressed as<sup>[82]</sup>:

$$q_{fs}'' \propto \frac{\dot{Q}_{rad}}{X_f}$$

Where  $\dot{Q}_{rad}$  stands for the radiative HRR per unit sample width in kW/m and  $X_f$  is flame height of upward fire spread in m.  $\dot{Q}_{rad}$  is expressed as:

$$\dot{Q}_{rad} = \frac{\chi_{rad}}{\chi_{ch}} \dot{Q}_{ch}$$

Where  $\dot{Q}_{ch}$  stands for chemical HRR per unit width (kW/m);  $\chi_{rad}$  is the radiative fraction of the combustion efficiency,  $\chi_{ch}$ . In general, the term  $\frac{\chi_{rad}}{\chi_{ch}}$  does not vary much between fuels and can be considered approximately constant. The flame height,  $X_f$ , is expressed as:

$$X_f \propto (\dot{Q}_{ch})^{2/3}$$

From above equations:

$$q_{fs}'' = \left( \frac{\chi_{rad}}{\chi_{ch}} \dot{Q}_{ch} \right)^{1/3}$$

Then it is got,

$$v^{1/2} = \frac{\delta^{1/2} \left( \frac{\chi_{rad}}{\chi_{ch}} \dot{Q}_{ch} \right)^{1/3}}{\Delta T_{ig} \left( \frac{\pi}{4} k \rho c_p \right)^{\frac{1}{2}}}$$

A simplified form is used in the 4910 Test Protocol where right hand side is identified as the fire propagation index (**FPI**) and Thermal Response Parameter (TRP). Thermal Response Parameter (TRP) is defined as:

$$TRP = \left( \frac{\pi}{4} k \rho c_p \right)^{\frac{1}{2}} (T_{ig} - T_0)$$

Where, k represents thermal conductivity,  $\rho$  features density and  $c_p$  indicates specific heat of the solid, respectively.  $T_{ig}$  is surface ignition temperature (K) and  $T_0$  features the ambient temperature (K). And the **FPI** calculation equation is shown in the following <sup>[13]</sup>:

$$\mathbf{FPI} = 750 \frac{\dot{Q}_{ch}^{1/3}}{TRP}$$

Where,  $\dot{Q}_{ch}$  stands for chemical HRR per unit width in the unit of kW/m. The ignition time equation could be expressed as <sup>[83]</sup>:

$$t_{ig} = \frac{\left( \frac{\pi}{4} k \rho c_p \right)^{\frac{1}{2}} (T_{ig} - T_0)}{(q_e'' - \chi q_{cr}'')^2}$$

Where incident heat flux in the unit of kW/m<sup>2</sup> is expressed by  $q_e''$ . The critical heat flux for ignition could be expressed by  $q_{cr}'$  in the unit of kW/m<sup>2</sup>.  $T_{ig}$  represents the surface ignition temperature in the unit of K, t features the test time and  $T_0$  stands for ambient temperature in the unit of K.  $\chi$  is the average heat loss as a fraction of the critical heat flux and considers it that heat losses are initially zero and increase as the solid is heated to its ignition temperature.

By calculation, the TRP of EPS (Cone (V)) is  $275.7 \text{ (kW}\cdot\text{s}^{1/2}/\text{m}^2)$  and **FPI** of EPS (Cone (V)) is  $2.5 \text{ (m/s}^{1/2})/(\text{kW/m})^{2/3}$ . TRP of EPS ETICS (Cone (V)) is  $165.9 \text{ (kW}\cdot\text{s}^{1/2}/\text{m}^2)$  and **FPI** of EPS ETICS (Cone (V)) is  $5.2 \text{ (m/s}^{1/2})/(\text{kW/m})^{2/3}$ . As for the same specimen, the pHRR of Cone (V) is much lower than it from Cone (H) although the **FPI** is the same. **FPI** of EPS (ICAL) is  $5.3 \text{ (m/s}^{1/2})/(\text{kW/m})^{2/3}$  and **FPI** of EPS ETICS (ICAL) is  $11.0 \text{ (m/s}^{1/2})/(\text{kW/m})^{2/3}$ . During test, a lot of EPS molten was observed in the bottom of specimen. It seems hard to predict EPS ETICS façade fire performance based on ICAL and Cone test results. With an aim to well understand EPS ETICS reaction-to-fire performance, the large-scale façade fire test was conducted by the JIS A 1310 method.

#### **H) The acceptable INDEX level based on JIS A 1310 method**

In the JIS A 1310 method, it is ruled that under heating intensity 1000 kW or 900 kW, if the lasting time ( $T \geq 500 \text{ }^\circ\text{C}$ ) of T4 or T5 is over 120 s, it would fail in the JIS A 1310 test. Comparably, if the lasting time ( $T \geq 500 \text{ }^\circ\text{C}$ ) of T4 or T5 is less than 120 s, it would pass the JIS A 1310 test. According to the temperature histories of test NO.24, NO.25, NO.32 and NO.33, test NO.23 and test NO.32 passed JIS A 1310 method. Test NO.25 and test NO.33 failed in JIS A 1310 method. Therefore, it is concluded that EPS ETICS specimen for which the **INDEX**  $\leq 0.825$  passes JIS A 1310 method, and EPS ETICS specimen for which the **INDEX**  $\geq 0.836$  are judged to be unacceptable. The region where the **INDEX** values are greater than 0.825 but less than 0.836 is uncertain. As for **FPI**, it could be used to classify the fire propagation risk before JIS A 1310 test. It shows that EPS ETICS specimen for which the **FPI**  $\leq 17.3$  passes JIS A 1310 method, and EPS ETICS specimen for which the **FPI**  $\geq 21.4$  are judged to be unacceptable. The region where the **INDEX** values are greater than 17.3 but less than 21.4 is uncertain.

#### **I) Summary**

In this study, the JIS A 1310 façade fire test method recently issued is employed to quantify fire risk of

EPS ETICS specimen varying heating intensity from 100 kW to 1100 kW, EPS thickness from 50 mm to 300 mm, polymer mortar type including SBR polymer mortar and acrylic resin mortar, reinforcement including one layer and two layer's glass fiber mesh, and opening edge treatment method differs from back-wrapping method to fire barrier method. During EPS ETICS façade fire tests in JIS A 1310 method, the serious both downward and upward fire spreading was observed. Comparison of different opening edge treatment methods indicates back-wrapping method could reduce the **INDEX** value. As for ETICS performed with the same EPS thickness, the **INDEX** value increases as the heating intensity changes from 300 kW to 1100 kW. It was found that the **INDEX** value versus EPS thickness used in EPS ETICS is linear with the same heating intensity. Compared with EPS ETICS performed SBR polymer mortar, Acrylic resin mortar has a low **INDEX** value. And two layer's fiber mesh reinforcement method is superior to one layer's mesh since the low **INDEX** value obtained from the EPS ETICS performed two layer's glass fiber mesh. Furthermore, a quantitative fire risk of JIS A 1310 façade fire test method is proposed on the basis of EPS burn area and façade surface temperature profiles. By testing and analyzing a series of EPS ETICS specimens, it is concluded that the **INDEX** evaluation method could easily clarify the different heating intensity, EPS thickness, polymer mortar type, reinforcement, EPS thickness and opening edge treatment method. EPS ETICS specimen for which the **INDEX**  $\leq 0.825$  or **FPI**  $\leq 17.3$  passes JIS A 1310 method, and EPS ETICS specimen for which the **INDEX**  $\geq 0.836$  or **FPI**  $\geq 21.4$  are judged to be unacceptable (i.e., Fail);  $0.825 \leq \mathbf{INDEX} \leq 0.836$  or  $17.3 \leq \mathbf{FPI} \leq 21.4$  is the critical level. Correlation between **FPI** and the **INDEX** value needs to be further verified by various façade materials.

In the current study, the chemical HRR used in FPI calculation is the peak of HRR histories, which is from the Cone test. Whether the peak is suitable or not is the subject for further study.



#### **4.3.5 Experimental study on temperature profile of an intermediate-scale window**

##### **ejected fire plume under an over-ventilated condition**

After London façade fire, which happened on June 14 of 2017, the attention over façade fire was increased sharply. Regarding the building performed with combustible façade, the flame ejected from a window of the room could be a potential ignition source. Fire performances of an intermediate-scale window ejected fire plume have received more and more attentions in the last decades. The flame heights and temperature distribution of fire plumes has been the subjects of plenty of fire research in the last decades <sup>[84-93]</sup>.

With respect to plume temperatures, the main emphasis of available researches are focused on temperature profile of an under-ventilated window ejected fire plume. Tang et al. discussed the temperature profile of an under-ventilated window ejected fire by carrying out tests which consists of a 0.8 m cubic fire compartment, a window opening varied from 0.20 m (H) × 0.30 m (W) to 0.35 m (H) × 0.35 m (W) and HRR differed from 128.3 to 244.4 kW<sup>[94]</sup>. LU et al. reported the merging behavior of two under-ventilated window ejected flames using a 0.8 m cubic fire compartment and window varied from 0.25 m (H) × 0.125 m (W) to 0.30 m (H) × 0.15 m (W) and HRR differed from 146 to 191 kW <sup>[95]</sup>. Temperature profile versus vertical distance of two thermal window ejected plumes are discussed by Lu et al employing a cubic with dimensions of 0.4 m with window opening varied from 0.20 m (H) × 0.10 m (W) to 0.10 m (H) × 0.20 m (W) and HRR differed from 39.9 kW to 48.8 kW <sup>[92]</sup>. A mathematical model about the temperature profile versus vertical distance of a window ejected fire plume was reported by using a 0.8 m cubic fire compartment with window opening varied from 0.20 m (H) × 0.30 m (W) to 0.35 m (H) × 0.35 m (W) and HRR differed from 128.3 to 244.4 kW <sup>[90]</sup>. The geometrical characteristics of externally venting flames was discussed by using a 0.60 m (L) × 0.90 m (H) × 0.60 m (W) fire compartment with window opening 0.20 m (H) × 0.50 m (W) and HRR varied from 79 kW to 233 kW <sup>[96]</sup>. Among the researches on temperature

distribution emerging from the opening of a fire compartment, the typical correlation between dimensionless temperature  $\Theta$  and vertical position  $z$  was proposed by Yokoi and recently re-examined by Lee & Delichatsios. Yokoi investigated the correlation between dimensionless temperature  $\Theta$  and vertical position under an well-ventilated condition by conducting a small-scale experiments using a 0.40 m (L)  $\times$  0.20 m (H)  $\times$  0.40 m (W) fire compartment with window opening varied from 0.10 m (H)  $\times$  0.046 m (W) to 0.10 m (H)  $\times$  0.32 m (W) (NO.7 in Yokoi's test ). Yokoi discussed correlation  $\Theta$  vs.  $\frac{z}{r_0}$  by using alcohol pan fire under a well-ventilated condition which had no clear flames in a small enclosure [84]. Therefore, the effect of flame behaviour on the Yokoi's plot was not discussed. Lee & Delichatsios re-examined the results of three Yokoi's cases and proposed a new correlation by replacing the local density  $\rho_z$  by the ambient air density  $\rho_g$  and replacing the Yokoi's length scale  $r_0$  by a new length scale  $\tilde{r}_1$  [91]. The correlation between dimensionless temperature  $\Theta$  and vertical position  $z$  in an under-ventilated condition has been reported in a large body of research, however, recently little knowledge of the correlation  $\Theta$  vs.  $\frac{z}{r_0}$  from an intermediate-scale fire compartment under an over-ventilated condition is available. In addition, flame behaviour effects on the Yokoi's plot is also unclear.

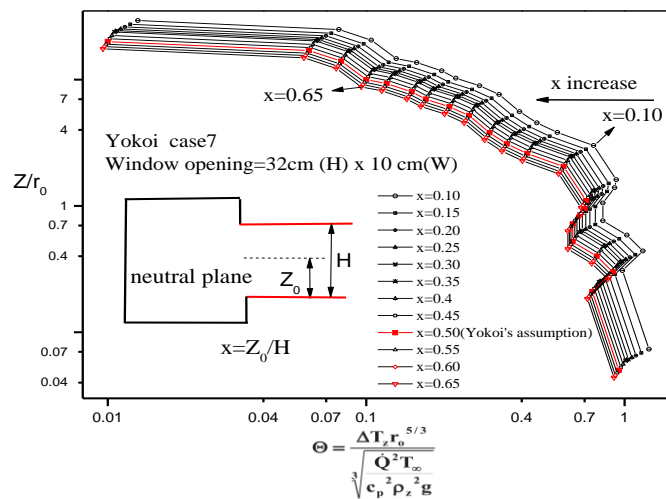


Fig.66 The effects of neutral plane height on the Yokoi's correlation was disclosed by replacing assumption 0.5H by using varied neutral plane height (case 7).

Regarding the over-ventilated fire, the neutral plane is assumed at the mid height of the window height by both Yokoi and Lee & Delichatsios. However, a stereoscopic PIV method employed by Bryant was used to investigate the velocity field distribution of window ejected fire from an ISO 9705 compartment. It was reported that the neutral plane height was observed to decrease when the inside energy release rate increases [97, 98], which was insistent with the results from results of NBSIR 82-2520 reports of National Bureau of Standard [99]. When the HRR increased from 34 kW to 511 kW, the neutral plane height reduced from 0.61H to 0.46H. According to the Yokoi's work, the length scale  $r_0 = \sqrt{\frac{WH}{2\pi}}$  was obtained on the basis of assumption that the neutral plane height was 0.5 H. Similarly, with the definition that neutral plane height is  $x$  H ( $x$  is from 0 to 1), the length scale considering varied neutral plane height could be written as  $r'_0 = \sqrt{\frac{W(1-x)H}{\pi}}$ . The effects of neutral plane height on the Yokoi's correlation was disclosed by replacing assumption 0.5H by using varied neutral plane height in Fig.66. Regarding the case 7 performed by Yokoi (assuming neutral plane height=0.5 H), the Yokoi's correlation between  $\Theta$  and  $Z/r_0$  varied apparently with the changing of neutral plane height, which was shown in Fig.66. Currently, little knowledge of the effects of neutral plane height on Yokoi's correlation under an over-ventilated condition is available.

In this part, the correlation between  $\Theta$  and  $Z/r_0$  were discussed under an over-ventilated condition by conducting a series of intermediate-scale tests with a 1.35 m (L)  $\times$  1.35 m (H)  $\times$  1.35 m (W) fire compartment with window opening varied from 0.91 m (H)  $\times$  0.41 m (W) to 0.91 m (H)  $\times$  0.91 m (W) and HRR differed from 200 kW to 1000 kW. The correlation between  $\Theta$  and  $Z/r_0$  was modified based on the test results by considering the influence of fire plume re-attaching-to-wall behaviours, varied neutral plane positions and window opening aspect n. In addition, the chamber dimension effects on the modified correlation was discussed by employing two different chambers Chamber 2 and Chamber 3.

#### A) Experiment description

Table 23 shows the test conditions description. The results are shown in the subtext. Fig.67 features the experimental temperature distribution of the opening. Fig.68 represents experimental temperature distribution of fire plume with heating intensity 300 kW, 600 kW and 900 kW. Fig.69 shows the typical temperature distribution over non-combustible wall. Fig.70 summarizes the typical heat flux density distribution over non-combustible wall. Fig.71 discloses the experimental temperature distribution vs. vertical height inside the chamber under different heating intensity.

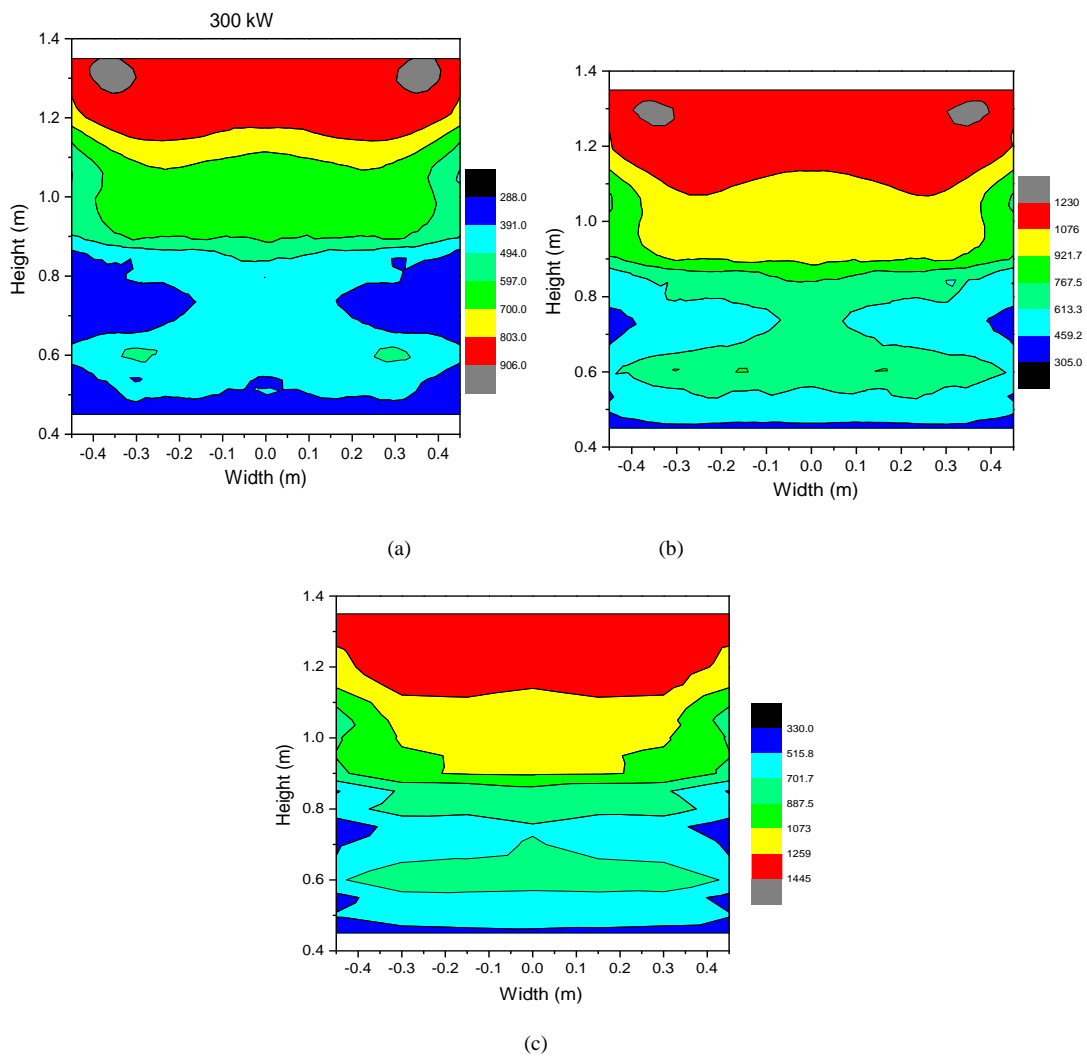


Fig.67 Temperature distribution comparison of the opening from simulation and experiment.

(a) experimental temperature distribution of the opening with heating intensity 300 kW (b) experimental temperature distribution of the opening with heating intensity 600 kW (d) experimental temperature distribution of the opening with heating intensity 900 kW

Table 23 Test conditions description

Tests	Chamber size	Opening width/mm	Opening height /mm	Opening aspect n	Heating intensity / kW
NO.1		510	910	1.12	300
NO.2		510	910	1.12	600
NO.3		710	910	1.56	300
NO.4		710	910	1.56	600
NO.5	chamber 1 (size in L × W × H = 1350 mm × 1350 mm × 1350 mm)	910	910	2.00	300
NO.6		910	910	2.00	400
NO.7		910	910	2.00	500
NO.8		910	910	2.00	600
NO.9		910	910	2.00	700
NO.10		910	910	2.00	800
NO.11		910	910	2.00	900
NO.12		910	910	2.00	1000
NO.13		910	610	2.98	300
NO.14		910	610	2.98	600
NO.15		910	410	4.44	300
NO.16		800	780	2.05	100
NO.17	chamber 2 (size in L × W × H = 900 mm × 800 mm × 780 mm)	800	780	2.05	200
NO.18		800	780	2.05	250
NO.19		800	780	2.05	300
NO.20		800	780	2.05	400
NO.21		910	910	2.00	200
NO.22	chamber 3 (size in L × W × H = 910 mm × 910 mm × 910 mm)	910	910	2.00	300
NO.23		910	910	2.00	400
NO.24		910	910	2.00	500
NO.25		910	910	2.00	600

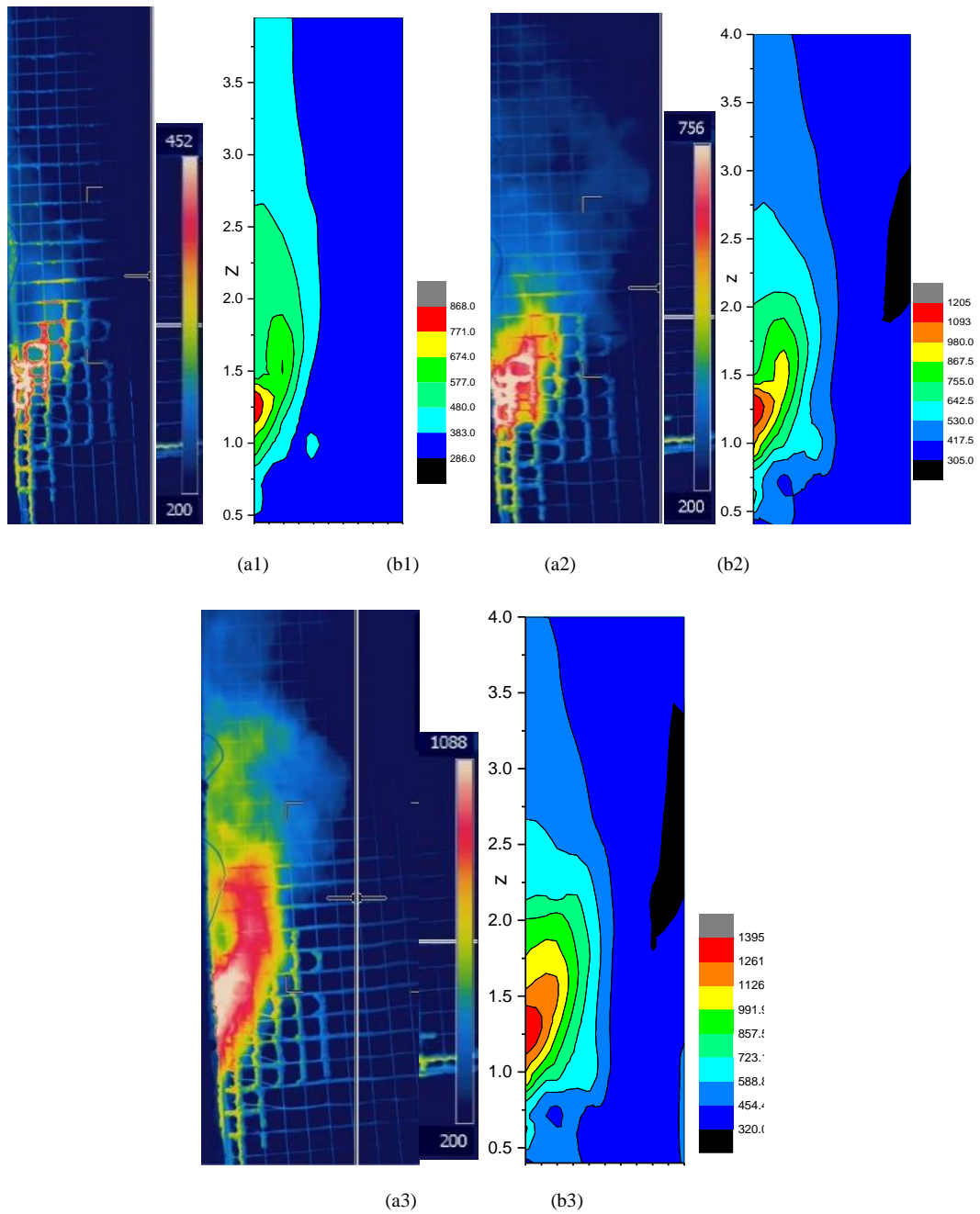


Fig.68 The temperature distribution of fire plume with heating intensity 300 kW, 600 kW and 900 kW

(a) The temperature profile from thermal camera (b) the temperature distribution from thermocouple mesh (1) heating intensity 300 kW (2) heating intensity 600 kW (3) heating intensity 900 kW

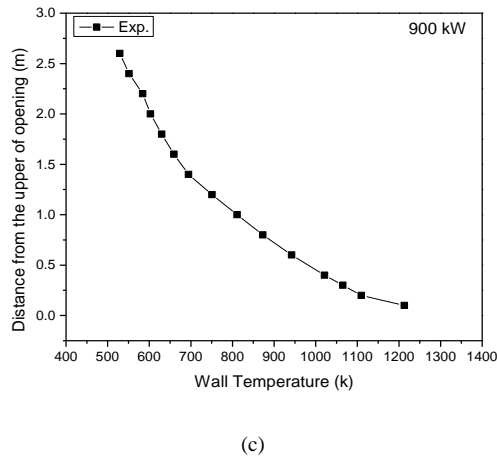
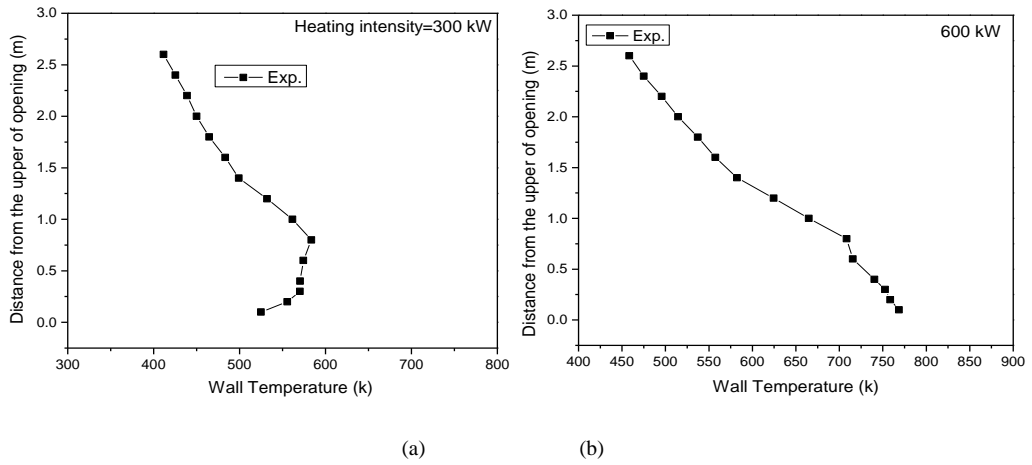


Fig.69 The typical temperature distribution over non-combustible wall

(a) Temperature profiles of 300 kW (b) temperature profiles of 600 kW (c) temperature profiles of 900 kW

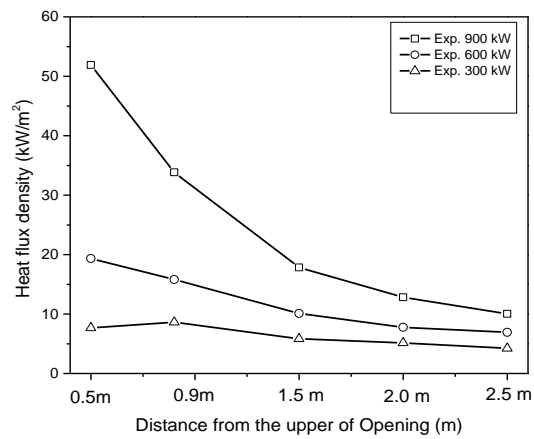


Fig.70 The comparison of typical heat flux density distribution over non-combustible wall and simulation results

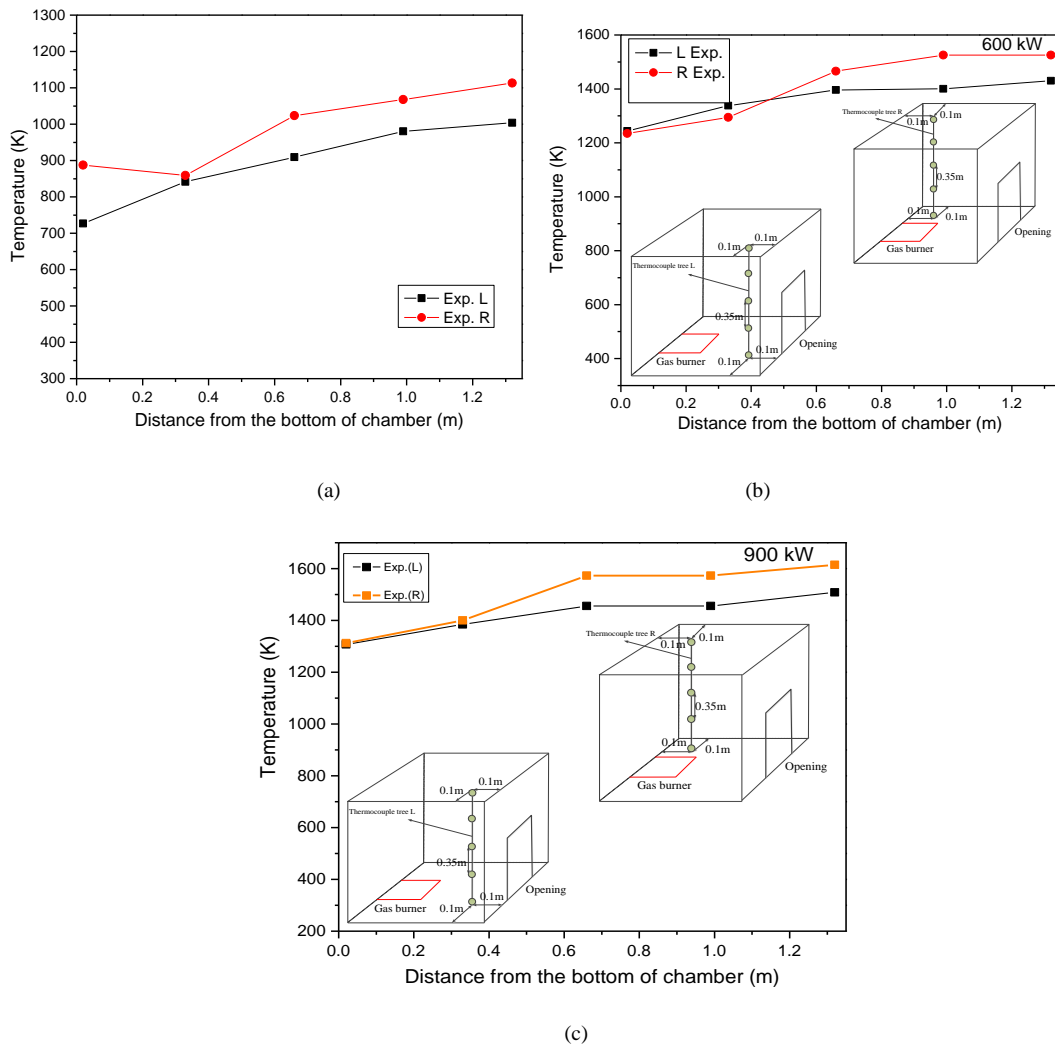


Fig.71 The temperature distribution vs. vertical height inside the chamber under different heating intensity.

- (a) Experimental thermocouple tree temperature profile (heating intensity 300 kW). (b) Experimental thermocouple tree temperature profile (heating intensity 600 kW). (c) Experimental thermocouple tree profile under heating intensity 900 kW.

## B) Chamber 2 and chamber 3

The two different chamber 2 and chamber 3 were used to discuss the effects of chamber dimension on the new correlation. Chamber 2 (Width  $\times$  Height  $\times$  Depth=800 mm  $\times$  780 mm  $\times$  900 mm) was with a 3.468 m<sup>2</sup> of inner surface area and Chamber 3 (Width  $\times$  Height  $\times$  Depth=910 $\times$ 910 $\times$ 910) was with a 4.1405 m<sup>2</sup> of inner surface area, which is shown in the Fig.72.





(a)



(b)



(c)

Fig.72 The description of chamber 1, chamber 2 and chamber 3

(a) Chamber 1 in the size of  $L \times W \times H = 1350 \text{ mm} \times 1350 \text{ mm} \times 1350 \text{ mm}$  (b) Chamber 2 in the size of  $L \times W \times H = 900 \text{ mm} \times 800 \text{ mm} \times 780 \text{ mm}$  (c) Chamber 3 in the size of  $L \times W \times H = 910 \text{ mm} \times 910 \text{ mm} \times 910 \text{ mm}$

**C) The new correlation considering fire plume re-attaching-to-wall to wall behaviors, varied**

**neutral plane and window opening aspect n**

Yokoi's correlation  $\Theta$  vs.  $\frac{z}{r_0}$  was discussed by using an alcohol pan fire under a well-ventilated condition where there was no clear flames in a small enclosure [84]. Fire plume re-attaching-to-wall effects on the Yokoi's correlation plot was unclear. After the assumption that neutral plane is defined as the half height of the opening (just as  $0.5 H$ ) and defining a length scale  $r_0 = \sqrt{\frac{WH}{2\pi}}$ , the correlation  $\Theta =$

$$\frac{\Delta T_z r_0^{5/3}}{\sqrt[3]{\dot{Q}^2 T_\infty / (c_p^2 \rho_z^2 g)}} = \text{function}\left(\frac{z}{r_0}\right)$$

was proposed. Here,  $\Theta$  is dimensionless temperature,  $\Delta T_z$  stands for the maximum temperature rise of location  $z$  ( $z=0$  located at the neutral plane),  $r_0$  is the Yokoi's length scale,  $\dot{Q}$  features the convection heat flow rate at the window,  $T_\infty$  represents the ambient temperature,  $\rho_z$  indicates the local plume density of the hot gases,  $g$  shows the acceleration due to gravity,  $z$  is the vertical distance from half the height of window,  $c_p$  is specific heat at constant pressure (usually  $c_p = 1$ ). The Yokoi's plots are usually divided into three typical regions, which are shown in Fig.73 (a). Fig.73 shows a physical interpretation of  $\Theta$  vs.  $\frac{z}{r_0}$  correlation by separating  $\Theta$  into three parts. In Regions 1 (near the exit with  $\frac{z}{r_0} < 1.5$ ) the reduction of dimensionless temperature  $\Theta$  with vertical height is small. In Regions 2 ( $1.5 \leq \frac{z}{r_0} < 10$ ), the dimensionless temperature  $\Theta$  vs.  $\frac{z}{r_0}$  is linear. In Regions 3 ( $10 \leq \frac{z}{r_0}$ ), the dimensionless temperature  $\Theta$  vs.  $\left(\frac{z}{r_0}\right)^{5/3}$  is linear. The distribution of three regions in the vertical position is described in the Fig.73 (b).

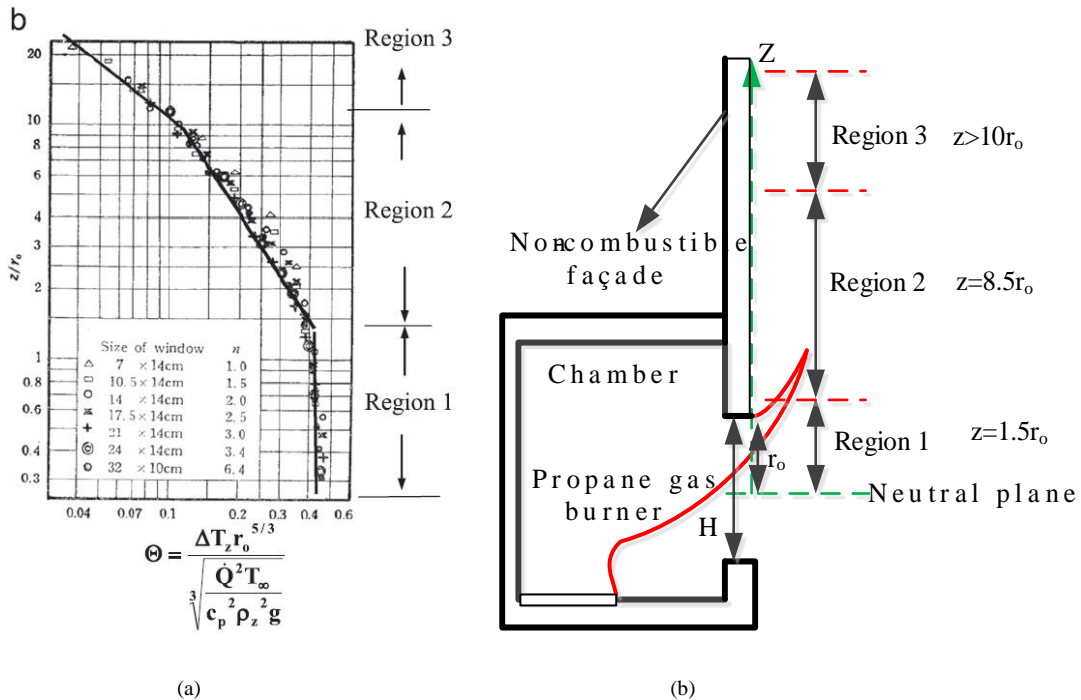


Fig.73 Temperature distributions from an window ejected fire (a) Yokoi's plot with three regions [84] (b) the distribution of three regions in the vertical position

#### D) Effects of opening aspect ( $n = \frac{2W}{H}$ ) on the Yokoi's correlation

Convective flow at the window is expressed by using Yokoi's equation with assumption that the neutral plane (N.P.) is half height of the window, the following is obtained [91]:

$$\dot{Q} = C_d c_p \rho_g \Delta T_g W \int_0^{0.5H} v dz \quad (1)$$

$C_d$  features the flow coefficient of the opening with a number of 0.7,  $c_p$  represents specific heat and  $\rho_g$  stand for density of hot gases.  $\Delta T_g$  stands for the gas temperature difference between hot layer inside the enclosure and ambient. The velocity  $v$  of outflow at height  $Z$  above the N.P. could be obtained:

$$v = \sqrt{\frac{2gZ\Delta T_g}{T_\infty}} \quad (2)$$

By inserting Eq.(2) into Eq.(1), and then integrating Eq.(2), the convective heat flow rate at the exit was got:

$$\dot{Q} = \frac{2}{3} \sqrt{2} C_d c_p \rho_g \Delta T_g W (0.5)^{3/2} H^{3/2} \sqrt{\frac{g\Delta T_g}{T_\infty}} \quad (3)$$

Finally, considering that equivalent radius  $r_0 = \sqrt{\frac{WH}{2\pi}}$  and then the dimensionless  $\Theta$  vs.  $\frac{z}{r_0}$  correlation takes the form:

$$\Theta = \frac{\Delta T_z r_0^{5/3}}{\sqrt[3]{\dot{Q}^2 T_\infty / \rho_z^2 c_p^2 g}} = 0.505 \left(\frac{\rho_z}{\rho_g}\right)^{2/3} \left(\frac{\Delta T_z}{\Delta T_g}\right) \left(2 \frac{W}{H}\right)^{1/6} = 0.505 \left(\frac{T_g}{T_z}\right)^{2/3} \left(\frac{\Delta T_z}{\Delta T_g}\right) n^{1/6} \quad (4)$$

From Eq.(6), it indicates that opening aspect  $n$  plays an important role in dimensionless temperature  $\Theta$ .

Regarding  $\frac{\rho_z}{\rho_g} = \frac{\Delta T_z}{\Delta T_g} = 1$  at the location  $z=0$ ,  $\Theta$  could be got in the form of  $\Theta = 0.505 n^{1/6}$ . It means that

Yokoi's dimensionless  $\Theta$  depends on the opening aspect  $n$ . The equation  $\frac{\Theta}{n^{1/6}} = \mathbf{constant}$  at  $z=0$  could be obtained.

#### E) Yokoi's correlation considering the varied neutral plane

It is a fact that the neutral plane usually varies with the change of HRR in the fixed test condition. It means

that assuming the neutral plane 0.5H may be inappropriate for a over-ventilated fire. Here, N.P. is at the  $xH$  ( $0 < x < 1$ ) of the opening height  $H$ , then convective flow at the window is expressed by using Yokoi's equation as:

$$\dot{Q} = C_d c_p \rho_g \Delta T_g W \int_0^{(1-x)H} v dz \quad (5)$$

Inserting Eq.(2) into Eq.(5) and integrating Eq.(5), at the exit, the convective heat flow rate becomes:

$$\dot{Q} = \frac{2}{3} \sqrt{2} C_d c_p \rho_g \Delta T_g W (1-x)^{3/2} H^{3/2} \sqrt{\frac{g \Delta T_g}{T_\infty}} \quad (6)$$

Using the new equivalent radius  $r'_0 = \sqrt{\frac{W(1-x)H}{\pi}}$  and Eq.(7), then the dimensionless temperature  $\Theta$  takes

the form:

$$\frac{\Delta T_z r'_0{}^{5/3}}{\sqrt[3]{\dot{Q}^2 T_\infty / \rho_z^2 c_p^2 g}} = 0.4528 \frac{1}{(1-x)^{1/6}} \left(\frac{T_g}{T_z}\right)^{2/3} \left(\frac{\Delta T_z}{\Delta T_g}\right) n^{1/6} = \text{function}\left(\frac{z}{r'_0}\right) \quad (8)$$

With an aim to increase the continuity of plot and to ignore the influence of opening aspect  $n$ , the new correlation Eq.(8) is derived as the following:

$$\Theta' = \frac{\Delta T_z r'_0{}^{5/3}}{\sqrt[3]{\dot{Q}^2 T_\infty / \rho_z^2 c_p^2 g \times n^6}} = \frac{0.4528}{(1-x)^{1/6}} \left(\frac{T_g}{T_z}\right)^{2/3} \left(\frac{\Delta T_z}{\Delta T_g}\right) = \text{function}\left(\frac{z}{r'_0}\right) \quad (9)$$

Where the N.P. is at the height of  $xH$ .

## F) The calculation methods of neutral plane $xH$

Fig.74 sketches the standard flow conditions in a rectangular (cubic-like) enclosure for steady-state post-flashover fires including the location of the neutral plane. The temperature inside the enclosure is the same everywhere. From the geometry, we get:

$$z_h + z_0 = H \quad (10)$$

From the conservation of mass, the flows in and out of the enclosure could be written in the followings

[100]:

$$\dot{m}_g = \frac{2}{3} C_d W \rho_g \sqrt{\frac{2(\rho_a - \rho_g)g}{\rho_g}} z_0^{3/2} \quad (11)$$

$$\dot{m}_a = \frac{2}{3} C_d W \rho_a \sqrt{\frac{2(\rho_a - \rho_g)g}{\rho_a}} z_h^{3/2} \quad (12)$$

$$\dot{m}_g = \dot{m}_a + \dot{m}_T \quad (13)$$

Substituting Eq. (12) and Eq. (11) into Eq. (10) and using Eq. (13), the following is obtained:

$$\frac{z_h}{z_0} = \left(\frac{\rho_a}{\rho_g}\right)^{1/3} \left(1 + \frac{\dot{m}_T}{\dot{m}_a}\right)^{2/3} \quad (14)$$

By using Eq. (10), it is got:

$$z_0 = \frac{H}{1 + \left(\frac{\rho_a}{\rho_g}\right)^{1/3} \left(1 + \frac{\dot{m}_T}{\dot{m}_a}\right)^{2/3}} \quad (15)$$

Where,  $\dot{m}_a$  features air inflow mass rate,  $\dot{m}_T$  stands for mass pyrolysis rate,  $H_0$  height of the opening,  $\rho_a$  density of ambient air,  $\rho_g$  density of gas inside the enclosure. The neutral plane (x H) could be decided by the following Eq. (16):

$$x = \frac{z_0}{H} = \frac{1}{1 + \left(\frac{\rho_a}{\rho_g}\right)^{1/3} \left(1 + \frac{\dot{m}_T}{\dot{m}_a}\right)^{2/3}} \quad (16)$$

Considering that the  $\rho_a = \frac{353}{T_a}$  and  $\rho_g = \frac{353}{T_g}$ , Eq. (16) could be rearranged into the following:

$$x = \frac{z_0}{H} = \frac{1}{1 + \left(\frac{T_g}{T_a}\right)^{1/3} \left(1 + \frac{\dot{m}_T}{\dot{m}_a}\right)^{2/3}} \quad (17)$$

From Eq. (17), it indicates that the neutral plane primarily depends on  $T_g$ ,  $\dot{m}_T$  and  $\dot{m}_a$ .

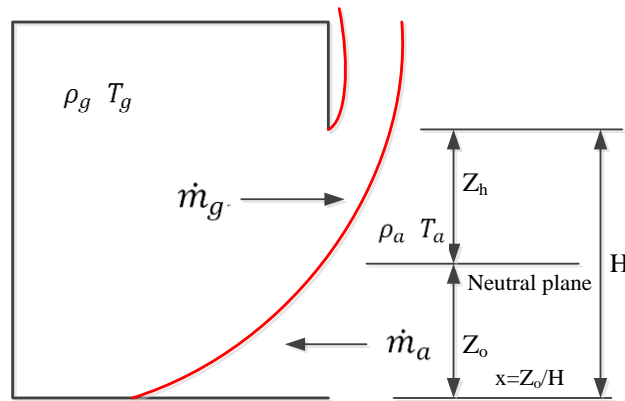


Fig.74 Sketch of flow condition in a rectangular (cubic-like) enclosure at post-flashover condition including the location of neutral plane [101].

◆Eq. (17) for under-ventilated fire

Experiments in ventilation-controlled fires inside rectangular cubic-like enclosures support that the burning rate versus mass rate of the air inflow could be expressed as the following equation <sup>[101]</sup>:  $\dot{m}_a = 0.50A\sqrt{H} - 0.50\dot{m}_T$ . Then Eq. (17) could be derived in the form:  $x = \frac{z_0}{H} = \frac{1}{1+(\frac{T_g}{T_a})^{1/3}(\frac{A\sqrt{H}}{\dot{m}_a}-1)^{2/3}}$  (18).

For under-ventilated conditions, the mass flow rate of inflow air from the opening could be given in the form of  $\dot{m}_a = 0.5A\sqrt{H}$  <sup>[102]</sup>. Then x could be calculated by  $x = \frac{z_0}{H} = \frac{1}{1+(\frac{T_g}{T_a})^{1/3}}$ .

◆Eq. (17) for over-ventilated fire

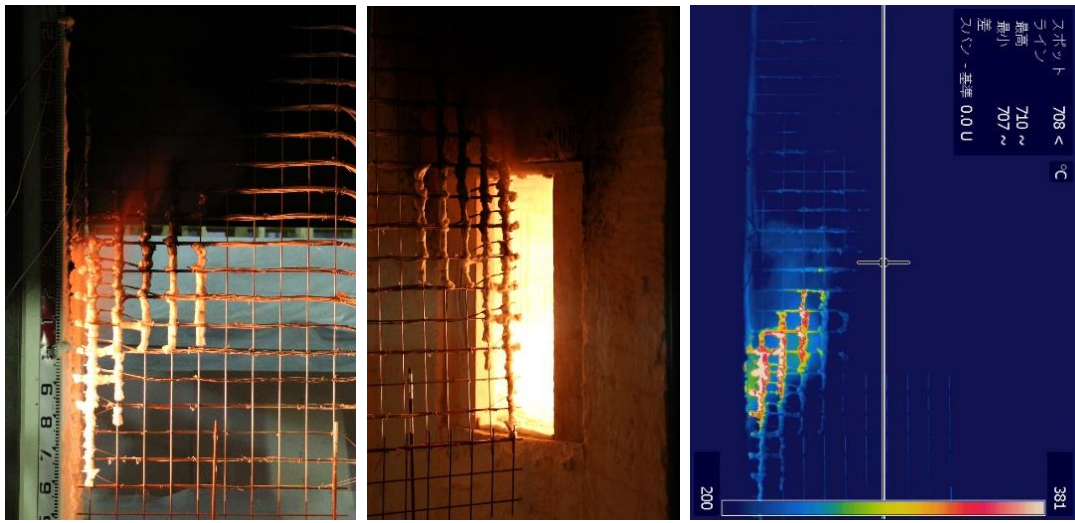
With respect to over ventilation condition, the HRR is independent of inflow of air, but heavily depend on the supply of propane gas. The neutral plane depends on the  $\dot{m}_T$  mass pyrolysis rate in kg/s and  $\dot{m}_a$  mass rate of air inflow in kg/s, and  $T_g$ . The propane combustion inside the chamber is believed to be stoichiometric under an over-ventilated condition. Regarding  $\dot{m}_a$ , it is assumed that all oxygen of inflow air was consumed by propane combustion, which is controlled by the stoichiometric coefficient. As for propane gas,  $\frac{\dot{m}_T}{\dot{m}_a} = \frac{1}{15.66} = 0.064$ . Finally, the neutral plane in the over-ventilated fire could be decided by

$$x = \frac{z_0}{H} = \frac{1}{1+1.04(\frac{T_g}{T_a})^{1/3}}.$$

### G) Comparison of Yokoi's and new correlation

The description of fire plume shape using chamber 1 with n=1.12, n=1.56, n=2.00, n=2.98 and n=4.44 are shown in Fig.75, Fig.76, Fig.77, Fig.78 and Fig.79, respectively. The side and front view of fire plume and the side view of fire plume by a thermal camera are used to show the flame behavior at a fixed heating intensity. The none-flame fire plume was observed at n=1.12-300 kW, n=1.56-300 kW and n=2.00-300 kW, which are disclosed in Fig.75, Fig.76 and Fig.77. Furthermore, the none-flame fire plume re-attaching-to-wall was found in the side view of fire plume using a thermal camera from Fig.75, Fig.76 and Fig.77. The

comparison of Yokoi and new correlation based on the test results is shown in Fig.80. Fig.80 (a) is the original Yokoi's plot. Fig.80 (b) is the new correlation plot of a strong fire plume (test NO.2, NO.4, NO.6, NO.7, NO.8, NO.9, NO.10, NO.11, NO.12, NO.13, NO.14, NO.15). Fig.80 (c) gives the correlation plot of a none-flame fire plume and with re-attaching-to-wall behaviors (test NO.1, NO.3 and NO.5). Considering that the fire plume re-attaching-to-wall behavior showed a heavy effect on the new correlation plot, here, the new correlation  $\theta'$  vs.  $\frac{z}{r_0}$  was divided into two type of plots consisting of the none-flame fire plume ejected from window and the fire plume with flames spilled out of window. As for the none-flame fire plume,  $\theta'$  vs.  $\frac{z}{r_0}$  is linear in the form of  $\frac{z}{r_0} = 6.86\theta' - 1.37$  in the region 1 with  $\frac{z}{r_0} \leq 1.5$ . In the region 2 ( $10 \geq \frac{z}{r_0} > 1.5$ ), the discontinuity was believed to be attributed to the fire plume re-attaching to wall effect, which disagrees with Yokoi's theory that the dimensionless temperature  $\theta$  vs.  $\frac{z}{r_0}$  is linear. The position of peaks a, b and c in Fig.80 (c) is inferred to have relationship with opening aspect n at the same heating intensity. The  $\theta'$  values of peaks a (n=1.12), b (n=1.56) and c (n=2.00) are 0.154, 0.182 and 0.265, respectively. Therefore, fire plume re-attaching-to-wall should not ignored when discussing the temperature profile of a none-flame fire plume. Regarding the fire plume with flames, it indicates that the continuity of new correlation  $\theta'$  vs.  $\frac{z}{r_0}$  shows a better continuity than Yokoi's plots in the region 1 with  $\frac{z}{r_0} \leq 1.5$ . The correlation  $\theta'$  vs.  $\frac{z}{r_0}$  is linear in the form of  $\frac{z}{r_0} = 10.24\theta' - 3.17$  with  $\frac{z}{r_0} \leq 1.5$  and  $\frac{z}{r_0} = -30.47\theta' + 15.26$  with  $10 \geq \frac{z}{r_0} > 1.5$ .



Chamber1-n=1.12-300 kW (a)

(b)

(c)



Chamber1-n=1.12-600 kW (a)

(b)

(c)

Fig.75 The description of fire plume shape using chamber 1 with n=1.12

(a) The side view of fire plume (b) The front view of fire plume (c) The side view of fire plume using a thermal camera





Chamber1-n=1.56-300 kW (a)

(b)

(c)



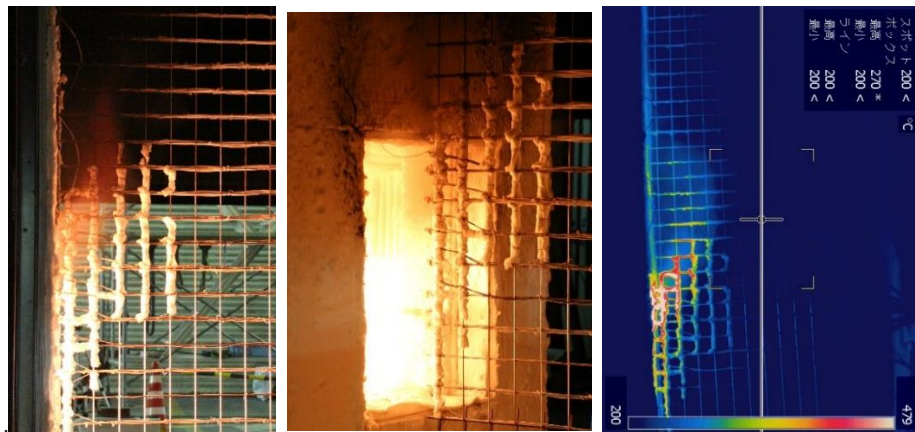
Chamber1-n=1.56-600 kW (a)

(b)

(c)

Fig.76 The description of fire plume shape using chamber 1 with n=1.56

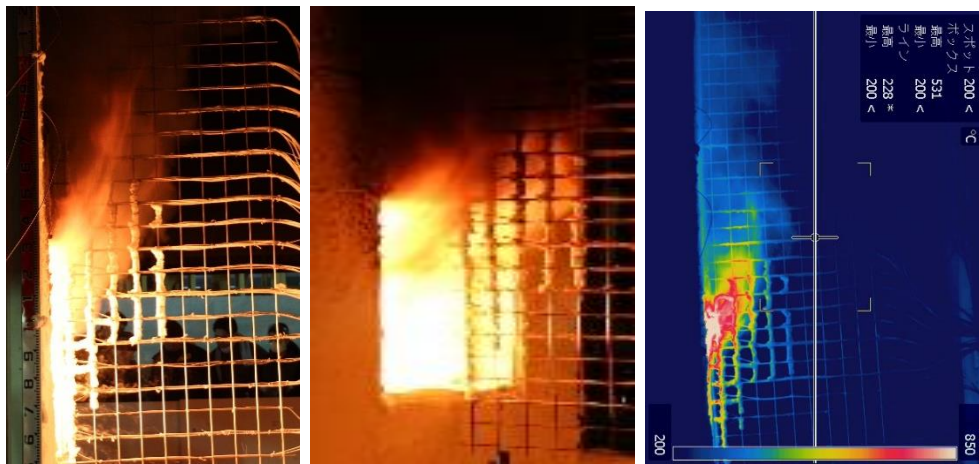
(a) The side view of fire plume (b) The front view of fire plume (c) The side view of fire plume using a thermal camera



Chamber1-n=2.00-300 kW (a)

(b)

(c)



Chamber1-n=2.00-600 kW (a)

(b)

(c)



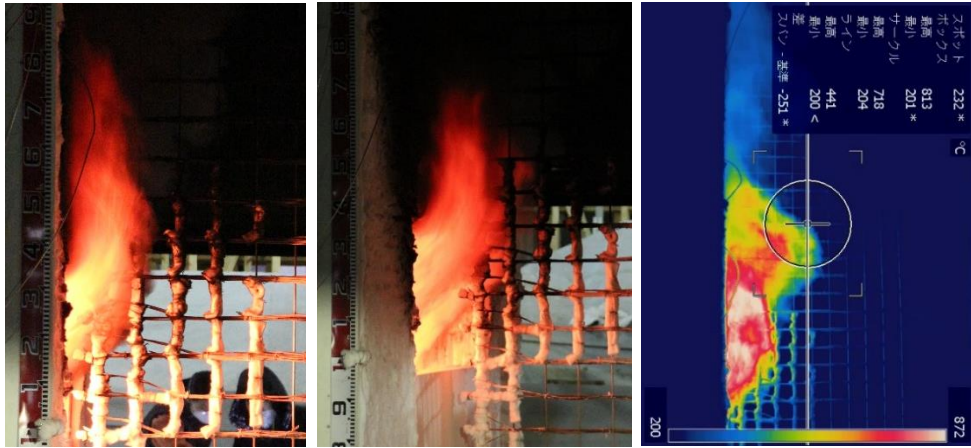
Chamber1-n=2.00-900 kW (a)

(b)

(c)

Fig.77 The description of fire plume shape using chamber 1 with n=2.00

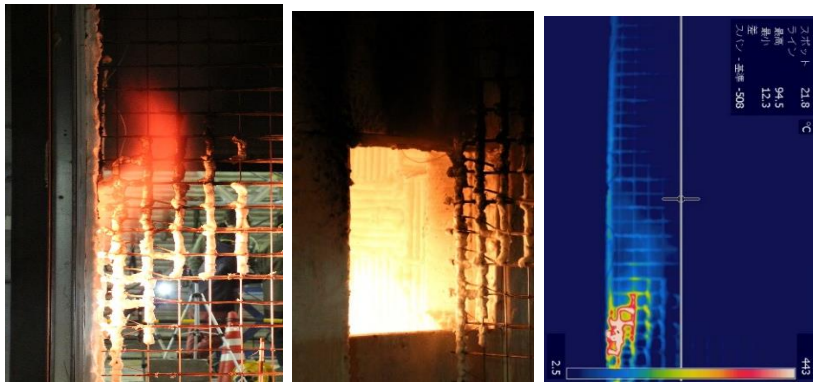
(a) The side view of fire plume (b) The front view of fire plume (c) The side view of fire plume using a thermal camera



Chamber1-n=4.44-300 kW (a) (b) (c)

Fig.78 The description of fire plume shape using chamber 1 with n=4.44

(a) The side view of fire plume (b) The front view of fire plume (c) The side view of fire plume using a thermal camera



Chamber1-n=2.98-300 kW (a) (b) (c)

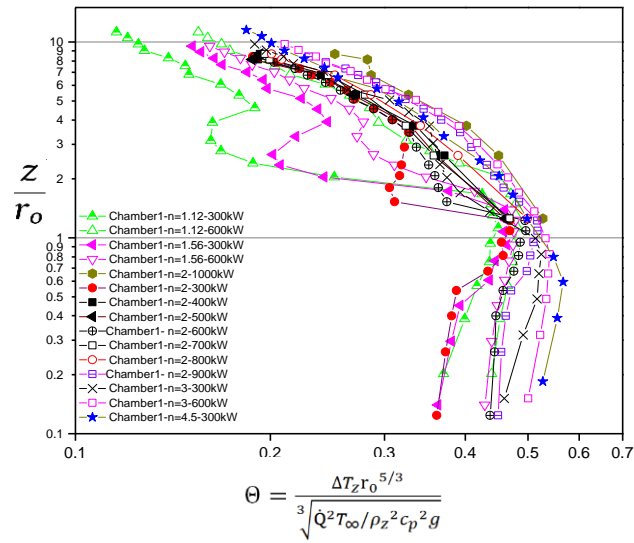


Chamber1-n=2.98-600 kW (a) (b) (c)

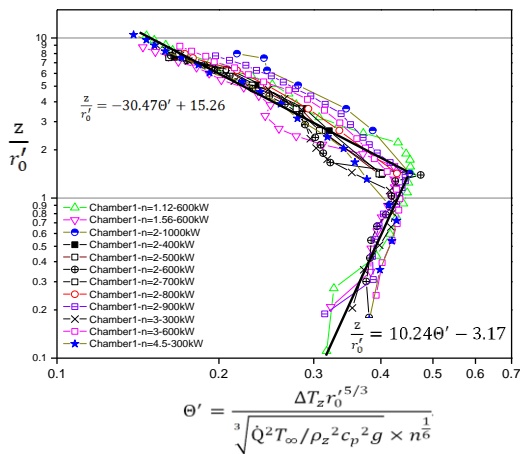
Fig.79 The description of fire plume shape using chamber 1 with n=2.98

(a) The side view of fire plume (b) The front view of fire plume (c) The side view of fire plume using a thermal camera

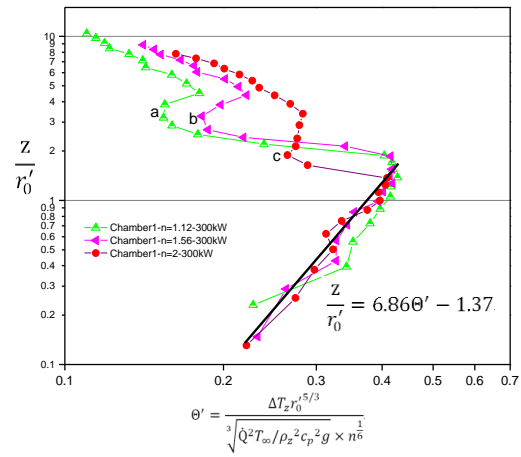




(a)



(b)



(c)

Fig.80 Comparison of Yokoi's plot and new correlation. (a)The original Yokoi's plot based on the test results (b) the new correlation plot of a strong fire plume(c) The new correlation plot of a non-flame fire plume.

## H) Chamber's dimension effects on the new correlation plot

With an aim to clarify the chamber dimension effects on the new correlation, a series of tests using chamber 2 and chamber 3 were conducted. The burner was the same with the chamber 1. The description

of fire plume shape using chamber 2 with  $n=2.05$  and heating intensity differed from 100 kW to 400 kW is shown in Fig.81 (test NO.16, NO.17, NO.18, NO.19 and NO.20). The description of fire plume shape using chamber 3 with  $n=2.00$  and heating intensity differed from 200 kW to 600 kW is shown in Fig.82 (test NO.21, NO.22, NO.23, NO.24 and NO.25). From the side view and front view of fire plume, the fire plume with flames were observed in these tests. The new correlation plots of  $\theta'$  vs.  $\frac{z}{r_0}$  from chamber 2 and chamber 3 are disclosed in Fig.83. The results described in Fig.83 showed that chamber dimension has no clear effects on new correlation plot when  $\frac{z}{r_0}$  varies from 1.5 to 10.

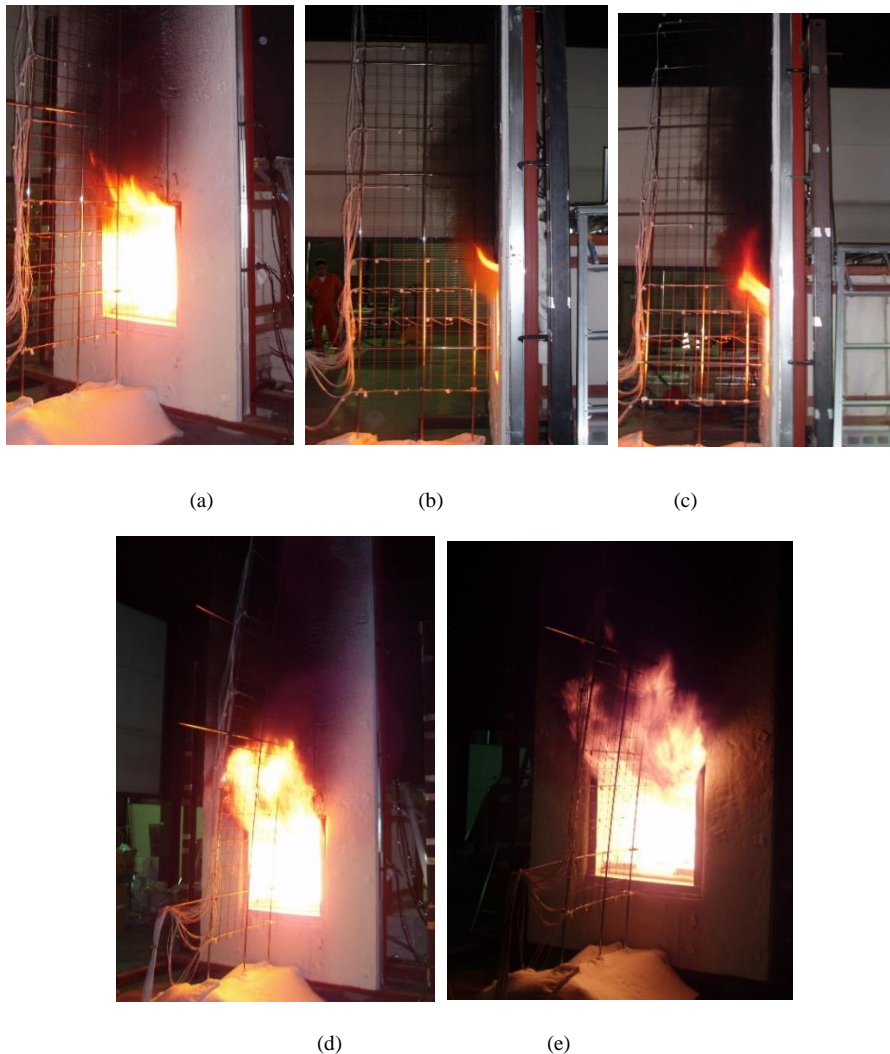


Fig.81 The description of fire plume shape using chamber 2 with  $n=2.05$

(a) The description of fire plume with heating intensity 100 kW (b) The description of fire plume with heating intensity 200 kW (c)

The description of fire plume with heating intensity 250 kW(d) The description of fire plume with heating intensity 300 kW(c) The description of fire plume with heating intensity 400 kW



(a)

(b)

(c)



(d)

(e)

Fig.82 The description of fire plume shape using chamber 3 with  $n=2.00$

(a) The description of fire plume with heating intensity 200 kW (b) The description of fire plume with heating intensity 300 kW (c) The description of fire plume with heating intensity 400 kW(d) The description of fire plume with heating intensity 500 kW(c) The description of fire plume with heating intensity 600 kW

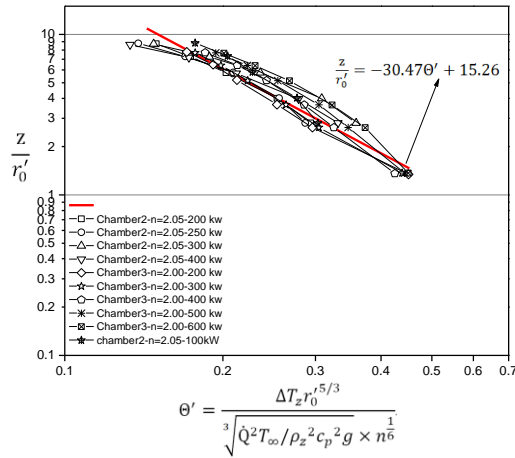


Fig.83 The effects of chamber dimension size on the new correlation plot by using chamber 2 and chamber 3

### I) Summary

In this study, temperature profile of an intermediate-scale window ejected fire plume under an over-ventilated condition was conducted by using Yokoi's correlation. The tests were carried out by using a 1.35 m (L) × 1.35 m (H) × 1.35 m (W) fire compartment (chamber 1) with window opening aspect varied from 1.12 to 4.44 and HRR differed from 200 kW to 1000 kW. The temperature profiles information was got by the k-type thermocouples tree, which was fixed at the location from the bottom of the opening to the upper of façade wall. The side and front view of fire plume behavior was recorded by a thermal camera. Fire plume re-attaching-to-wall behavior was observed and believed to have a heavy effect on the calculation of dimensionless temperature for the none-flame fire plume. By analysis of test results, it is concluded that the fire plume re-attaching to wall could resulted in a discontinuity on the Yokoi's plot in region 2 ( $10 \geq \frac{z}{r_0} > 1.5$ ). The window opening aspect  $n$  plays an important in the Yokoi's plot and the neutral plane height decrease as the heat release rate inside chamber increases. By taking into the above discussion, the new correlation  $\theta'$  vs.  $\frac{z}{r_0}$  was divided into two type of plots consisting of the none-flame fire plume ejected from window and the fire plume with flames spilled out of window. The new correlation is in the form of

$$\Theta' = \frac{\Delta T_z r_0^{5/3}}{\sqrt[3]{\dot{Q}^2 T_{\infty} / \rho z^2 c_p^2 g \times n^6}} = \frac{0.4528 \left(\frac{T_g}{T_z}\right)^{2/3} \left(\frac{\Delta T_z}{\Delta T_g}\right)}{(1-x)^{1/6}} = \text{function}\left(\frac{z}{r_0}\right),$$

where the neutral plane (N.P.) is calculated by the equation  $x = \frac{z_0}{H} = \frac{1}{1+1.04\left(\frac{T_g}{T_a}\right)^{1/3}}$ . The new length scale  $r_0'$  was defined as  $r_0' = \sqrt{\frac{W(1-x)H}{\pi}}$  (x is

ratio of neutral plane position  $z_0$  and window opening height H) without the assumption that neutral plane

is a constant 0.5 H. Regarding the none-flame fire plume, the fire plume re-attaching-to-wall behavior

showed a clear effect in the new correlation plots in the region 2 ( $10 \geq \frac{z}{r_0} > 1.5$ ). The discontinuity was

believed to be attributed to the fire plume re-attaching-to-wall effect, which disagrees with Yokoi's theory

that the dimensionless temperature  $\Theta$  vs.  $\frac{z}{r_0}$  is linear. The new correlation  $\Theta'$  vs.  $\frac{z}{r_0}$  in region 1 with

$\frac{z}{r_0} \leq 1.5$  was found to be  $\frac{z}{r_0} = 6.86\Theta' - 1.37$ . As for fire plume with flames spilled out of window, the

correlation  $\Theta'$  vs.  $\frac{z}{r_0}$  in region 1 with  $\frac{z}{r_0} \leq 1.5$  is in the form of  $\frac{z}{r_0} = 10.24\Theta' - 3.17$  and in region

2 with  $10 \geq \frac{z}{r_0} > 1.5$  is in the form of  $\frac{z}{r_0} = -30.47\Theta' + 15.26$ . Finally, the chamber dimension effects

on the new correlation was discussed by using two different chambers, chamber 2 and chamber 3. It

indicates that chamber dimension showed no clear effects on new correlation plot in region 2 with  $10 \geq$

$\frac{z}{r_0} > 1.5$ . The determination method of neutral plane and the classification basis of heating intensity inside

the chamber of none-flame fire plume and fire plume with flames are still needed to be further studied.

#### 4.3.6 Timber FPA test results and discussion

The FPA phased from Fire Testing Technology was employed to measure the mass loss rate (MLR) and chemical HRR. FPA test description and results consisting of MLR, HRR and THR are shown in Fig.84.

The flame of cedar specimen imposed to 15 kW/m<sup>2</sup> started from 334 s to 1160 s. The flames of cedar

specimen exposed to 45 kW/m<sup>2</sup> lasted from 13 s to 859 s. Fig.84 (a) features a flame during test. The dot

lines stands for experimental data. The black one features the results when cedar were exposed to external

heat flux 15 kW/m<sup>2</sup> in an air atmosphere. The blue one represents the results when cedar were exposed to



external heat flux  $45 \text{ kW/m}^2$  in an air atmosphere. It indicates both in low heat flux and high heat flux, MLR histories of pyrolysis model in Fig.84 (b) feature similar behaviour qualitatively with experimental results. When timber is exposed to high levels of irradiation, the change takes place in its internal structure, which is inferred to be accelerated by the increased temperatures. The representative HRR histories which shows two peaks are provided in Fig.84 (c). When the cedar exposed to external heat flux  $15 \text{ kW/m}^2$ , the first peak at  $t=390 \text{ s}$  in the curve exists after the initial heating stage, where it is believable that volatile pyrolysis gases are sufficient enough for ignition. After the first peak, a downward trend follows from  $390 \text{ s}$  to  $600 \text{ s}$ . Fig.85 features the FPA test scene description performed with different radiation flux.

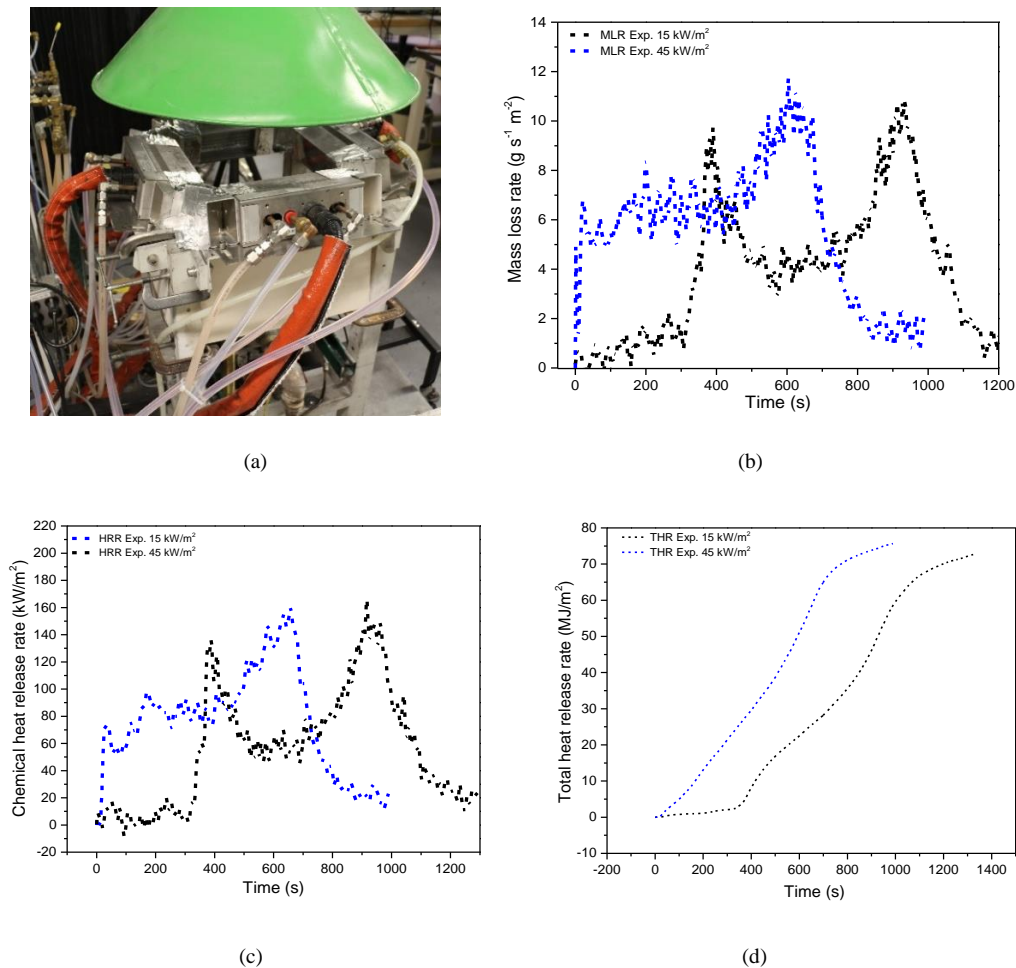


Fig.84 FPA test description and results

(a)The outlook of FPA facility (b) MLR of FPA test and pyrolysis model as a function of imposed external heat flux and time in an air atmosphere (c) chemical HRR of FPA test and pyrolysis model (d) THR of FPA test and pyrolysis model

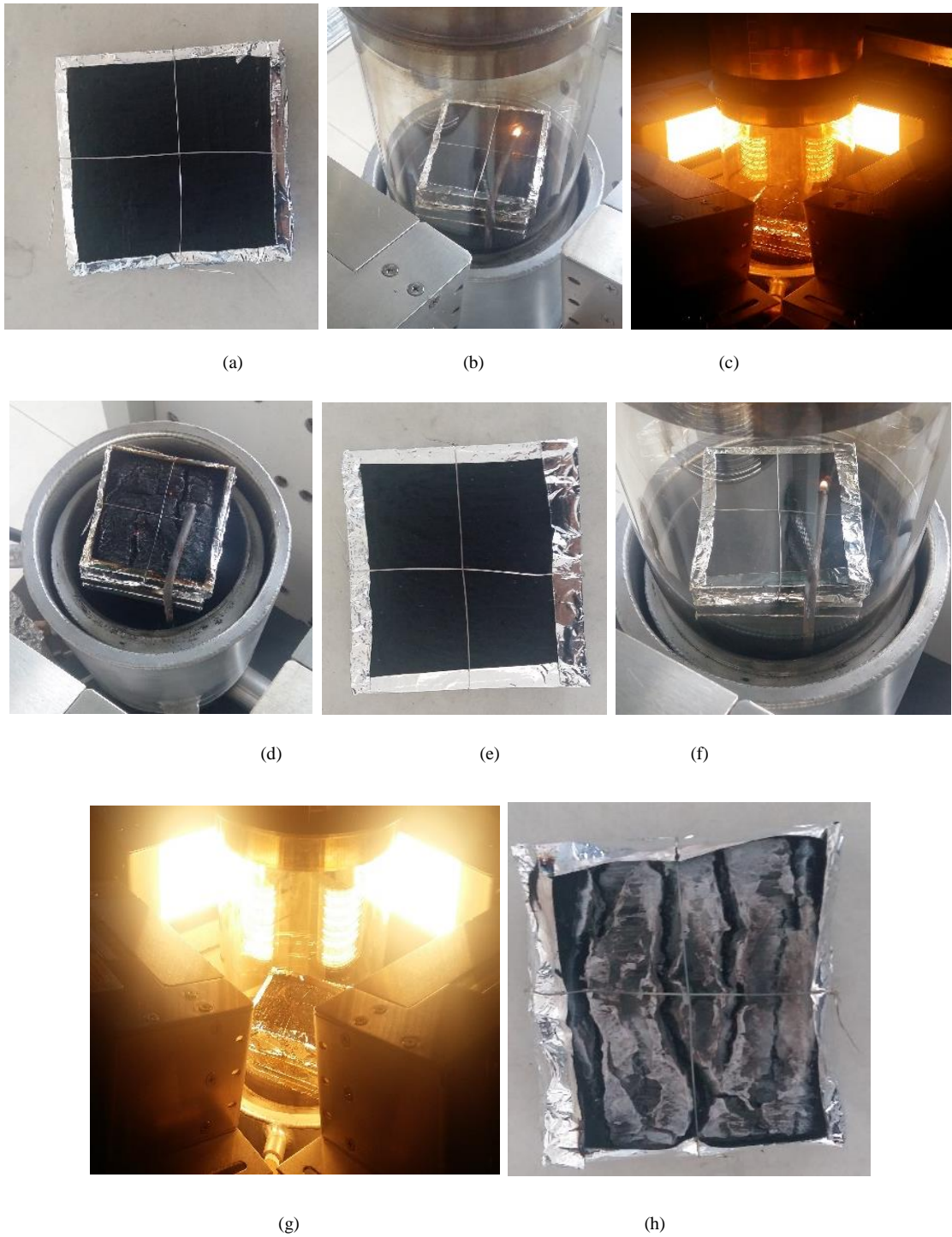


Fig.85 FPA test scene description performed with different radiation flux

(a) The description of specimen before test (b) The description prior to test with  $15 \text{ kW/m}^2$  (c) The description during test with  $15 \text{ kW/m}^2$  (d) The description after test with  $15 \text{ kW/m}^2$  (e) The description of specimen before test (f) The description prior to test with  $45 \text{ kW/m}^2$  (g) The description during test with  $45 \text{ kW/m}^2$  (h) The description after test with  $45 \text{ kW/m}^2$

#### 4.3.7 Timber façade fire results and discussion

The experiment method was according to the JIS A 1310 façade fire test method from Japan, just as shown in Fig.86. The experimental layout in our lab is shown in Fig.86 (a) and a simple sketch of experiment is described in Fig.86 (b). Fire test facility consisted of propane gas combustion chamber 1 (size in  $L \times W \times H = 1350 \text{ mm} \times 1350 \text{ mm} \times 1350 \text{ mm}$ ), fire spreading opening (size in  $L \times W = 910 \text{ mm} \times 910 \text{ mm}$ ), gas burner (size in  $L \times W = 600 \text{ mm} \times 600 \text{ mm}$ ), specimen substrate and specimen support frame. The opening size and opening aspect ratio are  $W \times H = 910 \text{ mm} \times 910 \text{ mm}$  and  $n=2$ , respectively. The chamber was with a  $10.1069 \text{ m}^2$  of inner surface area. It was used to produce different heating intensity fire, which was conducted by controlling high purity propane combustion. The gas burner was filled with the ceramic ball to ensure propane gas with a uniform speed. The specimen substrate was made by laying 2 pieces of 12 mm thickness calcium silicate board and the joint of the first layer was not overlapped with joint of second layer. Specimen support frame made of stainless steel was employed to support specimen substrate and the specimen tested. The interior surface of chamber was coated by a thickness of 25 mm ceramic fiber blanket. The test was carried out by laying a thickness of 19 mm cedar on the specimen support frame. The k-type thermocouples were used to record the temperature information varying test time. The thermocouples configuration was shown in Fig.86 (c). The thermocouples were fixed on both back façade surface and over façade surface in the height of 500 mm, 900 mm, 1500 mm, 2000 mm and 2500 mm away from the top of the opening, respectively. The HRR and THR were calculated by the common methodology Oxygen Consumption Calorimetry (OC). During OC measurement, the gas-analysis equipment recorded oxygen concentration ranged from 0.009% to 20.9 % in every two seconds. Before fire test, the 4 Liter alcohol combustion calibrated the whole equipment condition firstly. Then chamber heating intensity in kW was determined by controlling the mass flow of high purity propane. All the experiments were finished

in the Building Research of Institute of Japan located in Tsukuba. The test results are summarized in the following Fig.87 and Fig.88. Fig.87 features the experimental HRR and THR façade test. Fig.88 represents the experimental temperature profile of façade test.

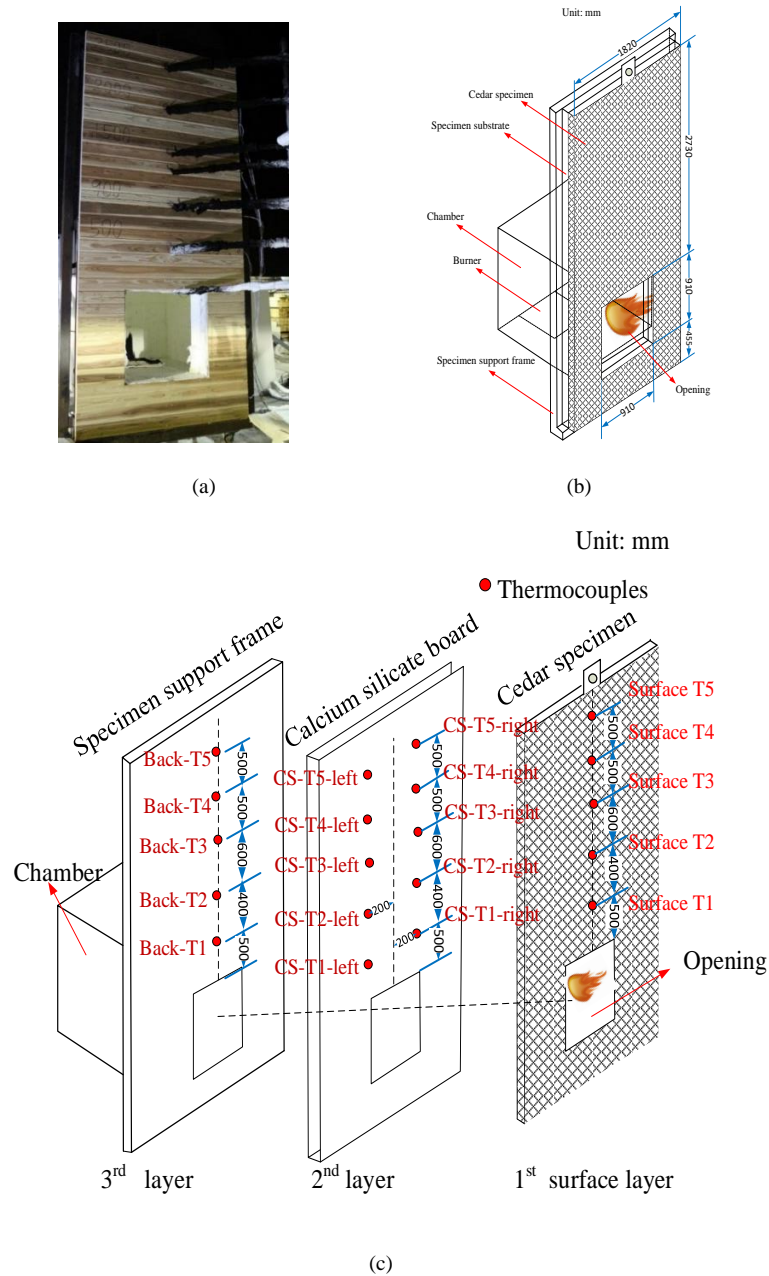
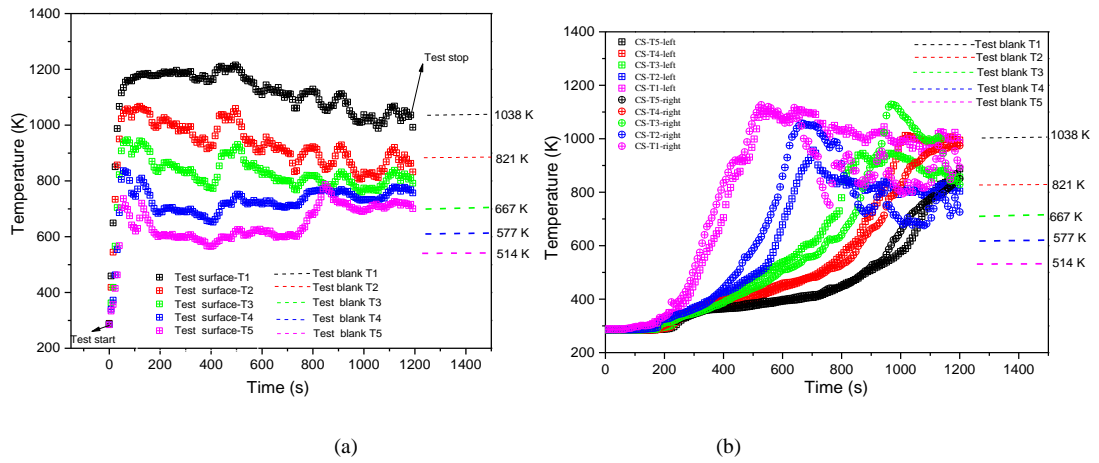


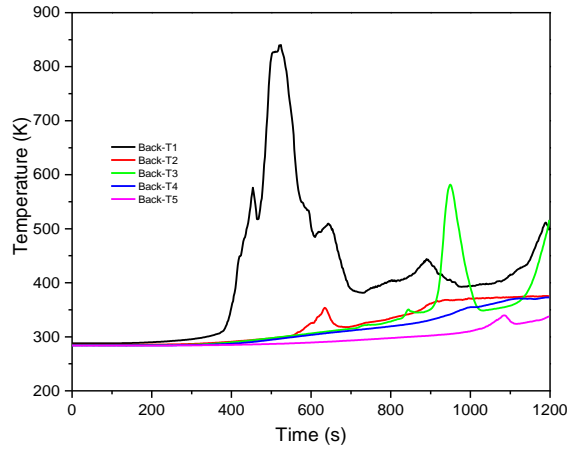
Fig.86 The description of experimental layout

The layout of test conditions (b) a simple model of experiment layout (c) the configuration of thermocouples on the mesh. The green ones is the usual thermocouple. The blue ones are the fire-retardant thermocouple, which is coated with a 2 mm thick of ceramic fiber tube.



(a)

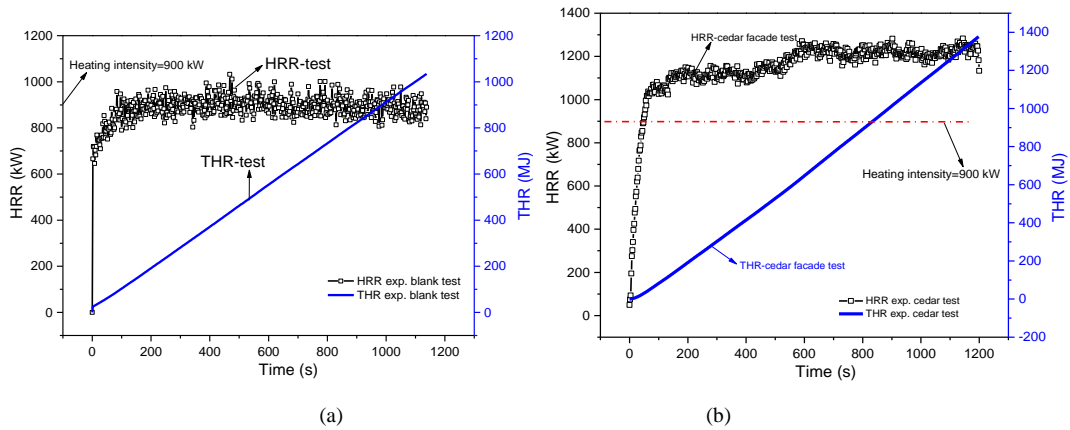
(b)



(c)

Fig.87 temperature profile of experiments façade test

(a) surface temperature distribution of test and model (b) back temperature distribution of test (c) comparison of experimental and simulated temperature profiles over calcium silicate board



(a)

(b)

Fig.88 HRR and THR of experiments (façade test) (a) HRR and THR of blank test (b) HRR and THR of cedar tests

## **4.4 Simulation results and discussion**

### **4.4.1 Modelling of EPS ETICS fire**

#### **A) Pyrolysis model of ETICS using Cone**

External Thermal Insulation Composite Systems (ETICS) have been used in buildings for several decades due to its thermal advantages, low cost and ease of application <sup>[57]</sup>. The principal design of ETICS includes wall construction, insulation material, cement bound mortar with reinforcement, rendering, and fixation by dowels and mortar <sup>[103]</sup>. The reaction-to-fire property of EPS ETICS need to be well understood.

Few attempts have been made to understand EPS ETICS façade reaction-to-fire performance. Our group in Japan has proposed the large-scale façade test method for evaluation of fire spread over combustible external wall systems <sup>[69]</sup>. And a series of EPS ETICS specimens varying EPS thickness, edge treatment, heating intensity and fire barrier have been tested and reported previously <sup>[70]</sup>. Although these large-scale results are helpful for EPS ETICS fire performance evaluation, a lack of knowledge concerning the components and layers was found. In addition, it is widely known that EPS ETICS are comprised of adhesive, EPS insulation material, reinforcement, base coat, anchors, and finishing coat. However, most current researches on the fire characteristics have concentrated on a single component, such as EPS, adhesive, polymer-modified concrete and finishing coat. Little knowledge of complete EPS ETICS reaction-to-fire performance from Cone Calorimeter testing was available.

Recently, computational fire models have significantly improved such that the most common models are capable of accurately predicting fire-induced conditions in an enclosure. Fire Dynamic Simulator (FDS) is a practical tool for simulating the fire-induced environment and it has been subjected to numerous validation studies <sup>[15]</sup>. ThermaKin developed by U.S. Federal Aviation Administration (FAA) is designed to

provide accurate and detailed pyrolysis model predictions <sup>[104]</sup>. It has been successfully applied to model the pyrolysis of charring polymers <sup>[105]</sup> and multilayer floor coverings <sup>[106]</sup>. Both ThermaKin2D and FDS6.5 are used in the present study to better understand the EPS ETICS reaction-to-fire performance.

In this study, EPS ETICS specimens are characterized by three layers from top to bottom, polymer cement mortar, cement mortar and EPS core. To identify the contribution of the individual layers to the pyrolysis dynamics of the composite, pyrolysis and Cone Calorimeter tests were performed to validate the model input parameters for the individual layers.

## B) Solid phase model

FDS has been subjected to numerous validation studies. The solid phase heat transfer model in FDS 6.5 assumes that solid surfaces consist of multiple layers, with each layer composed of multiple material components that can undergo multiple thermal degradation reactions. Heat conduction is assumed only in the direction normal to the surface. The surface is calculated by solving the heat conduction equation for the solid phase temperature  $T_s(x,t)$  <sup>[8, 16]</sup>, where  $\dot{q}_s''' = \dot{q}_{s,c}''' + \dot{q}_{s,r}'''$ :

$$\rho_s c_s \frac{\partial T_s}{\partial t} = \frac{\partial}{\partial x} \left( k_s \frac{\partial T_s}{\partial x} \right) + \dot{q}_s'''$$

The volumetric heat capacity and thermal conductivity of the solid could be defined as follows:

$$k_s = \sum_{\alpha=1}^{N_m} X_\alpha k_{s,\alpha} \quad \rho_s c_s = \sum_{\alpha=1}^{N_m} \rho_{s,\alpha} c_{s,\alpha}$$

The boundary condition of the front surface could be in the form of following:

$$-k_s \frac{\partial T_s}{\partial x}(0, t) = \dot{q}_c'' + \dot{q}_r''$$

## C) Finite-Rate Chemistry (Arrhenius Reaction)

In this study, a simple one-step forward reaction model is used. The EPS ETICS model from top to bottom consists of three layers, PCM (Polymer cement mortar, SBR (styrene-butadiene rubbers-latex)

content is 5.97% from TG method), CM (cement mortar) and EPS. The reactions for each layer are as follows:

Reaction 1:  $\text{PCM (1.0)} \rightarrow \text{SBR-G (0.0597)} + \text{CM (0.9413)}$ ;

Reaction 2:  $\text{EPS (1.0)} \rightarrow \text{PS\_M (1.0)}$ ;

Reaction 3:  $\text{PS\_M (1.0)} \rightarrow \text{PS\_G (1.0)}$ .

When the PCM layer is heated under irradiation, firstly the SBR contained in PCM will pyrolyze, which yields in a 5.97 % of gaseous SBR-G and 94.13 % of solid CM. Then EPS will melt and form polystyrene molten (PS\_M). Finally, the polystyrene melt decomposes to gaseous styrene (PS\_G).

#### D) Parameters model description

From top to bottom, it is made up by three layers, PCM (Polymer cement mortar, SBR (styrene-butadiene rubbers-latex) content is 5.97% by TG method), CM (cement mortar) and EPS. Here  $\rho$  is density in  $\text{kg/m}^3$ .  $c$  is specific heat capacity in  $\text{J}\cdot\text{kg}^{-1}\text{K}^{-1}$ .  $k$  is thermal conductivity in  $\text{W}\cdot\text{m}^{-1}\text{K}^{-1}$ . For ETICS, EPS is covered with coating. Here the coating materials from outside to inside are PCM (2 mm), CM (1 mm) and a layer of mesh made of fine fiber glass. It is believed that the mesh make no contribution for reaction-to-fire performance, presently, the mesh layer is ignored. The basic parameters are taken from an earlier publication by our group<sup>[107]</sup>. Input parameters of all components are listed in the Table 24.

Note: For SBR:  $\rho$  is  $1063 \text{ kg/m}^3$ <sup>[108]</sup>;  $c$  is  $1.89 \text{ kJ}\cdot\text{kg}^{-1}\text{K}^{-1}$ <sup>[109]</sup>; Heat of combustion is  $34.5 \text{ MJ/kg}$ <sup>[110]</sup>; For EPS: Heat of combustion is  $42.5 \text{ MJ/kg}$ <sup>[111]</sup>; Heat of melting is  $188\text{-}235 \text{ kJ/mol}$ <sup>[112]</sup>; the polymer beads collapse at about  $110\text{-}120 \text{ }^\circ\text{C}$ ; Complete volatilization occurs in the temperature range  $460\text{-}500 \text{ }^\circ\text{C}$ ; The heat of degradation of expanded polystyrene has been estimated to be at the order of  $912 \text{ J}\cdot\text{g}^{-1}$ <sup>[113]</sup>.



Table 24 Input parameters of all components

Component:	PCM	CM	SBR_G	EPS	PS_M	PS_G
State:	S	S	G	S	L	G
Density: kg/m <sup>3</sup>	1000	1200	950	15	1200	990 <sup>[114]</sup>
Heat capacity: J·kg <sup>-1</sup> ·K <sup>-1</sup>	1420	880	1890 <sup>[109]</sup>	1470+5T	1710+0.7T <sup>[10]</sup>	1800 <sup>[114]</sup>
Conductivity: W·m <sup>-1</sup> ·K <sup>-1</sup>	0.4 <sup>[115]</sup>	2-2.45e-3T+ 1.07e-6T <sup>2</sup> <sup>[115]</sup>	0.361 <sup>[109]</sup>	0.038	0.2+6e-5T <sup>[115]</sup>	1.35-8.82e-3T+ 1.43T <sup>2</sup> <sup>[116]</sup>
Transport: m/s	1e-5	1e-5	1e-5	1e-5	1e-5	1e-5
Emissivity	0.7	0.7	0.7	0.8 <sup>[117]</sup>	0.8 <sup>[117]</sup>	0.8
Absorption: m <sup>2</sup> /kg	10	10	10	10	10	10

Note: The density of PCM, CM, SBR\_G, EPS, PS\_M is provided by manufacture and also cited in reference <sup>[107]</sup>; Density and Heat capacity of PS\_G are from <sup>[114]</sup>; The conductivity of EPS is provided by manufacture; Transport, emissivity, and absorption are estimated by similar materials in FDS 6.5 Technical Reference Guide Volume 3: Validation

### E) Activation energy E and pre-exponential factor A of PCM pyrolysis

Knowing the SBR content in PCM, the simple PCM pyrolysis reaction can be written in PCM (1)→SBR-G(0.0597)+CM(0.9413). Plot of natural logarithm of heating rate versus the reciprocal temperature for volatile fractions  $\alpha=0.05, 0.1, 0.2, 0.5, 0.7, 0.9$  and  $0.99$  for PCM ( $r^2 > 0.97$ ) is described in Fig.89, which is based on the best estimates of E and A. Activation energy versus fractional weight loss for PCM is shown in Fig.90. Best estimates of E and A obtained from these figures are  $94.2 \text{ kJ/mol}$  and  $1.68 \times 10^6$ , respectively.

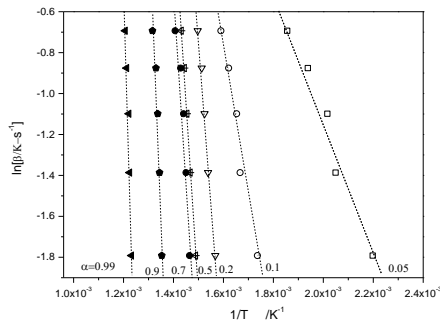


Fig.89 Plot of natural logarithm of heating rate versus the reciprocal temperature for volatile fractions  $\alpha= 0.05, 0.1, 0.2, 0.5, 0.7, 0.9$  and  $0.99$  for PCM.

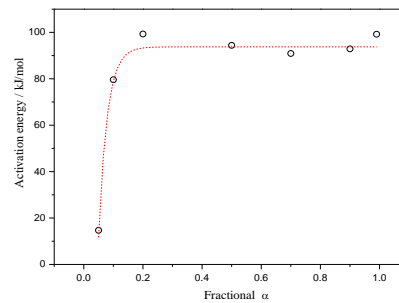


Fig.90 Activation energy vs. fractional weight loss for PCM

Reference [118] discussed the thermal decomposition of EPS in different gaseous environments, which is summarized in Fig.91. During thermal decomposition test, the oxygen concentration differed between 0 % and 50 %. It is observed that when the EPS is under poor oxygen (oxygen concentration from 0 % to 5 %) atmosphere, the activation energy (E) is much higher than it obtained from an oxygen-rich atmosphere. This is consistent with the phenomena that EPS is easy to pyrolyze in an oxygen-rich environment. Best estimates of E and A obtained from these figures are 172.5 kJ/mol and  $1.16 \times 10^8$ , respectively.

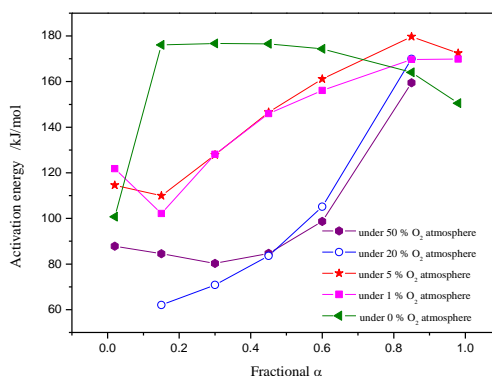


Fig.91 EPS activation energies varying with different conversion levels for different oxygen environments.

#### F) EPS pyrolysis experiment

EPS dependence of the evolution curve shape on the temperature is shown in Fig.92, which is got from TDMS. The main pyrolysis products are styrene, benzaldehyde, toluene, methylstyrene and ethybenzene. It agrees with the previous report of EPS pyrolysis product [119]. It is found that the peak of pyrolysis products rate of styrene, benzaldehyde, toluene, methylstyrene and ethybenzene are  $7.5 \times 10^{-9}$  mol/s,  $7.6 \times 10^{-10}$  mol/s,  $5.6 \times 10^{-10}$  mol/s,  $1.4 \times 10^{-10}$  mol/s and  $6.1 \times 10^{-11}$  mol/s, respectively. It indicates that the main EPS pyrolysis product is styrene. The yield of styrene started from 430 °C and reached a peak value at temperature of 660 °C. For simplification, EPS pyrolysis product is believed to be styrene in this study.

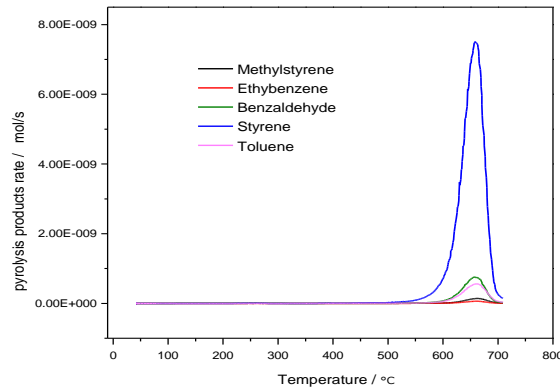


Fig.92 EPS dependence of the evolution curve shape on the temperature

### G) Model input parameter description

For EPS ETICS model, three reactions are characterized, reaction 1: PCM (1.0)→SBR-G (0.0597)+CM (0.9413), reaction 2: EPS (1.0)→PS\_M (1.0) and reaction 3: PS\_M (1.0)→PS\_G (1.0). When the PCM layer is heated under irradiation, firstly the SBR contained in PCM will pyrolyze, which yields in a 5.97 % of gaseous SBR-G and 94.13 % of solid CM. Then heat will go through CM layer to the EPS layer. When EPS is exposed to heat, it will melt to become PS\_M. Finally, the molten PS\_M will decompose to gaseous PS\_G. The E and A of reaction 1, reaction 2 and reaction 3 are  $A=1.68 \times 10^6$  and  $E=9.42 \times 10^4$  kJ/mol,  $A=1.6 \times 10^{-2}$  and  $E=0$  kJ/mol, and  $A=1.16 \times 10^8$  and  $E=1.73 \times 10^5$  kJ/mol, respectively. To estimate the EPS melt parameters, an EPS panel with a thickness of 10 cm and an area of 1 m<sup>2</sup> is heated by different radiation rates ranging from 20 kW/m<sup>2</sup> to 50 kW/m<sup>2</sup>. During test, the interface position as function of time for different radiation rate was recorded [120]. The heat reaction of reaction 1, reaction 2 and reaction 3 are  $1 \times 10^6$  kJ/mol,  $9 \times 10^4$  kJ/mol and  $2 \times 10^7$  kJ/mol, respectively. In this study, it is assumed that reaction 2 is infinitely fast.

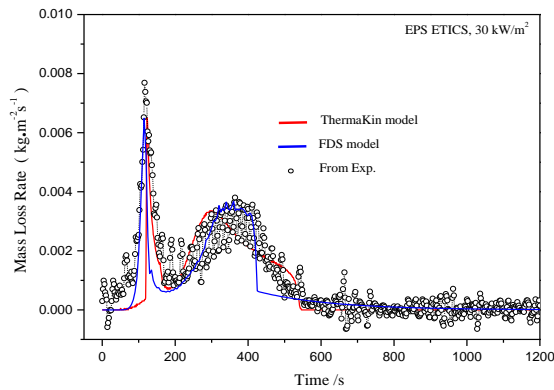
### H) EPS ETICS specimen Cone Calorimeter test

The Cone Calorimeter tests results for each EPS ETICS specimen were performed in duplicate. During

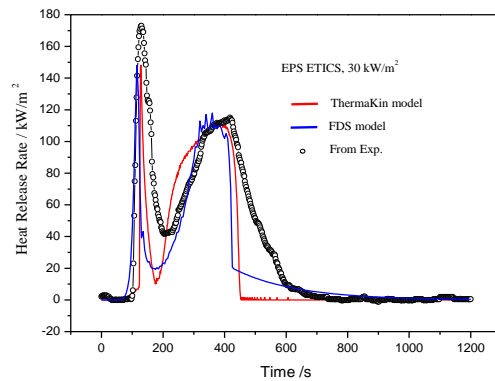
tests, two irradiation levels  $30 \text{ kW/m}^2$  and  $50 \text{ kW/m}^2$  are investigated. According to EPS ETICS specimen Cone Calorimeter test results, it is found that there are two peaks existing in the HRR histories. The first peak is attributed to PCM combustion since exterior PCM was ignited firstly. The second peak is mainly believed to be a result of EPS combustion. When the EPS ETICS specimen is under  $30 \text{ kW/m}^2$  irradiation for 96 s, the surface of specimen will be ignited. And when the EPS ETICS specimen is under  $50 \text{ kW/m}^2$  irradiation for 52 s, the surface of specimen will be ignited. This can be used to understand the fast vertical spread of EPS ETICS façade fires.

### I) Comparison of MLR and HRR from Cone tests and numerical models

By using the numerical set-ups described in the above, the three layers model is calculated by ThermaKin2D and FDS 6.5, respectively. Comparisons of Cone Calorimeter and numerical model results are shown in Fig.93. As discussed in the above, there are two peaks in EPS ETICS specimen MLR curves. The first peak is a result of the SBR pyrolysis and the second peak is due EPS pyrolysis. Comparison of results from FDS6.5 and ThermaKin2D shows that the numerical results from both FDS6.5 and ThermaKin2D agree with experiment.



(1)



(2)

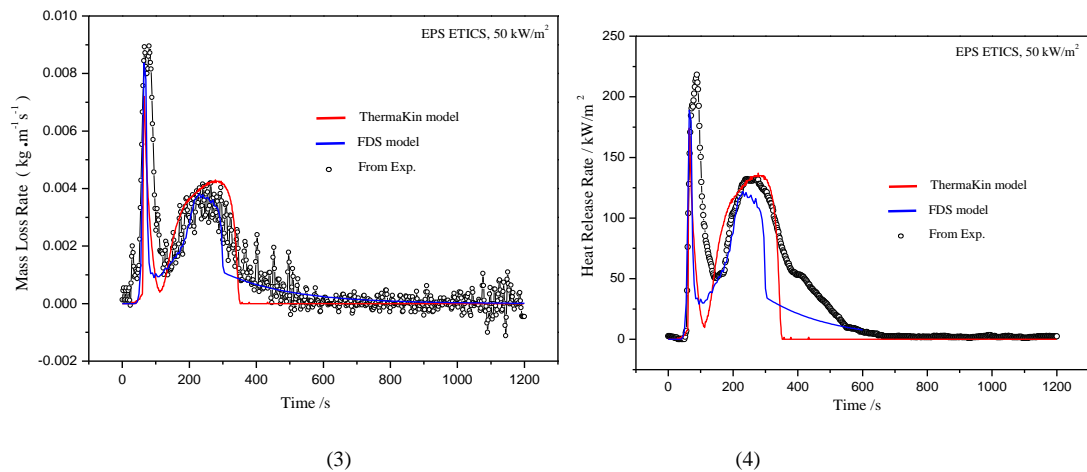


Fig.93 Comparison result of Cone and model

- (1) Mass loss rate distribution varying test time under 30 kW/m<sup>2</sup> irradiation (2) Heat release rate distribution varying test time under 30 kW/m<sup>2</sup> irradiation (3) Mass loss rate distribution varying test time under 50 kW/m<sup>2</sup> irradiation (4) Heat release rate distribution varying test time under 50 kW/m<sup>2</sup> irradiation

Regarding the temperature dependency of parameters, both of two numerical tools have developed a different function to approach real value for each parameter. In ThermaKin2D, all the property are defined as  $property = p^0 + p^1T + p^nT^n$ , where  $p^0$ ,  $p^1$  and  $p^n$  are constants, respectively. In current FDS 6.5, the temperature dependency of material properties could be easily modelled by using a T ramp function, which well defines the relationship between parameter and temperature. From Fig.93, it shows that the function modelled to define temperature dependency of parameter is successful in both ThermaKin2D and FDS6.5. It could be used to improve continuity of simulation.

Comparison of results with 30 irradiation kW/m<sup>2</sup> obtained from ThermaKin2D and FDS6.5 indicates that  $t_{peak1}$  from FDS is a little smaller than it got from ThermaKin2D. This is inferred to be ascribed to it that when FDS 6.5 is used to model a pyrolysis experiment, the gas phase can be turned off, which results in very fast run times even with detailed ramp functions for the temperature dependency of parameters. Two peaks of MLR and HRR from FDS 6.5 are nearly the same with it got from ThermaKin2D. Furthermore, it is found that there is a sharp decrease at about 420 s in MLR curves from both FDS6.5 and ThermaKin2D. As for the test at 50 kW/m<sup>2</sup>,  $t_{peak1}$  from FDS6.5 is nearly identical to that from ThermaKin2D. The first peak

of MLR from FDS6.5 is higher than it from ThermaKin2D. However, the second peak of MLR from FDS6.5 is lower than it from ThermaKin2D. It is also found that there is a sharp decrease at about 320 s in MLR curves from both FDS6.5 and ThermaKin2D.

Error of the calculated MLR and HRR curves shown in Fig.8 is approximately 13%-19 % compared with Cone Calorimeter test results. The discrepancies between the calculated and measured MLR and HRR curves could be explained by the fact that the flame heat flux is not accounted for in the FDS model. With an aim to evaluate the effects of flame heat flux on the MLR, a series of heat flux acted as flame heat flux were added to surface. The heat flux consists of external heat flux and flame heat flux. For example, heat flux 30 kW/m<sup>2</sup> means that there is no flame heat flux in simulation. Heat flux 37.5 kW/m<sup>2</sup> indicates that there is 7.5 kW/m<sup>2</sup> flame heat flux in simulation. Fig.94 shows MLR curves of FDS varying irradiation levels from 30 kW/m<sup>2</sup> to 37.5 kW/m<sup>2</sup> and 50 kW/m<sup>2</sup> to 56 kW/m<sup>2</sup>. It is found that the flame flux accounts for 15 % of external heat flux in FDS 6.5. Fig.94 gives MLR curves of ThermaKin2D varying flame heat flux irradiation from 0 kW/m<sup>2</sup> to 7.5 kW/m<sup>2</sup> in two tested cases. It is found that the flame flux accounts for 18.0 % of external heat flux in ThermaKin2D. As discussed above, error of the calculated MLR and HRR curves in Fig.94 could be well explained that the flame flux accounts for 15 % of external heat flux in FDS 6.5 and 18.0 % of external heat flux in ThermaKin2D. In FDS 6.5, although increasing external heat flux could give a better MLR peak agreement with experimental results, it also shortens the time to reach the peak. In ThermaKin2D, using a simple model to simulate flame heat flux seems insufficient since optimal flame heat flux is approximately defined before simulation. Furthermore in ThermaKin2D, the  $t_{peak}$  is also found to be shortened after adding flame heat flux. Therefore, a well modelling work of flame heat flux needs in the next step research.

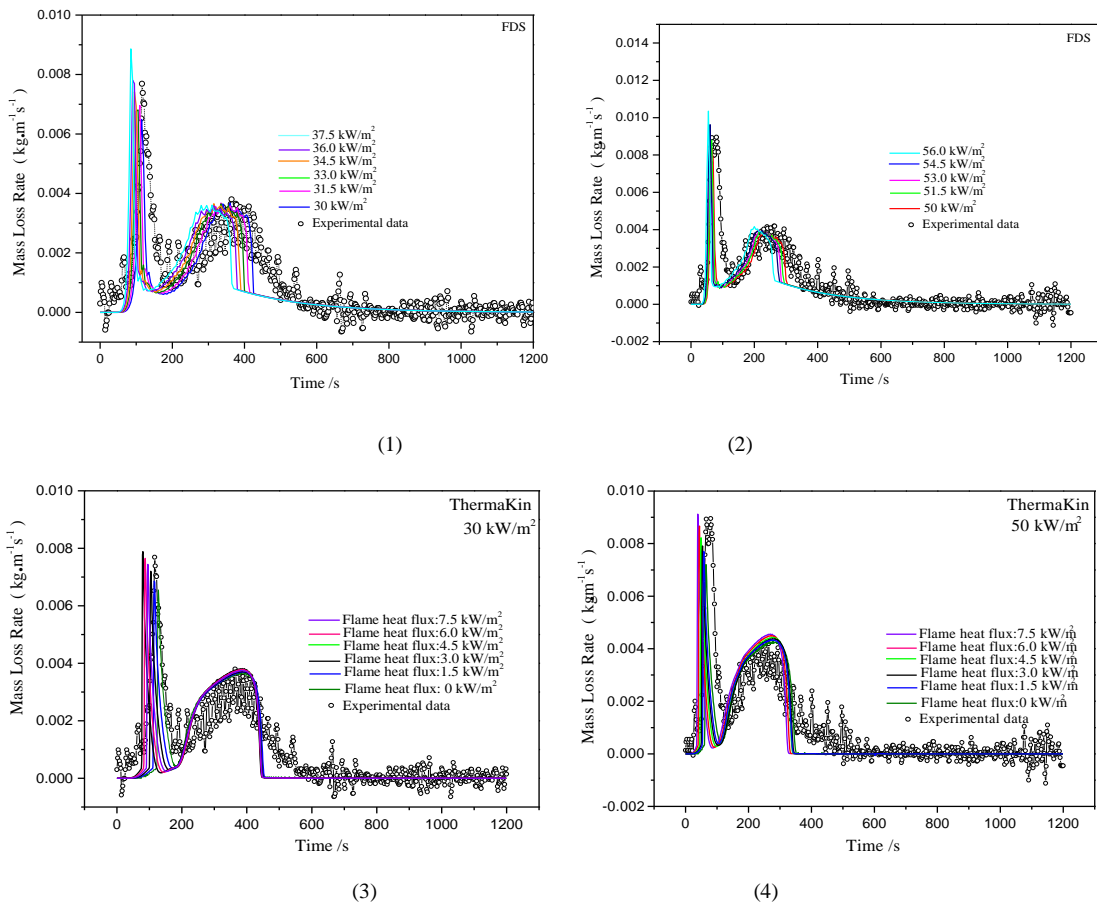


Fig.94 MLR curves of ThermaKin2D and FDS varying test time and flame heat flux

(1) Irradiation from 30 kW/m<sup>2</sup> to 37.5 kW/m<sup>2</sup> (2) Irradiation from 50 kW/m<sup>2</sup> to 56 kW/m<sup>2</sup> (3) Flame heat flux from 0 kW/m<sup>2</sup> to 7.5 kW/m<sup>2</sup> (4) Flame heat flux from 0 kW/m<sup>2</sup> to 7.5 kW/m<sup>2</sup>

## J) ETICS ICAL simulation

Just as previous stating, the reaction-to-fire performance of Cone seems insufficient to agree with the large scale real fire performance. Although this issue has not got the necessary attention currently, the new method for adequate evaluation the melt-flow building material which installed vertically would be proposed in future and is beyond the scope of current study. Here, the main work is to model the ICAL test in vertical direction and compare the simulation with experimental results. The pyrolysis model used in ICAL simulation is verified by the Cone test. The ICAL test of EPS ETICS was simulated using FDS 6.5,

which is shown in Fig.95. It was reported that results of large scale upward flame spread tests can be better explained by the ICAL than by the Cone because Cone (V) gives generally lower HRR than ICAL [121]. A wood products comparison of ICAL and Cone test (non-melt-drip material) showed that the difference between them were surprisingly small [122]. Thereby Cone (V) result is believed to equate ICAL result with respect to non-melt-drip materials. The large discrepancy existed in the experimental Cone (V) and ICAL under the same radiation indicates that melt-flow influence heavily on the measurement. The simulation of ICAL test shows that fire spread in vertical direction seems hard to be simulated using current version of FDS.

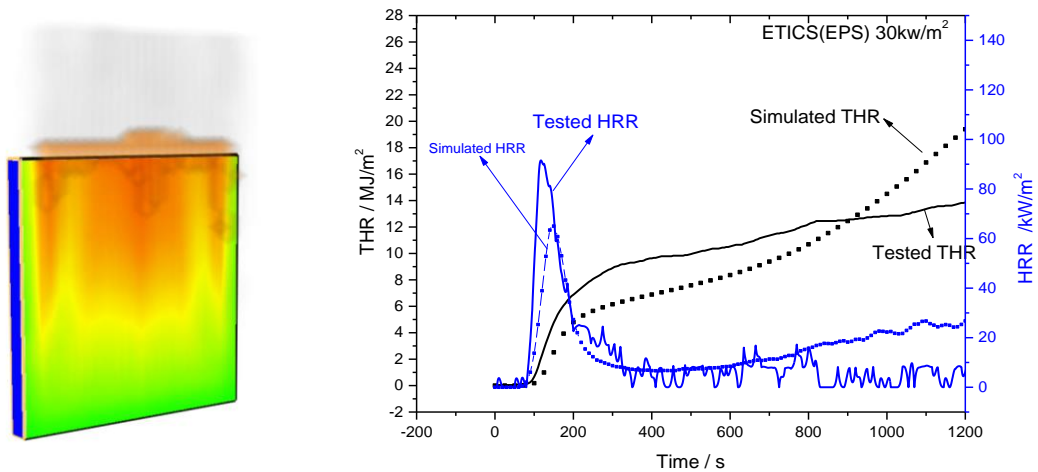


Fig.95 The description of EPS ETICS simulation (a) The simulation configuration (b) the comparison of simulated and tested HRR and THR.

### K) Summary

In this study, The EPS ETICS specimen was characterized into three separate layers. With accurate input parameters, the numerical mass loss rate and heat release rate prediction were performed by two useful tools, FDS6.5 and ThermaKin2D. For validation, pyrolysis experiment and Cone Calorimeter tests were conducted. In the MLR and HRR history from Cone Calorimeter test, the first peak was derived from SBR pyrolysis and the second peak was due to EPS pyrolysis. MLR and HRR predictions were found to be in a



reasonable agreement with the experimental data. The discrepancies between the calculated and measured MLR and HRR curves could be explained by it that the flame heat flux is not accounted for in the FDS model. In ThermaKin2D, although a simple flame heat flux model is developed to simulate the influence of flame on the materials surface. It seems insufficient since the optimal flame heat flux are needed to be predicted before simulation. Although increasing external heat flux in FDS6.5 or adding flame heat flux in ThermaKin2D could give a better MLR peak agreement with experimental results, the  $t_{\text{peak}}$  was found to be shortened. A well modelling work of flame heat flux is needed.

The large discrepancy existed in the experimental Cone (V) and ICAL under the same radiation indicates that melt-flow influence heavily on the measurement. The simulation of ICAL test shows that fire spread in vertical direction seems hard to be simulated using current version of FDS.

#### **4.4.2 Large eddy simulation of buoyant window ejected fire plume from intermediate-scale compartment fires using FireFOAM**

Regarding the building performed with combustible façade, the flame ejected from a window of the room could be a potential ignition source. Many numerical studies attempt to model the fire plume by using CFD tools in the past decades. Knowing the buoyancy-driven and momentum-driven fire plume are sensitive to the turbulence model, both RANS models <sup>[123-125]</sup> and LES <sup>[11]</sup> have been used to model the fire plumes. The utilization of RANS model to simulate fire plume is rare currently because of the significant discrepancies. Many recent numerical studies <sup>[16, 126-128]</sup> of fire plumes using LES model reduce the difficulties by resolving transient large turbulent eddies. The different versions of FDS code <sup>[14]</sup> developed in NIST have been successful used to probe into the modelling of fire plumes <sup>[129, 130]</sup>.

Regarding the fire plume behaviour of building façade systems, Simo and Gleb reproduced a numerical

model of the ISO 13785-2 test using FDS, then used the model to discuss the thermal environment effects on the façade fire and finally validated simulation results by comparing the experimental data by Yoshioka et al. <sup>[130]</sup>. The optimal 10 cm grid mesh size was got by the sensitivity analysis using FDS. With respect to another fire simulation tool called FireFOAM, it was concluded that the FireFOAM model could well reproduce small-scale fire plumes.

The present study for simulating the intermediate-scale fire plumes is conducted by an open source code called FireFOAM <sup>[131]</sup>, which is installed on the OpenFOAM <sup>[132]</sup> platform. The FireFOAM, developed by Yi et al. from FM Global and oriented to be used in simulation of large-scale industrial fires. It has been subjected to numerous validation studies <sup>[31, 133-139]</sup>. This paper presents a LES study of an intermediate-scale window ejected fire plumes and aimed at bringing insight into the ability and limitations of FireFOAM to simulate intermediate-scale buoyant fire plumes. The validation experiment, mathematical models, numerical setup of simulation are briefly summarized in section 2. Following this, the comparison of simulation and experiment is described and discussed.

#### **A) Numerical configuration**

The computational domain is described as a 5 m high in the vertical z-direction, 6.4 m deep in the wall normal x-direction, and 6 m wide in the span-wise y-direction, which is shown in Fig.96. As described in the above, the modified numerical configuration features a gas combustion chamber (size in  $L \times W \times H = 1.40 \text{ m} \times 1.40 \text{ m} \times 1.40 \text{ m}$ ), fire spreading chamber opening (size in  $L \times W = 0.90 \text{ m} \times 0.90 \text{ m}$ ), gas burner (size in  $L \times W = 0.60 \text{ m} \times 0.60 \text{ m}$ ) and the non-combustible façade wall (size in  $L \times W \times H = 4.10 \text{ m} \times 1.80 \text{ m} \times 0.25 \text{ m}$ ). The chamber opening size was modified from 0.91 m to 0.9 m in the current simulation to avoid the difficulty of mesh configuration and the extra computational cost. Wall boundary conditions correspond to a prescribed propane mass flow rate,  $k_{\text{sgs}} = 0$ . The boundaries around and top of the

computational domain were defined as the open flow type. In experiment, the thick ceramic fiber blanket was fixed on the internal surfaces of chamber. With an aim to use the similar condition in simulation, the five surfaces of chamber were defined as pyrolysis Region model, which is the irreversible Arrhenius solid reaction with a larger activation energy  $E$ . Regarding the computing resources, FireFOAM-2.2.x was run on supercomputer called Reedbush located at The University of Tokyo in Japan. The Reedbush system has each node with a Intel Xeon E5-2695v4 (Broadwell-EP 2.1 GHz 18 core) x2 socket, 12906.6 GF, 245 GB Mem, 153.6 GB/sec. Total subsystem is 508.3 TF and fat-tree with full bisection bandwidth (100 Gbps/node).

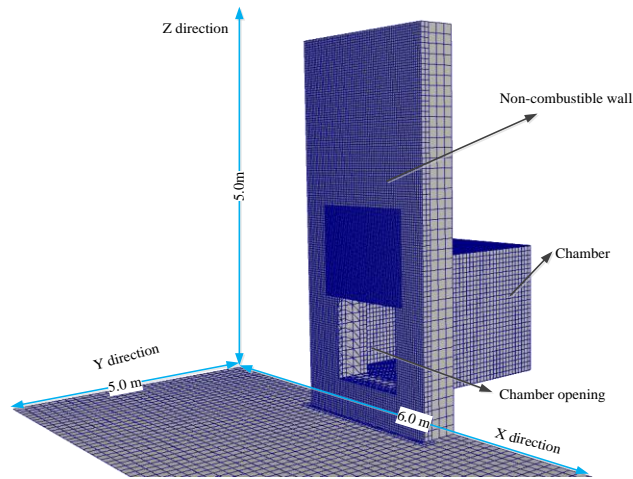


Fig.96 The computational domain (including the chamber)

## B) Grid convergence

The grid analysis of chamber was conducted by using different grid sizes inside the chamber  $\Delta_x \times \Delta_y \times \Delta_z = 100 \text{ mm} \times 100 \text{ mm} \times 100 \text{ mm}$  ,  $\Delta_x \times \Delta_y \times \Delta_z = 50 \text{ mm} \times 50 \text{ mm} \times 50 \text{ mm}$  ,  $\Delta_x \times \Delta_y \times \Delta_z = 25 \text{ mm} \times 25 \text{ mm} \times 25 \text{ mm}$  ,  $\Delta_x \times \Delta_y \times \Delta_z = 12.5 \text{ mm} \times 12.5 \text{ mm} \times 12.5 \text{ mm}$  and  $\Delta_x \times \Delta_y \times \Delta_z = 6.25 \text{ mm} \times 6.25 \text{ mm} \times 6.25 \text{ mm}$ . The resultant temperature was compared with it from the thermocouples tree located inside the chamber. Comparison of simulation and experiment shows that simulation performed

with a grid size in  $\Delta_x \times \Delta_y \times \Delta_z = 50 \text{ mm} \times 50 \text{ mm} \times 50 \text{ mm}$  gives a good result which is consistent with experiment results. The temperature profiles of inside chamber varying heating intensity are shown in Fig.97. Fig.97 (a) and Fig.97(b) feature the grid sensitivity analysis on the basis of temperature inside the chamber. Fig.97 (c) and Fig.97 (d) demonstrate the comparison of experimental temperature profile and simulation performed by 5 cm grid under heating intensity 300 kW and 600 kW.

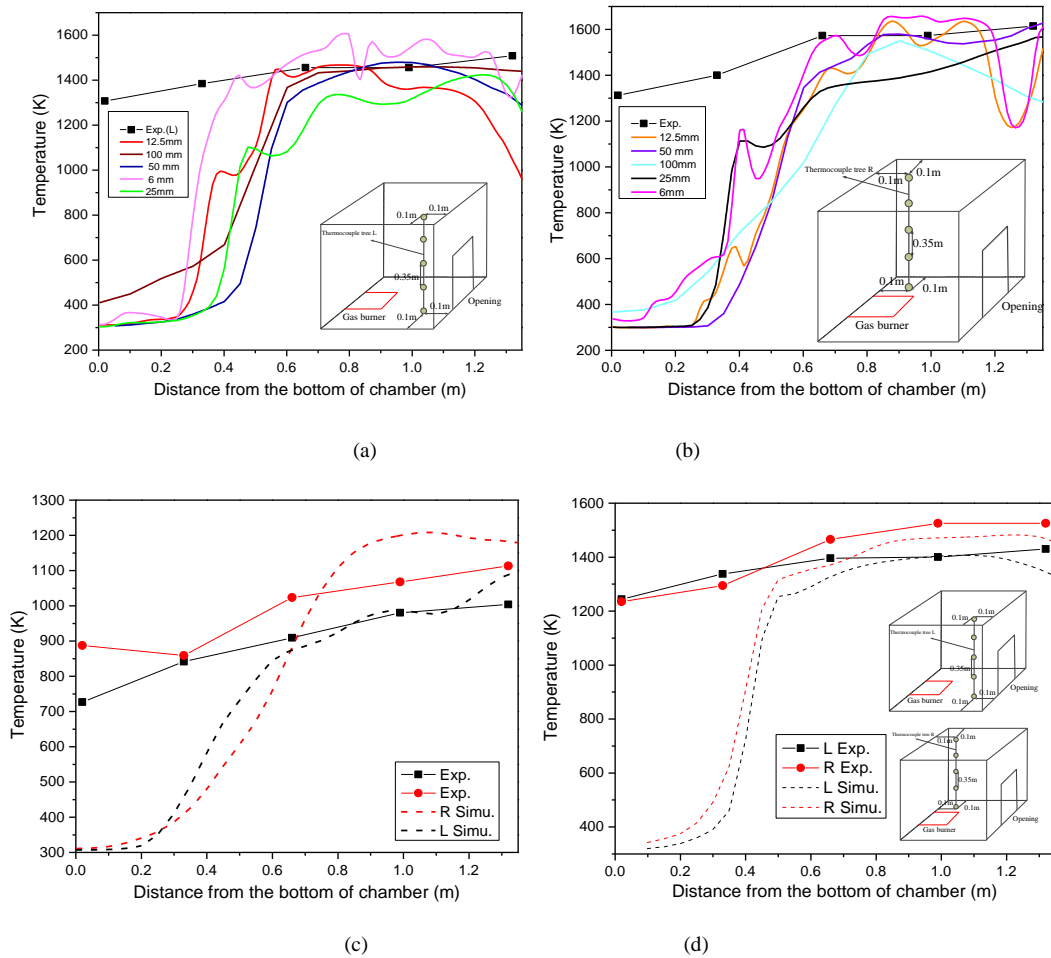
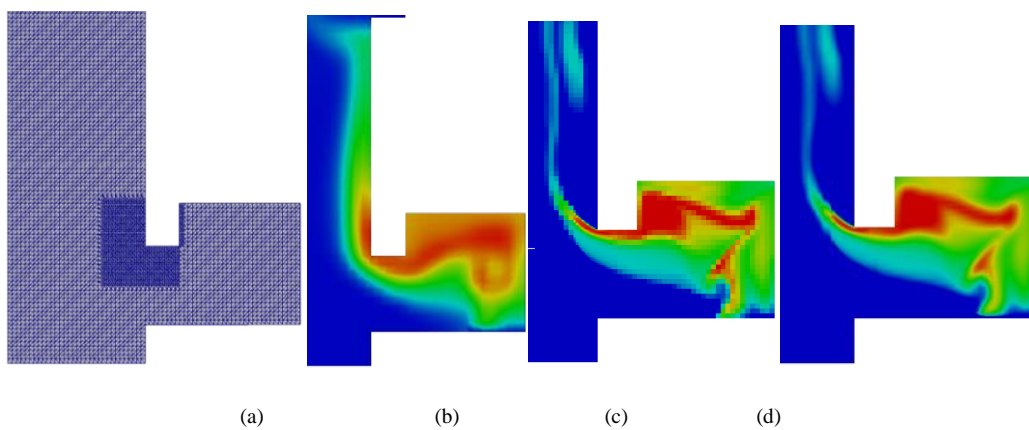


Fig.97 The temperature distribution vs. vertical height inside the chamber under different heating intensity. (a) Left T with heating intensity 900 kW (b) Right T with heating intensity 900 kW (c) heating intensity 300 kW. (d) heating intensity 600 kW.

It is known that fire plume shape at the opening is believed to be related with the momentum and buoyancy force of fire plume. In the scale modeling of continuum mechanics, the Froude number ( $Fr$ ) is used to describe the ratio of the flow inertia to the external field, which is shown in the following:  $Fr =$

$\frac{u}{\sqrt{gl}}$  [140]. In this study,  $u$  is a characteristic flow velocity in  $y$ -direction,  $g$  is in general a characteristic external field, and  $l$  is a characteristic length (thickness) fire flame at opening. The opening region shown in Fig.4 (a) is believed to be important for window fire simulation. The opening grid (region:  $-0.5 \text{ m} \leq x \leq 0.5 \text{ m}$ ,  $0 \text{ m} \leq y \leq 0.5 \text{ m}$ ,  $0.9 \text{ m} \leq z \leq 1.9 \text{ m}$ ) sensitivity was analyzed by  $\Delta_x \times \Delta_y \times \Delta_z = 100 \text{ mm} \times 100 \text{ mm} \times 100 \text{ mm}$ ,  $\Delta_x \times \Delta_y \times \Delta_z = 50 \text{ mm} \times 50 \text{ mm} \times 50 \text{ mm}$ ,  $\Delta_x \times \Delta_y \times \Delta_z = 25 \text{ mm} \times 25 \text{ mm} \times 25 \text{ mm}$ ,  $\Delta_x \times \Delta_y \times \Delta_z = 12.5 \text{ mm} \times 12.5 \text{ mm} \times 12.5 \text{ mm}$  and  $\Delta_x \times \Delta_y \times \Delta_z = 6.25 \text{ mm} \times 6.25 \text{ mm} \times 6.25 \text{ mm}$ . The temperature distribution and the velocity distribution  $U_y$  in  $y$  direction are described in Fig.98. The velocity varying opening height is shown in Fig.98 (g). It indicates that the minimum  $U_y$  was obtained when the grid size was used  $\Delta_x \times \Delta_y \times \Delta_z = 100 \text{ mm} \times 100 \text{ mm} \times 100 \text{ mm}$ . By calculation, the Fr number of opening grid  $\Delta = 100 \text{ mm}$ ,  $\Delta = 50 \text{ mm}$ ,  $\Delta = 25 \text{ mm}$  and  $\Delta = 6.25 \text{ mm}$  are 4.12, 4.70, 4.48, 3.79 and 3.00, respectively. From the above discussion and experimental observation, the fire plume re-attaching-to-wall observation is insistent with the grid  $\Delta = 100 \text{ mm}$ , whose Fr number is 3.00. It seems that when Fr number is smaller than 3.00, the fire plume features a re-attaching-to-wall phenomena, which agrees with experiment. The Fire Froude number (FFr) of this study is 0.26.



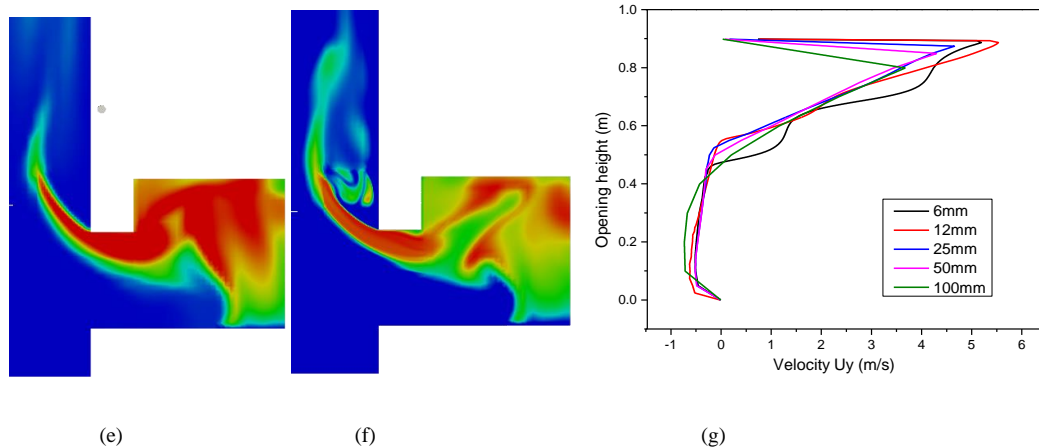


Fig.98 The representative temperature and velocity  $U_y$  (in y direction) distribution simulation performed with varied grid size from 100 mm to 6.125 mm of region near opening. (a) The position of refined grid near opening (b) grid size 100 mm (c) grid size 50 mm (d) grid size 25 mm (e) grid size 12.5 mm (e) grid size 6.125 mm (g) the velocity  $U_y$  distribution over opening height of simulation performed varied grid size.

During the experimental test, the fire plume spilled from the chamber was observed with no flame when the heating intensity was 300 kW. From the side view of fire plume with heating intensity of 600 kW and 900 kW, the turbulence flame thickness  $\delta_s$  takes a maximum 0.45 m. Therefore, combustion in a narrow region close to the wall and the computational grid should be solved accordingly. It is reported that, the main grid design criterion for wall-resolved LES is to place the first off-wall grid point (in the y - direction) inside the viscous sub-layer of the boundary layer flow <sup>[141, 142]</sup>. Regarding the momentum-driven turbulent boundary layer (MDTBL) and buoyancy driven turbulent boundaries (BDTBL), two estimation methods for  $\delta_{VSL}$  are available. Two  $\delta_{VSL}$  are got by using a representative value:  $\delta_{VSL} = 0.28 \text{ mm}$  and  $\delta_{VSL} = 0.71 \text{ mm}$ . In the following, we perform a grid sensitivity analysis of near-wall region and consider  $\Delta_{y_w} = 6.25 \text{ mm}, 12.5 \text{ mm}, 25 \text{ mm}, 50 \text{ mm}$  and  $100 \text{ mm}$ . ( $\Delta_{y_w}$  is the y-direction of the first off-wall computational grid cell). The grid with  $\Delta = 100 \text{ mm}$  is referred to as the baseline grid of surroundings. And the grid with  $\Delta = 50 \text{ mm}$  is referred to as the baseline grid of chamber region. The error caused by near-wall region is ignorable In this study, compared with large scale simulation. Fig.99 shows the typical information of temperature distribution with varied grid in the near-wall region. It was shown that grid size performed 6.25

mm was found to be insistent with experimental observation from the compared figures. Therefore, to avoid the huge computational cost and have a reasonable wall-resolved LES, only the mesh near wall was refined to  $\Delta_x \times \Delta_y \times \Delta_z = 6.25 \text{ mm}$  in the region:  $-0.6 \text{ m} \leq x \leq 0.6 \text{ m}, 0.4 \text{ m} \leq y \leq 0.45 \text{ m}, 1.3 \leq z \leq 2.3 \text{ m}$ .

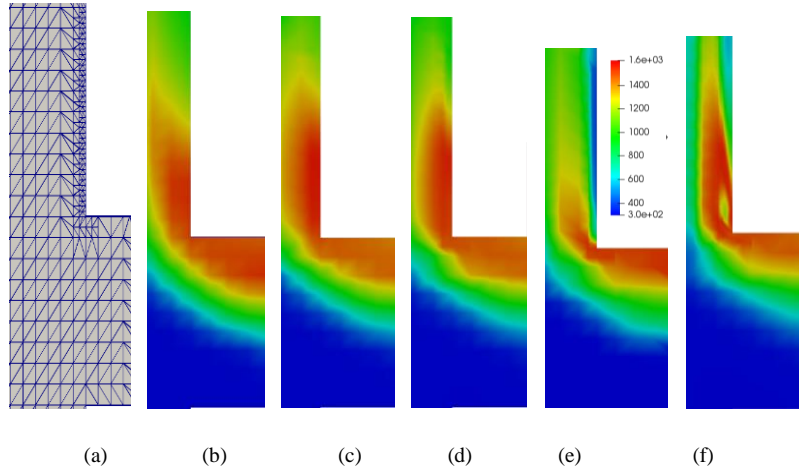


Fig.99 The representative temperature distribution of simulation with near wall region performed grid size from 100 mm to 6.25 mm. (a) The position of refined grid near opening (b) near wall grid size 100 mm (cells) (c) 50 mm (d) 25 mm (e) 12.5 mm (f) 6.25 mm

The computational grid was generated by an OpenFOAM mesh tool called SnappyHexMesh. The grid features three levels of resolution in the computation domain. The grid of chamber in the region ( $-0.7 \text{ m} \leq x \leq -0.7 \text{ m}, -1.4 \text{ m} \leq y \leq 0 \text{ m}, 0.40 \text{ m} \leq z \leq 1.80 \text{ m}$ ) was refined to  $\Delta_x \times \Delta_y \times \Delta_z = 50 \text{ mm} \times 50 \text{ mm} \times 50 \text{ mm}$ . The grid of window opening in the region ( $-0.5 \text{ m} \leq x \leq 0.4 \text{ m}, 0 \text{ m} \leq y \leq 0.4 \text{ m}, 0.4 \text{ m} \leq z \leq 1.3 \text{ m}$ ) was coarsen to  $\Delta_x \times \Delta_y \times \Delta_z = 100 \text{ mm} \times 100 \text{ mm} \times 100 \text{ mm}$ . The grid of chamber in the near wall region ( $-0.6 \text{ m} \leq x \leq 0.5 \text{ m}, 0.4 \text{ m} \leq y \leq 0.45 \text{ m}, 1.3 \text{ m} \leq z \leq 2.3 \text{ m}$ ) was refined to  $\Delta_x \times \Delta_y \times \Delta_z = 6.25 \text{ mm} \times 6.25 \text{ mm} \times 6.25 \text{ mm}$ . The grid of wall in the region ( $-0.7 \text{ m} \leq x \leq -0.7 \text{ m}, 0.39 \text{ m} \leq y \leq 0.42 \text{ m}, 0 \text{ m} \leq z \leq 4.1 \text{ m}$ ) was refined to  $\Delta_x \times \Delta_y \times \Delta_z = 50 \text{ mm} \times 50 \text{ mm} \times 50 \text{ mm}$ . The background of grid is in  $\Delta_x \times \Delta_y \times \Delta_z = 100 \text{ mm} \times 100 \text{ mm} \times 100 \text{ mm}$ . The total number of grid cells is about 0.4 million.

In all simulations, the Courant–Friedrichs–Lewy number was kept to be smaller than 0.5. RTE is solved every 10 flow time steps. The radioactive transfer equation was calculated by using a relatively coarse

discretization of angular space where the angular space was discretized into 48 solid angles.

### C) The effects of turbulence model on the temperature profile of window fire

Four turbulence models attempt to simulate window fire was conducted and compared, which are homogeneousDynOneEqEddy, lowReOneEqEddy, OneEqEddy and Smagorinsky. The former three turbulence models are belongs to one equation eddy viscosity model. In homogeneousDynOneEqEddy model, the behaviour of  $k$  was simulated by eddy viscosity SGS model by using a modelled balance equation. LowReOneEqEddy features a Low-Re  $k$ -equation eddy-viscosity model and oneEqEddy stands for a  $k$ -equation eddy-viscosity model. Smagorinsky is based on the eddy viscosity assumption, which postulates a linear relationship between the SGS shear stress and the resolved rate of strain tensor <sup>[35]</sup>. The typical temperature profiles of window fire performed with different turbulence models are shown in Fig.100. It indicates that the  $k$ -equation eddy-viscosity model could calculate the window fire well.

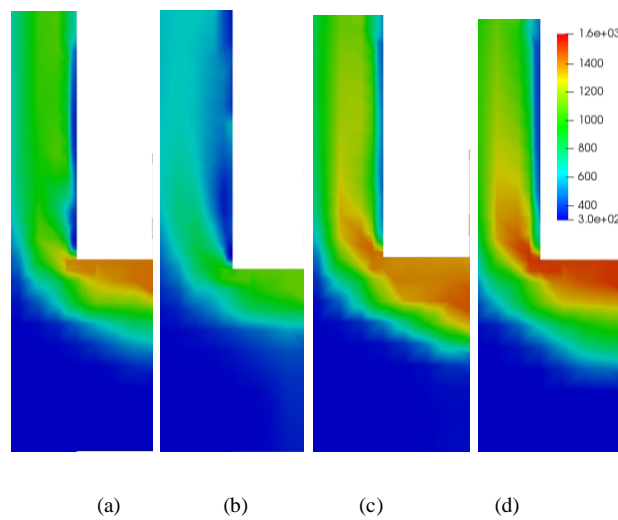


Fig.100 the typical temperature profile of window fire performed with different turbulence models

(a) homogeneousDynOneEqEddy (b) lowReOneEqEddy (c) Smagorinsky (d) OneEqEddy

### D) Temperature distribution of the window opening



Using the baseline grid presented in section 2.2, the LES simulations are found to provide a well-resolved description of compartment fire. Fig.101 presents representative temperature distribution of chamber opening  $900\text{ mm} \times 900\text{ mm}$  from simulation and experiment. The experimental temperature distribution was got by using the temperature profile of thermocouples mesh in  $50\text{ mm} \times 50\text{ mm}$ , which are shown in Fig.101 (a), Fig.101 (b) and Fig.101 (c). It indicates that temperature decreases sharply over opening height in experiment. The temperature discontinuity was found at the half of opening, which was inferred to be related with the neutral plane of window fire. Regarding the representative phenomena of window fire, the fire plume ejects from the upper of opening and cold air inflows from the bottom of opening. In general, the simulation results are consistent with the experimental temperature distribution. The main difference is located at the bottom of opening. In the simulation, the temperature of the bottom of chamber opening is lower than the experimental values.

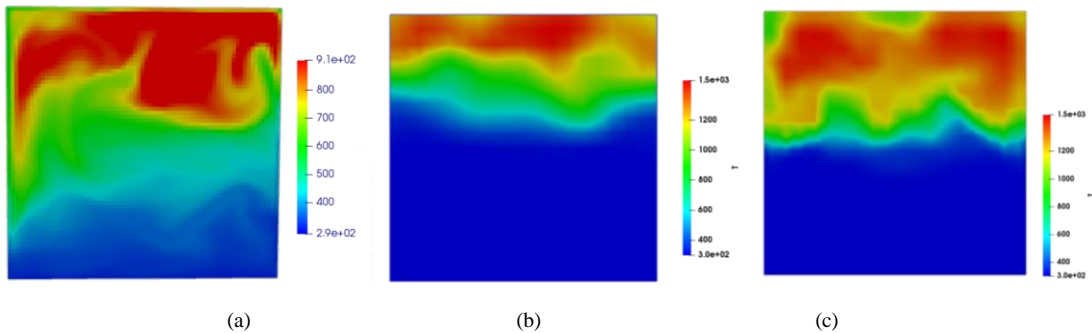


Fig.101 Temperature distribution of the opening from simulation.

(a) Heating intensity 300 kW (b) heating intensity 600 kW (c) heating intensity 600 kW

## E) Flames

Flame is an important characteristic parameter of fire plume spilled from window opening. In the experiment, the flame was recorded by a camera. In the front of window opening, a stainless mesh in  $100\text{ mm} \times 100\text{ mm}$  was used to represent flame behaviours and calculate the flame thickness and length. Furthermore, the temperature field was got by moving the thermocouple mesh in every  $0.15\text{ m}$ , which was

described in section 2.2. The iso-surface of fixed temperature could be calculated by Paraview (version 5.4.0) with 1341 points of temperature field data. In the simulation, an interpolation function surfaceSampling was used to feature the flame shape with a 0.05 of isoValue and a 1 second of writeInterval. The description of flame shapes from simulation and experiment with heating intensity 900 kW is shown in Fig.102. An example of temperature (from 773 k to 1400 k ) iso-surface of fire plume is disclosed in Fig.102 (a). The iso-surface of 773 K is believed to be the flame shape in this study, just as shown in Fig.102 (b). The flame length and thickness in vertical z direction and horizontal y direction are 1.18 m and 0.81 m from simulation, 1.45 m and 0.42 m from experimental iso-surface of 773 k. It indicates that the flame shape of heating intensity 900 kW could be well predicted by simulation, although a little difference was found at the thickness of flame.

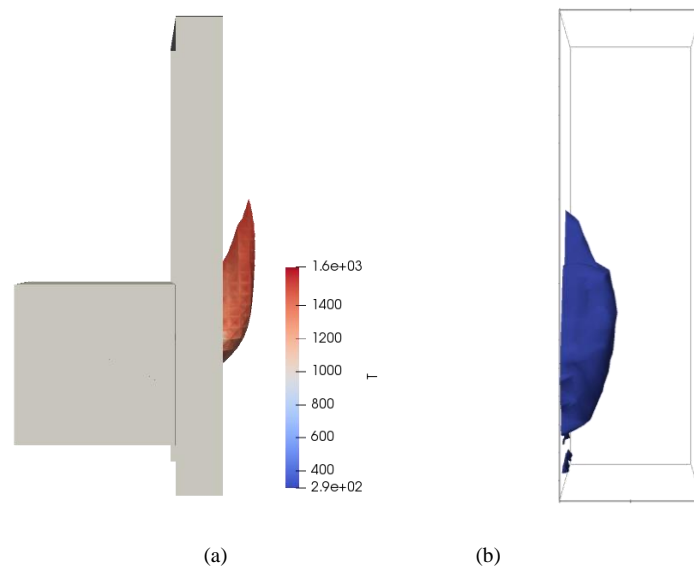


Fig.102 Description of flame shape from simulation and experiment with heating intensity 900 kW  
(a) The side view of flame shape from simulation (b) The side view of iso-surface 773 k of fire plume

Regarding the chamber with heating intensity 300 kW, the fire plume without flame was observed during test, which was shown in Fig.103 (a) and Fig.103 (b). The flame length and thickness in vertical z direction and horizontal y direction are 0.39 m and 0.26 m from simulation and 0.98 m and 0.24 m from experimental iso-surface of 773 k. The fire plume re-attaching-to-wall behavior was observed. The description of flame

shape from simulation and experiment with heating intensity 600 kW is disclosed in Fig.104. It indicates that the flame length and thickness in vertical z direction and horizontal y direction are 1.20 m and 0.31 m from simulation, 1.34 m and 0.30 m from experimental iso-surface of 773 k. It shows that the flame shape is mainly insistent with simulation results. The experimental 773 k iso-surface of fire plume was found to be longer in flame length than simulation and experimental image.

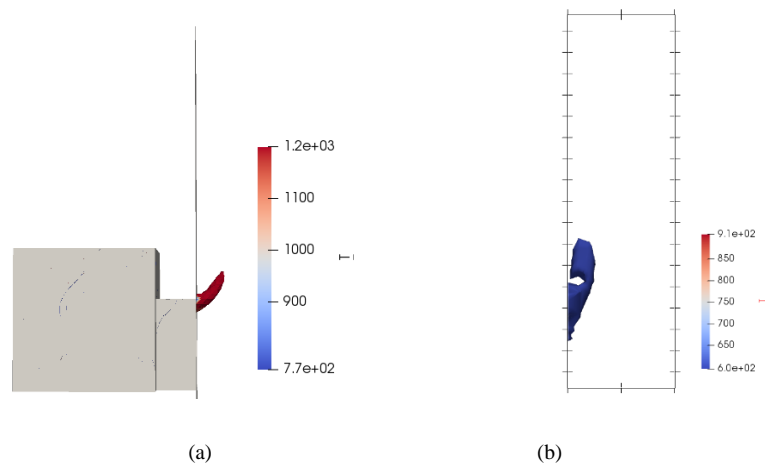


Fig.103 Description of flame shape from simulation and experiment with heating intensity 300 kW  
 (a) The side view of flame shape from simulation (b) The side view of iso-surface 773 k of fire plume

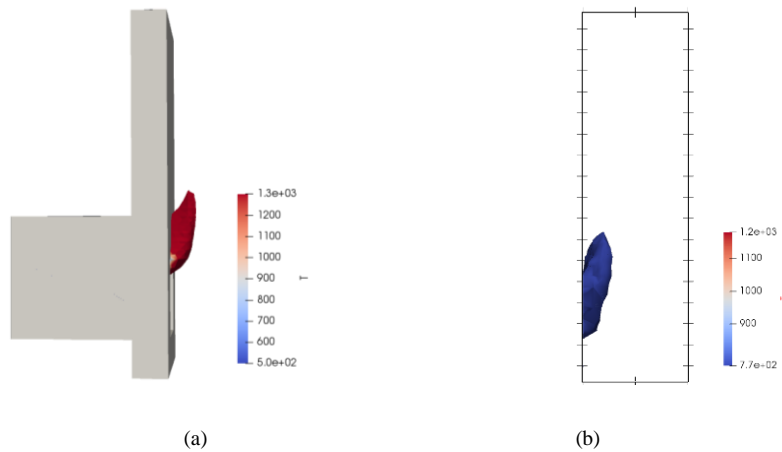


Fig.104 Description of flame shape from simulation and experiment with heating intensity 600 kW  
 (a) The side view of flame shape from simulation (b) The side view of iso-surface 773 k of fire plume

**F) Temperature profile of fire plumes**

The temperature distribution of flame is compared with three methods. It consists of thermal camera, simulation and thermocouple mesh. The temperature distribution of fire plume with heating intensity 300 kW, 600 kW and 900 kW is shown in Fig.105. Regarding the temperature information of fire plume performed heating intensity 300 kW, the simulation is found to be little higher than the values from thermal camera and thermocouple mesh. The temperature of thermocouple mesh is observed to be lower than the values from thermal camera, which is inferred to be attributed to the reduction of heat from the beads of thermocouple. This also could be used to explain the phenomena that the temperature of simulation is little higher than the values from the thermocouple mesh. The similar results are observed in the comparison of temperature distribution performed heating intensity 600 kW and 900 kW. It indicates that the fire plume temperature information could be predicted by simulation.

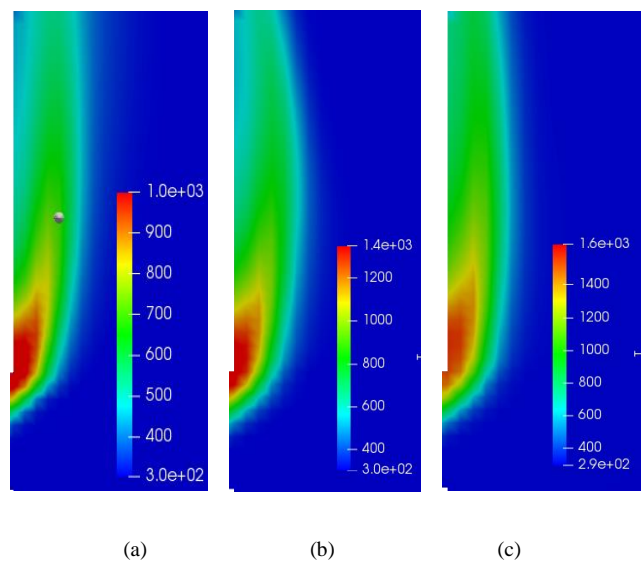


Fig.105 The temperature distribution of fire plume with heating intensity 300 kW, 600 kW and 900 kW (a) heating intensity 300 kW (b) heating intensity 600 kW (c) heating intensity 900 kW

### G) Temperature over façade wall

The temperature over non-combustible wall is very important in the façade fire spread. Usually, the window fire spilled from a window opening is believed to be a potential ignition source of façade fire. To

avoid the big influence of near-wall region computation during the test, the thermocouple was located in the 2 cm away from the wall. The comparison of typical temperature distribution over non-combustible wall and simulation results are summarized in the Fig.106. The comparison results of fire plume performed with 300 kW, 600 kW and 900 kW are shown in the Fig.106 (a), Fig.106 (b) and Fig.106 (c), respectively. The temperature profiles of fire plume with heating intensity of 300 kW is found to be not insistent with experimental results. However, the simulation of temperature information over wall shows a good agreement with experiments performed with 600 kW and 900 kW. This indicates that the calculation of fire plume without flames seems a little hard. Regarding the fire plume spilled from a window opening, the numerical modelling of transition from momentum-driven type to buoyancy-driven type fire plume is difficult in the current step.

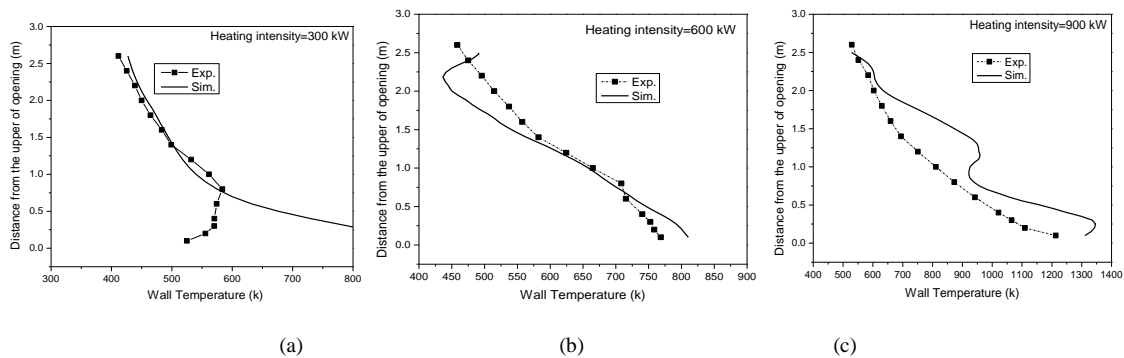


Fig.106 The comparison of typical temperature distribution over non-combustible wall and simulation results (a) temperature profiles of 300 kW (b) temperature profiles of 600 kW (c) temperature profiles of 900 kW

#### H) Heat flux density over non-combustible wall

The heat flux meters were installed to the surface of wall to feature the heat flux density during the test. The heat flux density of simulation of 600 kW and 900 kW showed a good agreement with the experimental values within the region near opening, which is shown in the Fig.107. The reduction of heat flux density of simulation from vertical 0.9 m to 2.5 cm is found to be much larger than values from experiments. Regarding the chamber performed 300 kW, the low heat flux density compared with experimental values

was inferred to be attributed to the fire plume without of flames. In the current version of FireFOAM, the heat flux density over wall received from flame is based on the theory described in section 2.2.5. Considering that the fire plume without flames was observed during test with heating intensity 300 kW, the simulation result is reasonable.

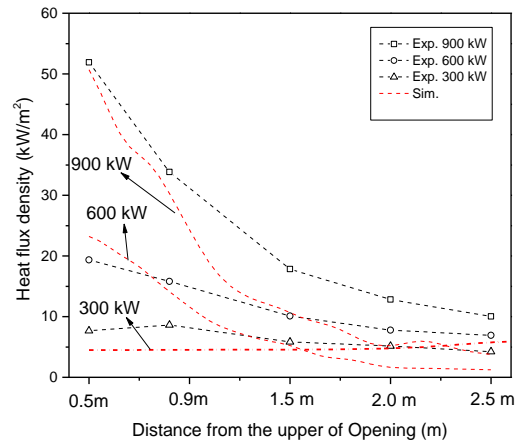


Fig.107 The comparison of typical heat flux density distribution over non-combustible wall and simulation results

## I) Summary

This part presents a numerical LES study of an intermediate-scale window ejected fire with an emphasis on the evaluation of the ability of FireFOAM (2.2.x) to simulate intermediate-scale buoyant fire plumes. Both simulation and experiment are conducted. It is found that with optimal configuration the simulation results are in a good agreement with experimental data on the basis of discussion on flames shapes, temperature vertical distribution inside the chamber, temperature distribution versus vertical distance over external facade surface, heat flux density and temperature over non-combustible walls. The discrepancies are found in the bottom temperature of fire compartment. Temperature profiles vs. vertical distance inside chamber of simulation was believed to be lower than experimental values in the region near bottom of chamber. The fire plume shape is sensitive to the grid size of window opening because of Fr number. In the experiment test, the velocity measurements was unavailable. And a limited set of heat flux meters were

used to provide the heat flux information over external non-combustible walls. In the following, the cedar façade fire simulation would be attempted using FireFOAM.

#### **4.4.3 Numerical study of cedar façade fire**

Many numerical studies attempt to model the façade fire by using computational fluid dynamics (CFD) tools in the past decades. A computational study on structural barrier to vertical spread of window spill plume along building exterior façade was conducted using FDS by Xing Xue-fei et al. <sup>[143]</sup>. María P. Giraldo investigated on some aspects of fire propagation through the ventilated cavity in ventilated façade systems by using FDS <sup>[144]</sup>. The ability of the FDS to simulate window ejected flames was evaluated by M. Duny <sup>[145]</sup>. It was concluded that overall predictions were in relatively good agreement on the basis of magnitude and distribution. Investigation on smoke spread in the cavity of a double-skin facade (DSF) was reported by Cheuk Lun Chow by using FDS <sup>[146]</sup>. Regarding another fire simulation tool FireFOAM, developed by Yi et al. from FM Global and has been subjected to numerous validation, it was concluded that the FireFOAM model performed well for fire plumes and vertical fire spread. However, the investigation on using FireFOAM to model façade fire is unavailable currently.

Traditionally, wood has been used less frequently for facades in the past decades. However, the wood market is evolving substantially because wood and modern wood-based facades are regarded to be a proper choice for a final facade cladding for new, modern architectural structures as well as for the process of reconstruction of the existing ones <sup>[147, 148]</sup>. The experimental timber façade fire experimental research have received focused attentions <sup>[70, 149-151]</sup>. With respect to the wood pyrolysis model of FireFOAM, it has been successfully modelled and validated <sup>[39, 152]</sup>.

The present study for simulating the cedar façade fire is carried out using an open source code FireFOAM. In this study, the experimental configuration including JIS A 1310 and FPA tests, numerical setup of

simulation are briefly summarized in section 2. Following this, comparison of simulation and experiment is described and discussed.

#### A) Numerical configuration

The computational domain is 5 m high in the vertical z-direction, 6.4 m deep in the wall normal x-direction, and 6 m wide in the span-wise y-direction, which is shown in Fig.108. The modified numerical configuration is made of the gas combustion chamber (size in  $L \times W \times H = 1.40 \text{ m} \times 1.40 \text{ m} \times 1.40 \text{ m}$ ), fire spreading chamber opening (size in  $L \times W = 0.90 \text{ m} \times 0.90 \text{ m}$ ), gas burner (size in  $L \times W = 0.60 \text{ m} \times 0.60 \text{ m}$ ) and the non-combustible façade wall (size in  $L \times W \times H = 4.10 \text{ m} \times 1.80 \text{ m} \times 0.25 \text{ m}$ ). The chamber opening size was modified from 0.91 m to 0.9 m in the current simulation to avoid the difficulty of mesh configuration and the extra computational cost. In experiment, the thick ceramic fiber blanket was fixed on the internal surfaces of chamber. With an aim to use the similar condition in simulation, the five surfaces of chamber were defined as pyrolysisRegion model, which is the irreversible Arrhenius solid reaction with a larger activation energy E.

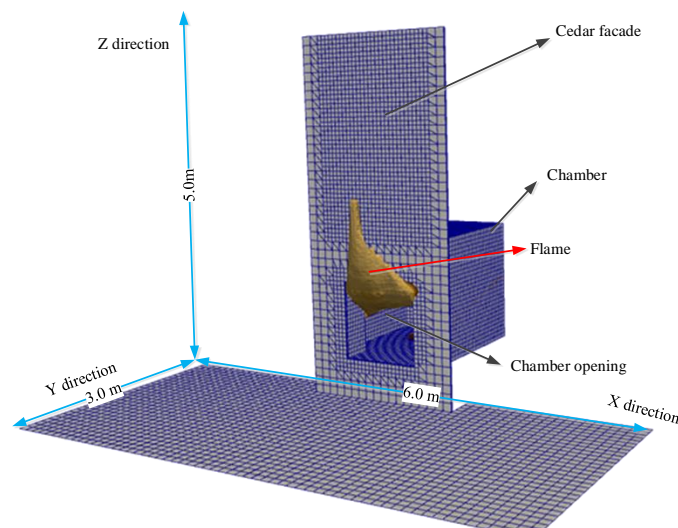


Fig.108 The computational domain for cedar façade fire simulation.



## B) The pyrolysis model of cedar

FPA test description and results consisting of MLR, HRR and THR are shown in Fig.109. The flame of cedar specimen imposed to  $15 \text{ kW/m}^2$  started from 334 s to 1160 s. The flames of cedar specimen exposed to  $45 \text{ kW/m}^2$  lasted from 13 s to 859 s. Fig.109 (a) features a flame during test. The dot lines represent tested data. The lines give the pyrolysis model results using the optimized material properties from the table 25. The black one features the results when cedar were exposed to external heat flux  $15 \text{ kW/m}^2$  in an air atmosphere. The blue one represents the results when cedar were exposed to external heat flux  $45 \text{ kW/m}^2$  in an air atmosphere. It indicates both in low heat flux and high heat flux, MLR histories of pyrolysis model in Fig.109 (b) feature similar behaviour qualitatively with experimental results. The representative HRR histories which shows two peaks are provided in Fig.109 (c). When the cedar exposed to external heat flux  $15 \text{ kW/m}^2$ , the first peak at  $t=390 \text{ s}$  in the curve takes place after the initial heating period, when volatile pyrolysis gases are sufficient enough for ignition by an external spark igniter. At this stage, the heat generated by combustion sustains the pyrolysis of wood which accompanies further release of more volatiles. After the first peak, a downward trend follows from 390 s to 600 s. The dip in the curve may be attributed to the formation of an insulating char layer, where heat transfer is more difficult and the pyrolysis process slows down <sup>[153]</sup>. The second peak at 931 s is considered to be resultant of the sample burn-through and char cracking, facilitating the escape of more volatiles <sup>[154]</sup>. Following the exhaustion of volatiles, flaming combustion ends and the HRR returns to a steady baseline. The final dip after 931 s in the HRR of the FPA test is most likely due to the lack of material below the pyrolysing fuel. In general, the first peak is derived from sufficient pyrolysis for gas ignition and the second peak is caused by sample burn-through and char cracking. The pyrolysis model results for THR using optimized material properties in Table 25 are plotted in Fig.109 (d). In general, the good agreements are observed in the comparison of model and experimental values. At high heat flux,  $45 \text{ kW/m}^2$ , the agreement of initial time degrades a little. In the

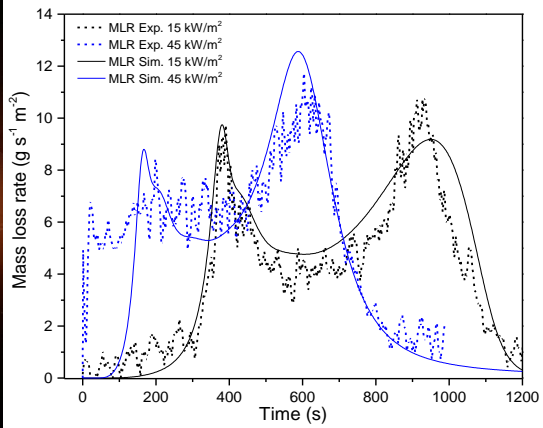
current version of FireFOAM, the water effects on the pyrolysis model is not taken into account.

Table 25 Optimized material properties for modelling

Items	Property	Unit	Value
Cedar	Thermal Conductivity	W/m <sup>2</sup> /K	0.09
	Density	kg/m <sup>3</sup>	500
	Heat Capacity	J/kg/K	800
	Emissivity/Absorptivity		0.17/0.17
Char	Thermal Conductivity	W/m <sup>2</sup> /K	0.12
	Density	kg/m <sup>3</sup>	52.3
	Heat Capacity	J/kg/K	900
	Emissivity/Absorptivity		0.85/0.85
Reaction	Pre-exponential Factor	s <sup>-1</sup>	2.75e7
	Activation Energy	J/mol	1.70e4
	Heat of Pyrolysis	J/kg	1e4
	Reaction Order		3.05



(a)



(b)

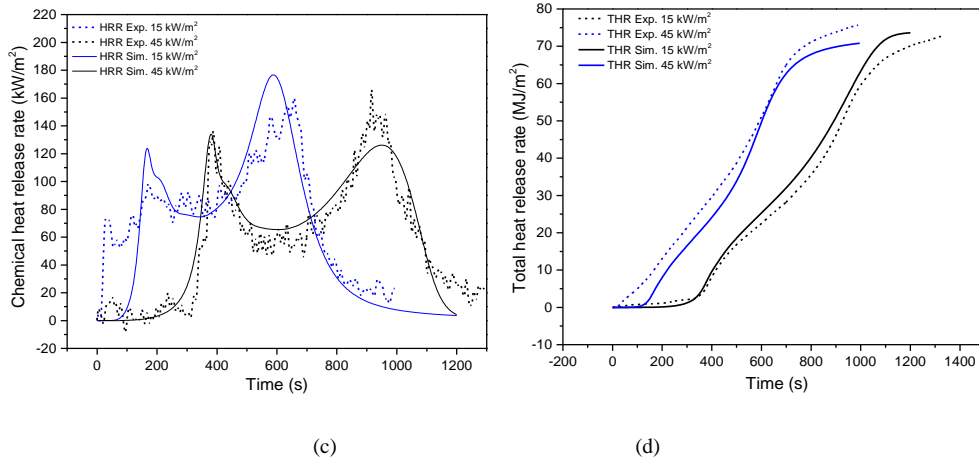


Fig.109 FPA test description and results comparison with model

(a) The description of FPA test at  $t=251s$  with radiation flux  $45kW/m^2$  (b) MLR of FPA test and pyrolysis model as a function of imposed external heat flux and time in an air atmosphere (c) chemical HRR of FPA test and pyrolysis model (d) THR of FPA test and pyrolysis model

### C) Grid configuration

The computational grid was generated by an OpenFOAM mesh tool called SnappyHexMesh. The grid features three levels of resolution in the computation domain. The grid of chamber in the region  $(-0.7 m \leq x \leq -0.7 m, -1.4 m \leq y \leq 0 m, 0.45 m \leq z \leq 1.85 m)$  was refined to  $\Delta_x \times \Delta_y \times \Delta_z = 50 mm \times 50 mm \times 50 mm$ . The grid of window opening in the region  $(-0.45m \leq x \leq 0.45 m, 0 m \leq y \leq 1 m, 0.4 m \leq z \leq 1.3 m)$  was coarsened to  $\Delta_x \times \Delta_y \times \Delta_z = 100 mm \times 100 mm \times 100 mm$ . The grid in the near façade region  $(-0.9 m \leq x \leq 0.9 m, 0.4 m \leq y \leq 0.45 m, 1.35 m \leq z \leq 3.95 m)$  was refined to  $\Delta_x \times \Delta_y \times \Delta_z = 6.25 mm \times 6.25 mm \times 6.25 mm$ . The grid in the region  $(-0.7 m \leq x \leq -0.7 m, 0.45 m \leq y \leq 0.95 m, 1.5 m \leq z \leq 4.1 m)$  was refined to  $\Delta_x \times \Delta_y \times \Delta_z = 25 mm \times 25 mm \times 25 mm$ . The background of grid is in  $\Delta_x \times \Delta_y \times \Delta_z = 100 mm \times 100 mm \times 100 mm$ . The total number of grid cells is 0.67 million. In all simulations, the Courant–Friedrichs–Lewy number was kept to be smaller than 0.9. RTE was solved every 10 flow time steps and in radiation module, the angular space was discretized into 48 solid angles.

#### D) The temperature

The façade fire test lasted for 20 min. Fig.110 represents the temperature profiles varying test condition including blank test and cedar façade fire test. In Fig.110 (a), the symbol circle features experimental value, the dash line indicates the blank test results. The line shows the numerical results. After the fire plume which ejects from compartment fire attached to cedar façade specimen, cedar specimen was ignited soon. The temperature over façade surface increases sharply, just as shown in Fig.110 (a) at the beginning of test. Then a downward trend follows from 69 s to 401 s. The dip in the curve is inferred to be attributed to the formation of an insulating char layer over cedar specimens, where heat transfer is difficult and the pyrolysis process slows down. The sudden flame enlargement was observed at about 400s during test. Another following peak, at about 850 s, is considered to be resultant of the cedar specimen burn-through and char cracking.  $\Delta$  represents the temperature increase of cedar fire test over blank test. The maximum temperature increase of  $\Delta T_1$ ,  $\Delta T_2$ ,  $\Delta T_3$ ,  $\Delta T_4$ ,  $\Delta T_5$  are 185 k, 250 k, 285 k, 267 k and 274 k, respectively. It shows in general, the agreement between experimental data and numerical results is good during the fully-developed phase, temperature histories of façade fire simulation in Fig.110 (a) represent similar behaviour qualitatively with experimental results. Discrepancies may be substantial for a particular time (for instance, in case T1, the simulated temperature is over-estimated by approximately 35% on average) but the overall qualitative trends are correctly captured.

Fig.110 (b) features the temperature distribution of back side of cedar specimens. Regarding the peak of back temperature T 1 showed at  $t=525s$ , it was inferred to be related with the deflagration caused by the mixture of air and volatile combustible gas, which is consistent with an appearance of peak in surface temperature histories. Then a downward trend follows because of specimen burn out and temperature approaches the value of blank test, which shows in the histories of back-T1 line.

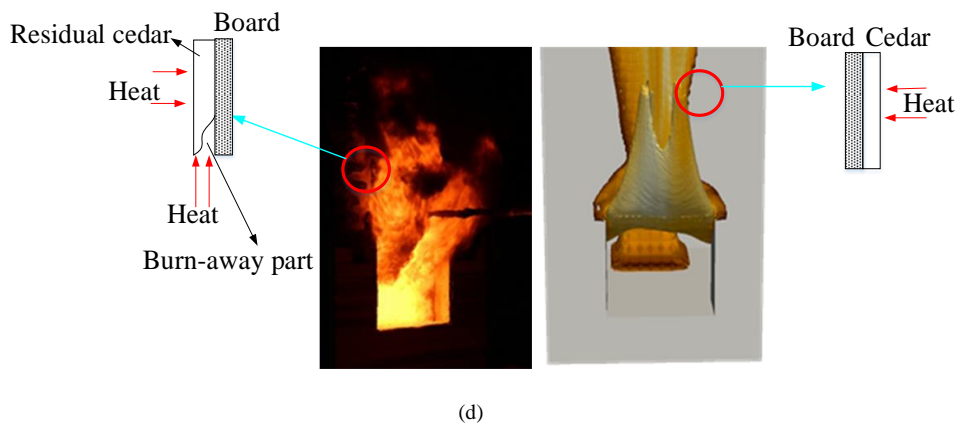
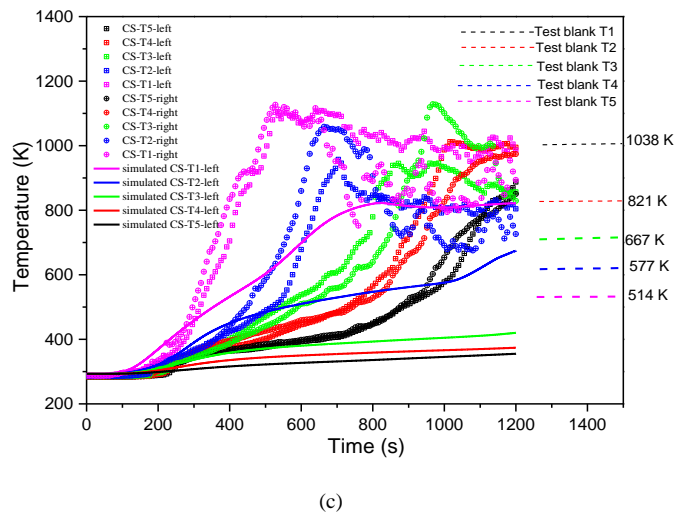
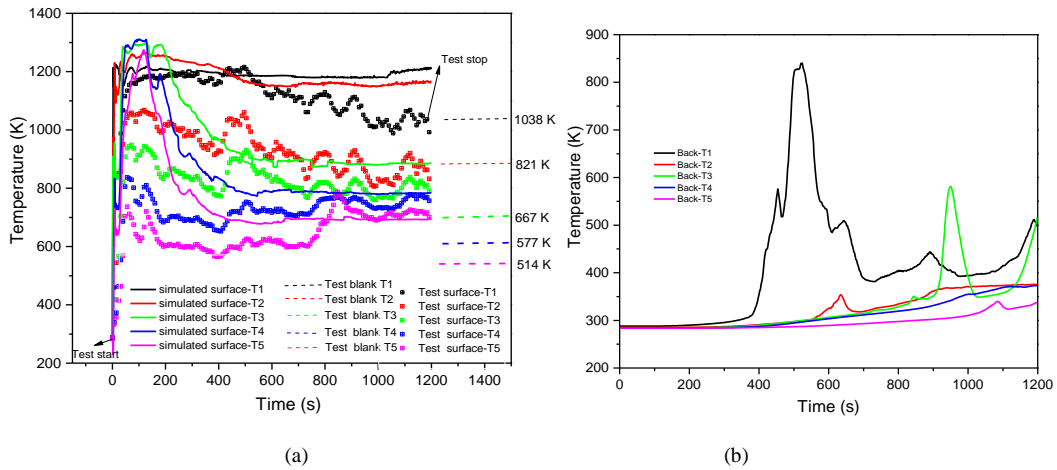


Fig.110 temperature profile comparison of experiments and simulation (façade test) (a) surface temperature distribution of test and model (b) back temperature distribution of test (c) comparison of experimental and simulated temperature profiles over calcium silicate board (d) the description of combustion difference between experiments and simulation over façade surface

## E) HRR and THR

Fig.111 features the HRR and THR comparison of simulation and façade fire test. Fig.111 (a) represents the results of blank test and blank simulation. It is found that both HRR and THR of blank simulation shows a good agreement with results of blank test. As shown by the HRR curves, there are two main differences. The simulated HRR shows smoother than tested HRR histories. Furthermore, a time delay shows in the experimental HRR line at the beginning of test. However in the simulation, no time delay is found because of the utilization of modified Eddy Dissipation Combustion Model (EDM) model and C3H8 irreversible infinite reaction model.

Fig.111 (b) shows the HRR and THR results of cedar façade fire test and simulation results. The evolution of the HRR and THR seems to be reproduced, although discrepancies exist in a particular period of time. At the beginning of test, the simulated HRR is over-estimated by approximately 12 % on average). Then the simulated HRR is under-estimated by approximately 15 % on average. Regarding the THR curves of façade fire test, the simulated THR is over-estimated before 600 s by about 10 % and under-estimated after 900s by about 13 % on average. Consequently, it is concluded that the amount of energy released could be correctly estimated.

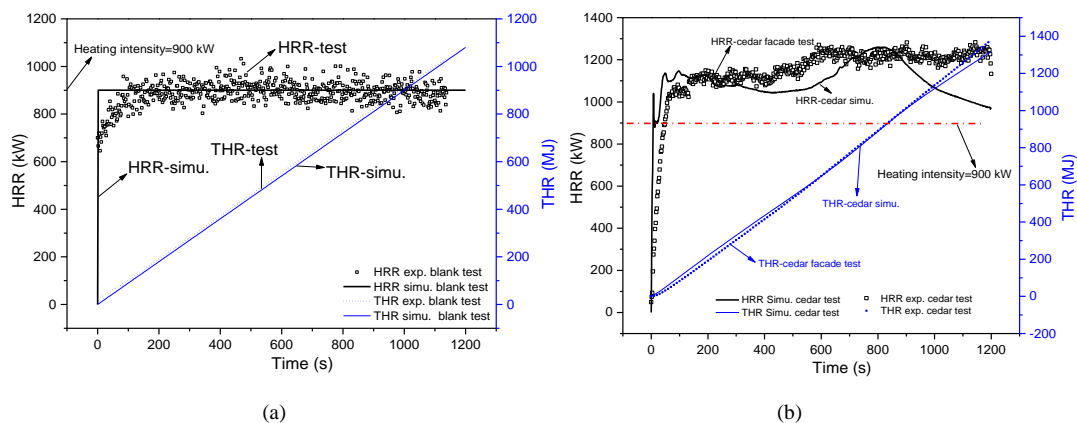


Fig.111 HRR and THR comparison of experiments and simulation (blank test and façade test)

(a) HRR and THR comparison of blank test and blank simulation (blank test means on cedar exist on façade wall) (b) HRR and THR comparison of cedar experiments and cedar simulation

## F) Flames

Fig.112 features the flame shapes of both simulation and façade fire test. Flames of test are disclosed from (a) to (d). It was observed that the cedar façade was ignited soon after fire plume attached to façade surface, just as shown in Fig.112 (b). The carbon layer was formed fast (shown in Fig.112 (c)). Finally, when the test times approached the 20 min, most of façade cedar was burn out, which is disclosed in Fig.112 (d). The simulated flames are described from (e) to (k) in every 200 s. Comparison of simulated and tested flames indicates that the evolution of the flames seems to be well reproduced

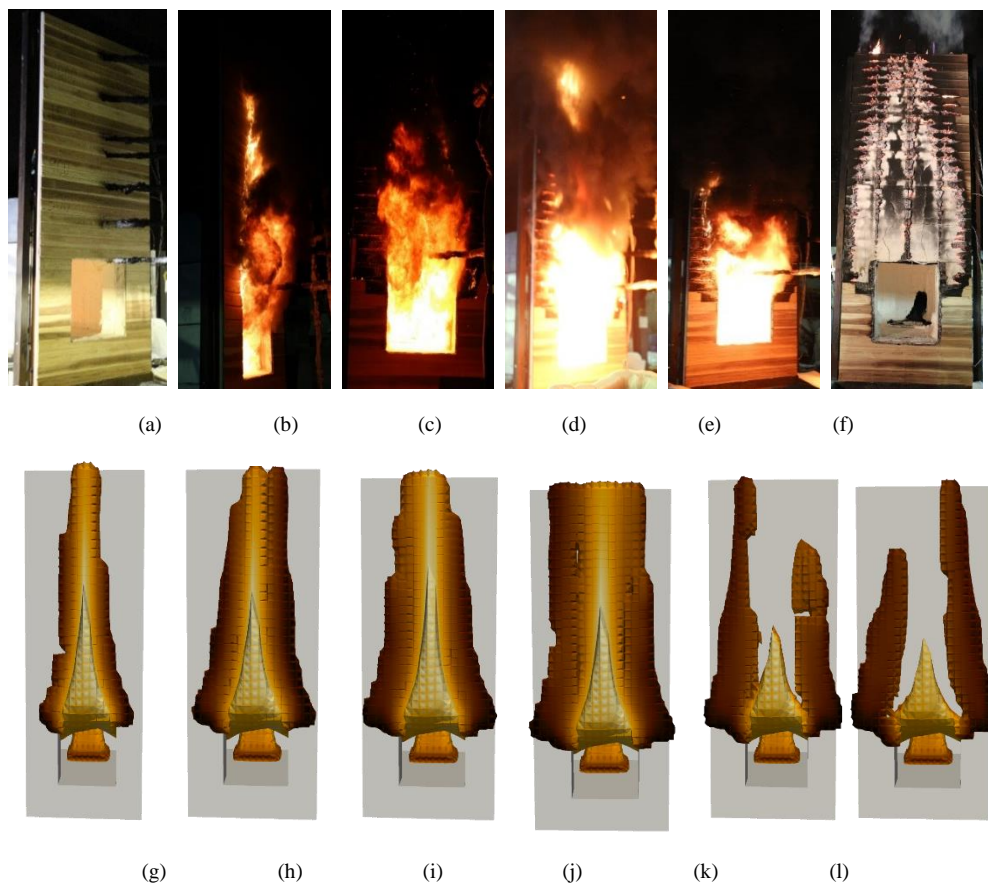


Fig.112 The description of cedar façade fire test varying test time

(a) test t=2 s (b) test t=200 s (c) test t=400 s (d) test t=468 s (e) test t =800 s (f) test t =1200s (g) model t=200 s (h) model t=400 s  
(i) model t=600 s (j) model t=800 s (k) model t=1000 s (l) model t=1200 s

During the test, flame shapes varying test time were captured by a camera. Due to buoyancy force,

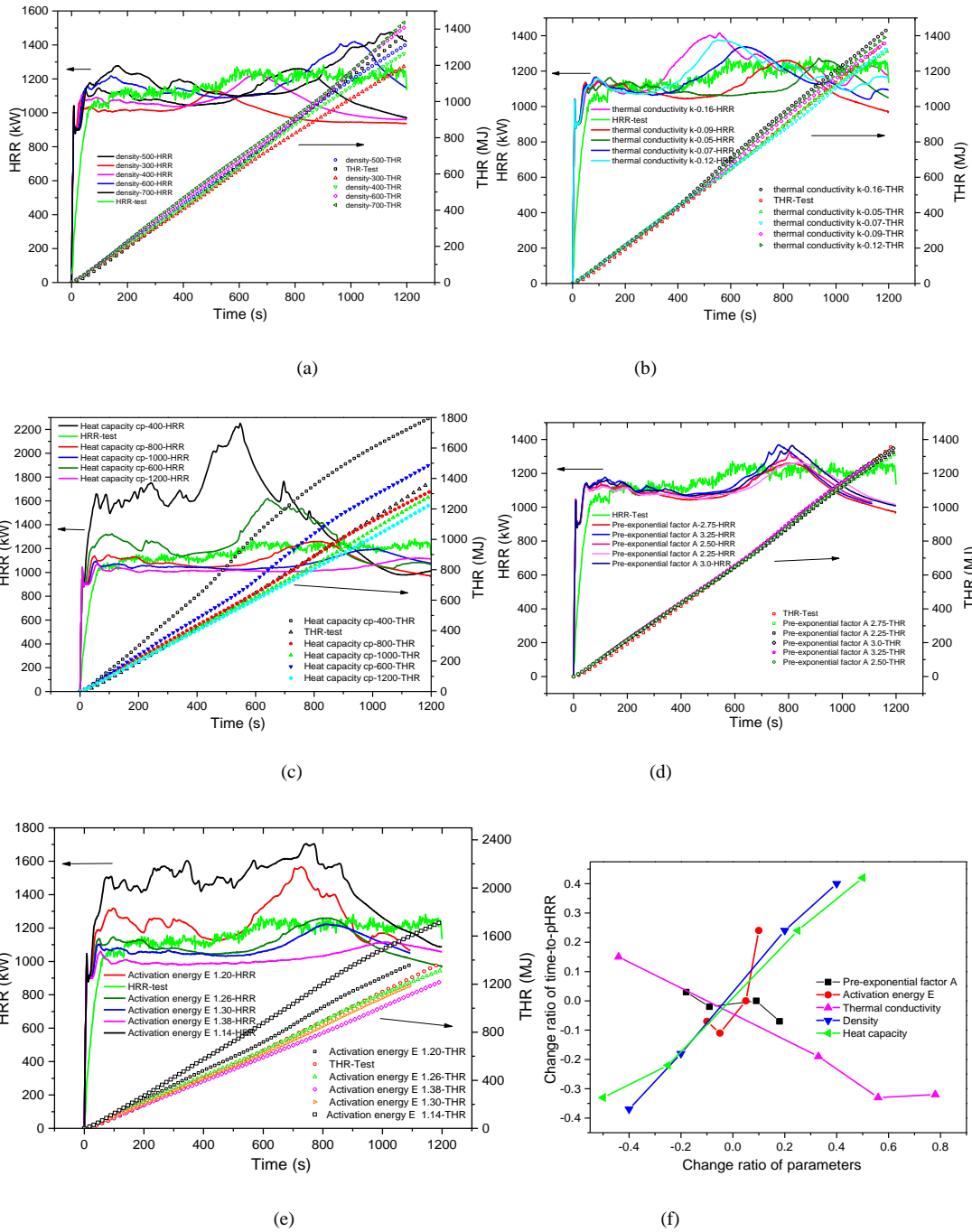
vertical flame spread seems much faster. The change of the fire growth rates among the different stages is mainly attributed to the volatiles combustion. After a layer of carbon formed by the pyrolysis of cedar, the volatiles produce speed was reduced because of thermal resistance caused by fire retardant.

#### **G) Parameters of cedar effects on the HRR of cedar façade fire predicted performance**

The façade fire performance is up to the property of façade material. In this study, the effects of cedar parameters on time-to-pHRR, pHRR (peak HRR) and THR curves are clarified by conducting a series of simulation varying parameters variety. The parameters varied from thermal density, conductivity, heat capacity and pyrolysis reaction parameters. The simulated HRR and THR curves varying above mentioned parameters are disclosed in the Fig.113. Fig.113 (a), Fig.113 (b), Fig.113 (c), Fig.113 (d) and Fig.113 (e) feature the cedar density sensitivity, cedar thermal conductivity k sensitivity, cedar heat capacity sensitivity, cedar pre-exponential factor A sensitivity and cedar activation energy E sensitivity, respectively. The change ratio of parameters effects on the time-to-pHRR, pHRR and THR of cedar façade fire are disclosed in Fig.113 (f), Fig.113 (g), and Fig.113 (h), respectively. The time-to-pHRR is believed to be an important factor of façade fire performance. Fig.113 (f) indicates that the density, thermal conductivity and heat capacity of cedar versus time-to-pHRR are nearly linear. The importance of parameters over time-to-pHRR of cedar façade fire are ranked in the followings: activation energy > Density > heat capacity > thermal conductivity > pre-exponential factor A. Fig.113 (g) shows that the importance of parameters over pHRR of cedar façade fire are ranked in the followings: activation energy > heat capacity > density > pre-exponential factor A > thermal conductivity. Fig.113 (h) shows that the importance of parameters over THR of cedar façade fire are ranked in the followings: activation energy > heat capacity > density > pre-exponential factor A > thermal conductivity. In general, it seems important to use fire retardant technology to increase activation energy of cedar pyrolysis ratio, which would result in low short time-to-pHRR, low



pHRR and THR. Furthermore, increase of heat capacity could effectively reduce pHRR and THR. High density of cedar would show a large time-to-pHRR of cedar façade fire.



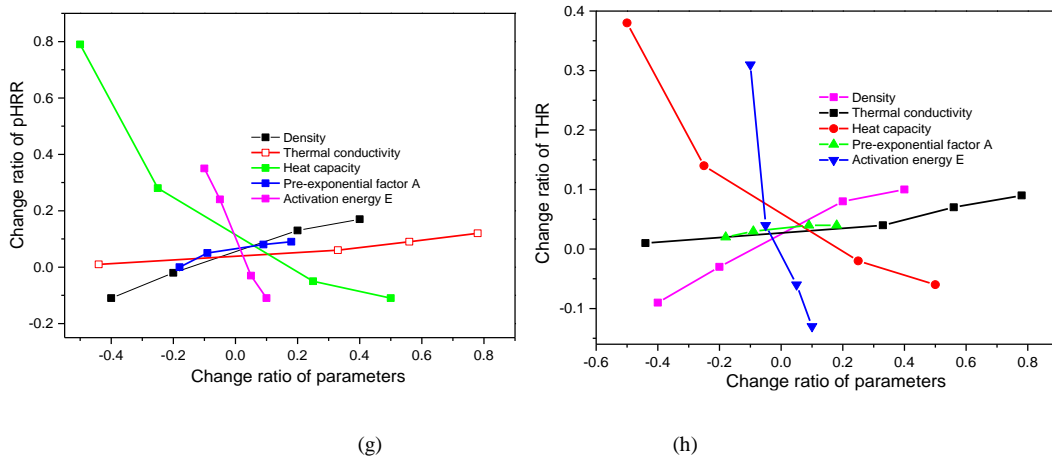


Fig.113 Parameters of cedar effects on the HRR and THR of cedar façade fire

- (a) Density sensitivity (b) thermal conductivity  $k$  sensitivity (c) heat capacity  $c_p$  sensitivity (d) pre-exponential factor  $A$  sensitivity (e) activation energy  $E$  sensitivity (f) parameters variety effects on the change rate of time-to-pHRR (g) parameters variety effects on the change rate of pHRR (h) parameters variety effects on the change rate of THR

## H) Cedar façade fire stop methods

Regarding the large scale façade fire test, it is very hard to conduct because of expensive cost and difficulty of controlled test condition. However, the merit of computational simulation could easily overcome this demerit of experiment method. After the JIS A 1310 façade fire simulation, a traditional fire stop method is discussed in the subtext by conducting a series of simulation, which varies the distance between the upper of window and fire stop, the width of fire stop. In this part, with an aim to describe the fire stop effects on the cedar façade fire vertical spread model, the heating intensity was increased from 0.9 M to 1.2 M because of computational cost. Therefore, all the discussion is under the 1.2M heating intensity. Fig.114 shows the research flows in this part. Firstly, the impact of the distance between the upper of window and fire stop versus cedar façade fire spread is disclosed (Fig.114 (a)). Then the effects of the width of fire stop would be discussed (Fig.114 (b) and Fig.114 (c)), respectively.

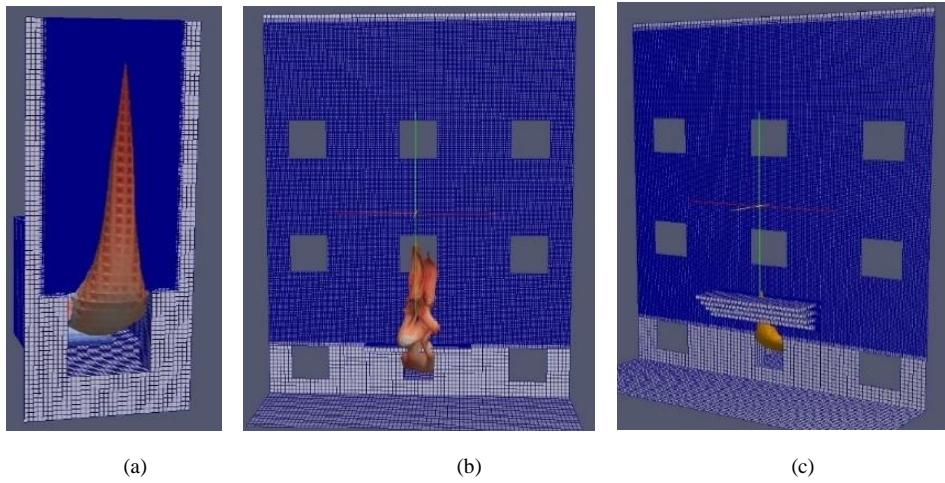


Fig.114 The research flow of this part

(a)The description of window fire (b) the description of distance between the upper of window and fire stop (c) the description of width and length of fire stop

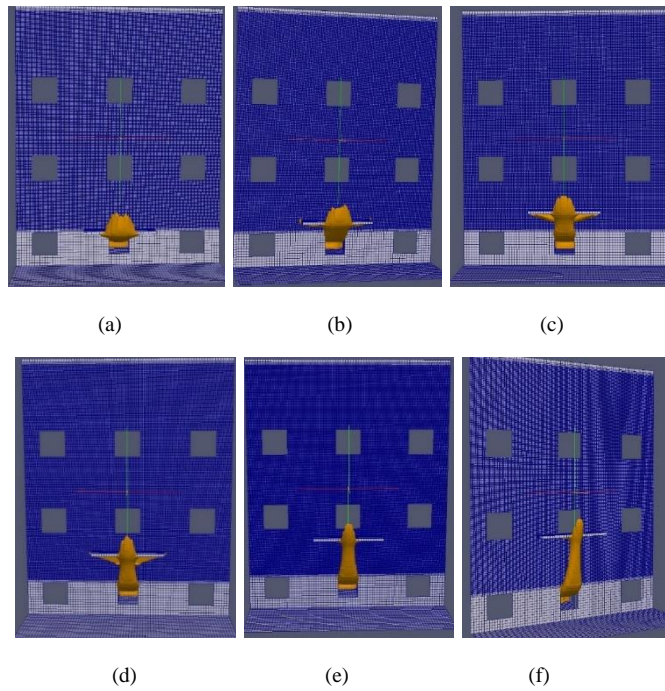


Fig.115 The flame comparison at  $t=6$  s performed with different distances between the upper of window and fire stop (width $\times$ length=0.5 m $\times$ 2.0m) (a)0 m (b) 0.4 m (c) 0.8 m (d) 1.2 m (e) 1.6 m (f) 2.0 m

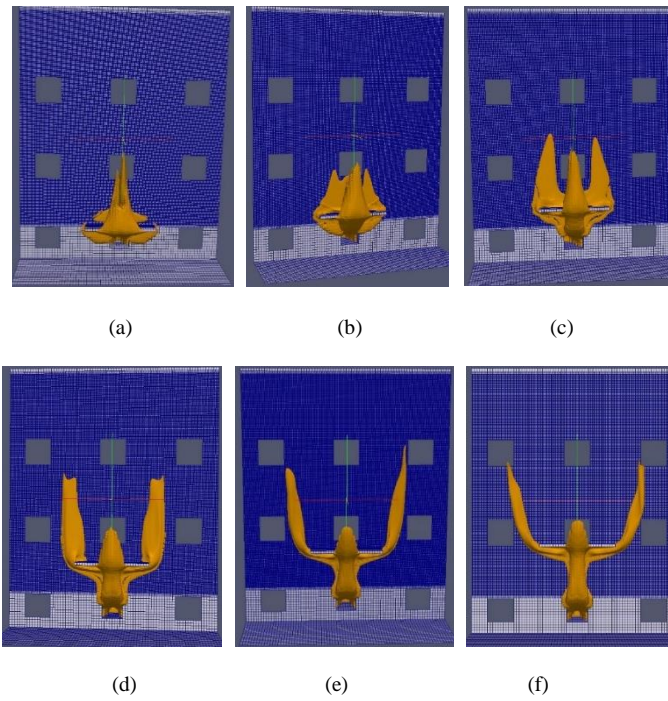


Fig.116 The flame comparison at  $t=50$  s performed with different distances between the upper of window and fire stop (width $\times$ length=0.5 m $\times$ 2.0m) (a)0 m (b) 0.4 m (c) 0.8 m (d) 1.2 m (e) 1.6 m (f) 2.0 m

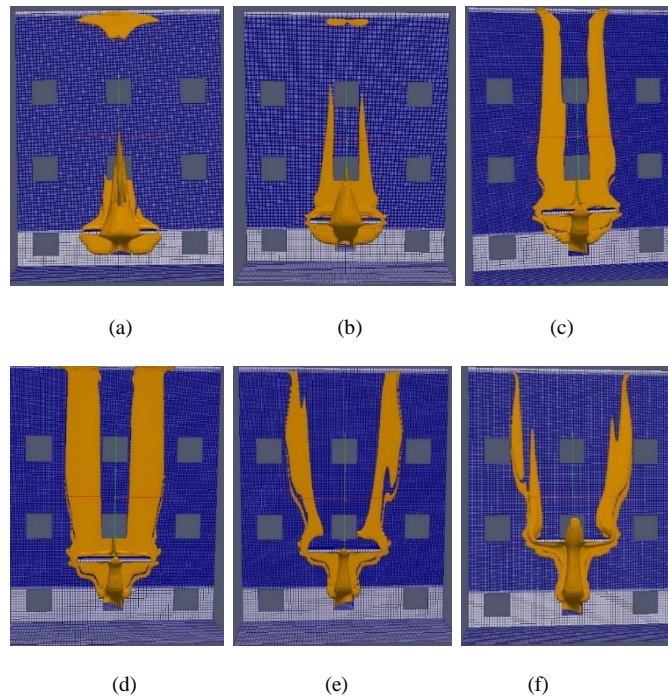


Fig.117 The flame comparison at  $t=100$  s performed with different distances between the upper of window and fire stop (width $\times$ length=0.5 m $\times$ 2.0m) (a)0 m (b) 0.4 m (c) 0.8 m (d) 1.2 m (e) 1.6 m (f) 2.0 m

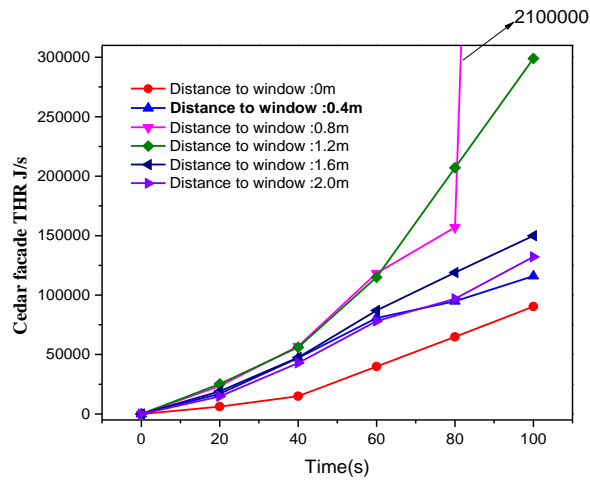


Fig.118 The simulated THR of cedar façade fire varying the distance between the upper of window and fire stop

Fig.115, Fig.116 and Fig.117 features the flame comparison at  $t=6$  s,  $t=50$  s and  $t=100$  s performed with different distances between the upper of window and fire stop, respectively. Fig.118 uses the figure to show the simulated HRR of cedar façade fire varying the distance between the upper of window and fire stop. It is found that as the distance increase the total heat release rate of cedar rises. Although when the fire stop board installed directly to the upper of window showed a lowest THR among six configurations, this method is hard to be performed in the real construction because of architectural aesthetics. It is obvious that the distance between the window and fire stop effects heavily on the window fire spread. The distance should be designed to avoid the 0.8 m and 1.2 m because when the fire stop performed with these two distance, the fast spread flame and highest THR are found (see Fig.118). In the following, the width of fire stop influence over fire spread is discussed by conducting a series of simulation. The width of fire stop varies from 0.3 m, 0.5 m, 0.7 m, 0.9 m, 1.1 m and 1.3 m. The distance used here is a constant value of 0.4 m.



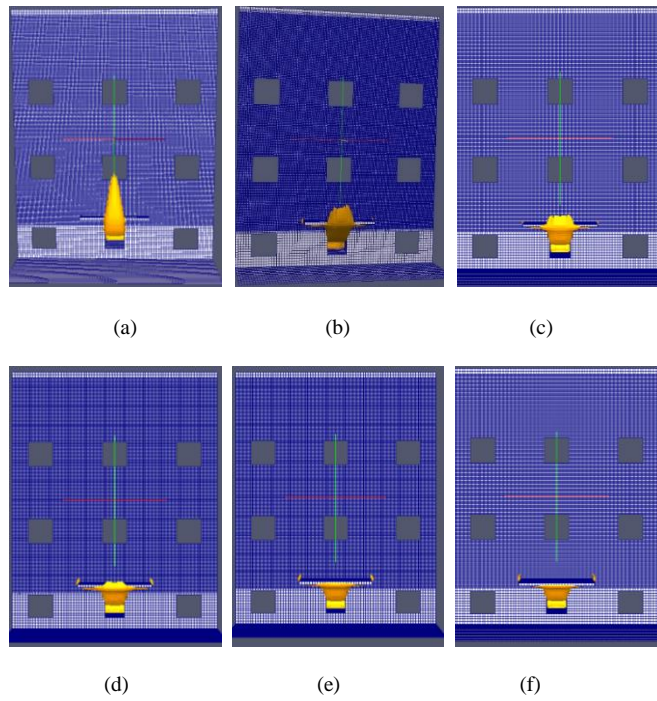


Fig.119 The flame comparison at  $t=6$  s performed with different distances between the upper of window and fire stop (distance=0.4m, length=2m) (a)0.3 m (b) 0.5 m (c) 0.7 m (d) 0.9 m (e) 1.1 m (f) 1.3 m

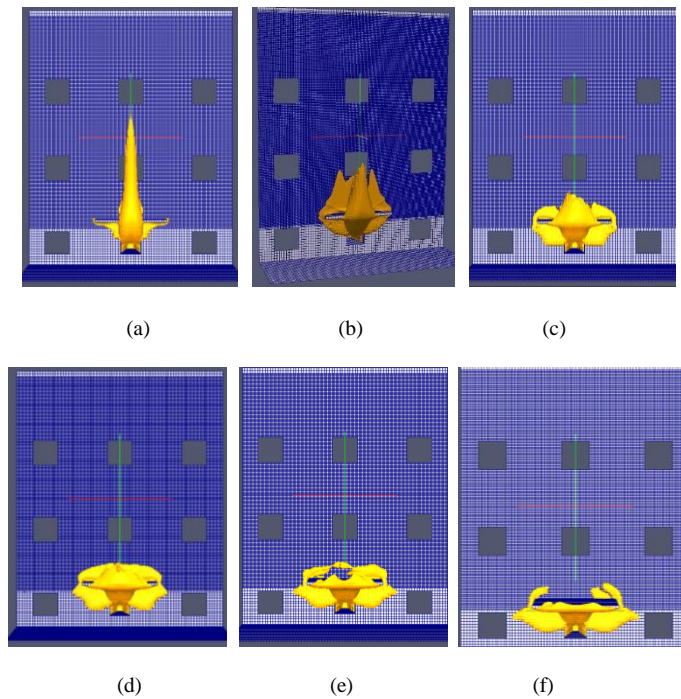


Fig.120 The flame comparison at  $t=50$  s performed with different distances between the upper of window and fire stop (distance=0.4m, length=2m) (a)0.3 m (b) 0.5 m (c) 0.7 m (d) 0.9 m (e) 1.1 m (f) 1.3 m

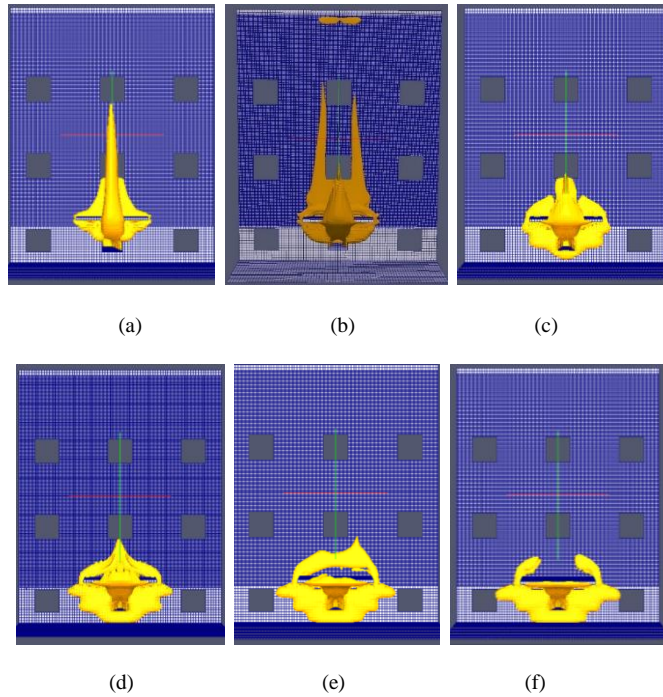


Fig.121 The flame comparison at t=100 s performed with different distances between the upper of window and fire stop (distance=0.4m, length=2m) (a)0.3 m (b) 0.5 m (c) 0.7 m (d) 0.9 m (e) 1.1 m (f) 1.3 m

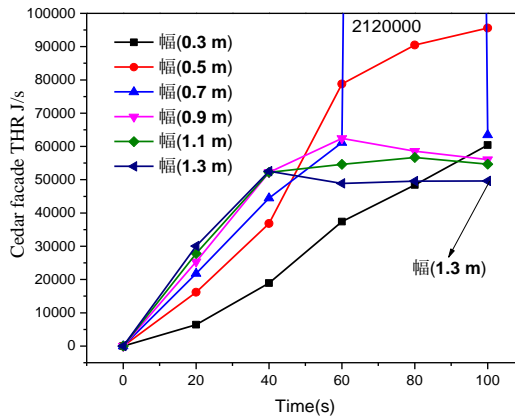


Fig.122 Cedar façade THR varying different fire stop width and time

Fig.119, Fig.120 and Fig.121 features the flame comparison at t=6 s, t=50 s and t=100 s performed with different width of fire stop, respectively. Fig.122 uses the figure to show the simulated HRR of cedar façade fire varying width of fire stop using a constant distance 0.4 m. It is found that before 80 s, the narrow 0.3 m fire stop has the low THR. Regarding the simulation results of 100 s, the THR of case performed with a 0.3 m width seems larger than the value of 0.9 m, 1.1 m and 1.3m. The 1.3 m width of fire stop showing

the good fire prevention capacity is easily to be understood. Regarding the width of 0.5 m and 0.7 m, a sharp increase exist in the curves. It is hard to make a conclusion which is good among the width of 0.9 m, 1.1 m and 1.3 m, the balance between fire prevention and architectural aesthetics is necessary to be taken into account. Here, the discussion is just based on the difference of fire prevention capacity. Before the determination of optimal fire stop configuration, the numerical prediction prefers to be conducted. Just as above discussion, the width of fire stop should be not 0.7 m and 0.5m under the fixed test conditions.

#### 4.5 Summary

In this part, the utilization of CFD in external building fire is presented by a series of simulations and tests. The simulations consist of EPS ETICS Cone, ETICS ICAL, ETICS façade fire, Cedar pyrolysis fire and cedar façade fire. The experimental results include Cone in the horizontal and vertical direction, ICAL test, façade fire of ETICS and cedar façade, FPA test of cedar and the calibration test of JIS A 1310 varying with the opening aspects and heating intensity.

The conclusions based on simulation are described in the followings:

- A) **Pyrolysis modelling.** With respect to simulation works, it is concluded that with accurate input parameters, the numerical mass loss rata and heat release rate prediction could be performed by FDS6.5. MLR and HRR predictions were found to be in a reasonable agreement with the measurements. The discrepancies between the calculated and measured MLR and HRR curves could be explained by the fact that the flame heat flux is not accounted for in the FDS model. In ThermaKin2D, although a simple flame heat flux model is used to simulate the effects of appearance of flame on the materials surface. It seems insufficient since the optimal flame heat flux are needed to be predicted before simulation. Although increasing external heat flux in FDS6.5 or adding flame



heat flux in ThermaKin2D could give a better MLR peak agreement with experimental results, the  $t_{\text{peak}}$  was found to be shortened. A well modelling work of flame heat flux is needed

- B) **LES modelling of window ejected fire plume.** A numerical large eddy simulation (LES) study of buoyant window spill plume from intermediate-scale compartment fires using FireFOAM (2.2.x) is presented. It is found that with optimal configuration the simulation results are in a good qualitative agreement with experimental data on the basis of discussion on flames shapes, temperature vertical distribution inside the chamber, temperature distribution versus vertical distance over external facade surface, heat flux density and temperature over non-combustible walls. The discrepancies are found in the bottom temperature of fire compartment. Temperature profiles vs. vertical distance inside chamber of simulation was believed to be lower than experimental values in the region which is near the bottom of the chamber.
- C) **LES modelling of cedar facade fire.** A numerical large eddy simulation (LES) study of cedar façade fire with an emphasis on the evaluation of the ability of FireFOAM (2.2.x) is disclosed. The simulation results are in a good qualitative agreement with experimental data on the basis of discussion on flames shapes, temperature distribution of over external cedar façade surface, temperature profiles of back cedar façade, heat release rate and total heat release rate over test time. The discrepancies are found that temperature profiles vs. vertical distance over cedar façade surface was higher than experimental values. The effects of cedar parameters on time-to-pHRR, pHRR (peak HRR) and THR curves were clarified by conducting a series of simulation varying from thermal density, conductivity, heat capacity and pyrolysis reaction parameters. The importance of parameters over time-to-pHRR, pHRR and THR of cedar façade fire are discussed. Utilization of fire retardant technology to increase activation energy of cedar pyrolysis ratio would be an effective method to increase time-to-pHRR and lower pHRR and THR. Furthermore, increase of heat

capacity could effectively reduce pHRR and THR. High density of cedar would have a big time-to-pHRR of cedar façade fire.

- D) **Fire-stop configuration effects on a three layer's cedar façade of building.** It is found that both the position and width of fire stop would show heavily effects on the cedar façade fire spread. It is found that the distance should be designed to avoid the 0.8 m and 1.2 m because when the fire stop performed with these two distance, the fast spread flame and highest THR are found. Just as above discussion, the width of fire stop should be not 0.7 m and 0.5m under the fixed test conditions. It is hard to make a conclusion which is good without the analysis of balance between fire prevention and architectural aesthetics, which is necessary to be taken into account. In this part, the discussion is conducted by comparing the difference of fire prevention capacity. Before the determination of optimal fire stop configuration, it is better to conduct the numerical prediction firstly.

In addition, the The conclusions based on experimental works are described in the followings:

- A) **EPS ETICS facade fire.** EPS melt-flow showed an obvious impact on the HRR measurement of EPS ETICS. The traditional test method, for example, Cone and ICAL, seems hard to well evaluate the reaction-to-fire performance of EPS ETICS. The suitable fire risk bench-scale method of EPS ETICS is needed. it is found that EPS ETICS specimen indicates that bench-scale Cone test and intermediate-scale ICAL test are not suitable for evaluation of EPS ETICS reaction-to-fire performance. Because melt-drip effect is believed to have a clear effect on HRR and THR measurement. The recently issued JIS A 1310 standard façade fire test method could be employed to quantify fire risk of EPS ETICS specimen varying heating intensity from 100 kW to 1100 kW, EPS thickness from 50 mm to 300 mm, polymer mortar type including SBR polymer mortar and acrylic resin mortar, reinforcement including one layer and two layer's glass fiber mesh, and

opening edge treatment method differs from back-wrapping method to fire barrier method. The quantitative fire risk of JIS A 1310 standard façade fire test method is proposed on the basis of EPS burn area and façade surface temperature profiles. It is concluded that the INDEX evaluation method could easily clarify the different heating intensity, EPS thickness, polymer mortar type, reinforcement, EPS thickness and opening edge treatment method. EPS ETICS specimen for which the INDEX  $\leq 0.825$  passes JIS A 1310 standard method, and EPS ETICS specimen for which the INDEX  $\geq 0.836$  are judged to be unacceptable (i.e., Fail); the region where the INDEX values are greater than 0.825 but less than 0.836 is uncertain. Correlation between FPI and the INDEX value are needed to be further study. Furthermore, a series of EPS ETICS specimens varied with opening edge treatment and EPS thickness are tested according to JIS A 1310 façade fire test method by using different heating intensity from 300 kW to 1100 kW. On the basis of a small EPS burn area, a low peak temperature, a low time (20 min) averaged temperature and heat flux density of HF1, back-wrapping method is believed to be a good opening edge treatment used in EPS ETCIS building. The time (20 min) averaged temperature of T1 to T5 versus EPS thickness is nearly linear regarding the same heating intensity 300 kW or 600 kW when the EPS thickness differs between 50 mm and 300 mm.

- B) **Temperature profile of buoyant window spill plume from intermediate-scale compartment fires under an over-ventilated condition.** Temperature profile of buoyant window spill plume from intermediate-scale compartment fires under an over-ventilated condition was conducted by using Yokoi's correlation. By taking into the above discussion, the new correlation  $\theta'$  vs.  $\frac{z}{l_0}$  was divided into two type of plots consisting of the none-flame fire plume ejected from window and the fire plume with flames spilled out of window. The new correlation is in the form of  $\theta' =$

$$\frac{\Delta T_z r_0'^{5/3}}{\sqrt[3]{\dot{Q}^2 T_\infty / \rho_z^2 c_p^2 g \times n^6}} = \frac{0.4528}{(1-x)^{1/6}} \left(\frac{T_g}{T_z}\right)^{2/3} \left(\frac{\Delta T_z}{\Delta T_g}\right) = \text{function}\left(\frac{z}{r_0'}\right) , \text{ where the neutral plane (N.P.) is}$$

calculated by the equation  $x = \frac{z_0}{H} = \frac{1}{1+1.04\left(\frac{T_g}{T_a}\right)^{1/3}}$ . The new length scale  $r_0'$  was defined as  $r_0' =$

$$\sqrt{\frac{W(1-x)H}{\pi}}$$

(x is ratio of neutral plane position  $z_0$  and window opening height H ) without the

assumption that neutral plane is a constant 0.5 H . Finally, the chamber dimension effects on the new correlation was discussed by using two different chambers, chamber 2 and chamber 3. It indicates that chamber dimension showed no clear effects on new correlation plot in region 2 with  $10 \geq \frac{z}{r_0'} > 1.5$  .The determination method of neutral plane and the classification basis of heating intensity inside the chamber of none-flame fire plume and fire plume with flames are still needed to be further studied.

**The research for further study is reported.** The simulated results using CFD tools are grid-dependent, parameters-dependent and configuration-dependent. The description that which is better is beyond the scope of this work. However, it is clear that complex pyrolysis models could be reproduced by current version of FDS and ThermaKin. And the flexible of gird configuration and accuracy results impel the FireFOAM to be more and more popular in fire research field.

## 5. Conclusions

In this study, a series of tests and simulation were conducted to report the utilization of CFD in the internal and external building fire.

**Utilization of CFD in the internal building fire.** The conclusions are described in the followings:

- A) The numerical simulation is necessary for fire research. It has many advantages: 1. Low cost, short time and high accuracy. 2. A method for calculating Navier-Stokes equation (N-S) without computer. 3. Rapid computer development 4. Useful prediction before experimental test. 5. Complex architecture and building materials shows a new and big challenge for building safety. By using this method, the problems in building fire tests could be potentially solved.
  - B) In this part, the MLR and HRR of polymers were simulated by employing FDS code. With the accurate input parameters and without considering melt model, the MLR and HRR curves derived from FDS simulation agree with experimental Cone test. The results depends heavily on mesh size. Calculation time step has no serious effect on simulation results. Melt materials are hard to be simulated by FDS code. Currently, the continuity of simulation history needs to be improved.
  - C) The value of conductivity, emissivity, and density versus pMLR is linear, respectively. However, the pMLR reduced as the heat capacity increased. The activation energy shows a heavy effect on the pMLR.
  - D) Regarding the model-box simulation, it is found that the simulated HRR is grid-dependent. The big discrepancy of temperature histories of urethane model-box test is found in the both simulations performed 5 cm and 10 cm. The simulated temperature histories is steadier than experimental values.
- B) Regarding the mode-box test using None-Nurate performed 10 cm, the comparison of simulation and experiment indicates that simulated results are grid-dependent.

**Utilization of CFD in the external building fire.** The conclusions are described in the followings:

- A) **EPS ETICS pyrolysis modelling.** It is concluded that with accurate input parameters, the numerical mass loss rate and heat release rate prediction could be performed by FDS6.5. MLR and HRR predictions were found to be in a reasonable agreement with the measurements. The discrepancies between the calculated and measured MLR and HRR curves could be explained by the fact that the flame heat flux is not accounted for in the FDS model. In ThermaKin2D, although a simple flame heat flux model is used to simulate the effects of appearance of flame on the materials surface. It seems insufficient since the optimal flame heat flux are needed to be predicted before simulation. Although increasing external heat flux in FDS6.5 or adding flame heat flux in ThermaKin2D could give a better MLR peak agreement with experimental results, the  $t_{\text{peak}}$  was found to be shortened. A well modelling work of flame heat flux is needed.
- B) **LES modelling of window ejected fire plume.** A numerical large eddy simulation (LES) study of buoyant window spill plume from intermediate-scale compartment fires using FireFOAM (2.2.x) is presented. It is found that with optimal configuration the simulation results are in a good qualitative agreement with experimental data on the basis of discussion on flames shapes, temperature vertical distribution inside the chamber, temperature distribution versus vertical distance over external facade surface, heat flux density and temperature over non-combustible walls. The discrepancies are found in the bottom temperature of fire compartment. Temperature profiles vs. vertical distance inside chamber of simulation was believed to be lower than experimental values in the region which is near the bottom of the chamber.
- C) **LES study of cedar façade fire.** A numerical large eddy simulation (LES) study of cedar façade fire with an emphasis on the evaluation of the ability of FireFOAM (2.2.x) is disclosed. The

simulation results are in a good qualitative agreement with experimental data on the basis of discussion on flames shapes, temperature distribution of over external cedar façade surface, temperature profiles of back cedar façade, heat release rate and total heat release rate over test time. The discrepancies are found that temperature profiles vs. vertical distance over cedar façade surface was higher than experimental values. The effects of cedar parameters on time-to-pHRR, pHRR (peak HRR) and THR curves were clarified by conducting a series of simulation varying from thermal density, conductivity, heat capacity and pyrolysis reaction parameters.

- D) **Fire-stop configuration effects on the facade fire.** Regarding the fire stop configuration in a three layer's cedar façade of building, it is found that both the position and width of fire stop would show heavily effects on the cedar façade fire spread. It is found that the distance should be designed to avoid the 0.8 m and 1.2 m because when the fire stop performed with these two distance, the fast spread flame and highest THR are found. Just as above discussion, the width of fire stop should be not 0.7 m and 0.5m under the fixed test conditions. Before the determination of optimal fire stop configuration, it is better to conduct the numerical prediction firstly.

In addition, the new founding from experimental works is summarized in the subtext.

- A) **Fire risk evaluation of EPS ETICS.** It is found that EPS ETICS specimen indicates that bench-scale Cone test and intermediate-scale ICAL test are not suitable for evaluation of EPS ETICS reaction-to-fire performance. Because melt-drip effect is believed to have a clear effect on HRR and THR measurement. The recently issued JIS A 1310 standard façade fire test method could be employed to quantify fire risk of EPS ETICS specimens. The quantitative fire risk of JIS A 1310 standard façade fire test method is proposed on the basis of EPS burn area and façade surface temperature profiles. It is concluded that the **INDEX** evaluation method could easily clarify the

different heating intensity, EPS thickness, polymer mortar type, reinforcement, EPS thickness and opening edge treatment method. EPS ETICS specimen for which the **INDEX**  $\leq 0.825$  passes JIS A 1310 standard method, and EPS ETICS specimen for which the **INDEX**  $\geq 0.836$  are judged to be unacceptable (i.e., Fail); the region where the **INDEX** values are greater than 0.825 but less than 0.836 is uncertain.

B) **Opening edge treatment and EPS thickness influence on EPS ETICS facade fire.** A series of EPS ETICS specimens varied with opening edge treatment and EPS thickness are tested according to JIS A 1310 façade fire test method by using different heating intensity from 300 kW to 1100 kW. On the basis of a small EPS burn area, a low peak temperature, a low time (20 min) averaged temperature and heat flux density of HF1, back-wrapping method is believed to be a good opening edge treatment used in EPS ETCIS building. The time (20 min) averaged temperature of T1 to T5 versus EPS thickness is nearly linear regarding the same heating intensity 300 kW or 600 kW when the EPS thickness differs between 50 mm and 300 mm.

C) **Experimental temperature profile of window ejected fire plume.** Temperature profile of buoyant window spill plume from intermediate-scale compartment fires under an over-ventilated condition was conducted by using Yokoi's correlation. By taking into the above discussion, the new correlation  $\theta'$  vs.  $\frac{z}{r'_0}$  was divided into two type of plots consisting of the none-flame fire plume ejected from window and the fire plume with flames spilled out of window. The new

correlation is in the form of 
$$\theta' = \frac{\Delta T_z r'_0{}^{5/3}}{\sqrt[3]{\dot{Q}^2 T_\infty / \rho_z^2 c_p^2 g \times n^6}} = \frac{0.4528}{(1-x)^{1/6}} \left(\frac{T_g}{T_z}\right)^{2/3} \left(\frac{\Delta T_z}{\Delta T_g}\right) = \text{function}\left(\frac{z}{r'_0}\right),$$

where the neutral plane (N.P.) is calculated by the equation  $x = \frac{z_0}{H} = \frac{1}{1+1.04\left(\frac{T_g}{T_a}\right)^{1/3}}$ . The new

length scale  $r'_0$  was defined as  $r'_0 = \sqrt{\frac{W(1-x)H}{\pi}}$  (x is ratio of neutral plane position  $z_0$  and

window opening height H ) without the assumption that neutral plane is a constant 0.5 H . The



chamber dimension effects on the new correlation was discussed by using two different chambers, chamber 2 and chamber 3. It indicates that chamber dimension showed no clear effects on new correlation plot in region 2 with  $10 \geq \frac{z}{r_0} > 1.5$ . The determination method of neutral plane and the classification basis of heating intensity inside the chamber of none-flame fire plume and fire plume with flames are still needed to be further studied.

Finally, the research direction for further study based on above discussion is listed.

- A) The simulated results using CFD tools are grid-dependent, parameters-dependent and configuration-dependent. However, it is clear that complex pyrolysis models could reproduce using current version of FDS and ThermaKin. In future, the flexible of grid configuration and accuracy results makes the FireFOAM to be more and more popular in fire research field. The melt-flow model is needed in the current version of CFD.
- B) The current CFD is insufficient to simulate combustion which is accompanied with heavy smoke and volatile combustion gas. The time to generate flashover is much faster than experimental ones. This is inferred to be attributed to the mixing-control model.
- C) FireFOAM could show a merit in flame simulation. The ThermaKin is suitable for multi-layer or multi-reaction modeling. The mixing-control model needs to improve.
- D) In the current version of FDS, the dynamic mesh is not available. This limitation restricts the application of FDS in the materials which had serious melt-flow. Furthermore, the continuity of simulation history needs to be improved.
- E) When the complex combustion status combined with the yield of pyrolysis products of under-ventilation fire and over-ventilation fire, it is hard to reproduce by using current version of FDS.

The current version of FDS is not suitable for complex flame spread and pyrolysis gas diffusion.

The predicted time to generate flashover is much shorter than experimental time.

- F) The mixing-control model for combustion is not suitable for complex flame spread and combustible gas diffusion.

## 6. References

- [1] Y. Nishio, H. Yoshioka, T. Noguchi, M. Kanematsu, T. Ando, Y. Hase, T. Hayakawa, Fire spread caused by combustible facades in Japan, *Fire Technology* 52(4) (2016) 1081-1106.
- [2] B. Zhou, H. Yoshioka, T. Noguchi, T. Ando, Effects of opening edge treatment and EPS thickness on EPS external thermal insulation composite systems (ETICS) façade reaction-to-fire performance based on JIS A1310 standard façade fire test method, *Fire and materials* (2017).
- [3] F. Moukalled, L. Mangani, M. Darwish, *The finite volume method in computational fluid dynamics*, (2016).
- [4] G.-H. Yeoh, K.K. Yuen, *Computational fluid dynamics in fire engineering: theory, modelling and practice*, Butterworth-Heinemann 2009.
- [5] K. Yang, L. Chang, UNDSAFE-I: A computer Code for Buoyant Flow in an Enclosure, NASA STI/Recon Technical Report N 77 (1977).
- [6] G. Cox, R. Chitty, S. Kumar, Fire modelling and the King's Cross fire investigation, *Fire Safety Journal* 15(1) (1989) 103-106.
- [7] W. Chow, W. Wong, A study of the fire aspect of atria in Hong Kong, *Proceed. 3rd International Symposium on Fire Safety Science*, University of Edinburgh, Scotland, UK, 1991, pp. 335-344.
- [8] K. McGrattan, S. Hostikka, R. McDermott, J. Floyd, C. Weinschenk, K. Overholt, *Fire dynamics simulator technical reference guide volume 1: mathematical model*, NIST special publication 1018(1) (2013) 175.
- [9] S. Stoliarov, R. Lyon, *ThermaKinetic model of burning*, Federal Aviation Administration Technical Note, DOT/FAA/AR-TN08/17, 2008.
- [10] S.I. Stoliarov, S. Crowley, R.E. Lyon, G.T. Linteris, Prediction of the burning rates of non-charring polymers, *Combustion and Flame* 156(5) (2009) 1068-1083.
- [11] Y. Wang, P. Chatterjee, J.L. de Ris, Large eddy simulation of fire plumes, *Proceedings of the Combustion Institute* 33(2) (2011) 2473-2480.
- [12] <https://spectrum.ieee.org/tech-talk/computing/hardware/global-race-toward-exascale-will-drive-supercomputing-ai-to-masses>.
- [13] C.A. Harper, *Handbook of building materials for fire protection*, McGraw Hill Professional 2003.
- [14] K. McGrattan, S. Hostikka, J. Floyd, H. Baum, R. Rehm, W. Mell, R. McDermott, *Fire dynamics simulator (version 5), technical reference guide*, NIST special publication 1018(5) (2017).
- [15] C.L. Ho, K.Y. Li, M.J. Spearpoint, Numerical simulation of scale-model smoke contamination of upper atrium levels by a channelled balcony spill plume, *Fire and materials* 37(8) (2013) 581-596.
- [16] Y. Xin, J. Gore, K. McGrattan, R. Rehm, H. Baum, Large eddy simulation of buoyant turbulent pool fires, *Proceedings of the Combustion Institute* 29(1) (2002) 259-266.
- [17] D.F. Young, B.R. Munson, T.H. Okiishi, W.W. Huebsch, *A brief introduction to fluid mechanics*, John Wiley & Sons 2010.
- [18] H. Tennekes, J.L. Lumley, *A first course in turbulence*, MIT press 1972.
- [19] A.N. Kolmogorov, The local structure of turbulence in incompressible viscous fluid for very large Reynolds numbers, *Dokl.*

Akad. Nauk SSSR, 1941, pp. 299-303.

[20] A. Leonard, Energy cascade in large-eddy simulations of turbulent fluid flows, *Advances in geophysics*, Elsevier 1975, pp. 237-248.

[21] O. Reynolds, On the dynamical theory of incompressible viscous fluids and the determination of the criterion, *Philosophical Transactions of the Royal Society of London. A* 186 (1895) 123-164.

[22] D.J. Mavriplis, Mesh generation and adaptivity for complex geometries and flows, *Handbook of Computational Fluid Mechanics*, Elsevier 1996, pp. 417-459.

[23] E. Fadlun, R. Verzicco, P. Orlandi, J. Mohd-Yusof, Combined immersed-boundary finite-difference methods for three-dimensional complex flow simulations, *Journal of computational physics* 161(1) (2000) 35-60.

[24] J.W. Deardorff, Stratocumulus-capped mixed layers derived from a three-dimensional model, *Boundary-Layer Meteorology* 18(4) (1980) 495-527.

[25] A. Bejan, *Convection heat transfer*, John Wiley & Sons 2013.

[26] B.F. Magnussen, B.H. Hjertager, On mathematical modeling of turbulent combustion with special emphasis on soot formation and combustion, *Symposium (international) on Combustion*, Elsevier, 1977, pp. 719-729.

[27] S.I. Stoliarov, I.T. Leventon, R.E. Lyon, Two-dimensional model of burning for pyrolyzable solids, *Fire and materials* 38(3) (2014) 391-408.

[28] S. Stoliarov, R. Lyon, ThermoKinetic model of burning for pyrolyzing materials, *Fire Safety Science* 9 (2008) 1141-1152.

[29] S.I. Stoliarov, R.E. Lyon, ThermoKinetic model of burning, *Federal Aviation Administration William J. Hughes Technical Center* 2008.

[30] Y.Z. Li, C. Huang, J. Anderson, R. Svensson, I. Haukur, B. Husted, M. Runefors, J. Wahlqvist, Verification, validation and evaluation of FireFOAM as a tool for performance design, 2017.

[31] N. Ren, Y. Wang, S. Vilfayeau, A. Trouvé, Large eddy simulation of turbulent vertical wall fires supplied with gaseous fuel through porous burners, *Combustion and Flame* 169 (2016) 194-208.

[32] N. Ren, Y. Wang, S. Vilfayeau, A. Truvé, Large eddy simulation of turbulent wall fires, 8 th US National Combustion Meeting Paper 070FR-0056, 2013.

[33] A. Yoshizawa, K. Horiuti, A statistically-derived subgrid-scale kinetic energy model for the large-eddy simulation of turbulent flows, *Journal of the Physical Society of Japan* 54(8) (1985) 2834-2839.

[34] F. Nicoud, F. Ducros, Subgrid-scale stress modelling based on the square of the velocity gradient tensor, *Flow, turbulence and Combustion* 62(3) (1999) 183-200.

[35] J. Smagorinsky, General circulation experiments with the primitive equations: I. The basic experiment, *Monthly weather review* 91(3) (1963) 99-164.

[36] F. Jiang, J. De Ris, H. Qi, M. Khan, Radiation blockage in small scale PMMA combustion, *Proceedings of the Combustion Institute* 33(2) (2011) 2657-2664.

[37] J.G. Quintiere, *Fundamentals of fire phenomena*, Wiley Online Library 2006.

[38] S. Welch, P. Rubini, Three-dimensional simulation of a fire-resistance furnace, *Fire Safety Science* 5 (1997) 1009-1020.

- [39] M. Chaos, Spectral aspects of bench-scale flammability testing: application to hardwood pyrolysis, *Fire Safety Science* 11 (2014) 165-178.
- [40] ISO 5660-1: Reaction to fire tests - Heat release, smoke production and mass loss rate - Part 1: Heat release rate (cone calorimeter method).
- [41] ISO/TS 17431:2006 - Fire tests-- Reduced-scale model box test.
- [42]河原崎政行,菊地伸一,田坂茂樹,土橋常登,鈴木秀和,長尺の薬剤処理木材における材内の薬剤分布と模型箱試験による防火性能の評価, (2012).
- [43] J.H. Flynn, L.A. Wall, General treatment of the thermogravimetry of polymers, *J Res Nat Bur Stand* 70(6) (1966) 487-523.
- [44] R.E. Lyon, An integral method of nonisothermal kinetic analysis, *Thermochimica Acta* 297(1-2) (1997) 117-124.
- [45] R.-s. Han, G.-q. Zhu, G.-w. Zhang, Experiment study on the ignition point of XPS foam plastics, *Procedia Engineering* 52 (2013) 131-136.
- [46] D. Pau, C. Fleischmann, M. Spearpoint, K. Li, Thermophysical properties of polyurethane foams and their melts, *Fire and materials* 38(4) (2014) 433-450.
- [47] 日本建築学会, 建築材料の熱 空気 湿気物性値, 丸善, 2001.
- [48] ISO 14696:, Reaction-to-fire tests - determination of fire and thermal parameters of materials, products and assemblies using an intermediate-scale calorimeter (ICAL), 2009.
- [49] JIS A 1310 standard test: 2015. Test method for fire propagation over building facades.
- [50] ASTM E 2058-13, Standard Test Methods for Measurement of Synthetic Polymer Material Flammability Using a Fire Propagation Apparatus (FPA). ASTM International, West Conshohocken, PA, 2013, DOI: 10.1520/E2058-13, [www.astm.org](http://www.astm.org).
- [51] ISO 12136:2011, Reaction to Fire tests – Measurement of Material Properties Using a Fire Propagation Apparatus. International Organization for Standardization, Geneva, Switzerland.
- [52] M. Chaos, M.M. Khan, N. Krishnamoorthy, J.L. de Ris, S.B. Dorofeev, Evaluation of optimization schemes and determination of solid fuel properties for CFD fire models using bench-scale pyrolysis tests, *Proceedings of the Combustion Institute* 33(2) (2011) 2599-2606.
- [53] M.M. Khan, J.L. De Ris, S.D. Ogden, Effect of moisture on ignition time of cellulosic materials, *Fire Safety Science* 9 (2008) 167-178.
- [54] M.U. Bromba, H. Ziegler, Application hints for Savitzky-Golay digital smoothing filters, *Analytical Chemistry* 53(11) (1981) 1583-1586.
- [55] K.-C. Tsai, Orientation effect on cone calorimeter test results to assess fire hazard of materials, *Journal of hazardous materials* 172(2-3) (2009) 763-772.
- [56] A. Kolbrecki, Model of fire spread out on outer building surface, *Bulletin of the Polish Academy of Sciences Technical Sciences* 63(1) (2015) 135-144.
- [57] E. Barreira, V.P. de Freitas, Experimental study of the hygrothermal behaviour of External Thermal Insulation Composite Systems (ETICS), *Building and environment* 63 (2013) 31-39.
- [58] S. Doroudiani, H. Omidian, Environmental, health and safety concerns of decorative mouldings made of expanded polystyrene

in buildings, *Building and environment* 45(3) (2010) 647-654.

[59] S. Bakhtiyari, L. Taghi-Akbari, M. Barikani, The effective parameters for reaction-to-fire properties of expanded polystyrene foams in bench scale, *Iran Polym J* 19 (2010) 27-37.

[60] X. Huang, Q. Wang, Y. Zhang, Y. Yin, J. Sun, Thickness effect on flame spread characteristics of expanded polystyrene in different environments, *Journal of Thermoplastic Composite Materials* 25(4) (2012) 427-438.

[61] Y.F. Chen, L. Yang, S. Zhuang, Study on the combustion characteristic of adhesive polystyrene, *Applied Mechanics and Materials*, Trans Tech Publ, 2014, pp. 191-193.

[62] A. Muthadhi, S. Kothandaraman, Experimental investigations on polymer-modified concrete subjected to elevated temperatures, *Materials and structures* 47(6) (2014) 977-986.

[63] H.Y. Zhang, V. Kodur, B. Wu, L. Cao, F. Wang, Thermal behavior and mechanical properties of geopolymer mortar after exposure to elevated temperatures, *Construction and Building Materials* 109 (2016) 17-24.

[64] U. Berardi, B.J. Meacham, N.A. Dembsy, Y.-G. You, Fire Performance Assessment of a Fiber Reinforced Polymer Wall Panel Used in a Single Family Dwelling, *Fire Technology* 50(6) (2014) 1607-1617.

[65] Q.T. Nguyen, P. Tran, T.D. Ngo, P.A. Tran, P. Mendis, Experimental and computational investigations on fire resistance of GFRP composite for building façade, *Composites Part B: Engineering* 62 (2014) 218-229.

[66] I.B. Pečur, D. Bjegović, L. Boström, B. Milovanović, M. Hajduković, ETICS fire performance test, *International Workshop on Performance, Protection & Strengthening of Structures Under Extreme Loading* (5; 2015), 2015.

[67] G.J. Griffin, A.D. Bicknell, G.P. Bradbury, N. White, Effect of construction method on the fire behavior of sandwich panels with expanded polystyrene cores in room fire tests, *Journal of fire sciences* 24(4) (2006) 275-294.

[68] Q. Xu, C. Jin, G. Griffin, Y. Jiang, Fire safety evaluation of expanded polystyrene foam by multi-scale methods, *Journal of Thermal Analysis and Calorimetry* 115(2) (2014) 1651-1660.

[69] H. Yoshioka, H.-C. Yang, M. Tamura, M. Yoshida, T. Noguchi, M. Kanematsu, K. Koura, Y. Ozaki, Study of Test Method for Evaluation of Fire Propagation along Façade Wall with Exterior Thermal Insulation, *Fire Science and Technology* 30(1) (2011) 27-44.

[70] H. Yoshioka, Y. Nishio, M. Tamura, M. Yoshida, T. Noguchi, Y. Ohmiya, M. Kanematsu, T. Ando, K. Koura, T. Tomatsu, Façade tests on fire propagation along combustible exterior wall systems, *Fire Science and Technology* 33(1) (2014) 1-15.

[71] Y. Nishio, H. Yoshioka, T. Noguchi, T. Ando, M. Tamura, Experimental study on fire propagation over combustible exterior facades in Japan, *MATEC Web of Conferences*, EDP Sciences, 2013, p. 04001.

[72] E. Mikkola, T. Hakkarainen, A. Matala, Fire safety of EPS insulated facades in residential multi-storey buildings, *MATEC Web of Conferences*, EDP Sciences, 2013, p. 04002.

[73] E. Antonatus, Fire safety of etics with EPS material properties and relevance for fire safety during transport, construction and under end use conditions in external thermal insulation component systems, *MATEC Web of Conferences*, EDP Sciences, 2013, p. 02008.

[74] M. Kumm, J. Söderström, A. Lönnermark, EPS insulated façade fires from a fire and rescue perspective, *MATEC Web of Conferences*, EDP Sciences, 2013, p. 05003.

[75] D. Bjegovic, I.B. Pecur, B. Messerschmidt, B. Milovanovic, M. Alagusic, Influence of fire barriers on fire performance of

facades with combustible insulation, MATEC web of conferences, EDP Sciences, 2016, p. 05006.

[76] M. Hajduković, N. Knez, F. Knez, J. Kolšek, Fire performance of external thermal insulation composite system (ETICS) facades with expanded polystyrene (EPS) insulation and thin rendering, *Fire Technology* 53(1) (2017) 173-209.

[77] B.N. Taylor, *Guidelines for Evaluating and Expressing the Uncertainty of NIST Measurement Results* (rev, DIANE Publishing 2009).

[78] M.M. Hirschler, Repeatability and reproducibility of fire tests for cigarette ignition of upholstered furniture composites, *Fire and materials* 22(1) (1998) 25-37.

[79] J. Urbas, BDMC interlaboratory cone calorimeter test programme, *Fire and materials* 26(1) (2002) 29-35.

[80] A. Tewarson, M. Khan, Flame propagation for polymers in cylindrical configuration and vertical orientation, *Symposium (International) on Combustion*, Elsevier, 1989, pp. 1231-1240.

[81] A. Tewarson, M. Khan, P.K. Wu, R.G. Bill, Flammability evaluation of clean room polymeric materials for the semiconductor industry, *Fire and materials* 25(1) (2001) 31-42.

[82] M. Delichatsios, K. Saito, Upward fire spread: key flammability properties, similarity solutions and flammability indices, *Fire Safety Science* 3 (1991) 217-226.

[83] V. Babrauskas, *The cone calorimeter*, SFPE handbook of fire protection engineering, Springer 2016, pp. 952-980.

[84] S. Yokoi, Temperature Distribution of Hot Gas Spurting out of the Window of Burning Concrete Building, pp.89-103, Japanese Ministry of Construction, Building Research Institute Report 34, 1960.

[85] P. Thomas, M. Law, The projection of flames from buildings on fire, *Fire Prevention Science and Technology* 10 (1972) 19-26.

[86] I. Oleszkiewicz, Heat transfer from a window fire plume to a building façade, *Asme Htd* 123 (1989) 163-170.

[87] J. Quintiere, T.G. Cleary, Heat flux from flames to vertical surfaces, *Fire Technology* 30(2) (1994) 209-231.

[88] Y. Ohmiya, Y. Hori, K. Safimori, T. Wakamatsu, Predictive method for properties of flame ejected from an opening incorporating excess fuel, *Fire Safety Science* 4 (2000) 375-386.

[89] J.-i. Yamaguchi, T. Tanaka, Temperature profiles of window jet plume, *Fire Science and Technology* 24(1) (2005) 17-38.

[90] K. Himoto, T. Tsuchihashi, Y. Tanaka, T. Tanaka, Modeling thermal behaviors of window flame ejected from a fire compartment, *Fire Safety Journal* 44(2) (2009) 230-240.

[91] Y.-P. Lee, M. Delichatsios, Y. Ohmiya, The physics of the outflow from the opening of an enclosure fire and re-examination of Yokoi's correlation, *Fire Safety Journal* 49 (2012) 82-88.

[92] L. Hu, F. Tang, M. Delichatsios, K. Lu, A mathematical model on lateral temperature profile of buoyant window spill plume from a compartment fire, *International Journal of Heat and Mass Transfer* 56(1-2) (2013) 447-453.

[93] F. Tang, L. Hu, M. Delichatsios, K. Lu, W. Zhu, Experimental study on flame height and temperature profile of buoyant window spill plume from an under-ventilated compartment fire, *International Journal of Heat and Mass Transfer* 55(1-3) (2012) 93-101.

[94] K. Lu, L. Hu, M. Delichatsios, F. Tang, Z. Qiu, L. He, Merging behavior of facade flames ejected from two windows of an under-ventilated compartment fire, *Proceedings of the Combustion Institute* 35(3) (2015) 2615-2622.

[95] K. Lu, J. Wang, L. Hu, Vertical temperature profile of fire-induced facade thermal plume ejected from a fire compartment

window with two adjacent side walls, *Applied Thermal Engineering* 113 (2017) 70-78.

[96] E.K. Asimakopoulou, D.I. Kolaitis, M.A. Founti, Geometrical characteristics of externally venting flames: Assessment of fire engineering design correlations using medium-scale compartment-façade fire tests, *Journal of Loss Prevention in the Process Industries* 44 (2016) 780-790.

[97] R.A. Bryant, Evaluating practical measurements of fire-induced vent flows with stereoscopic PIV, *Proceedings of the Combustion Institute* 33(2) (2011) 2481-2487.

[98] R.A. Bryant, A comparison of gas velocity measurements in a full-scale enclosure fire, *Fire Safety Journal* 44(5) (2009) 793-800.

[99] K.D. Steckler, J.G. Quintiere, W.J. Rinkinen, Flow induced by fire in a compartment, *Symposium (international) on combustion*, Elsevier, 1982, pp. 913-920.

[100] B. Karlsson, J. Quintiere, *Enclosure fire dynamics*, CRC press 1999.

[101] M.A. Delichatsios, G.W. Silcock, X. Liu, M. Delichatsios, Y.-P. Lee, Mass pyrolysis rates and excess pyrolysate in fully developed enclosure fires, *Fire Safety Journal* 39(1) (2004) 1-21.

[102] M.A. Delichatsios, Y.-P. Lee, P. Tofilo, A new correlation for gas temperature inside a burning enclosure, *Fire Safety Journal* 44(8) (2009) 1003-1009.

[103] R. Nilica, H. Harmuth, Mechanical and fracture mechanical characterization of building materials used for external thermal insulation composite systems, *Cement and Concrete Research* 35(8) (2005) 1641-1645.

[104] S.I. Stoliarov, S. Crowley, R.N. Walters, R.E. Lyon, Prediction of the burning rates of charring polymers, *Combustion and Flame* 157(11) (2010) 2024-2034.

[105] G. Linteris, Numerical simulations of polymer pyrolysis rate: Effect of property variations, *Fire and materials* 35(7) (2011) 463-480.

[106] M.B. McKinnon, S.I. Stoliarov, Pyrolysis model development for a multilayer floor covering, *Materials* 8(9) (2015) 6117-6153.

[107] Zhao X S, Sakamoto A, Nishio YH, Noguchi TF, Tamura MM, Yoshioka HK, Nakamura M, Modelling of upward flame spread on Exterior Insulation and Finish System, *Architectural Institute of Japan* 2014: 345-348. (In Japanese).

[108] M. Abdel-Aziz, A. Badran, A. Abdel-Hakem, F. Helaly, A. Moustafa, Styrene-butadiene rubber/lead oxide composites as gamma radiation shields, *Journal of applied polymer science* 42(4) (1991) 1073-1080.

[109] E. Grieco, M. Bernardi, G. Baldi, Styrene-butadiene rubber pyrolysis: Products, kinetics, modelling, *Journal of Analytical and Applied Pyrolysis* 82(2) (2008) 304-311.

[110] P. Rybiński, G. Janowska, M. Józwiak, M. Józwiak, Thermal stability and flammability of styrene-butadiene rubber (SBR) composites, *Journal of Thermal Analysis and Calorimetry* 113(1) (2013) 43-52.

[111] J. Troitzsch, *International plastics flammability handbook: principles-regulations-testing and approval*, Hanser 1983.

[112] K. Pielichowski, J. Njuguna, *Thermal degradation of polymeric materials*, iSmithers Rapra Publishing 2005.

[113] S. Mehta, S. Biederman, S. Shivkumar, Thermal degradation of foamed polystyrene, *Journal of Materials Science* 30(11) (1995) 2944-2949.



- [114] W.D. Baasel, Preliminary chemical engineering plant design, Van Nostrand Reinhold 1990.
- [115] M.K. Kumaran, International Energy Agency energy conservation in buildings and community systems programme Heat, air and moisture transfer through new and retrofitted insulated envelope parts:[IEA](Hamtie); Annex 24 Task 3/Final report: Material properties, Laboratorium Bouwfysica, Dep. Burgerlijke Bouwkunde, KU-Leuven, Leuven, Belgium 5 (1996) 23.
- [116] <https://m.cameochemicals.noaa.gov/>.
- [117] J. Hallman, J. Welker, C. Sliepcevich, Polymer surface reflectance-absorptance characteristics, Polymer Engineering & Science 14(10) (1974) 717-723.
- [118] P. Kannan, J.J. Biernacki, D.P. Visco Jr, W. Lambert, Kinetics of thermal decomposition of expandable polystyrene in different gaseous environments, Journal of Analytical and Applied Pyrolysis 84(2) (2009) 139-144.
- [119] P. Kusch, G. Knupp, Headspace-SPME-GC-MS identification of volatile organic compounds released from expanded polystyrene, Journal of Polymers and the Environment 12(2) (2004) 83-87.
- [120] Shemesh J, Yeoh GH. Development of a generalised EPS fire model. 1st Asia-Oceania symposium on fire safety materials science and engineering, 2015, Suzhou, China, pp.12-13.
- [121] Y. Hasemi, M. Yoshida, R. Kikuchi, E. Yamamoto, R. Takaike, Heat release rates measured by the cone calorimeter and intermediate scale electrical radiant panels, Thirteenth meeting of the ujn panel on fire research and safety, 1996.
- [122] M. Janssens, J. Urbas, Comparison of Small and Intermediate Scale Heat Release Data, Proceedings of Interflam, 1996, pp. 26-29.
- [123] F. Tamanini, Reaction rates, air entrainment and radiation in turbulent fire plumes, Combustion and Flame 30 (1977) 85-101.
- [124] H. You, G. Faeth, Buoyant axisymmetric turbulent diffusion flames in still air, Combustion and Flame 44(1-3) (1982) 261-275.
- [125] N. Crauford, S. Liew, J. Moss, Experimental and numerical simulation of a buoyant fire, Combustion and Flame 61(1) (1985) 63-77.
- [126] Y. Xin, J.P. Gore, K.B. McGrattan, R.G. Rehm, H.R. Baum, Fire dynamics simulation of a turbulent buoyant flame using a mixture-fraction-based combustion model, Combustion and Flame 141(4) (2005) 329-335.
- [127] T. Ma, J. Quintiere, Numerical simulation of axi-symmetric fire plumes: accuracy and limitations, Fire Safety Journal 38(5) (2003) 467-492.
- [128] H.-Y. Wang, M. Coutin, J.-M. Most, Large-eddy-simulation of buoyancy-driven fire propagation behind a pyrolysis zone along a vertical wall, Fire Safety Journal 37(3) (2002) 259-285.
- [129] R. Sun, M.A. Jenkins, S.K. Krueger, W. Mell, J.J. Charney, An evaluation of fire-plume properties simulated with the Fire Dynamics Simulator (FDS) and the Clark coupled wildfire model, Canadian Journal of Forest Research 36(11) (2006) 2894-2908.
- [130] S. Hostikka, G. Bytskov, Numerical simulations of the ISO 13785-2 façade fire tests, MATEC web of conferences, EDP Sciences, 2016, p. 03003.
- [131] FireFOAM. Available from: <https://github.com/fireFoam-dev>.
- [132] OpenFOAM, Available from: <http://www.opencfd.co.uk/openfoam/>.
- [133] G. Maragos, P. Rauwoens, B. Merci, Application of FDS and FireFOAM in large eddy simulations of a turbulent buoyant

helium plume, *Combustion Science and Technology* 184(7-8) (2012) 1108-1120.

[134] N. Ren, Y. Wang, A. Trouvé, Large eddy simulation of vertical turbulent wall fires, *Procedia Engineering* 62 (2013) 443-452.

[135] C. Wang, J. Wen, Z. Chen, Simulation of large-scale LNG pool fires using FireFoam, *Combustion Science and Technology* 186(10-11) (2014) 1632-1649.

[136] Y.P. Almeida, P.L. Lage, L.F.L. Silva, Large eddy simulation of a turbulent diffusion flame including thermal radiation heat transfer, *Applied Thermal Engineering* 81 (2015) 412-425.

[137] S. Vilfayeau, N. Ren, Y. Wang, A. Trouvé, Numerical simulation of under-ventilated liquid-fueled compartment fires with flame extinction and thermally-driven fuel evaporation, *Proceedings of the Combustion Institute* 35(3) (2015) 2563-2571.

[138] M. Chaos, M.M. Khan, N. Krishnamoorthy, P. Chatterjee, Y. Wang, S.B. Dorofeev, Experiments and modeling of single-and triple-wall corrugated cardboard: Effective material properties and fire behavior, *Fire and materials* (2011) 625-636.

[139] N. Ren, D. Zeng, K. Meredith, M. Chaos, Y. Wang, CFD Modeling of Fire Growth between Vertical Paper Rolls, *Proceedings of the Ninth US National Combustion Meeting*, Cincinnati, Ohio, 2015.

[140] F. Steward, Prediction of the height of turbulent diffusion buoyant flames, *Combustion Science and Technology* 2(4) (1970) 203-212.

[141] U. Piomelli, E. Balaras, Wall-layer models for large-eddy simulations, *Annual review of fluid mechanics* 34(1) (2002) 349-374.

[142] M. Hölling, H. Herwig, Asymptotic analysis of the near-wall region of turbulent natural convection flows, *Journal of Fluid Mechanics* 541 (2005) 383-397.

[143] X. Xue-fei, Z. Jing-yan, L. Yan-feng, A computational study on structural barrier to vertical spread of window spill plume along building exterior façade, *Procedia Engineering* 52 (2013) 475-482.

[144] M.P. Giraldo, A. Lacasta, J. Avellaneda, C. Burgos, Computer-simulation study on fire behaviour in the ventilated cavity of ventilated façade systems, *MATEC Web of Conferences*, EDP Sciences, 2013, p. 03002.

[145] M. Duny, D. Dhima, J. Garo, H. Wang, Numerical investigation on window ejected facade flames, *Journal of Building Engineering* 8 (2016) 305-312.

[146] C.L. Chow, Numerical studies on smoke spread in the cavity of a double-skin facade, *Journal of Civil Engineering and Management* 17(3) (2011) 371-392.

[147] J. Ivanović-Šekularac, J. Čikić-Tovarović, N. Šekularac, Application of wood as an element of façade cladding in construction and reconstruction of architectural objects to improve their energy efficiency, *Energy and Buildings* 115 (2016) 85-93.

[148] B. Östman, D. Brandon, H. Frantzich, Fire safety engineering in timber buildings, *Fire Safety Journal* 91 (2017) 11-20.

[149] D. Dhima, M. Duny, J.-P. Garo, H.-Y. Wang, Q. Jullien, Experimental Study on Vertical Wooden Façade Combustion, *Procedia Engineering* 210 (2017) 520-527.

[150] T. Hakkarainen, T. Oksanen, Fire safety assessment of wooden facades, *Fire and materials* 26(1) (2002) 7-27.

[151] B. Östman, L. Tsantaridis, Fire scenarios for multi-storey façades with emphasis on full-scale testing of wooden façades, *Fire Technology* 51(6) (2015) 1495-1510.

[152] G. Agarwal, M. Chaos, Y. Wang, D. Zeinali, B. Merci, Pyrolysis Model Properties of Engineered Wood Products and

Validation Using Transient Heating Scenarios, Proceedings of the 14th International Conference and Exhibition on Fire Science and Engineering, Interscience Communications, Royal Holloway College Nr Windsor, UK, 2016, pp. 143-154.

[153] D.C.O. Marney, L.J. Russell, Combined Fire Retardant and Wood Preservative Treatments for Outdoor Wood Applications – A Review of the Literature, *Fire Technology* 44(1) (2008) 1-14.

[154] M. Spearpoint, J. Quintiere, Predicting the burning of wood using an integral model, *Combustion and Flame* 123(3) (2000) 308-325.

# Acknowledgement

I am deeply grateful to my supervisor, Prof. Takafumi Noguchi, at the lab of Building Material Engineering, Department of Architecture, Graduate School of Engineering, The University of Tokyo for teaching and encouraging me throughout my graduate school years.

I thank Dr. Hideki Yoshioka at the National Institute for Land Infrastructure Management (NILIM) of Japan for the kind instruction and meaningful discussion throughout all experiments.

I gratefully acknowledge Prof. Yoshifumi Ohmiya from Tokyo University of Science, Prof. Ryozo Ooka, Prof. Ritsu Dobashi and Prof. Ryoma Kitagaki for the kind instruction and meaningful discussion of partial content.

I gratefully acknowledge Yi Wang, Ning Ren, Gaurav Agarwal and Dong Zeng from FM Global for the help on the short-term FM Global visit and FireFOAM discussion.

I thank Mr. Masamichi Tamura, Mr. Yutaka Tanaike and Mr. Tatsuo Ando from the University of Tokyo for preparation of the experiment. I gratefully acknowledge assistant professor Dr. Yuhei Nishio and students Miki Nakamura and Yuji Kanda from Tokyo University of Science for the help in façade experimental operation. I acknowledge the program of Research Fellowship for Young Scientists (DC2) which comes from Japan Society for the Promotion of Science for providing the fund for life and experiments. This work is supported by JSPS KAKENHI Grant Number JP17J00899.

I also thank Ms. Kumiko Sadamoto for the support of various office works and all the members of the labs for technical supports in experiments. I gratefully acknowledge Prof. Tomohiro Naruse for providing a study space in Building Research Institute of Japan for nearly two years.

Finally, I would like to thank my parents, wife and baby for their spiritual supports.